F-246

NASA Contractor Report 3893

Transition and Mixing in Axisymmetric Jets and Vortex Rings

Gary A. Allen, Jr., and Brian J. Cantwell

NASA

NASA Contractor Report 3893

Transition and Mixing in Axisymmetric Jets and Vortex Rings

Gary A. Allen, Jr., and Brian J. Cantwell

Stanford University
Stanford, California

NASA

National Aeronautics
and Space Administration

**Scientific and Technical
Information Branch**

1986

Entrance Stone To Newgrange Passage Grave Near Boyne River, Ireland [from M.J. O'Kelly].

ABSTRACT

A class of impulsively started, axisymmetric, laminar jets produced by a time dependent point source of momentum are considered. The jets studied are different flows, each initially at rest in an unbounded fluid. The time dependence of the point source of momentum categorizes the specific type of jet under investigation. The study of these flows is conducted at three levels of detail discussed below.

1. A generalized set of analytic creeping flow solutions are derived, along with a method of flow classification.

2. From this generalized set, there are three specific creeping flow solutions which are studied in detail: the vortex ring, the round jet, and the ramp jet. This detailed study involves derivation of vorticity, stream function, entrainment diagrams, and evolution of time lines through computer animation. From the entrainment diagrams, critical points are derived and analyzed. It was found that flow geometry was dictated by the properties and location of these critical points. In addition, these critical points undergo bifurcation and topological transformation with changing Reynolds number. These bifurcations and transformations represent a form of transition for which specific Reynolds numbers were calculated. A state space trajectory was derived describing the topological behavior of these critical points. This state space derivation was based on continuity, and boundary

conditions, and was performed prior to actual solution of the momentum equation. From this state space derivation it was found that three states of motion are universal for all axisymmetric jets.

3. The third level of study examines the axisymmetric round jet which was solved numerically using the unsteady laminar Navier Stokes equations. These equations were shown to be self similar for the round jet. The boundary conditions used in this numerical solution are the steady solution of the round jet discovered by Landau (1944), and the unsteady dipole. The numerical method utilized a second order central difference scheme solved by an implicit matrix method. The matrix solver was a direct method which used a new forward-backward technique that greatly reduced storage requirements. The numerical method solved the round jet up to a Reynolds number of 30 for a 60×60 point mesh. From the data generated, computer animations were produced. These animations showed each of the three states of motion for the round jet, including the $Re = 30$ case.

TABLE OF CONTENTS

LIST OF FIGURES

LIST OF TABLES

LIST OF SYMBOLS

a		Taylor series coefficient
a_{ii}		A_j submatrix element
A		Landau-Squire constant
A_j		subblock matrix, main diagonal
A_m	App. A	Fourier coefficient
b		Taylor series coefficient
b_{ii}^k		B_j^k subvector element
B		finite difference Navier Stokes equation term
$\vec{B}$		vector potential
$\tilde{B}$		finite difference vorticity
B_r		vector potential magnitude in the radial direction
B_θ		vector potential magnitude in the θ direction
B_ϕ		vector potential magnitude in the ϕ direction
B_j^k		subblock matrix, off diagonal
B_m	App. A	second order pole independent solution of J_m
c		Taylor series coefficient
c_k		coefficient used in spline polynomial
c_j	App. A	dummy coefficient used in series solution
c_k	App. A	dummy coefficient used in series solution
c_m	App. A	series end coefficient

C		finite difference Navier Stokes equation term
$\widetilde{C}$		finite difference vorticity
d		Taylor series coefficient
D		finite difference Navier Stokes equation term
$\widetilde{D}$		finite difference vorticity equation term
D_1		dipole coefficient
D_j		multipole coefficient (tesseral)
D_m	App. A	hard driver polynomial
$D_m^{(B)}$	App. A	hard driver polynomial of second order pole type
$D_m^{(G)}$	App. A	hard driver polynomial of first order pole type
$\hat{e}_r$		spherical polar unit vector in radial direction
$\hat{e}_x$		Cartesian unit vector in the x direction
$\hat{e}_y$		Cartesian unit vector in the y direction
$\hat{e}_\theta$		spherical polar unit vector in the θ direction
$\hat{e}_\phi$		spherical polar unit vector in the ϕ direction
E		finite difference Navier Stokes equation term
$\widetilde{E}$		finite difference vorticity equation term
E_m	App. A	easy polynomial, positive m type
$\bar{E}_m$	App. A	hard function, positive m type
$E_m^{(B)}$	App.A	positive m type easy polynomial, 2nd order pole
$E_m^{(G)}$	App.A	positive m type easy polynomial, 1st order zero

I		impulse
j		node point index in θ direction
j	App. A	dummy integer index
J		force
J	App. A	vorticity radial component (jet function)
J_m	App. A	jet function with index
k		step size in θ direction
k	App. A	dummy integer index
$\hat{k}$	App. A	forcing rate
K		forcing rate
l		dummy integer index
L		length unit
L_j		transfer matrix
m		jet function index
M	App. A	confluent hypergeometric function
M		finite difference Navier Stokes equation term
n		number of node points (one direction)
n	App. A	dummy integer index
N		finite difference Navier Stokes equation term
$\tilde{N}$		finite difference vorticity equation term
p		state space coordinate
p'		transformed pressure p

$\hat{p}$		fluid pressure
$p_{\theta_c = 0}$		on-axis value of state space p
P	App. A	Legendre polynomial
$\hat{P}$		momentum source strength
$P_l{}^1$		first order associated Legendre polynomial
q		state space coordinate
$q_{\theta_c \neq 0}$		off-axis value of state space q
Q		square triblock matrix
r		radius
r'		transformed radius
R		transformed boundary condition vector
R	App. A	radial component of the stream function
$\tilde{R}$		finite difference vorticity equation term
R_j		transfer vector
R_1		vorticity radial dipole component
Re		Reynolds number
Re_1		first transition Reynolds number
Re_2		second transition Reynolds number
S	App. A	self similar radial coordinate
t		time
t'		transformed time t
T		time unit

u	velocity in the radial direction (same as u_r)
$\hat{u}(t)$	heaviside step function
u_i	velocity vector, tensor form
$u_i{}'$	transformed velocity u_i
$\vec{u}$	velocity vector
u_r	velocity magnitude in the radial direction
u_θ	velcoity magnitude in the θ direction
u_ϕ	velcoity magnitude in the ϕ direction
U	self similar radial velocity
U	square upper triangular form matrix
U_j	transfer matrix
v	velocity in the θ direction
V	self similar θ velocity
W	self similar vorticity
$\tilde{W}$	transformed vorticity
$\overline{W}$	computed vorticity
x	self similar Cartesian coordinate
$\overline{x}$	physical space Cartesian coordinate
x_{ij}	X_j sub vector element
x_i	Cartesian position vector tensor form
$x_i{}'$	transformed Cartesian vector x_i
$\vec{x}$	position vector

y	self similar Cartesian coordinate
$y_{i,j}$	Y_j subvector element
$\vec{y}$	dummy vector
$\overline{y}$	physical space Cartesian coordinate
Y	vorticity solution variable
$\overline{Y}$	boundary condition vector
Y_j	subblock vector, boundary conditions
$Y_{i,j}$	vorticity variable in discrete form
Z	stream function solution variable
$Z_{i,j}$	stream function variable in discrete form

Greek Symbols

α		vorticity nonlinear scale function
α	App. A	dummy index
$\tilde{\alpha}$		dummy parameter
β		stream function nonlinear scale function
$\tilde{\beta}$		dummy parameter
γ		body force potential
$\tilde{\gamma}$		body force potential
Γ		off-axis q coefficient
δ		stretched angular coordinate
$\hat{\delta}(t)$		Dirac delta function
$\delta(t)$	App. A	Dirac delta function
ΔR_1		vorticity radial dipole component error
ΔW		vorticity error
ϵ		perturbation value
$\tilde{\epsilon}$		dummy parameter
η		switch-over angle parameter
$\tilde{\eta}$		angular coordinate (cosine)
θ		angular coordinate
$\tilde{\theta}$		switch-over angle
θ_c		critical point θ coordinate

θ_n		θ angle present value
θ_{n+1}		θ angle next guess
λ		rate-of-stretch knob
λ	App. A	dummy variable used in generating function
Λ		off-axis q coefficient
Λ_m	App. A	orthogonality normalizing constant
T		under relaxation constant
$\tilde{\mu}$		dummy parameter
ν		kinematic viscosity
ρ		fluid density
τ	App. A	natural log of time
ξ		self similar radial coordinate
ξ_c		critical point ξ coordinate
ξ_∞		far field boundary coordinate
$\hat{\xi}_c$		off-axis ξ_c value
π		classic pi, circumference divided by diameter
ϕ		angular coordinate
Φ	App. A	generalized function
ψ		axisymmetric stream function
ψsp		transformed axisymmetric stream function
$\psi_{potential}$	App. A	irrotational axisymmetric stream functions
ω		vorticity in the phi direction (same as ω_ϕ)

$\vec{\omega}$		vorticity vector
ω_r		vorticity magnitude in the radial direction
ω_θ		vorticity magnitude in the theta direction
ω_ϕ		vorticity magnitude in the phi direction
$\Omega_m^{(B)}$	App. A	generating function for B_m
$\Omega_m^{(G)}$	App. A	generating function for G_m

Chapter I

INTRODUCTION

Fascination with fluid motion has been an activity of mankind since earliest history. The photograph on the front page of this thesis is from the Newgrange passage grave in the Boyne Valley, Ireland. The tomb was constructed by preliterate rule-of-thumb engineers around 2500 BC (almost as old as the Great Pyramid of Egypt), and is covered with swirls and spirals that might easily be described by the topological methods used in this thesis. One can imagine these ancient engineers looking into the Boyne river not far from the tomb, seeing vortices and eddies forming in the water, and while contemplating both their beauty and complexity, reproducing them on the walls of the tombs. Our work is a continuation of this ancient fascination, employing newly developed techniques for understanding how and why these shapes are formed.

1. Objectives Of The Research

The fundamental philosophy of the research was to study flows of such simple geometry that they would be mathematically tractable and yet of sufficient complexity that many of the basic motions of viscous unsteady fluid flow would appear. This led to the study of an infinite fluid with a point momentum disturbance. Three simplifying assumptions that were made in studying this flow are: incompressibility, Newtonian fluid, and axisymmetry.

2. History Of The Study Of Axisymmetric Jets

The earliest analytic realization of this type of flow was by M.J.M. Hill who published the spherical vortex solution of the Navier Stokes equations in 1894. The next major analytic breakthrough was the exact solution of steady round jet found by L.D. Landau in 1944 with an independent discovery by H.B. Squire in 1951. Probably the first numerical study of the unsteady round jet was performed by Ma and Ong in 1971. Their method was formulated in cylindrical coordinates and carried out with the primary aim of computing the propagation of the jet front into stagnant fluid. Following this work a linearized analytic solution (Stokes solution) of the unsteady jet was found by C. Sozou in 1979. This was preceded by a numerical solution in spherical coordinates by C. Sozou and W.M. Pickering (1971) of the unsteady round jet up to a Reynolds number of 12.5. The work of Sozou and Pickering advanced understanding of the axisymmetric round jet but failed to address several key aspects of this flow. Most important of these was that, while the flow had been solved in terms of the unsteady stream function, none of the flow topology becomes apparent unless the flow is studied in terms of its unsteady particle paths. It was found by B. Cantwell in 1980 that the topology of particle paths undergoes critical point bifurcation and transformation at certain key Reynolds numbers. This discovery was made using the linearized Stokes solution found earlier by Sozou. The application of critical point theory to fluid mechanics was in itself not a new idea. Poincare himself had made applications of this theory to fluid study (circa 1880). More recently, Oswatitsch (1958) and Lighthill (1963) classified certain critical points which can occur near a rigid boundary. A.E. Perry and B.D. Fairlie (1974) were one of the earliest researchers to use critical point theory in the context

of A.A. Andronov's (1971) p, q state space maps for studying fluid mechanics. Cantwell used the p, q map as a means of quantitatively understanding the critical point bifurcation process as a form of transition. Questions were raised as to whether the technique could be applied to a numerical computation of the nonlinear round jet and as to the role of nonlinearity in the transition process. This is where the present work entered the tale of events.

3. Problem Approach

It was felt early in the study that a different approach from that of Sozou and Pickering would have to be taken. Our own goal was to fully describe the transition process and to push the Reynolds number as high as possible based on available computer resources. Though our method is extremely stable it is also expensive (the usual tradeoff), and was stopped at Re = 30.0 although higher Reynolds numbers could be computed at added cost. This value is more than double the highest Reynolds number previously reported by Sozou and Pickering, which was Re = 12.50. Our prime objective was to apply topological methods to the numerically solved axisymmetric jet. As with the linearized solution, it was found that the numerical solution undergoes only two (topological) transitions with Reynolds number, and after the second and last transition (which occurs at Re = 7.54) the topology remains unchanged at all higher computed Reynolds numbers. It should be emphasized that this topological invariance is a consequence of the assumption of axisymmetry, and it is suspected that a non-axisymmetric round jet would be subject to an infinite sequence of transitions and concomitant great topological complexity. As shall later be discussed, since the round jet has a similarity solution its

stream function or particle paths for a given Reynolds number can be represented in a single plot which is valid for all time. Since, at a given Reynolds number, the entire flow history can be very compactly stored and manipulated, it was apparent that this flow lent itself well to making computer animations. These computer animations were found to be indispensable aids in understanding the flow dynamics and as teaching aids.

4. Cases For Study

Another aspect of the study was that, with the exception of autonomous flows like the round jet and special cases like the Hill's spherical vortex, jet flows cannot, in general, be represented by self similar coordinates. On the other hand, it was found that all jet flows are self similar in the creeping (Re → 0) approximation where the Navier-Stokes equations reduce to the Stokes equations. This discovery essentially opened up a whole new line of inquiry in devising solutions to these creeping flows. In this thesis, two creeping flows were studied in considerable detail, along with the round jet. These flows are the vortex ring and its complementary flow, the ramp jet. The family of creeping flows was also studied in a wider sense and generalized solutions for an infinite variety a flow types are provided. The discovery of these generalized solutions, coupled with the capability of computer animation, has now provided the investigator with a new form of fluid experimentation. Though the computer can never replace the laboratory in studying fluids, the computer can provide very "clean" flows in the context of no outside perturbations or unwanted boundary conditions.

Chapter II

PROBLEM DEFINITION

1. Fundamental Assumptions and Equation Formulation

The Navier Stokes equation is cast in the following form:

$$\frac{D\vec{u}}{Dt} = \frac{-\nabla \hat{p}}{\rho} + \vec{g} + \nu \nabla^2 \vec{u} \qquad (2.1)$$

where $\vec{u}$ is the velocity vector, $\hat{p}$ is pressure, ρ is density, $\vec{g}$ is the body force vector, and ν is kinematic viscosity. Equation (2.1) already contains assumptions of incompressibility, and a Newtonian constitutive relation with constant viscosity. It is desired to convert Eq. (2.1) into a vorticity form so as to remove pressure and the body force from the equation.

The following vector identities will be used in the development and are given without proof:

$$y \times (\nabla \times \vec{y}) = \frac{1}{2}\nabla (\vec{y} \cdot \vec{y}) - \vec{y} \cdot \nabla \vec{y} \qquad (2.2)$$

$$\nabla \times \nabla f = 0 \qquad (2.3a)$$

$$\nabla \cdot (\nabla \times \vec{y}) = 0 \qquad (2.3b)$$

$$\nabla^2 \vec{y} = \nabla (\nabla \cdot \vec{y}) - \nabla \times (\nabla \times \vec{y}) \qquad (2.4)$$

$$\nabla \times (\vec{y} \times \vec{z}) = \vec{y}(\nabla \cdot \vec{z}) - \vec{z}(\nabla \cdot \vec{y}) + (\vec{z} \cdot \nabla)\vec{y} - (\vec{y} \cdot \nabla)\vec{z} \qquad (2.5)$$

where $\vec{y}, \vec{z}$ are vector quantities, and f is a scalar.

For an incompressible fluid the continuity equation becomes

$$\nabla \cdot \vec{u} = 0 . \qquad (2.6)$$

Vorticity is defined as

$$\nabla \times \vec{u} = \vec{\omega} . \qquad (2.7)$$

Combining equations (2.7) and (2.3b) shows that the vorticity is solenoidal

$$\nabla \cdot \vec{\omega} = 0 . \qquad (2.8)$$

The body force vector is assumed to be derivable from a potential function

$$\vec{g} = -\nabla \gamma \qquad (2.9)$$

where γ is a scalar function. Equation (2.2) is employed replacing $\vec{y}$ with $\vec{u}$ and combined with (2.1) via the material derivative convective term. Equation (2.9) is also combined with (2.1), along with (2.7) giving

$$\frac{\partial \vec{u}}{\partial t} - \vec{u} \times \vec{\omega} = -\nabla \left[\frac{p}{\rho} + \gamma + \frac{(\vec{u} \cdot \vec{u})}{2} \right] + \nu \nabla^2 \vec{u} . \qquad (2.10)$$

The curl is taken of (2.10). The identity of (2.3a) eliminates all of the gradient quantities of (2.10), and use of (2.4) with (2.6) and (2.8) proves that curl and the Laplacian commute for this particular problem. The result becomes

$$\frac{\partial \vec{\omega}}{\partial t} - \nabla \times (\vec{u} \times \vec{\omega}) = \nu \nabla^2 \vec{\omega} . \qquad (2.11)$$

Equation (2.5) is now employed with (2.6) and (2.8) along with the definition of the material derivative, changing (2.11) into

$$\frac{D\vec{\omega}}{Dt} = (\vec{\omega} \cdot \nabla)\,\vec{u} + \nu\,\nabla^2\vec{\omega}\ . \tag{2.12}$$

Equation (2.12) is the basic equation for this study in vector notation. Spherical polar coordinates are selected as the appropriate coordinate system. Let

$$\vec{\omega} = \omega_r\,\hat{e}_r + \omega_\theta\,\hat{e}_\theta + \omega_\phi\,\hat{e}_\phi \tag{2.13}$$

$$\vec{u} = u_r\,\hat{e}_r + u_\theta\,\hat{e}_\theta + u_\phi\,\hat{e}_\phi \tag{2.14}$$

where $\hat{e}_r,\ \hat{e}_\theta,\ \hat{e}_\phi$ are spherical polar unit vectors, and $\omega_r,\ \omega_\theta,\ \omega_\phi,\ u_r,$ $u_\theta,$ and u_ϕ are scalar quantities. In spherical polar coordinates, (2.12) becomes

$$\frac{\partial \omega_r}{\partial t} = \vec{\omega} \cdot \nabla u_r - \vec{u} \cdot \nabla \omega_r + \tag{2.15}$$

$$+ \nu \left[\nabla^2\omega_r - \frac{2\omega_r}{r^2} - \frac{2}{r^2 \sin \theta} \frac{\partial(\omega_\theta \sin \theta)}{\partial \theta} - \frac{2}{r^2 \sin \theta} \frac{\partial \omega_\phi}{\partial \phi} \right]$$

$$\frac{\partial \omega_\theta}{\partial t} = \vec{\omega} \cdot \nabla u_\theta - \vec{u} \cdot \nabla \omega_\theta + \frac{1}{r}(\omega_\theta u_r - u_\theta \omega_r) +$$

$$+ \nu \left[\nabla^2\omega_\theta + \frac{2}{r^2} \frac{\partial \omega_r}{\partial \theta} - \frac{\omega_\theta}{r^2 \sin^2 \theta} - \frac{2 \cos \theta}{r^2 \sin^2 \theta} \frac{\partial \omega_\phi}{\partial \phi} \right] \ . $$

$$\tag{2.16}$$

$$\frac{\partial \omega_\phi}{\partial t} = \vec{\omega} \cdot \nabla u_\phi - \vec{u} \cdot \nabla \omega_\phi + \frac{1}{r} (\omega_\phi u_r - u_\phi \omega_r) + \tag{2.17}$$

$$+ \frac{\cot \theta}{r} \left(\omega_\phi u_\theta - \omega_\theta u_\phi \right) +$$

$$+ \nu \left[\nabla^2 \omega_\phi + \frac{2}{r^2 \sin \theta} \frac{\partial \omega_r}{\partial \phi} + \frac{2 \cos \theta}{r^2 \sin^2 \theta} \frac{\partial \omega_\theta}{\partial \phi} - \frac{\omega_\phi}{r^2 \sin^2 \theta} \right] \quad .$$

These equations should be used in conjunction with the vector potential equation so as to ensure that continuity (2.6) is satisfied. The vector potential is defined as

$$\vec{u} = \nabla \times \vec{B} \quad . \tag{2.18}$$

By identity (2.3b) it can be seen that continuity is satisfied. Equation (2.18) is expanded into spherical polar coordinates giving

$$u_r = \frac{1}{r \sin \theta} \left(\frac{\partial (B_\phi \sin \theta)}{\partial \theta} - \frac{\partial B_\theta}{\partial \phi} \right) \tag{2.19}$$

$$u_\theta = \frac{1}{r} \left(\frac{1}{\sin \theta} \frac{\partial B_r}{\partial \phi} - \frac{\partial (r B_\phi)}{\partial r} \right) \tag{2.20}$$

$$u_\phi = \frac{1}{r} \left(\frac{\partial (r B_\theta)}{\partial r} - \frac{\partial B_r}{\partial \theta} \right) \tag{2.21}$$

where

$$\vec{B} = B_r \, \hat{e}_r + B_\theta \, \hat{e}_\theta + B_\phi \, \hat{e}_\phi \tag{2.22}$$

The definition of vorticity (2.7) is similarly expanded giving

$$\omega_r = \frac{1}{r \sin \theta} \left[\frac{\partial(u_\phi \sin \theta)}{\partial \theta} - \frac{\partial u_\theta}{\partial \phi} \right] \tag{2.23}$$

$$\omega_\theta = \frac{1}{r} \left[\frac{1}{\sin \theta} \frac{\partial u_r}{\partial \phi} - \frac{\partial(r u_\phi)}{\partial r} \right] \tag{2.24}$$

$$\omega_\phi = \frac{1}{r} \left[\frac{\partial(r u_\theta)}{\partial r} - \frac{\partial u_r}{\partial \theta} \right] \tag{2.25}$$

Equations (2.15) to (2.25) represent the complete set of equations necessary to solve the unsteady nonaxisymmetric incompressible Navier Stokes problem. However, it is plain that these equations are very complex and a further simplification is desirable. This next approximation is the assumption of axisymmetry

$$\frac{\partial}{\partial \phi} = 0 \ ,$$

and no swirl

$$u_\phi = 0 \ .$$

Both of these approximations are often lumped together as the assumption of axisymmetry, without specifically mentioning "no swirl" which in principle could occur in an axisymmetric problem. With this approximation equations (2.24), (2.23), (2.21), (2.15), and (2.16) disappear. The remaining set becomes

$$\frac{\partial \omega_\phi}{\partial t} \;=\; -\left(u_r \; \frac{\partial \omega_\phi}{\partial r} + \frac{u_\theta}{r} \; \frac{\partial \omega_\phi}{\partial \theta} \right) + \frac{\omega_\phi \, u_r}{r} + \tag{2.26}$$

$$+ \; \frac{\cot \theta}{r} \; \omega_\phi \, u_\theta \; + \nu \left[\nabla^2 \omega_\phi - \frac{\omega_\phi}{r^2 \sin^2 \theta} \right]$$

$$u_r \;=\; \frac{1}{r \sin \theta} \; \frac{\partial (B_\phi \sin \theta)}{\partial \theta} \tag{2.27}$$

$$u_\theta \;=\; -\frac{1}{r} \; \frac{\partial (r \, B_\phi)}{\partial r} \tag{2.28}$$

$$\omega_\phi \;=\; \frac{1}{r} \left(\frac{\partial (r u_\theta)}{\partial r} - \frac{\partial u_r}{\partial \theta} \right) \; . \tag{2.29}$$

2. Governing Equations

A further simplification is possible if (2.26) is combined with continuity (2.6) to eliminate some terms and if the Stokes stream function is defined as

$$\psi(r,\theta) \;=\; r \sin \theta \, B_\phi \; . \tag{2.30}$$

To simplify notation, subscripts are dropped with the following redefinitions: $\omega_\phi = \omega, \;\; u_r = u, \;\; u_\theta = v.$

The equations of motion become

$$\frac{\partial}{\partial t} (r \omega) \; + \; \frac{\partial}{\partial r} (r u \omega) \; + \; \frac{\partial}{\partial \theta} (v \omega) \tag{2.31}$$

$$=\; \nu \left\{ \frac{1}{r} \frac{\partial}{\partial \theta} \left[\frac{1}{\sin \theta} \frac{\partial}{\partial \theta} \left(\omega \sin \theta \right) \right] + \frac{\partial^2}{\partial r^2} \left(r \omega \right) \right\}$$

$$u = \frac{1}{r^2 \sin\theta} \frac{\partial\psi}{\partial\theta} \qquad (2.32)$$

$$v = \frac{-1}{r \sin\theta} \frac{\partial\psi}{\partial r} \qquad (2.33)$$

$$r\omega = \frac{\partial}{\partial r}(rv) - \frac{\partial u}{\partial\theta} . \qquad (2.34)$$

3. Self Similarity

To bring about even further simplification it is desirable to find a self similar

form. Self similarity can be deduced by finding a transformation for which the

Navier Stokes equations and the boundary conditions are invariant. To find this

transformation, (2.1) is cast into a Cartesian tensor form

$$\frac{\partial u_i}{\partial t} + u_j \frac{\partial u_i}{\partial x_j} = \frac{-1}{\rho} \frac{\partial p}{\partial x_i} + g_i + \nu \frac{\partial^2 u_i}{\partial x_j \partial x_j} \qquad (2.35)$$

where x_i is a Cartesian coordinate. The Navier Stokes equations can be sub-

jected to a stretching transformation by the following change of variables:

$$u_i = \tilde{\alpha} u_i' \qquad (2.36)$$

$$x_i = \tilde{\beta} x_i' \qquad (2.37)$$

$$t = \tilde{\gamma} t' \qquad (2.38)$$

$$p = \tilde{\mu} p' \qquad (2.39)$$

$$g_i = \tilde{\epsilon} g_i' \qquad (2.40)$$

One may insert equations (2.36) - (2.40) into (2.35) giving:

$$\left(\frac{\tilde{\alpha}}{\tilde{\gamma}}\right)\frac{\partial u_i'}{\partial t'} + \left(\frac{\tilde{\alpha}^2}{\tilde{\beta}}\right)u_j'\frac{\partial u_i'}{\partial x_j'} \qquad (2.41)$$

$$= \quad -\left(\frac{\tilde{\mu}}{\tilde{\beta}}\right)\frac{1}{\rho}\frac{\partial p'}{\partial x_i'} + (\tilde{\epsilon})g_i' + \left(\frac{\tilde{\alpha}}{\tilde{\beta}^2}\right)\nu\frac{\partial^2 u_i'}{\partial x_j'\,\partial x_j'} \quad .$$

For (2.41) to be invariant under the transformation the following must be true:

$$\frac{\tilde{\alpha}}{\tilde{\gamma}} = \frac{\tilde{\alpha}^2}{\tilde{\beta}} = \frac{\tilde{\mu}}{\tilde{\beta}} = \tilde{\epsilon} = \frac{\tilde{\alpha}}{\tilde{\beta}^2} \quad . \qquad (2.42)$$

Replacing (2.42) into (2.36) - (2.40) forms the following Lie group:

$$u_i = \tilde{\alpha}\,u_i' \qquad (2.43)$$

$$x_i = \tilde{\alpha}^{-1}\,x_i' \qquad (2.44)$$

$$t = \tilde{\alpha}^{-2}t' \qquad (2.45)$$

$$p = \tilde{\alpha}^2 p' \qquad (2.46)$$

$$g_i = \tilde{\alpha}^3 g_i' \quad . \qquad (2.47)$$

By the Pythagorean theorem the spherical polar radial coordinate has the same invariance as (2.44):

$$r = \tilde{\alpha}^{-1} r' \quad . \tag{2.48}$$

Combining (2.48) with (2.43) and (2.32) the stream function transformation is

$$\psi = \tilde{\alpha}^{-1} \psi' \quad . \tag{2.49}$$

The transformation of (2.43) - (2.49) shows that the Navier Stokes equation will admit a solution that is invariant under the stretching (2.43) - (2.47). However not all solutions of the Navier Stokes equation have this property of invariance and to determine whether a particular solution has this property (without actually solving the equations) one must also examine the invariance properties of the boundary conditions. The boundary conditions of an unsteady axisymmetric jet are as follows.

For the far field r → ∞ the solution goes to an unsteady dipole:

$$\psi = \frac{\nu^2 t \, \text{Re}^2}{4\pi r} \sin^2 \theta \quad . \tag{2.50}$$

For the near field r → 0 the solution goes to the steady Landau Squire solution:

$$\psi = \nu r \left[\frac{2 \sin^2 \theta}{A - \cos \theta} \right] \tag{2.51a}$$

where A is a parameter which depends on the Reynolds number, Re.

$$\frac{\text{Re}^2}{16\pi} = A + \frac{4}{3} \frac{A}{A^2 - 1} - \frac{A^2}{2} \ln \left[\frac{A+1}{A-1} \right] \quad . \tag{2.51b}$$

By inserting (2.48) and (2.45) into (2.50) and (2.51a), it can be seen that these equations satisfy the transformation of (2.49). It can now be concluded that an axisymmetric round jet solution can be found that is invariant under the stretching transformations of (2.43) - (2.47).

The analysis just performed can also be done on the linearized version of (2.35) which is

$$\frac{\partial u_i}{\partial t} = \frac{-1}{\rho} \frac{\partial p}{\partial x_i} + g_i + \nu \frac{\partial^2 u_i}{\partial x_j \partial x_j} \quad . \tag{2.52}$$

The analogue of (2.42) for the linear case is

$$\frac{\tilde{\alpha}}{\tilde{\gamma}} = \frac{\tilde{\mu}}{\tilde{\beta}} = \tilde{\epsilon} = \frac{\tilde{\alpha}}{\tilde{\beta}^2} \quad . \tag{2.53}$$

The consequent group is

$$u_i = \tilde{\alpha} \, u_i' \tag{2.54}$$

$$x_i = \tilde{\beta} \, x_i' \tag{2.55}$$

$$t = \tilde{\beta}^2 \, t' \tag{2.56}$$

$$p = \frac{\tilde{\alpha}}{\tilde{\beta}} \, p' \tag{2.57}$$

$$g_i = \frac{\tilde{\alpha}}{\tilde{\beta}^2} \, g_i' \quad . \tag{2.58}$$

Without the convective term the problem is underdetermined leaving two coefficients $\tilde{\alpha}$ and $\tilde{\beta}$ in the group of (2.54) - (2.58). This is a happy consequence since the additional parameter $\tilde{\beta}$ allows one to satisfy a wider class of boundary conditions. For this reason the linear (creeping) solutions are invariant under the two-parameter stretching transformation (2.54) - (2.58). Now that the invariant group is established it is possible to derive the self similar forms. Both (2.45), (2.44) and (2.55), (2.56) lead to:

$$\frac{x_i}{\sqrt{t}} \;=\; \frac{\tilde{\alpha}^{-1} x_i'}{\sqrt{\tilde{\alpha}^{-2} t'}} \;=\; \frac{\tilde{\beta} x_i'}{\sqrt{\tilde{\beta}^2 t'}} \;=\; constant \qquad (2.59)$$

The Pythagorean theorem with judicious selection of a constant transforms (2.59) into the self similar spherical polar radial coordinate

$$\xi \;=\; \frac{r}{\sqrt{\nu t}} \; . \qquad (2.60)$$

By similar reasoning, (2.49) and (2.45) give

$$\frac{\psi}{t^{\frac{1}{2}}} \;=\; \frac{\tilde{\alpha}^{-1} \psi'}{(\tilde{\alpha}^{-2} t')^{\frac{1}{2}}} \;=\; constant \; . \qquad (2.61)$$

Again by appropriate selection of a constant, (2.61) can be converted into a dimensionless self similar stream function $G(\xi, \theta)$

$$\psi(r, \theta) \;=\; \hat{P} \, \nu^{-\frac{1}{2}} \, t^{\frac{1}{2}} \, G(\xi, \theta) \qquad (2.62)$$

where $\hat{P}$ in the case of a jet would be the strength of the momentum source.

This process can be performed on all the dependent variables of the transform group. A more generalized system of self similar dimensionless variables uses the Stokes solution group of equations, (2.54) - (2.58), where

$$\tilde{\alpha} = \tilde{\beta}^{\,2m-1} . \qquad (2.63)$$

This in turn gives the following dimensionless self similar variables

$$u\,(r,\,\theta) = \hat{P}\,\nu^{-\frac{3}{2}}\,t^{m-\frac{1}{2}}\,U\,(\xi,\,\theta) \qquad (2.64)$$

$$v\,(r,\,\theta) = \hat{P}\,\nu^{-\frac{3}{2}}\,t^{m-\frac{1}{2}}\,V(\xi,\,\theta) \qquad (2.65)$$

$$\psi(r,\,\theta) = \hat{P}\,\nu^{-\frac{1}{2}}\,t^{m+\frac{1}{2}}\,G\,(\xi,\,\theta) \qquad (2.66)$$

$$\omega\,(r,\,\theta) = \hat{P}\,\nu^{-2}\,t^{m-1}\,W\,(\xi,\,\theta) . \qquad (2.67)$$

4. The Creeping Flow, Re → 0 Analysis

The variables of (2.64) - (2.67) are equivalent to those derived from the Navier Stokes solution group of (2.43) - (2.47) for the case m = 0 and when inserted into the Navier Stokes equations eliminate the time. This shall be done in Chapter V where the finite difference equations will be derived. Of more immediate interest is the Stokes equation. The equations of (2.31) - (2.34) can be used to describe creeping flow or Stokes flow if the nonlinear convective terms of

(2.31) is removed. These equations, when combined with (2.64) - (2.67), give

$$\frac{\partial}{\partial \xi} \left[\xi^2 \frac{\partial W}{\partial \xi} \right] + \xi^3 \frac{\partial W}{\partial \xi} + \frac{1}{\sin \theta} \frac{\partial}{\partial \theta} \left[\sin \theta \frac{\partial W}{\partial \theta} \right]$$

$$- \left[\frac{1}{\sin^2 \theta} + (m-1)\xi^2 \right] W = 0 \qquad (2.68)$$

$$U = \frac{1}{\xi^2 \sin \theta} \frac{\partial G}{\partial \theta} \qquad (2.69)$$

$$V = \frac{-1}{\xi \sin \theta} \frac{\partial G}{\partial \xi} \qquad (2.70)$$

$$-\xi W = \frac{\partial^2 G}{\partial \xi^2} + \frac{\partial}{\partial \theta} \left[\frac{1}{\sin \theta} \frac{\partial G}{\partial \theta} \right] \ . \qquad (2.71)$$

This system of equations can be solved, in general, and this is done in Appendix A. This chapter will focus only on three particular solutions which are the dipole form solutions for m = -1, 0, 1. The dipole form is assumed; let

$$W(\xi, \theta) = \sin \theta \, J(\xi) \ . \qquad (2.72)$$

Equation (2.68) with (2.72) substituted becomes

$$\frac{d^2 J}{d\xi^2} + \left[\frac{\xi}{2} + \frac{2}{\xi} \right] \frac{dJ}{d\xi} - \left[\frac{2}{\xi^2} + m - 1 \right] J = 0 \ . \qquad (2.73)$$

Before proceeding with the solution of (2.73) let us define the Reynolds number which first necessitates examining the particle path equations.

$$\frac{dr}{dt} = u \tag{2.74}$$

$$\frac{d\theta}{dt} = \frac{v}{r} . \tag{2.75}$$

Substituting (2.60), (2.64) and (2.65) into (2.74) and (2.75) gives

$$\frac{d\xi}{d\tau} = \text{Re}^2 \, U - \frac{\xi}{2} \tag{2.76}$$

$$\frac{d\theta}{d\tau} = \text{Re}^2 \, \frac{V}{\xi} \tag{2.77}$$

where

$$\tau = \ln t \tag{2.78}$$

and the Reynolds number is defined as

$$\text{Re} = \left[\frac{\hat{P} \, t^m}{\nu^2} \right]^{\frac{1}{2}} . \tag{2.79}$$

With Reynolds number established we now solve (2.73) by means of the Frobrenius method. The details of this procedure are lengthy and are described in Appendix A. The key boundary condition in all three flows is the dipole of (2.50). The solutions in terms of dimensionless, self similar vorticity and stream function along with the Reynolds number are provided for cases m = -1, 0, 1 which correspond to the vortex ring, round jet, and ramp jet. Also provided is the forcing function $F(t)$ located at the origin, which acts as a point momentum source creating the flow. $F(t)$ is derived by recognizing that impulse is

conserved in these jet flows which provides an integral of constraint. This integral of constraint was examined in detail by Cantwell (1981). The precise mathematics for finding $F(t)$ is found in App. A (Eqs. A-94 through A-103). We can now state the three solutions for $m = -1, 0, 1$:

Vortex Ring, m = -1

$$F(t) = \left[\frac{I}{\rho}\right] \hat{\delta}(t) \qquad\qquad (2.80)$$

where $\hat{\delta}(t)$ = Dirac delta function, and I = impulse.

$$\hat{P} = \frac{I}{\rho} \qquad units\ L^4/T \qquad\qquad (2.81)$$

$$Re = \left[\frac{I}{\rho \nu^2 t}\right]^{\frac{1}{2}} \qquad\qquad (2.82)$$

$$W(\xi, \theta) = \frac{\sin\theta}{16\,\pi} \frac{\xi}{\sqrt{\pi}} e^{\frac{-\xi^2}{4}} \qquad\qquad (2.83)$$

$$G(\xi, \theta) = \frac{\sin^2\theta}{4\pi} \left[\frac{1}{\xi} erf\left(\frac{\xi}{2}\right) - \frac{1}{\sqrt{\pi}} e^{\frac{-\xi^2}{4}}\right] . \qquad\qquad (2.84)$$

Round Jet, m = 0

$$F(t) = \left[\frac{J}{\rho}\right] \hat{u}(t) \qquad\qquad (2.85)$$

$$\hat{P} = \frac{J}{\rho} \qquad units\ L^4/T^2 \qquad\qquad (2.86)$$

where $\hat{u}(t)$ = Heaviside step function, and J = force.

$$\mathrm{Re} = \left[\frac{J}{\rho \, \nu^2} \right]^{\frac{1}{2}} \tag{2.87}$$

$$W(\xi,\theta) = \frac{\sin \theta}{4\pi} \left\{ \frac{1}{\sqrt{\pi}} \frac{e^{\frac{-\xi^2}{4}}}{\xi} + \frac{1}{\xi^2} \left[1 - erf\left(\frac{\xi}{2}\right) \right] \right\} \tag{2.88}$$

$$G(\xi,\theta) = \frac{\sin^2\theta}{8\pi} \left\{ \xi - \frac{2}{\sqrt{\pi}} e^{\frac{-\xi^2}{4}} + \left(\frac{2}{\xi} - \xi \right) erf\left(\frac{\xi}{2}\right) \right\} \tag{2.89}$$

Ramp Jet, m = 1

$$F(t) = \left(\frac{K}{\rho} \right) t \tag{2.90}$$

$$\hat{P} = \frac{K}{\rho} \qquad units \ L^4/T^6 \tag{2.91}$$

$$\mathrm{Re} = \left[\frac{Kt}{\rho \nu^2} \right]^{\frac{1}{2}} \tag{2.92}$$

$$W(\xi, \theta) = \frac{\sin \theta}{2\pi} \left\{ \frac{1}{\sqrt{\pi}} \frac{e^{\frac{-\xi^2}{4}}}{\xi} + \left[\frac{1}{\xi^2} - \frac{1}{2} \right] \left[1 - erf\left(\frac{\xi}{2}\right) \right] \right\} \tag{2.93}$$

$$G(\xi, \theta) = \frac{\sin^2\theta}{4\pi} \left\{ \left[\frac{\xi^3}{4} + \xi \right] \left[1 - erf\left[\frac{\xi}{2} \right] \right] + \frac{1}{\xi} erf\left[\frac{\xi}{2} \right] \right.$$

$$\left. - \left[1 + \frac{\xi^2}{2} \right] \frac{1}{\sqrt{\pi}} e^{\frac{-\xi^2}{4}} \right\} . \qquad (2.94)$$

These equations provide the basis for our analytic studies in this work. In passing, it should be noted that in (2.87), (the Reynolds number for the round jet), there is no length scale which can be derived from the governing flow parameters. This identifies the round jet as a very special case. It should also be pointed out that the round jet is exempt from the controversy over Eulerian and Lagrangian frames of reference for observing flow structure. This was shown in Cantwell (1981) and is a consequence of the invariance of the round jet under a stretching transform as was shown earlier in this chapter. It should be pointed out, however, that this property does not exist for the cases of m $\neq$ 0, except in the creeping limit. It is clear now that the round jet is a very special problem which lends itself well to analysis. Its near and far field behavior are analytic and because of its self-similar nature it is exempt from many of the mathematical difficulties encountered in most fluid studies. This makes the round jet an excellent vehicle for investigating the more complicated aspects of viscous unsteady flow.

Chapter III

STATE SPACE AND CRITICAL POINTS

In this chapter we shall develop techniques for isolating and classifying critical points. The topology and Reynolds number behavior of these critical points will be examined. The critical points are derived from the particle path equations which repeated from (2.76) through (2.79) are

$$\frac{d\xi}{d\tau} = \text{Re}^2 \, U - \frac{\xi}{2} \tag{3.1}$$

$$\frac{d\theta}{d\tau} = \text{Re}^2 \, \frac{V}{\xi} \tag{3.2}$$

$$\text{Re} = \left[\frac{\hat{P} \, t^m}{\nu^2} \right]^{\frac{1}{2}} \tag{3.3}$$

1. Description Of Critical Points

Critical points occur at coordinates ξ_c, θ_c such that (3.1) and (3.2) are both equal to zero. Equations (3.1) and (3.2) may be expanded in Taylor series around the critical point as

$$\frac{d\xi}{d\tau} \; = \; a(\xi - \xi_c) + b\,(\theta - \theta_c) \tag{3.4}$$

$$\frac{d\theta}{d\tau} \; = \; c\,(\xi - \xi_c) + d\,(\theta - \theta_c) \tag{3.5}$$

where $a, b, c,$ and d are constants. These equations can be restructured in the form used by Poincaré and Andronov (1971):

$$\frac{d\xi}{a\,(\xi - \xi_c) + b\,(\theta - \theta_c)} \; = \; \frac{d\theta}{c\,(\xi - \xi_c) + d\,(\theta - \theta_c)} \; = \; d\tau \; . \tag{3.6}$$

If these equations are autonomous (τ does not appear explicitly except in $d\tau$), one may cast the equations into a second order differential equation:

$$\frac{d^2\xi}{d\tau^2} + p\,\frac{d\xi}{d\tau} + q\,\xi \; = \; 0 \tag{3.7}$$

or

$$\frac{d^2\theta}{d\tau^2} + p\,\frac{d\theta}{d\tau} + q\,\theta \; = \; 0 \tag{3.8}$$

where

$$p \; = \; -(a + d) \tag{3.9}$$

$$q \; = \; ad - bc \; . \tag{3.10}$$

At this point the problem takes on a new perspective since it is recognized that (3.7) and (3.8) are both equations for the damped harmonic oscillator where

the damping and spring force would determine p and q (which is the same for both equations). The parameters p and q can be found by using (3.9) and (3.10) and derivatives of (3.1) and (3.2), i.e.,

$$a = \frac{\partial}{\partial \xi} \left(\frac{d\xi}{d\tau} \right) \Bigg|_{\substack{\xi=\xi_c \\ \theta=\theta_c}} \tag{3.11}$$

$$b = \frac{\partial}{\partial \theta} \left(\frac{d\xi}{d\tau} \right) \Bigg|_{\substack{\xi=\xi_c \\ \theta=\theta_c}} \tag{3.12}$$

$$c = \frac{\partial}{\partial \xi} \left(\frac{d\theta}{d\tau} \right) \Bigg|_{\substack{\xi=\xi_c \\ \theta=\theta_c}} \tag{3.13}$$

$$d = \frac{\partial}{\partial \theta} \left(\frac{d\theta}{d\tau} \right) \Bigg|_{\substack{\xi=\xi_c \\ \theta=\theta_c}} \tag{3.14}$$

Equations (3.7) and (3.8) have the same characteristic equation

$$\tilde{\alpha}^2 + p\,\tilde{\alpha} + q = 0 \ . \tag{3.15}$$

The solution of this quadratic equation is

$$\tilde{\alpha} = -\frac{1}{2} \left(p \pm \sqrt{p^2 - 4q} \right) \ . \tag{3.16}$$

Using (3.16) we can divide up p , q space into particular regions which will

have distinctive topologies. Figure 3-1 shows these particular regions in p , q space with their critical points displayed. This plot shown in Fig. 3-1 goes by many different names, i.e., p , q space, stability diagram, Poincaré map, etc.

The four critical points of prime interest in this paper correspond to values of p $\geq$ 0. The first of these is the stable focus which exists for q $>$ $p^2/4$. The stable focus represents a region in p , q space where (3.16) is imaginary. Next is the star point for $p^2 = 4q$ where the radical of (3.16) goes to zero. The stable node is for $p^2/4 >$ q $>$ 0, which represent a real value of (3.16). Finally, the saddle point is for q $<$ 0.

As an example of how one of these topologies is formed we will examine the case of the stable focus. In this case the solutions of the two equations (3.7) and (3.8) are behaving as decaying sinusoidal functions, both equations with the same frequency and rate of decay. These equations can be coupled together to form a Lissajou figure where two coordinates decaying as damped sinusoids form a two dimensional spiral, spiraling inward with time. In the case of the stable center (p = 0) solution (3.7) and (3.8) are not decaying, but are pure sinusoids. In this case one has a family of concentric closed curves (circles or ellipses).

2. Universality Of The p, q Trajectory

The location and identification of critical points of solution is only part of the analysis. As shall soon be demonstrated, it is possible to predict the flow
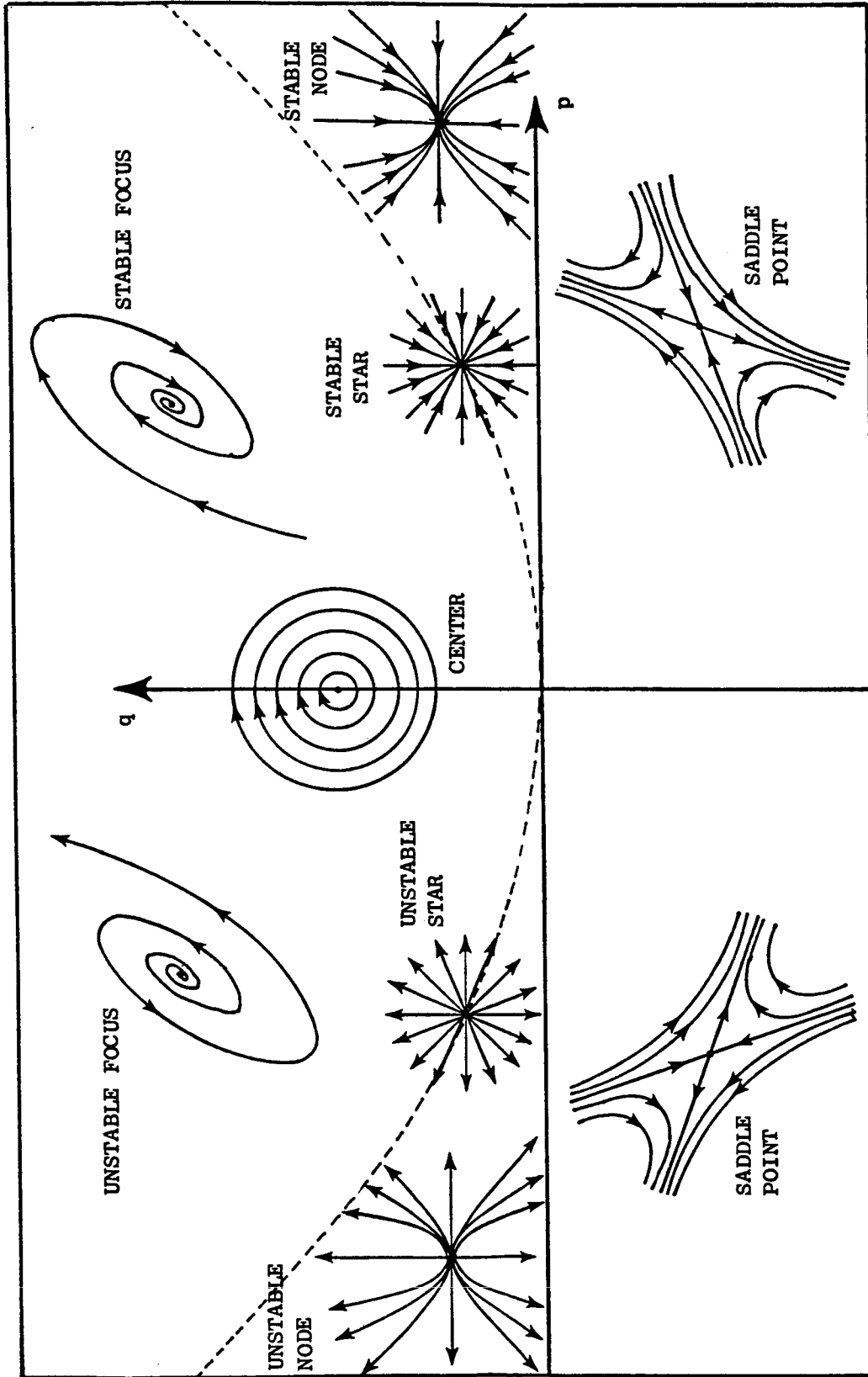
Figure 3-1 Critical Point Topologies in p, q Space

trajectory in p, q space prior to solution of the momentum equation. Having such a p, q trajectory, one can anticipate the flow topology and the manner in which it will change with Reynolds number without having to solve difficult equations. This method is developed by first combining (3.1) and (3.2) with (3.4) and (3.5)

$$U = \frac{1}{\text{Re}^2} \left[a(\xi - \xi_c) + b(\theta - \theta_c) + \frac{\xi}{2} \right] \tag{3.17}$$

$$V = \frac{\xi}{\text{Re}^2} \left[c\,(\xi - \xi_c) + d(\theta - \theta_c) \right] \tag{3.18}$$

where a, b, c, and d are as yet undetermined.

Continuity is the principal equation needed for this analysis. In spherical polar coordinates, continuity is

$$\frac{1}{r} \frac{\partial}{\partial r}(r^2 u) + \frac{1}{\sin \theta} \frac{\partial}{\partial \theta}\,(v \sin \theta) = 0 \ . \tag{3.19}$$

Equation (3.19) is easily converted to nondimensional, self similar form by using the earlier velocity definitions, giving

$$2U + \xi\,\frac{\partial U}{\partial \xi} + \frac{\partial V}{\partial \theta} + \frac{\cos \theta}{\sin \theta}\,V = 0 \ . \tag{3.20}$$

We can now take (3.17) and (3.18) with appropriate derivatives and combine them with (3.20) giving

$$\sin\theta\left[2a\,(\xi-\xi_c)+2b\,(\theta-\theta_c)+\xi(\frac{3}{2}+a+d)\right] \qquad (3.21)$$

$$+\,\xi\cos\theta\left[c(\xi-\xi_c)+d(\theta-\theta_c)\right]\;=\;0\;.$$

In examining the $p,\,q$ behavior of critical points at arbitrary locations in the physical space of the flow it is sufficient to study three possible cases in the upper half plane (which is effectively the whole plane, since the problem is symmetric by definition), namely $\theta=0,\;0<\theta<\pi$, and $\theta=\pi$ for any ξ.

Case 1: $\theta_c=0$

$$\cos\theta\;\approx\;1-\frac{\theta^2}{2}$$

$$\sin\theta\;\approx\;\theta\;.$$

The boundary condition due to axisymmetry is: $V=0$ therefore by (3.18) $c=0$. Inserting the above into (3.21)

$$2a(\xi-\xi_c)+2b\theta+\xi\left[\frac{3}{2}+a+d\right]+\xi d\left[1-\frac{\theta^2}{2}\right]\;=\;0\;.$$

Now let $\theta \to \theta_c, \quad \xi \to \xi_c,$ utilize (3.9), the above equation becomes:

$$p \;=\; d + \frac{3}{2} \;. \tag{3.22}$$

Now combining equations (3.9), (3.10), (3.22), and keeping in mind that $c = 0$ for this case, we find that

$$q \;=\; \left[p - \frac{3}{2}\right]\left[\frac{3}{2} - 2p\right] \;. \tag{3.23}$$

Case 2: $0 < \theta_c < \pi$

For this case $\sin \theta$ is always nonzero. Let $\theta \to \theta_c, \quad \xi \to \xi_c$ in (3.21) which becomes:

$$p \;=\; \frac{3}{2} \;. \tag{3.24}$$

Case 3: $\theta_c = \pi$

$$\cos \theta \;\approx\; -1 + \frac{(\pi - \theta)^2}{2}$$

$$\sin \theta \;\approx\; \pi - \theta$$

Boundary condition due to axisymmetry: $V = 0$, therefore by (3.18) $c = 0$.

Insert the above in (3.21) and one obtains:

$$2a\left(\xi - \xi_c\right) + 2b\left(\theta - \pi\right) + \xi\left[\frac{3}{2} + a + d\right] + \xi\left[1 - \frac{(\pi - \theta)^2}{2}\right] = 0 \ .$$

Now let $\theta \to \theta_c$, $\xi \to \xi_c$ and utilize (3.11) and the above equation becomes

$$p = d + \frac{3}{2} \tag{3.25}$$

which is the identical result found for the case of $\theta_c = 0$. Likewise the same equation as (3.23) will be generated for $\theta_c = \pi$. This should be no major surprise since nowhere in this p, q theory has a direction-of-flow been assumed, so $\theta_c = 0$, $\theta_c = \pi$ should have identical trajectories. The trajectories derived from (3.23) and (3.24) can now be plotted, see Figure 3-2.

We are now in a position to make some rather sweeping statements about the flow. For example: The class of axisymmetric flows under study cannot form unstable nodes, unstable foci, or stable centers. A stable focus will only form off the axis of the flow (p = 3/2). Likewise, a star point can form off-axis at (p , q) = (3/2, 9/16) and on axis at (1, 1/4). The latter point corresponds to zero flow. These statements can be made before the momentum equation is considered. The results come solely from continuity and similarity which is a consequence of the nature of the time dependent force which drives the flow.
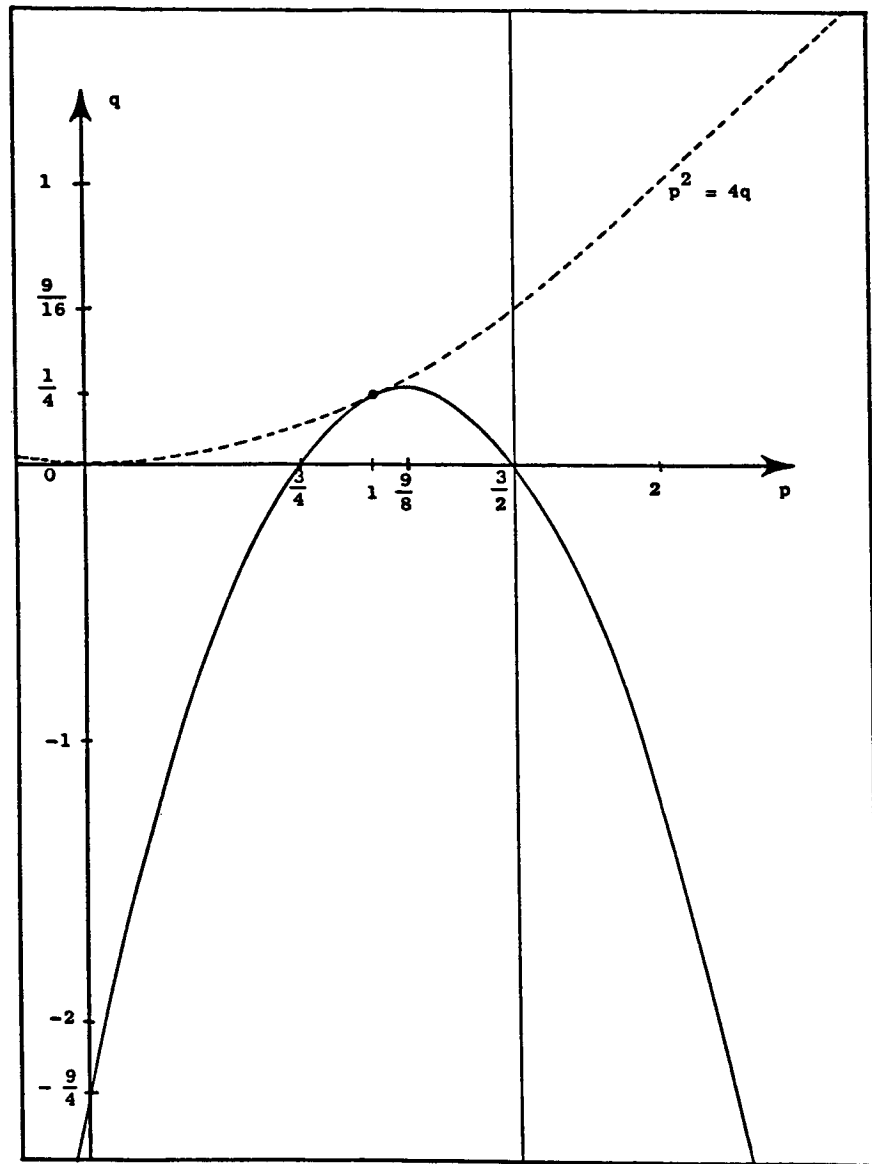
Figure 3-2.   State Space With Axisymmetric Trajectory

Figure 3-2 is valid for all self-similar axisymmetric flows.

However, for a specific flow such as the round jet there is some extraneous information that will have to be removed. (Just as there is in a generalized solution to a differential equation prior to application of boundary conditions.) In determining the relevant parts of Figure 3-2 it is recognized that the geometry of a round jet is bracketed by two limiting aspects: The near field aspect, which is the steady Landau-Squire solution (2.51a), and the far field aspect, which is the unsteady dipole (2.50). Each of these solutions can be cast into the particle path form of (3.1) and (3.2) through (2.69) and (2.70), these equations in turn can be operated on by (3.11) - (3.14) which provide us p and q through (3.9) and (3.10). The results are the following.

Landau-Square Solution:

$$G_0(\xi,\theta) \quad = \quad \frac{1}{\mathrm{Re}^2} \, \frac{2 \, \xi \sin^2 \theta}{A - \cos \theta} \tag{3.26}$$

where A is defined in (2.51b), $p = 5/4$, and $q = 1/4$.

Unsteady Dipole:

$$G_\infty(\xi,\theta) \quad = \quad \frac{\sin^2 \theta}{4\pi\xi} \tag{3.27}$$

where $p = 7/4$, and $q = -1/2$. See also Cantwell (1981, pp. 378-379). Both of

these points are on the parabola given by (3.23) which describes critical points on the axis of the flow.

3. Topological Transition

In getting from $(p, q) = (5/4, 1/4)$ to $(7/4, -1/2)$ the trajectory must pass through $(3/2, 0)$ where the line $p = 3/2$ for the case of "off-axis critical points" intersects the parabola for "on-axis critical points." Now the question arises whether the line $p = 3/2$ can have negative or positive values of q for the round jet.

It has been found in other studies on critical points that the total number of node points subtracted from the total number of saddle points is an invariant of the flow. If the p, q trajectory starts out at $(5/4, 1/4)$ with a stable node and ends at $(5/4, 1/4)$ with a saddle point, then somewhere in route two node points will have to be produced so that the total remains unchanged. The intersection at $(3/2, 0)$ provides such an opportunity since just as the on-axis parabola crosses from the node domain to the saddle domain in Fig. 3-2, it can produce through bifurcation new stable nodes on the $p = 3/2$ line. However, one should recognize that the two off-axis stable nodes actually represent a single critical line centered on the axis of the jet. When viewed from a perspective looking along the axis of the jet, the off-axis critical line is a ring whose parameter increases with Reynolds number. So the process of bifurcation involves the

splitting of a single on-axis stable node critical *point* into an off-axis stable nodal *line*. This change in the topology of the flow represents a form of transition since the changes occur at specific values of the Reynolds number.

If we redraw Fig. 3-2 for the specific case of the round jet, see Fig. 3-3, we see that at $q = 9/16$ the off-axis critical point (line) becomes a star point and then for $q > 9/16$ the off-axis critical point becomes a stable focus. This topological transformation at $(p, q) = (3/2, 9/16)$ represents a second transition after the first transition already mentioned.

4. The Three Flow States For The Round Jet

It is now recognized that the round jet has three possible topologies or states which are partitioned by two transition Reynolds numbers Re_1 and Re_2. Let us describe these states:

State 1: $0 \leq Re < Re_1$
One on-axis stable node.

State 2: $Re_1 \leq Re < Re_2$

One on-axis saddle point and, one off-axis stable node critical line forming a ring around the axis of symmetry.

State 3: $Re_2 < Re$

One on-axis saddle point and, one off-axis stable focus critical line forming a ring around the axis of symmetry.

As the reader can now see, the method of p, q analysis is very powerful, for without having defined or solved a momentum equation we know all the possible topologies of viscous axisymmetric round jet and all the possible modes of topological transition.

Before closing this chapter we should examine a paradox that arises from this method. The state of rest (zero flow) is described by the on-axis star at (p, q) = (1, 1/4). This may not be immediately apparent to the reader unless it is recalled that the coordinate system from which the p, q trace is derived (ξ, θ) has time embedded within it (see Eq. 3.1). Therefore if one were to draw a circle in physical space this same circle would appear to be shrinking in (ξ, θ) space (like drawing a circle on an inflated balloon and letting the air leak out).

It so happens that only a star point has this feature of the flow field rushing in a purely radial direction towards the critical point in the center. Unfortunately the p , q trace displayed in Fig. 3-3 never reaches the star point at $(p,\ q) =$ (1, 1/4). The only star point admitted by an axisymmetric jet is the star critical line at (3/2, 9/16) which is off-axis and not representative of a stationary flow. The closest an axisymmetric jet gets to (1, 1/4) is the Landau-Squire solution of (5/4, 1/4). What compounds the paradox is that
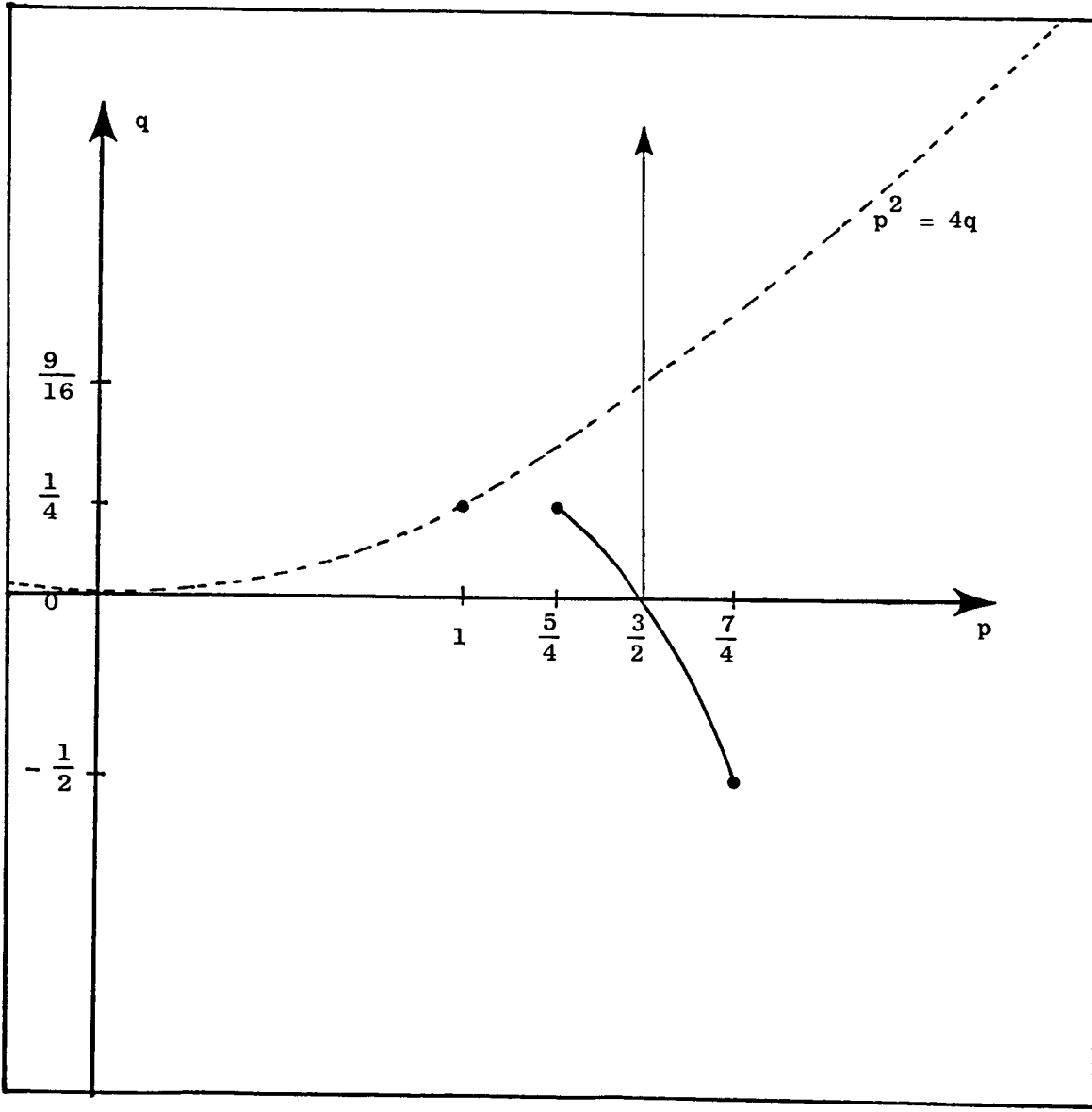
Figure 3-3. State Space With Round Jet Trajectory.

the Landau-Squire solution admits the zero flow case, $Re = 0$, $A \to \infty$ but its

p , q   is still (5/4, 1/4).   In other words the limit $Re \to 0$ corresponds to

a topologically different flow from the case $Re = 0$.

Lastly, we should address the question of nonautonomous flows, that is,

flows where the Reynolds number is time dependent. The p , q   method of

analysis can be used in a different manner on nonautonomous flows. There is

nothing that prevents one from freezing the particle paths for a given time, utiliz-

ing equations (3.11) - (3.14), and calculating an instantaneous p , q. If one

presupposes, as an assumption, that the self similar coordinate is valid for nonau-

tonomous flows of all Reynolds number (which is true in general only as $Re \to$

0), then a trajectory identical to Fig. 3-2 can be produced.

The difficulty with nonautonomous problems is that the particle path equa-

tions are constantly changing. In both the autonomous and nonautonomous

problem one can take the particle path equations (3.1) and (3.2) and generate a

field of vectors of unit length which would show the direction of particle paths at

a given point and at a given instant. tunnel model). A plot of these vectors is

called an "entrainment diagram". The entrainment diagram in the autonomous

problem does not change with time. Therefore in the autonomous case if one

takes a particular point and follows its trajectory in time, its trajectory will

always be tangent to the vectors of its entrainment diagram.

This trajectory of a particular point through time will be referred to as an "integrated particle path". However, in the nonautonomous problem the entrainment diagram is constantly changing. One can take the entrainment diagram of time t_1 and overlay it with a particle path of $0 \leq t_1 \leq t_2$ where times 0 and t_2 mark the end points of the particle path trajectory. The vectors on the entrainment diagram need not be tangent to the integrated particle path trajectory except at the point of the particle path trajectory that was made at t_1. Each of these instantaneous entrainment diagrams will have a flow topology with critical points that can be studied in a p , q context.

However, this p , q context is different from the autonomous example because time can play a part. One must recast (3.4) and (3.5) as

$$\frac{d\xi}{d\tilde{\alpha}} \;=\; a\,(\xi - \xi_c) + b(\theta - \theta_c) \tag{3.28}$$

$$\frac{d\theta}{d\tilde{\alpha}} \;=\; c\,(\xi - \xi_c) + d\,(\theta - \theta_c) \tag{3.29}$$

where $\tilde{\alpha}$ is just a dummy independent variable. One can produce a "pseudo particle path" for an instantaneous time by integrating (3.28) and (3.29) in $\tilde{\alpha}$. The "pseudo particle paths" have nothing to do with real particle paths but merely serve as a vehicle for observing instantaneous topologies. Standard p , q

analysis can be applied to this "pseudo particle path" and it is from here that instantaneous nonautonomous p , q values have their basis.

Chapter IV

LINEARIZED RESULTS

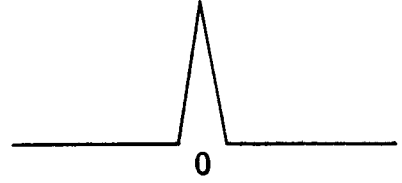## 1. Creeping Flow Particle Path Equations

In Chapter II the linearized solutions in terms of vorticity and stream function are developed for the cases of the vortex ring, round jet, and ramp jet. In Chapter III the chief methods of analysis were developed in terms of the particle path and p , q plot. As the reader is probably aware, in unsteady fluid mechanics particle paths are the most desirable means for displaying fluid motion. All three of the linear flows appear as simple dipoles in the stream function and vorticity. In terms of these variables much of the flow topology and influence of critical points is not apparent. We shall use Eqs. (2.69), (2.70), (2.76) and (2.77) so that the particle path equations become

$$\frac{d\xi}{d\tau} = \frac{\mathrm{Re}^2}{\xi^2 \sin\theta} \frac{\partial G}{\partial \theta} - \frac{\xi}{2} \tag{4.1}$$

$$\frac{d\theta}{d\tau} = -\frac{\mathrm{Re}^2}{\xi^2 \sin\theta} \frac{\partial G}{\partial \xi} \tag{4.2}$$

where $\tau = \ln t$. The stream functions derived in Chapter II Eqs. (2.84), (2.89), and (2.94) are inserted into (4.1) and (4.2) giving:
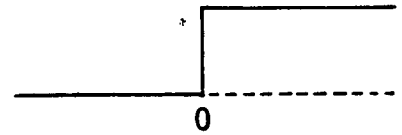
Vortex Ring $(m = -1)$: $Re = \left[\dfrac{I}{\rho \nu^2 t} \right]^2$

$$\frac{d\xi}{d\tau} = \frac{Re^2 \cos\theta}{2\pi\xi^2} \left[\frac{1}{\xi} \, erf\left(\frac{\xi}{2} \right) - \frac{e^{\frac{-\xi^2}{4}}}{\sqrt{\pi}} \right] - \frac{\xi}{2} \tag{4.3}$$

$$\frac{d\theta}{d\tau} = \frac{Re^2 \sin\theta}{4\pi\xi^3} \left[\frac{1}{\xi} \, erf\left(\frac{\xi}{2} \right) - \left(1 + \frac{\xi^2}{2} \right) \frac{e^{\frac{-\xi^2}{4}}}{\sqrt{\pi}} \right] . \tag{4.4}$$

Round Jet $(m = 0)$: $Re = \left[\dfrac{J}{\rho\nu}^2 \right]^{\frac{1}{2}}$

$$\frac{d\xi}{d\tau} = \frac{Re^2 \cos\theta}{2\pi\xi^2} \left[\left(\frac{1}{\xi} - \frac{\xi}{2} \right) erf\left(\frac{\xi}{2} \right) + \frac{\xi}{2} - \frac{e^{\frac{-\xi^2}{4}}}{\sqrt{\pi}} \right] - \frac{\xi}{2} \tag{4.5}$$

$$\frac{d\theta}{d\tau} = \frac{Re^2 \sin\theta}{4\pi\xi^3} \left[\left(\frac{1}{\xi} + \frac{\xi}{2} \right) erf\left(\frac{\xi}{2} \right) - \frac{\xi}{2} - \frac{e^{\frac{-\xi^2}{4}}}{\sqrt{\pi}} \right] . \tag{4.6}$$

Ramp Jet $(m = 1)$: $Re = \left[\dfrac{Kt}{\rho\nu^2} \right]^{\frac{1}{2}}$
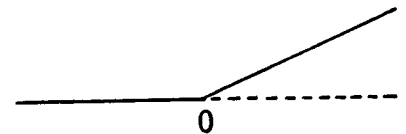
$$\frac{d\xi}{d\tau} = \frac{Re^2 \cos\theta}{2\pi\xi^2} \left[\left(\frac{1}{\xi} - \frac{\xi^3}{4} - \xi \right) erf\left(\frac{\xi}{2} \right) \right.$$

$$\left. + \frac{\xi^3}{4} + \xi - \frac{1}{\sqrt{\pi}} \left(1 + \frac{\xi^2}{2} \right) e^{\frac{-\xi^2}{4}} \right] - \frac{\xi}{2} \qquad (4.7)$$

$$\frac{d\theta}{d\tau} = \frac{Re^2 \sin\theta}{4\pi\xi^3} \left[\left(\frac{1}{\xi} + \frac{3\xi^3}{4} + \xi \right) erf\left(\frac{\xi}{2} \right) \right.$$

$$\left. - \frac{3\xi^3}{4} - \xi - \frac{1}{\sqrt{\pi}} \left(1 - \frac{3\xi^2}{2} \right) e^{\frac{-\xi^2}{4}} \right] . \qquad (4.8)$$

It should be reemphasized that the Reynolds number functional form with respect to time is different for each flow (see Eq. 3.3).

2. Critical Point Analysis Of The Creeping Solutions

Equations (4.3) through (4.8) represent the actual equations used to plot particle paths and locate and characterize critical points. These are integrated numerically to produce computer animations of the respective flows. Critical points are found by setting the right-hand sides of the particle path (4.1) and (4.2) equal to zero, and finding the value of (ξ_c, θ_c) for a given Reynolds number. The method of analysis is the same for all three flows. The vortex ring will be used as an example case since it is the most mathematically compact. If (4.4) is examined, one finds that it will go to zero for $\theta = 0$ or where the expression in parenthesis of (4.4) goes to zero. This expression can be cast as a transcendental equation for ξ_c.

$$\xi_c = 2 \left\{ \ln \left[\frac{\xi_c + \frac{\xi_c^3}{2}}{\sqrt{\pi} \, erf\left(\frac{\xi_c}{2}\right)} \right] \right\}^{\frac{1}{2}} \tag{4.9}$$

This equation is in an iteratively stable form and quickly converges to a root $\xi_c = 3.0224$, (which shall be called $\hat{\xi}_c$). Where (4.4) goes to zero, so the root which causes (4.3) to go to zero must also be found to isolate the critical point. Setting the left-hand side of (4.3) to zero gives

$$Re^2 = \frac{\pi \, \xi_c^3}{\left[\frac{1}{\xi_c} \, erf\left(\frac{\xi_c}{2}\right) - \frac{1}{\sqrt{\pi}} \, e^{\frac{-\xi_c^2}{4}} \right] \cos \theta_c} \tag{4.10}$$

For the on-axis case of $\theta_c = 0$, (4.10) becomes a straightforward function $Re = f(\xi_c)$, until $\xi_c = \hat{\xi}_c$. At this point bifurcation is possible since (4.4) is zero for $\theta_c \neq 0$.

The bifurcation Reynolds number can be calculated by setting ξ_c in (4.10) equal to $\hat{\xi}_c$. Thus

$$\theta_c = \pm \arccos \left[\left(\frac{18.1749}{Re} \right)^2 \right] . \tag{4.11}$$

It was found that for $\theta_c = 0$, (which is the angle at bifurcation) the Reynolds number is $Re = 18.1749$. This is the first transition Reynolds number (Re_1 as referred to in Chapter III). Equation (4.11) also establishes the precise location of

the off-axis critical point after bifurcation since it provides θ_c for any given Re and it is known that $\xi_c = \hat{\xi}_c$ for the off-axis critical point.

For the on-axis critical point for $Re > Re_1$, we continue to use (4.10) with $\theta_c = 0$, except now $\xi_c > \hat{\xi}_c$. The method of determining the location of critical points is the same for the other two flows as just shown for the vortex ring. Equation (4.11) can be generalized as

$$\theta_c = \pm \text{ arc cos}\left[\left(\frac{Re_1}{Re}\right)^2\right] \tag{4.12}$$

The results of this method when performed on all three flows is shown in Table 4-1.

Table 4-1

First Transition Constants

Flow Type	M	$\hat{\xi}_c$	Re_1
Vortex Ring	-1	3.0224	18.1749
Round Jet	0	1.7633	6.7806
Ramp Jet	1	1.2821	3.7386

One difficulty that is immediately apparent in Table 4-1 is that the values of Re_1 are beyond the domain of validity for a creeping flow approximation. In the case of the round jet this is not as bad as it might seem since in Chapter II it was shown that the topology for autonomous flows is a consequence of continuity. As shall later be shown, the main consequence of the creeping approximation in the round jet geometry is that the jet is of shorter length along the axis of symmetry, the spreading angle of the off-axis critical points is too large, and the value of Re_1, (and Re_2) is different. However, the basic topology in this approximation is correct. In the case of the nonautonomous flows (ramp jet and vortex ring), there are more significant problems. As mentioned in Chapter II these flows are self similar in ξ only in the creeping approximation and as the creeping approximation loses validity so does the use of this coordinate and the topologies that are a consequence. This fact has been observed by Glezer (1982) in his experimental work for the turbulent vortex ring. They used the self similar variable of $r/(It)^{1/4}$, (where I is the impulse), and also found an additional critical point on the axis of symmetry. Thus the nonautonomous creeping solution provides only a partially complete topology and transition behavior.

One other aspect of Table 4-1 is that Re_1 seems to be diminishing as m increases. Though it has not yet been determined, it might be found that for sufficiently large m, Re_1 will occur for values that are within the creeping approximation which would represent very interesting subjects for low Reynolds number experiments.

We now return to our example problem of the vortex ring and examine the situation for $Re > Re_1$. The values of p, q can be calculated for the vortex ring by taking (4.3) and (4.4), inserting them into (3.13) - (3.16) and utilizing the definitions of (3.11) and (3.12). The resultant equations require considerable algebraic manipulation and are quite long. However, they can be simplified by recognizing that in the on-axis case, $(\theta_c = 0)$, q is given by (3.23) which is solely a function of p. Therefore only p needs to be calculated. This is given by

$$p_{\theta_c=0} = \frac{3}{2} - \frac{Re^2}{4\pi\xi_c^2} \left[\frac{1}{\sqrt{\pi}} \left(\frac{\xi_c}{2} + \frac{1}{\xi_c} \right) e^{-\xi_c^2/4} - \frac{1}{\xi_c^2} erf\left(\frac{\xi_c}{2} \right) \right] . \quad (4.13)$$

As was shown earlier, ξ_c is solely a function of Re for $\theta_c = 0$ and can be found by using (4.10). Next, for $\theta_c \neq 0$ it is already known that $p = 3/2$, so only q needs to be found. The very complicated equation for q is reduced by recalling that $\xi_c = \hat{\xi}_c$ for $\theta_c \neq 0$, and utilizing (4.12). After much algebra and lengthy hand computations one finds that

$$q_{\theta_c \neq 0} = \Gamma + \Lambda \, Re^4 \quad (4.14)$$

where for the vortex ring:

$$\Gamma = -0.3209 \, 5$$

$$\Lambda = 2.9413 \times 10^{-6}$$

Equation (4.14) is the basis for calculating the second transition where the off-axis critical point transforms from a stable node to a stable focus. This transition occurs at the parabola shown in Fig. 3-2, which is

$$q = \frac{p^2}{4} .$$

(4.15)

One can now set $p = 3/2$ yielding $q = 9/16$ and insert this result into (4.14) giving $Re_2 = 23.4105$, which is the second transition Reynolds number for the vortex ring. The angle θ_c at which the second transition occurs can be calculated from (4.12). The method used for the vortex ring can be applied to the round jet and ramp jet -- the results of which are shown in Table 4-2, (Re_1 is restated from Table 4-1 for comparison). Γ and Λ in Table 4-2 refer to Eq. (4.14).

Table 4-2

Second Transition Constants

Flow Type	M	Re_1	Re_2	Γ	Λ	θ_c @ Re_2 (deg)
Vortex Ring	-1	18.1749	23.4105	-0.32095	2.9413×10^{-6}	52.9343
Round Jet	0	6.7804	10.0909	-0.14405	6.8143×10^{-5}	63.1605
Ramp Jet	1	3.7386	5.7887	-0.11849	6.0652×10^{-4}	65.3468

For $Re > Re_2$ there are no further topological changes for the axisymmetric problem. As $Re \to \infty$ the off-axis critical point remains a stable focus and its q value goes to infinity as can be seen in (4.14). The off-axis critical point angle θ_c goes to $\pi/2$ for infinite Reynolds number as is shown by (4.12). This, of course, is a consequence of the creeping approximation. For the limiting behavior of the on-axis critical point p , q values, one uses (4.13) with Re eliminated by substituting (4.10). The resultant equation will yield values for p in the limit of $Re \to 0$ where $\xi_c \to 0$, and $Re \to \infty$ where $\xi_c \to \infty$. This same procedure can be used in the round jet and ramp jet. The q values can be determined in all three flows by employing (3.23) and inserting the respective values of p. The result of this analysis is that for the vortex ring limit $Re \to 0$, (p , q) = (1, 1/4), and in both the round jet and ramp jet limit $Re \to 0$, (p , q) = (5/4, 1/4) is found. For the case of $Re \to \infty$ in all three jets (p , q) = (7/4, -1/2). This is consistent with intuition which would suggest a far-field dipole behavior for all three flows. Now p , q plots can be drawn for all three flows. These are shown in Figure 4-1. With the p , q plots of Fig. 4-1 and the equations developed in this chapter, one can describe how the respective flows will behave without integrating the particle path equations. The vortex ring will have an infinite Reynolds number at $t = 0$ (recall that Re is proportional to $1/t^{1/2}$). Its off-axis critical point will have an infinite q value so the flow will be rolling up very rapidly around the stable focus.
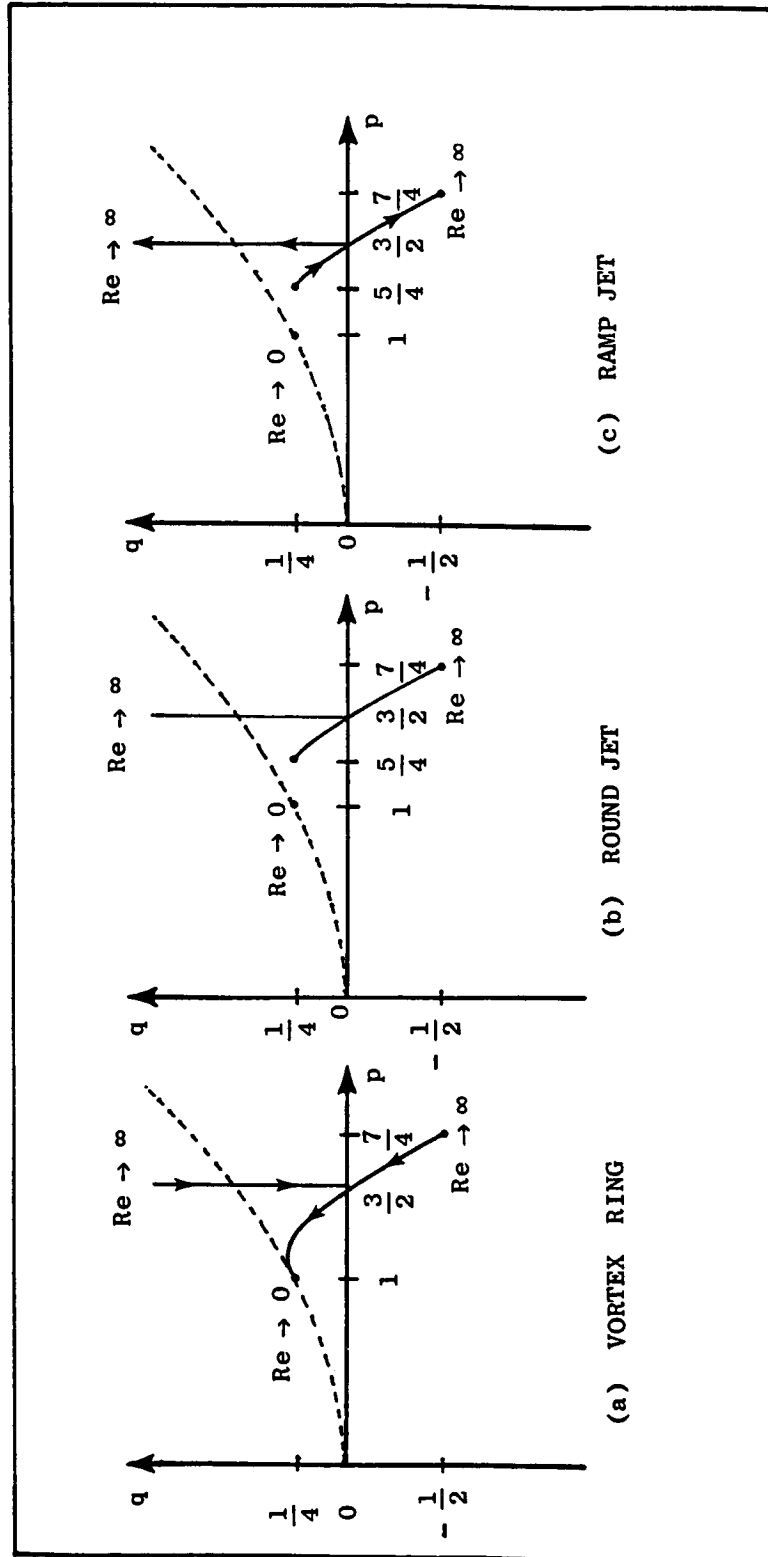
Fig. 4-1: State Space Showing p (Re), q (Re) Trajectories of a) Vortex Ring, b) Round Jet, c) Ramp Jet.

The critical point will be at $\theta_c = 90°$ initially but its angle will diminish as time progresses just as q decreases. As the q value approaches the star point on the q $=$ p 2/4 parabola, the rate of roll-up will be so slow as to be imperceptible. When (p , q) goes below (3/2, 1/4) and the second transition occurs (actually the first transition chronologically in the vortex ring), roll-up will cease altogether, only straining and translation occurs thereafter. As time progresses, θ_c for the off-axis point diminishes until Re $=$ Re$_1$ is reached. After this "first" transition, the now simplified topology with one on-axis critical point revolves with increasing q but diminishing p along the p , q parabola for the on-axis critical point. Eventually after infinite passage of time the (p, q) value of (1, 1/4) is attained (the zero flow star) and the flow comes to rest. In the round jet the p , q trajectory and critical points are static because the flow is autonomous. This permits the realization of flows which stay in the same topological state for all time. Thus it is possible to study a state of motion which is only a transient phenomenon in a nonautonomous flow. The ramp jet is the complement of the vortex ring (due to Re being proportional to $t^{1/2}$), as compared to $t^{-1/2}$ except for the fact that like the round jet this flow also has the start paradox at (p , q) $=$ (5/4, 1/4). The single stable node later bifurcates at the first transition (which is now chronologically correct). The on-axis saddle goes to (7/4, –1/2) at infinite time. The off-axis stable node point goes through second transition to a stable focus and attains infinite q at $\theta_c = 90°$ at infinite time. With the ramp jet we can anticipate an initially sluggish flow

starting to roll up with the rate of roll-up getting faster with time (the opposite

of the vortex ring).

Chapter V

THE NUMERICAL METHOD

1. Derivation Of The Finite Difference Equation.

In the previous chapters and in Appendix A the Stokes and Navier Stokes equations were examined in the context of analytic solutions. It was shown in Chapter II that the round jet (m = 0) has a self similar solution to the Navier Stokes equation. The Navier Stokes equation and vorticity definition can be recast into this self similar form by inserting equations (2.66) and (2.67) into (2.31) - (2.34) using the self similar coordinate of (2.60) giving

$$\xi^2 \frac{\partial^2 W}{\partial \xi^2} + \left[2\xi - \frac{1}{\sin \theta} \frac{\partial G}{\partial \theta} + \frac{\xi^3}{2} \right] \frac{\partial W}{\partial \xi}$$

$$+ \left[\xi^2 - \frac{1}{\sin^2 \theta} + \frac{1}{\xi \sin \theta} \frac{\partial G}{\partial \theta} - \frac{\cos \theta}{\sin^2 \theta} \frac{\partial G}{\partial \xi} \right] W + \frac{\partial^2 W}{\partial \theta^2}$$

$$+ \left[\cot \theta + \frac{1}{\sin \theta} \frac{\partial G}{\partial \xi} \right] \frac{\partial W}{\partial \theta} = 0 ; \qquad (5.1)$$

$$W = \frac{-1}{\xi^3 \sin \theta} \left[\xi^2 \frac{\partial^2 G}{\partial \xi^2} + \frac{\partial^2 G}{\partial \theta^2} + \cot \theta \frac{\partial G}{\partial \theta} \right] . \qquad (5.2)$$

Experience has shown that (5.1) and (5.2) need to be cast into a more gen-

eralized form before conversion to a finite difference equation. The more general-ized form for (5.1) is

$$\left[h^2 N \right] \frac{\partial^2 Y}{\partial \xi^2} + \left[2hB \right] \frac{\partial Y}{\partial \xi} + [C] Y$$

$$+ \left[k^2 D \right] \frac{\partial^2 Y}{\partial \delta^2} + \left[2 kE \right] \frac{\partial Y}{\partial \delta} = 0 \qquad (5.3)$$

where

$$M = \frac{\xi^4}{2} \sin^2 \theta - 2\xi^2 \sin^2 \theta - \xi\beta \sin \theta \frac{\partial \delta}{\partial \theta} \frac{\partial Z}{\partial \delta} \qquad (5.4)$$

$$N = \frac{\xi^3}{h^2} \alpha \sin^2 \theta \qquad (5.5)$$

$$B = \frac{1}{2h} \left[2\xi^3 \sin^2 \theta \frac{\partial \alpha}{\partial \xi} + \alpha M \right] \qquad (5.6)$$

$$C = \xi^3 \sin^2\theta \frac{\partial^2 \alpha}{\partial \xi^2} + \frac{\partial \alpha}{\partial \xi} M + \alpha \left[2\xi \sin^2\theta + 3\beta \sin \theta \frac{\partial \delta}{\partial \theta} \frac{\partial Z}{\partial \delta} - \xi \right.$$

$$\left. - \xi \cos \theta \left(\frac{\partial \beta}{\partial \xi} Z + \beta \frac{\partial Z}{\partial \xi} \right) \right] \qquad (5.7)$$

$$D = \frac{\xi}{k^2} \sin^2 \theta \, \alpha \left(\frac{\partial \delta}{\partial \theta} \right)^2 \qquad (5.8)$$

$$E = \frac{\alpha \xi}{2k} \left\{ \sin^2\theta \frac{\partial^2 \delta}{\partial \theta^2} + \frac{\partial \delta}{\partial \theta} \left[(\sin\theta\cos\theta + \sin\theta \left(\frac{\partial \beta}{\partial \xi} Z + \beta \frac{\partial Z}{\partial \xi} \right) \right] \right\}$$

(5.9)

The dependent variables used are

$$W(\xi,\theta) = \frac{1}{\xi^2} \alpha(\xi) Y(\xi,\theta)$$

(5.10)

$$G(\xi,\theta) = \beta(\xi) Z(\xi,\theta)$$

(5.11)

$$\alpha(\xi) = \frac{1}{4\pi} \left[\frac{\xi e^{-\frac{\xi^2}{4}}}{\sqrt{\pi}} + 1 - erf\left(\frac{\xi}{2} \right) \right]$$

(5.12)

$$\beta(\xi) = \frac{1}{4\pi} \left[\frac{\xi}{2} - \frac{e^{-\frac{\xi^2}{4}}}{\sqrt{\pi}} + \left(\frac{1}{\xi} - \frac{\xi}{2} \right) erf\left(\frac{\xi}{2} \right) \right] .$$

(5.13)

The equation (5.12) is the radial component of the creeping vorticity solution of (2.88). Equation (5.13) is the radial component of the creeping stream function of (2.89). Both of these relations will be referred to as "nonlinear scale functions". The singularity of $1/\xi$ in (5.13) is removable as $\xi \to 0$ because for small ξ

$$erf\left[\frac{\xi}{2} \right] \approx \frac{\xi}{\sqrt{\pi}} .$$

The coordinate δ is an angular coordinate for use in mesh stretching based on θ and the Reynolds number

$$\delta = \delta(\theta, Re) \quad . \tag{5.14}$$

Equation (5.14) was introduced into (5.1) by the following equations

$$\frac{\partial W}{\partial \theta} = \frac{\partial \delta}{\partial \theta} \frac{\partial W}{\partial \delta} \tag{5.15}$$

$$\frac{\partial^2 W}{\partial \theta^2} = \left[\frac{\partial \delta}{\partial \theta}\right]^2 \frac{\partial^2 W}{\partial \delta^2} + \frac{\partial^2 \delta}{\partial \theta^2} \frac{\partial W}{\partial \delta} \quad . \tag{5.16}$$

The specific "theta stretching algorithm" will be discussed later in this chapter.

The more generalized form of the vorticity definition (5.2) is

$$\left[h^2 \widetilde{N}\right] \frac{\partial^2 Z}{\partial \xi^2} + \left[2h\widetilde{B}\right] \frac{\partial Z}{\partial \xi} + \left[\widetilde{C}\right] Z + \left[k^2 \widetilde{D}\right] \frac{\partial^2 Z}{\partial \delta^2}$$

$$+ \left[2k\widetilde{E}\right] \frac{\partial Z}{\partial \delta} = \widetilde{R} \tag{5.17}$$

$$\widetilde{N} = \left(\frac{\xi}{h}\right)^2 \beta \sin \theta \tag{5.18}$$

$$\widetilde{B} = \frac{1}{h} \sin \theta \, \xi^2 \frac{\partial \beta}{\partial \xi} \tag{5.19}$$

$$\widetilde{C} = \xi^2 \sin \theta \frac{\partial^2 \beta}{\partial \xi^2} \tag{5.20}$$

$$\widetilde{D} = \frac{\beta}{k^2} \sin \theta \left(\frac{\partial \delta}{\partial \theta}\right)^2 \tag{5.21}$$

$$\widetilde{E} = \frac{\beta}{2k} \left[\sin \theta \frac{\partial^2 \delta}{\partial \theta^2} - \cos \theta \frac{\partial \delta}{\partial \theta}\right] \tag{5.22}$$

$$\tilde{R} \;=\; -\,\xi\alpha Y \sin^2\theta \; . \tag{5.23}$$

The variables h and k which appear in (5.3) - (5.22) are at this stage just dummy variables. If we subject (5.3) and (5.17) to a second-order finite difference we have the following

$$(N+B)Y_{i+1,j} \;+\; (N-B)Y_{i-1,j} + [C-2(N+D)]\,Y_{i,j}$$

$$+ \; (D+E)Y_{i,j+1} + (D-E)Y_{i,j-1} \;=\; 0 \; ; \tag{5.25}$$

$$\left[\, \tilde{N} + \tilde{B} \,\right] Z_{i+1,j} \;+\; \left[\, \tilde{N} - \tilde{B} \,\right] Z_{i-1,j} + \left[\, \tilde{C} - 2(\tilde{N} + \tilde{D}\,) \,\right] Z_{i,j} \; .$$

$$+ \; \left[\, \tilde{D} + \tilde{E} \,\right] Z_{i,j+1} + [\, \tilde{D} - \tilde{E} \,]\, Z_{i,j-1} \;=\; \tilde{R} \; . \tag{5.26}$$

Equations (5.25) and (5.26) form the basis of a "two step" method of solution where vorticity is solved for first and then used to solve for the stream function. Terms ξ and δ will now be defined in a finite difference context

$$\xi \;=\; ih \tag{5.27}$$
$$\delta \;=\; jk \tag{5.28}$$

where i and j are integers marking a particular node in an n $\times$ n square mesh. We can see now that h, and k are step sizes in the ξ and δ direction. The coefficients N, B, C, etc., are the same as defined for the partial differential equations in (5.4) - (5.9). The following derivatives have a finite difference approximation

$$\frac{\partial Z}{\partial \xi} = \frac{Z_{i+1,j} - Z_{i-1,j}}{2h} \qquad (5.29)$$

$$\frac{\partial Z}{\partial \delta} = \frac{Z_{i,j+1} - Z_{i,j-1}}{2k} \; . \qquad (5.30)$$

Equation (5.29) is employed in (5.7) and (5.9) while (5.30) is used in (5.4) and (5.7). The equations (5.25) and (5.26) represent the actual finite difference equations used in the software.

2. Boundary Conditions In The Near Field

At this point we should examine the boundary conditions in the context of this numerical scheme. Figure 5-1 shows the computational mesh which is n points by n points, with the boundary conditions as shown in Figure 5-1. The computational domain is actually a semicircle.

However, if one were to visualize this semicircle as a spread-out Japanese fan one could imagine taking the pivot pin out of the base of the fan and unfolding it into a square piece of paper. This is represented in Fig. 5-1 where the radial and angular component have been mapped into a Cartesian system with the line $\xi = 0$ corresponding to the point momentum source. The boundaries at $\theta = 0$ and $\theta = \pi$ are both on the axis of the jet and have the same boundary conditions of vorticity and stream function being equal to zero. For the near field ($\xi = 0$) , we employ the Landau-Squire solution.
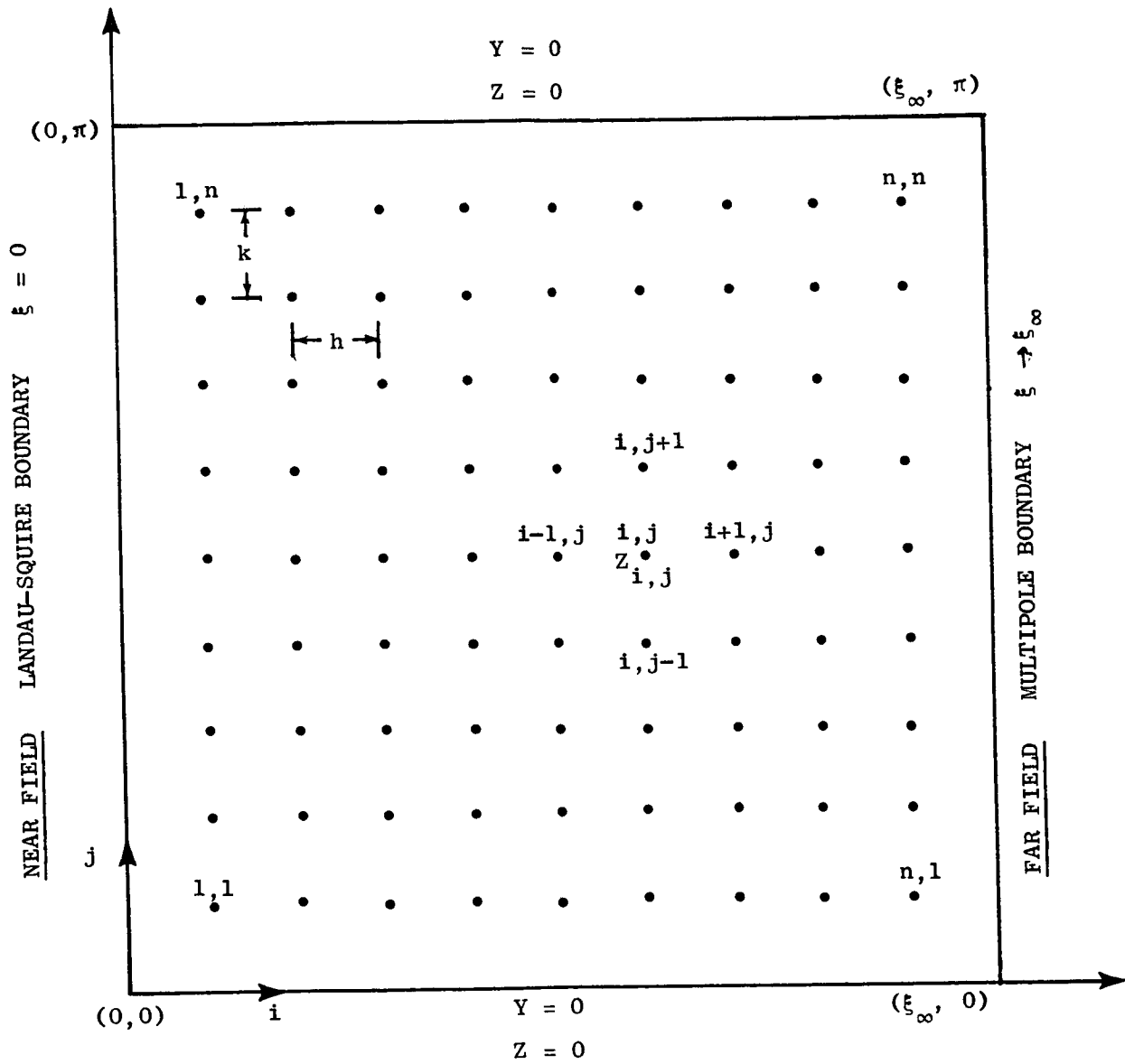
Figure 5-1. The Computational Domain

The dimensionless self similar stream function of the Landau-Squire solution is provided by (3.26) which when combined with (5.13) and (5.11) gives

$$\lim_{\xi \to 0} Z(\xi,\delta) = \frac{16 \pi \sin^2 \theta}{\text{Re}^2 (A - \cos \theta)} \qquad (5.31)$$

where A is defined by (2.51b).

For the vorticity at $\xi \to 0$, we start with (2.51a) and insert this into (2.34) via (2.32) - (2.33) and then develop an expression for vorticity in physical coordinates (Eq. A-115 of App. A). This result is cast into a dimensionless self similar form via (2.67). When combined with (5.10) and (5.12), one obtains

$$\lim_{\xi \to 0} Y(\xi,\delta) = \frac{16 \pi (A^2 - 1) \sin \theta}{\text{Re}^2 (A - \cos \theta)^3} \qquad . \qquad (5.32)$$

Equations (5.31) and (5.32) are the $\xi \to 0$ boundary conditions used in the software although (5.32) needs to be algebraically manipulated to show its equivalence. It is convenient to tie up loose ends at this point regarding the parameter A of the Landau-Squire solution which is related to the Reynolds number in (2.51b). In Fig. 5-2 we see that as $\text{Re} \to 0$, $A \to \infty$ and as $\text{Re} \to \infty$, $A \to 1$. Equation (2.51b) can be expanded into an infinite series giving,

$$\frac{\text{Re}^2}{16 \pi} = \sum_{n=0}^{\infty} \left[\frac{9 + 8n}{9 + 6n} \right] \frac{1}{A^{2n+1}} \qquad . \qquad (5.33)$$

From (5.33) we can see the asymptotic expansion in (5.34)
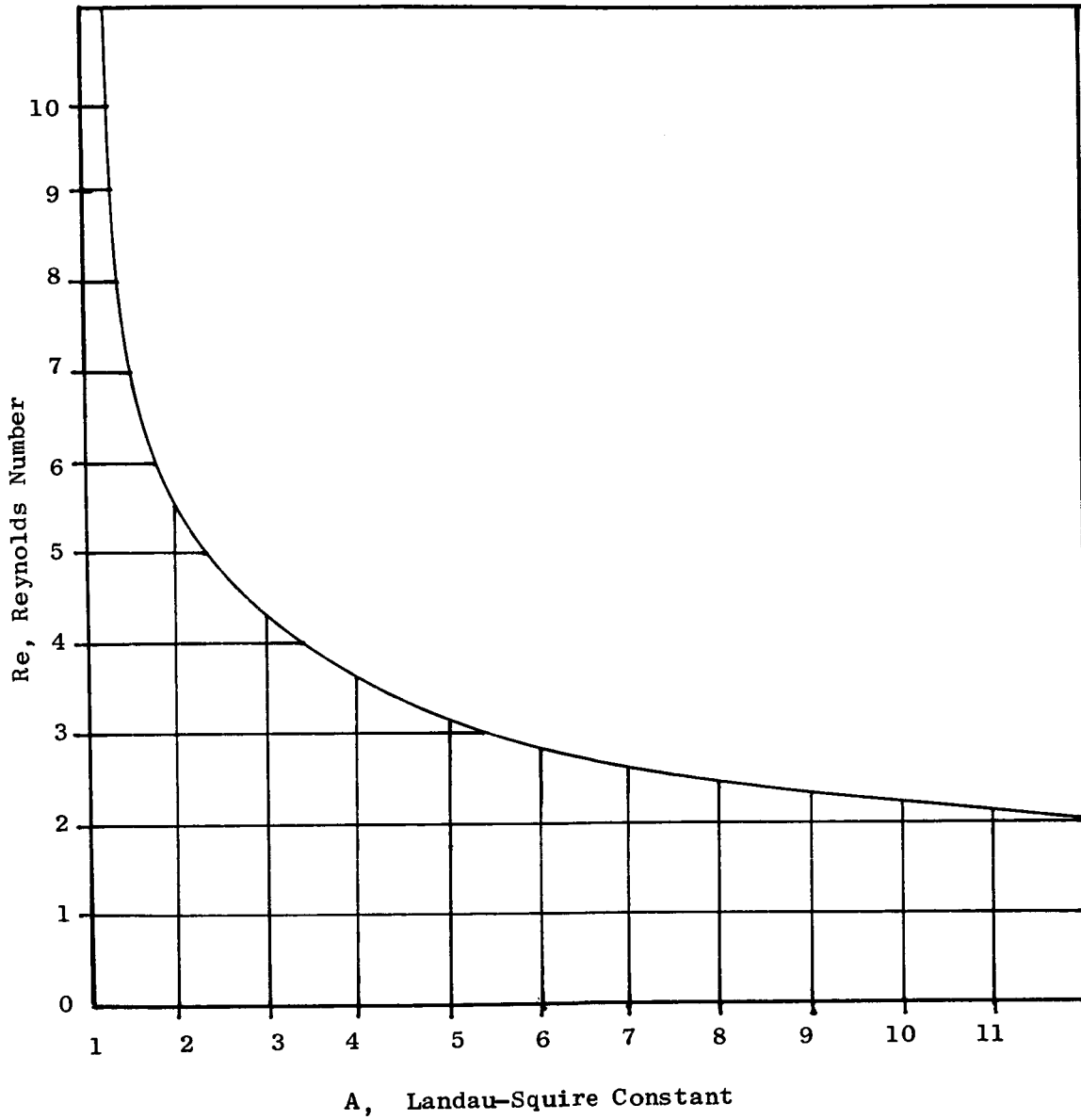
Figure 5-2. Plot of A vs Re.

$$\frac{Re^2}{16\,\pi} \approx \lim_{A \to \infty} \frac{1}{A} \ . \tag{5.34}$$

If (5.34) is inserted in (5.31) or (5.32) and $A \to \infty$ it can be observed that the Reynolds number dependence cancels out in both equations as $Re \to 0$. While it is straightforward to calculate Re for a given A it is remarkably difficult to calculate A for given Re. No stable implicit iterating scheme has been discovered for (2.51b). Because (2.51b) is basically a corner function, one finds that Newton-Raphson schemes and bisection schemes will fail unless one is very careful. This is due to the fact that for one leg of the function a slight change in A causes an extreme change in Re while for the other leg a slight change in Re causes an extreme change in A (see Fig. 5-2). Therefore if an interating scheme is tuned for one leg it will fail for the other and no scheme seems to work well for both. The approach eventually used was to employ a brute force bisection iterator for small A and to employ the asymptotic relation (5.34) for large A ($A > 50.2880$, $Re < 1.0$). Though this method works it is slow and inefficient. The author feels that a better method can be found and suggests either two iterators customized for $Re \geq 4.5$ and $Re < 4.5$ (which is roughly the turning point in this corner function) or attacking (5.33) by using the relation $A = 1 + \epsilon$ where ϵ is assumed to be small (efforts at this approach have so far been fruitless).

3. Boundary Condition In The Far Field

The remaining boundary condition that needs to be examined is the far field ($r \to \infty$) boundary. Placing the dipole boundary as expressed by (2.50) at a

finite location was tried initially but undesirable oscillations and degraded convergence rates were a consequence. One positive aspect that was noted though, was that the near-field behavior of the solution including critical point location q values, etc. was strongly dominated by the Landau-Squire solution boundary of (5.32). One could have almost anything as a far field boundary (including garbage as was discovered) and provided it was far enough away, have little effect on the near field solution. This aspect emboldened us to try different approaches to the far field boundary. The far field vorticity was quite straightforward and was simply set to zero. Vorticity dies off as a variation of some Gaussian function, in an unbounded problem, and has been observed to drop by tens of orders of magnitude in the range of ξ used.

The approach we ultimately decided to use for the far field boundary condition involved the axisymmetric irrotational multipole solution described by Eq. (A-113). The far field portion of (A-113) was selected, combined with (2.66) to provide the self similar stream function.

$$G(\xi,\theta) \quad = \quad \frac{1}{\text{Re}^2} \sum_{j=1}^{\infty} D_j \frac{\sin\theta \, P_j^1(\cos\theta)}{\xi^j} \tag{5.35}$$

where D_j is a constant, and $P_j^1(\cos\theta)$ is a first order associated Legendre polynomial. The far field dipole solution of (2.50) when combined with (2.66) gives

$$G_{dipole}(\xi,\theta) \quad = \quad \frac{1}{4\pi} \frac{\sin^2\theta}{\xi} \tag{5.36}$$

With (5.36) we can calculate D_1 in (5.35) and find that it is

$$D_1 = \frac{\text{Re}^2}{4\pi} \quad . \tag{5.37}$$

The D_1 coefficient we get for free, but the multipole coefficients (also known as tesserals) for D_j, where $j \geq 2$ require some extra effort in the form of Fourier integrals and the integral form of the Poisson equation. Because the first order associated Legendre polynomial is a complete orthogonal function, we may recast (5.35) by Fourier theory into the following integral

$$D_l = \text{Re}^2 \, \xi^l \left(\frac{2l+1}{2} \right) \frac{(l-1)!}{(l+1)!} \int_0^\pi G(\xi,\theta) \, P_l{}^1 (cos \; \theta) \, d\theta \quad . \tag{5.38}$$

The self similar stream function $G(\xi,\theta)$ seen in (5.38) is found by starting with an expression for vorticity by combining (2.18) with (2.7) and (2.4) giving

$$\nabla(\nabla \cdot \vec{B}) - \nabla^2 \vec{B} = \vec{\omega} \quad . \tag{5.39}$$

To go beyond this point we follow Batchelor [1967] in recognizing that if the vorticity normal to the surface of the control volume containing our flow is equal to zero, then the following gauge (a Columb gauge) is appropriate

$$\nabla \cdot \vec{B} = 0 \quad . \tag{5.40}$$

Equation (5.39) combined with (5.40) is now a Poisson equation which has the following integral form

$$\vec{B} = \frac{1}{4\pi} \int_{control \; volume} \frac{\vec{\omega}(\vec{x}')}{|\vec{x} - \vec{x}'|} \, d^3 x' \tag{5.42}$$

where $\vec{x}$ is a position vector within the control volume. In the axisymmetric case, $\vec{B}$ has only one component B_ϕ which is related to $g(\xi,\theta)$ via (2.30) and (2.62). One then replaces the $G(\xi,\theta)$ of (5.38) with (5.42) and proceeds to integrate. One can integrate the resultant equation by brute force replacing $|\vec{x} - \vec{x}'|$ with a "law of cosines" expression leading to relations involving elliptic integrals, or one can replace $|\vec{x} - \vec{x}'|$ with a Green's function

$$\frac{1}{|\vec{x} - \vec{x}'|} = \sum_{l=0}^{\infty} \sum_{m=-l}^{l} \frac{r'^{\,l}}{r^{l+1}} \left[\frac{(l-m)!}{(l+m)!} \right] P_l^m (\cos \theta') \, P_l^m (\cos \theta) \, e^{im(\phi-\phi')}$$

$$(5.43)$$

We must employ the axisymmetric form of vorticity and vector potential

$$\vec{\omega}(\vec{x}') = -\omega_\phi \sin \phi' \, \hat{e}_x + \omega_\phi \cos \phi' \, \hat{e}_y \qquad (5.44)$$

$$\vec{B}(\vec{x}) = \frac{\psi}{r \sin \theta} \left[-\sin \phi \, \hat{e}_x + \cos \phi \, \hat{e}_y \right] \qquad (5.45)$$

where $\hat{e}_x$ and $\hat{e}_y$ are Cartesian unit vectors. Equations (5.43) - (5.45) are inserted into (5.42) and the real part is taken. The result is then inserted into (5.38) and the stream function and vorticity are converted to their self similar form via (2.66) - (2.67). The resultant equation is integrated employing the orthogonality relations for $\cos \phi$ and $P_l^1(\cos \theta)$ giving

$$D_l = \frac{\text{Re}^2}{2} \left[\frac{(l-1)!}{(l+1)!} \right] \int_0^{\xi_\infty} \int_0^{\pi} W(\xi', \theta') \xi'^{\,l+2} P_l^1(\cos \theta') \sin \theta' \, d\theta' \, d\xi' \quad .$$

$$(5.46)$$

The integration of (5.46) requires that either an analytic form of vorticity be known or a table of numerical values be provided for numerical integration. Equation (5.46) is the equation actually used in the software to find D_l, where (5.35) could be used via (5.10) and (5.11) to define a Dirichlet boundary condition. The parameter ξ_∞ is the ξ value where the multipole boundary condition is imposed and presupposes that the vorticity for $\xi \geq \xi_\infty$ is sufficiently small as to be negligible. Only the first six terms of the series are used $(l \leq 6)$ with the belief that extra terms would be buried in the numerical error.

It was later found that greater stability in the solution could be achieved if a Neumann rather than Dirichlet boundary condition was used for the stream function at ξ_∞. This was brought about by restructuring the finite difference equation (5.26) for the nth node points in an $n \times n$ mesh as follows:

$$
\left[\tilde{N} + \tilde{B} \right] \left(2h \left. \frac{\partial Z}{\partial \xi} \right|_{\xi=\xi_\infty} \right) + 2\tilde{N} Z_{n-1,j} + \left[\tilde{C} - 2(\tilde{A} + \tilde{D}) \right] Z_{n,j}
$$

$$
+ \left[\tilde{D} + \tilde{E} \right] Z_{n,j+1} + \left[\tilde{D} - \tilde{E} \right] Z_{n,j-1} = \tilde{R}
$$

$$
(5.47)
$$

where

$$
\frac{\partial Z}{\partial \xi} = \frac{1}{\beta} \left[\frac{dG}{d\xi} - Z \frac{d\beta}{d\xi} \right]
$$

and

$$
1 \leq j \leq n
$$

The partial derivatives in (5.47) are found analytically from (5.13) and (5.35). The vorticity boundary condition for ξ_∞ was kept as a Dirichlet type with $Y(\xi_\infty, \theta) = 0$. Going to the Neumann boundary condition on stream function, Z enhanced the convergence rate and significantly reduced oscillation in the far field solution due to boundary condition mismatch.

Equation (5.46) has a nice side benefit in that over all solution accuracy can be measured by comparing the D_1 value calculated by (5.46), to the analytic value given by (5.37). The D_1 value actually used in the boundary condition of (5.35) was the value given by (5.37). The numerical calculation of (5.46) involved using the latest iteration of $W(\xi, \theta)$ and integrating by Simpson's rule in the ξ direction and in the θ direction. The integrating formula used was the following, showing the ξ direction integral as an example:

$$\int_0^{\xi_\infty} f(y)\,dy = \frac{h}{3}\left[f_0 + 4U + 2E + \frac{17}{8} f_{n-2} + \frac{27}{8}\left(f_{n-1} + f_n \right) + \frac{9}{8} f_{n+1} \right]$$

$$(5.48)$$

where

$$U = f_1 + f_3 + f_5 + \cdots + f_{n-3}$$

$$E = f_2 + f_4 + f_6 + \cdots + f_{n-4}$$

$$f_{n+1} = f(\xi_\infty)$$

$$f_0 = f(0)$$

$$\xi_\infty = h(n+1)$$

For (5.48) there are n node points between the two boundary node points at 0 and n + 1, where h is the step size between each node point. The θ integration is the same as (5.48) except π is the upper limit instead of ξ_∞ and a metric term is introduced to account for the theta stretching algorithm.

4. The Angular Coordinate Mesh Stretcher

In (5.14) we showed that the angular coordinate δ used in the numerical computation is based on θ and Reynolds number. Up until now the δ coordinate has been left in general terms. The purpose of this coordinate is to act as a mesh stretcher so that computational points may be transferred from regions with low gradients and low truncation error to regions where the gradients and truncation error are high. A similar stretcher for ξ has not been developed because more points can be bunched near the origin by simply reducing the value of ξ_∞, and bringing the multipole boundary condition in closer. The discovery of the most appropriate theta stretcher was achieved by a long process of trial and error. The ultimate version arose from the realization that the stretcher needed two control "knobs" to be effective. One knob controlled the angle at which no stretching occurred. This angle is referred to as $\tilde{\theta}$ with greatest concentration of node points near the axis of the jet. The other knob was λ, "rate-of-stretch" which could be set to zero where $\delta = \theta$ or to some

number causing a rearrangement of points but not affecting the influence of $\tilde{\theta}$. The resultant stretcher is

$$\delta = \left[1 + \lambda(e^{-\eta} - 1) \right] \theta - \lambda\pi \left[e^{\frac{-\eta}{\pi}\theta} - 1 \right] \tag{5.49a}$$

$$\tilde{\theta} = -\frac{\pi}{\eta} \ln \left[\frac{1}{\eta} \left(1 - e^{-\eta} \right) \right] \tag{5.49b}$$

where

δ = the stretched coordinate in radians

λ = rate-of-stretch knob

θ = the physical space angle in radians

η = the switch-over angle parameter

$\tilde{\theta}$ = switch-over angle .

To find $\tilde{\theta}$ "switch-over angle" (rads) one uses (5.49b) with η as the single parameter.

One unfortunate aspect of (5.49a) is that while it is straightforward to go from θ to δ, it is difficult to go from δ to θ because (5.49a) is transcendental. To go from δ to θ one uses the following iterating formula

$$\theta_{n+1} = \frac{\left[\delta - \lambda\,\pi \right] + \pi \left[\frac{\eta}{\pi}\theta_n + 1 \right] \lambda\, e^{-\frac{\eta}{\pi}\theta_n}}{\left[1 + \lambda \left(e^{-\eta} - 1 \right) \right] + \eta\,\lambda\, e^{-\frac{\eta}{\pi}\theta_n}} \tag{5.50}$$

where θ_n is the present guess of theta and θ_{n+1} the next guess. This formula is based on Newton-Raphson and is quite stable, converging in approximately ten iterations. The first guess for starting θ_n is δ. In the equations where θ appears explicitly, (5.50) is used to calculate its value.

Equation (5.49a) has several advantages as a stretcher: $\delta = 0$ for $\theta = 0$ just as $\delta = \pi$ for $\theta = \pi$ no matter what value of λ or η is selected thereby ensuring that the boundary conditions of $\theta = 0, \pi$ are not disturbed by the stretcher. While the function is valid only for the region of $0 \leq \theta \leq \pi$, $0 \leq \delta \leq \pi$ it is singled valued and continuous in all derivatives.

The $\tilde{\theta}$ marks the angle where node points are being removed from the parameter region of larger angle and added to the region of smaller angle. The appropriate value for η is readily found by realizing that all the major action of the flow must occur in the region of $0 \leq \theta \leq \tilde{\theta}$. The region defined by $\tilde{\theta}$ is a cone where the flow geometry (in State 3) is a mushroom shape that must fit snugly inside this cone (see Fig. 5-3A). This stretch algorithm has been referred to as a Japanese Fan coordinate stretcher. In Fig. 5-3B we can see an unstretched mesh (radial mesh not shown). As the Reynolds number is increased, coordinate mesh lines are transferred over from one side of $\tilde{\theta}$ to another causing greater density near the axis at $\theta = 0$. This is shown in Figs. 5-3C and 5-3D for increasing Re. This is analogous to a closing Japanese fan where the density of fan pleats increases as the fan closes. One of the fortunate observations of this research was that the spreading angle of the State 3 round jet along with the
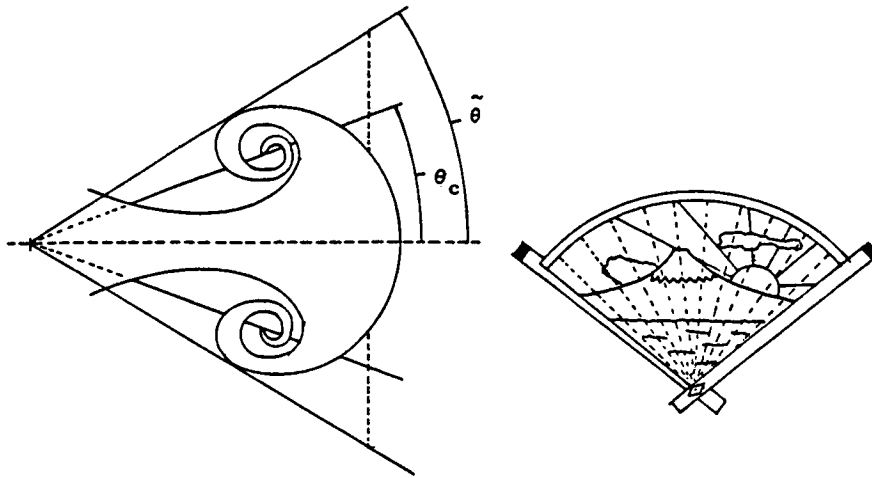
Figure 5-3A. Switch-Over Cone of the Theta Stretcher.
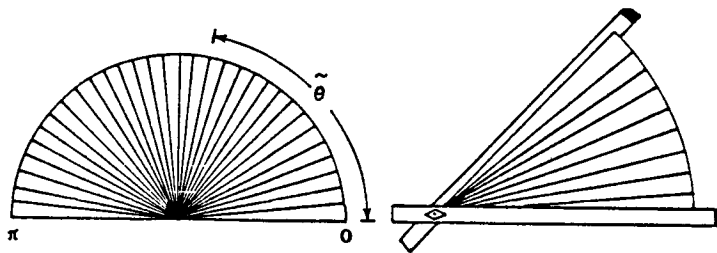
Figure 5-3B.
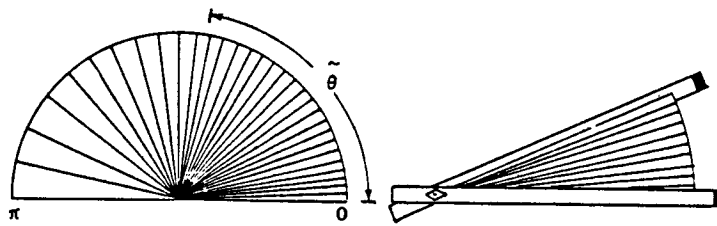
Figure 5-3C.
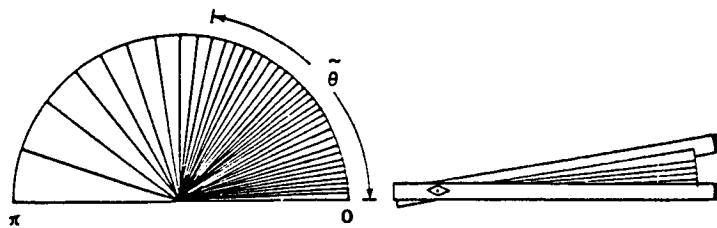
Figure 5-3D.

Figure 5-3A-D. The Theta Stretcher as a Japanese Fan.

q parameter of (p, q) space is a linear function of Reynolds number (contrary to the Re^4 dependence flow, see Eqs. 4.12 and 4.14). This assumes that the numerical method has not become ill conditioned (stiff), at which point it becomes Reynolds number invariant. This makes deriving an empirical formula for $\eta = f(Re)$ quite simple. All that is required is two data points and knowing at what Reynolds number a given mesh will go stiff necessitating a finer mesh. The λ "rate-of-stretch" parameter was likewise assumed to be a linear function of Reynolds number and was described by a similar empirical formula based on two data points which was refined with higher Reynolds number. λ was tuned by first establishing the correct η by knowing the basic flow geometry and tuning λ to higher values until the region outside the "switch-over cone" started to oscillate unnaturally, at which point λ was backed down until the whole flow field was uniformly smooth. One aspect of the theta stretcher that should be understood by the reader is that it was not activated until the Reynolds number was greater than 10. For Re $\leftarrow$ 10 the value of λ was zero and the stretcher was inactive, resulting in a mesh of constant step size.

5. The Matrix Solver

We can now address the method of actually solving the finite difference equations of (5.25) and (5.26), which employs a special linear system solver. The linear system to be solved is the classic one of $\mathbf{Q}\,\overline{X} = \overline{Y}$, where $\mathbf{Q}$ is a square sparse matrix, and $\overline{X}$ and $\overline{Y}$ are column vectors. The matrix $\mathbf{Q}$ con-

tains the finite difference equation, $\bar{X}$ is the solution vector, and $\bar{Y}$ is the right-hand side of the finite difference equation plus boundary condition terms. Since both finite difference equations (5.25) and (5.26) are two-dimensional, second-order central difference equations, the molecule or stencil used to solve for one node point is made up of five points, see Fig. 5-3. The linear system that will solve a mesh based on this five-point molecule is the tri-block system which is analogous to the tri-diagonal system except that each of the elements along the

Fig. 5-4. Control Difference Molecule

diagonal are made up of matrices rather than scalar elements. The arrangement

of this system is shown in (5.51)

$$
\begin{bmatrix}
A_1 & B_1^2 & & & & & \\
B_1^1 & A_2 & B_2^2 & & & \bigcirc & \\
& B_2^1 & A_3 & B_3^2 & & & \\
& & B_3^1 & A_4 & \ddots & & \\
& \bigcirc & & \ddots & \ddots & & \\
& & & B_{n-2}^1 & A_{n-1} & B_{n-1}^2 \\
& & & & B_{n-1}^1 & A_n
\end{bmatrix}
\begin{bmatrix}
X_1 \\ X_2 \\ X_3 \\ \cdot \\ \cdot \\ X_{n-1} \\ X_n
\end{bmatrix}
=
\begin{bmatrix}
Y_1 \\ Y_2 \\ Y_3 \\ \cdot \\ \cdot \\ Y_{n-1} \\ Y_n
\end{bmatrix}
\qquad (5.51)
$$

<div align="center">

Q matrix $\bar{X}$ vector $\bar{Y}$ vector

</div>

The subblocks of A_j, B_j^1, B_j^2 X_j Y_j have the following form:

$$
A_j =
\begin{bmatrix}
a_{11} & a_{21} & & & \bigcirc & \\
a_{12} & a_{22} & a_{32} & & & \\
& a_{23} & a_{33} & a_{43} & & \\
& & \ddots & \ddots & \ddots & \\
& \bigcirc & & a_{ii} & a_{n,n-1} \\
& & & a_{n-1,n} & a_{nn}
\end{bmatrix}
\qquad
X_j =
\begin{bmatrix}
x_{1j} \\ x_{2j} \\ x_{3j} \\ \cdot \\ \cdot \\ x_{ij} \\ \cdot \\ x_{nj}
\end{bmatrix}
\qquad (5.52)
$$

$$B_j^k = \begin{bmatrix} b_{11}^k & & & & & \bigcirc & \\ & b_{22}^k & & & & & \\ & & b_{33}^k & & & & \\ & & & b_{44}^k & & & \\ & & \bigcirc & & b_{11}^k & & \\ & & & & & & \\ & & & & & & b_{nn}^k \end{bmatrix} \qquad Y_j = \begin{bmatrix} y_{1j} \\ y_{2j} \\ y_{3j} \\ \vdots \\ y_{1j} \\ \vdots \\ y_{nj} \end{bmatrix} \qquad (5\text{-}53)$$

where $k = 1$ or 2, and a_{ii}, $a_{i,i\pm1}$, x_{ij}, y_{ij}, b_{ii}^k are scalar matrix elements. The matrix subblock A_j of (5.52) is a tri-diagonal matrix while B_j^k of (5.53) is a simple diagonal matrix. Using (5.26) as an example we can demonstrate how a finite difference equation is loaded in this linear system, which in this example, is centered on the node point at i,j. For the j subblock

$$a_{i-1,i} = \tilde{N} - \tilde{B}$$

$$a_{i,i} = \tilde{C} - 2(\tilde{N} + \tilde{D})$$

$$a_{i+1,i} = \tilde{N} + \tilde{B}$$

$$b_{ii}^2 = \tilde{D} + \tilde{E}$$

$$y_{ij} = \tilde{R}$$

For the j - 1 subblock,

$$b_{ii}^1 = \tilde{D} - \tilde{E}$$

The computational domain is made up of $n \times n$ points (not including the boundaries), see Fig. 5-1. One can see that for the case of $i = 1$ the Landau Squire boundary has to be taken into account due to $i - 1, j$ component of the finite difference equation. This is done by setting the $a_{i-1,i}$ element for the A_j subblock equal to zero and taking the appropriate form of the Landau Squire solution multiplied by $-(\tilde{N} - \tilde{B})$ and added to y_{ij}. The multipole boundary is treated similarly while the $\theta = 0, \pi$ boundaries result in the appropriate b_{ii}^k elements being zeroed. Equation (5.51) is solved by getting it into an upper triangular form and solving by back substitution. The matrix in upper triangular form $U \, \overline{X} = \overline{R}$ is the following:

$$
\begin{bmatrix}
I & U_1 & & & & \\
 & I & U_2 & & & \\
 & & I & U_3 & & \\
 & & & \ddots & \ddots & \\
 & & & & I & U_{n-1} \\
 & & & & & I
\end{bmatrix}
\begin{bmatrix}
X_1 \\
X_2 \\
X_3 \\
\vdots \\
X_{n-1} \\
X_n
\end{bmatrix}
=
\begin{bmatrix}
R_1 \\
R_2 \\
R_3 \\
\vdots \\
R_{n-1} \\
R_n
\end{bmatrix}
\qquad (5\text{-}54)
$$

where I is the $n \times n$ identity matrix. The equations relating (5.54) with (5.51)

are first the "boot strap equation"

$$U_1 = \left[\left(B_1^2 \right)^{-1} A_1 \right]^{-1} \tag{5.55}$$

$$A_1 R_1 = Y_1$$

Then the "downward sweep equations":

$$L_j = A_j - B_{j-1}^1 U_{j-1} \tag{5.57}$$

$$U_j = \left[\left(B_j^2 \right)^1 L_j \right]^{-1} \tag{5.58}$$

$$L_j R_j = Y_j - B_{j-1}^1 R_{j-1} \tag{5.59}$$

There is then the "backward sweep bootstrap"

$$X_n = R_n \tag{5.60}$$

with finally the "backward sweep equation"

$$X_{j-1} = R_{j-1} - U_{j-1} X_j \tag{5.61}$$

Equations (5.60) and (5.61) provide the solution. There is a problem with this method involving the storage of the U_j matrices. The storage requirements in the $\mathbf{Q} \overline{X} = \overline{Y}$ system, not including zeros and the solution vector $\overline{X}$ are given by the equation

$$\# \ of \ elements = 6n^2 - 4n \tag{5.62}$$

For the $\overline{U} \overline{X} = \overline{R}$ system, not including zeros, 1's and the solution vector is

$$\# \ of \ elements \ = \ n^3 \tag{5.63}$$

If one is using a mesh of 60×60 points where $n = 60$ then the storage required by $\mathbf{Q} \ \overline{X} = \overline{Y}$ is 21,360 while the storage required by $\mathbf{U} \ \overline{X} = \overline{R}$ is 216,000. This order of magnitude greater storage requirement is a consequence of the U_j submatrices being nonsparse because they are the result of matrix inversions. The order of magnitude greater storage requirement does not need to be accepted because the $\mathbf{U} \ \overline{X} = \overline{R}$ system is only an intermediate step and contains the same information as $\mathbf{Q} \ \overline{X} = \overline{Y}$. The answer to this dilemma is to keep only the U_{j-1} submatrix when calculating L_j in (5.57) and to throw U_{j-1} away afterwards. When the downward sweep is complete the U_j matrices will have to be regenerated in order to provide the solution vector in (5.61). This requires the following additional equation

$$U_{j-1} \ = \ \left(B_{j-1}^1 \right)^{-1} \left(A_j - B_j^2 \ U_j^{-1} \right) \tag{5.64}$$

This equation, called the "yo-yo sweep" equation is actually just a backward sweep equation that is a companion to (5.61). Using (5.64), U_{j-1} is generated for (5.61) and the old U_j is thrown away. This technique of regenerating U_j by the yo-yo sweep is essentially trading off a factor of two increase in computer time for an order of magnitude increase in storage. There is a difficulty in (5.64) however, which is that this equation appears to amplify round-off error.

The mechanism of this round-off error amplification is not fully understood and deserves further study. For the purposes of this problem a fix was found by

$C-2$

periodically "refreshing" the U_j matrix by using a stored version rather than regenerating it by (5.64). The frequency of refresh was found by taking a linear system with a known solution vector whose Q matrix was ill conditioned. The solution vector calculated was then closely observed and whenever the roundoff error became significant (i.e., observable) the U_j submatrix would be refreshed.

The maximum matrix ever calculated by this technique was for an 80 $\times$ 80 computation mesh which corresponds to a 6400 $\times$ 6400 element Q matrix (all elements including zeros).

6. The Under Relaxation Method

Next we examine the under relaxation method used to solve for vorticity and stream function. This was the price we had to pay for the simplicity of a two-step (vorticity solved then stream function) solution method. The under relaxation used was

$$G_{n+1} = G_n + \Upsilon \left[G_{n+1}^* - G_n \right] \tag{5.65}$$

for

$$\Upsilon = 1 \qquad 0 \leq \text{Re} < 5.0 \tag{5.66}$$

$$\Upsilon = 0.7 \qquad 5.0 \leq \text{Re} < 6.0 \tag{5.67}$$

$$\Upsilon = 0.1 \qquad 6.0 \leq \text{Re} \tag{5.68}$$

where

G_n = the previous iteration stream function matrix;

G_{n+1}^{*} = the latest calculated stream function;

G_{n+1} = the under relaxed stream function;

Υ = the under relaxation scalar whose values are shown in (5.66) to (5.68).

The region of $5.0 \leq Re < 6.0$ encloses the first transition where, due to the critical point bifurcation, it was necessary to under relax. For $\Upsilon = 1$ (5.65) is made inactive. So for $Re < 5.0$ there is no under relaxation. Under relaxation, when it was in force, would occur with every iteration of the two-step cycle.

7. Solution Method Overview

The software is cold started at a low Reynolds (typically $Re = 0.1$) and the solver is primed with the creeping solution for the nonlinear scale functions

$$Y(\theta) = \sin \theta \qquad (5.69)$$

$$Z(\theta) = \sin^2\theta \qquad (5.70)$$

With these scale functions as a first iterate the next iteration is found for the vorticity scaling function $Y_{i,j}$ through (5.25) via the linear solver with $Z_{i,j}$ held fixed. With the updated vorticity the multipole constants are also updated via (5.46). The vorticity solution is then used with (5.26) to solve for the stream function scaling function $Z_{i,j}$ by use of the linear solver. With the new stream

function $Z_{i,j}$ the vorticity is recomputed as before through (5.25). The new vorticity is compared against the previous iterate. If the difference is sufficiently small between two successive iterations then the solution is considered converged. If not, then the cycle repeats until convergence or until the iteration limit is reached and the program aborted. In the case of convergence the values of vorticity, stream function, and multipole constants are written onto disk. The Reynolds number is usually incremented by 1. The Landau-Squire constant is recomputed along with the mesh stretching parameters and under-relaxation constant. The previous solution is used as a priming first iterate and the cycle is continued until convergence for the new Reynolds number. This process continues from a creeping Reynolds number of 0.1, incrementing first by 0.9 and then by units of 1 until the Reynolds number is sufficiently high that acceptable accuracy with a given mesh is no longer attainable. Software validation for this system is relatively straightforward. The "*nonlinear* scale functions" (in this case a misnomer) for the linear solution are now in equations (5.69) and (5.70). If the convective terms in the software are disabled and a creeping form of the Landau-Squire solution is used as a boundary condition, then the resultant solution will always be (5.69) and (5.70). Therefore it is a simple matter of comparison to see if the software is error free. Likewise the far-field boundary condition can be replaced by the Landau-Squire solution (which is also used in the near field) for a test of the validity of a solution which includes the convective terms. For this case the Landau-Squire solution would be the observed result for the entire computational domain. This makes error detection a matter of com-

parison with an analytic result. Because of these tests we have a high level of confidence in the validity of our method and software.

8. Some Unsuccessful Approaches

Finally, we would not want the reader to be left with the impression that the method described was found without going down some deadends, or without realizing that there are better approaches than the one used. A deadend approach that cost us a lot of time made use of a formulation in terms of the following equations:

$$
\frac{1}{1 - \tilde{\eta}^2} \frac{\partial}{\partial \xi} \left[\frac{\partial \tilde{W}}{\partial \xi} + \tilde{W} \left(\frac{\xi}{2} + \frac{1}{\xi^2} \frac{\partial G}{\partial \tilde{\eta}} \right) \right] \tag{5.71}
$$
$$
+ \frac{1}{\xi^2} \frac{\partial}{\partial \tilde{\eta}} \left[\frac{\partial \tilde{W}}{\partial \tilde{\eta}} - \tilde{W} \left(\frac{1}{1 - \tilde{\eta}^2} \frac{\partial G}{\partial \xi} \right) \right] = 0
$$

$$
\tilde{W} = \frac{\partial^2 G}{\partial \xi^2} + \frac{1 - \tilde{\eta}^2}{\xi^2} \frac{\partial^2 G}{\partial \tilde{\eta}^2} \tag{5.72}
$$

where $\tilde{\eta} = \cos \theta$.

Equations (5.71) and (5.72) represent a compact form of equations (5.1) and (5.2). Because of their symmetrical form it is tempting to think that an analytic solution can be found (though we have not found it). The deadend that we encountered involved trying to convert (5.71) and (5.72) into a single central difference equation while retaining the simple structure of the equations. We

found out that the multi-valued nature of $\tilde{\eta} = \cos\theta$ near $\theta = 0$ and π plus the need for a 13 point finite difference molecule created unavoidable problems in the boundary conditions. There were two alternative approaches to the numerical solution that were considered but not used. One of these two alternate schemes would have involved inserting (5.72) into (5.71) and expanding the result into a finite difference equation with stream function as the single dependent variable. This finite difference equation would then be solved by a symmetric penta-diagonal block solver using Newtonian iteration. This approach has a number of advantages: one pass solver, no relaxation constants, single boundary conditions, etc. The main drawback is that the finite difference equation is so long that it is very difficult to avoid transcription errors without having access to an algebra program such as MACSYMA. The second scheme involved writing (5.71) and (5.72) together in a single linear system with the stream function and vorticity stacked in a single solution vector. This method had the advantages of having relatively straightforward difference equations, no relaxation constant and boundary conditions on a single variable (stream function). The disadvantage is that the linear algebra in the matrix solver is very messy requiring a customized algorithm for the unsymmetric diagonals. However, when we look back with the clear vision of hindsight, this second scheme might have been the best way to go. The customized solver would have been trouble. However, we too had to write a special solver for our tri-block system anyway, so the added complexity of the custom solver would not have been that great. The customized single pass solver without relaxation would have certainly been faster. If the reader intends to

investigate a problem similar to ours it is recommended that the second scheme be investigated first before reproducing our actually used approach or resorting to the first scheme.

Chapter VI

COMPUTATIONAL RESULTS

1. Flows Computed By The Program MAVIN

The numerical method described in Chapter V was developed in a program named MAVIN. The source listings of all the software developed in this work, including MAVIN, are presented in App. C. MAVIN was run on the Control Data Corp. computer, CDC 7600 at NASA Ames Research center. MAVIN was used in two basic grid configurations. The first grid configuration was for a 30 point by 30 point mesh ($n = 30$) with a far field boundary radius (ξ_∞) set at 15. The results for the 30×30 cases displayed in App. B started with Re = 0.1. Then Re = 1.0 was computed, thereafter the Reynolds number was increased by units of 1 until Re = 30 was reached. Plots for the 30 cases appear in App. B, Fig. B-1 (Re = 0.1) up to Fig. B-30 (Re = 30). The second grid configuration used the finer mesh of 60 points by 60 points, with the same far field boundary radius at $\xi_\infty = 15$. The 60×60 mesh led to more accurate results than the 30×30 mesh but suffered from the usual tradeoff of being much more expensive to run. As a consequence, only 10 Reynolds numbers were computed, specifically Re = 4, 6, 10, 15, 17, 20, 23, 25, 27 and 30. The results for these cases appear in App. B in Figs. B-31 to B-40. For each

Reynolds number MAVIN generated a matrix representing vorticity, and a matrix for stream function. MAVIN also generated six multipole constants used in the far field boundary condition, the far field boundary location ξ_∞, the mesh size n, the Reynolds number, and the theta stretcher beta parameter.

2. The Arch Spline Used in Data Reduction

The data were outputted as ASCII format records, transferred to disk storage on a VAX computer and archived on magnetic tape. The discrete points represented in the $n \times n$ matrices of vorticity and stream function had to be transformed into a continuous polynomial format for subsequent processing. This was achieved by applying the following spline polynomial to the data

$$f(\xi, \theta) \;=\; \xi^2 \left(c_1\theta^3 + c_2\theta^2 + c_3\theta + c_4 \right) \;+\; \xi \left(c_5\theta^3 + c_6\theta^2 + c_7\theta + c_8 \right)$$

$$+ \; c_9\theta^3 + c_{10}\theta^2 + c_{11}\theta + c_{12} \tag{6.1}$$

where $f(\xi,\theta)$ can represent either vorticity or stream function and the c_k are constants found by fitting the spline technique polynomial to the MAVIN matrices. The spline used is represented in Figs. 6-1, 6-2 and 6-3, which show a hypothetical case of a 6 point by 6 point mesh ($n = 6$). The two dimensional spline function is a second-order polynomial in the ξ direction and a third-order polynomial in the angular (θ or δ) direction. Figure 6-1 shows how each spline passes through three points in the radial direction (for fixed θ). One can see how for Region 1 the spline is matched to the value of node 0, represented by D_1 (Dirichlet match). Nodes 0 and 7 are boundary condition node points for

this 6×6 mesh. The spline from node 0 is then matched at node 1 and node

matched at node 1 and node 2. The region 2 spline has its values matched at

nodes 1, 2, and 3 as represented by D_2.
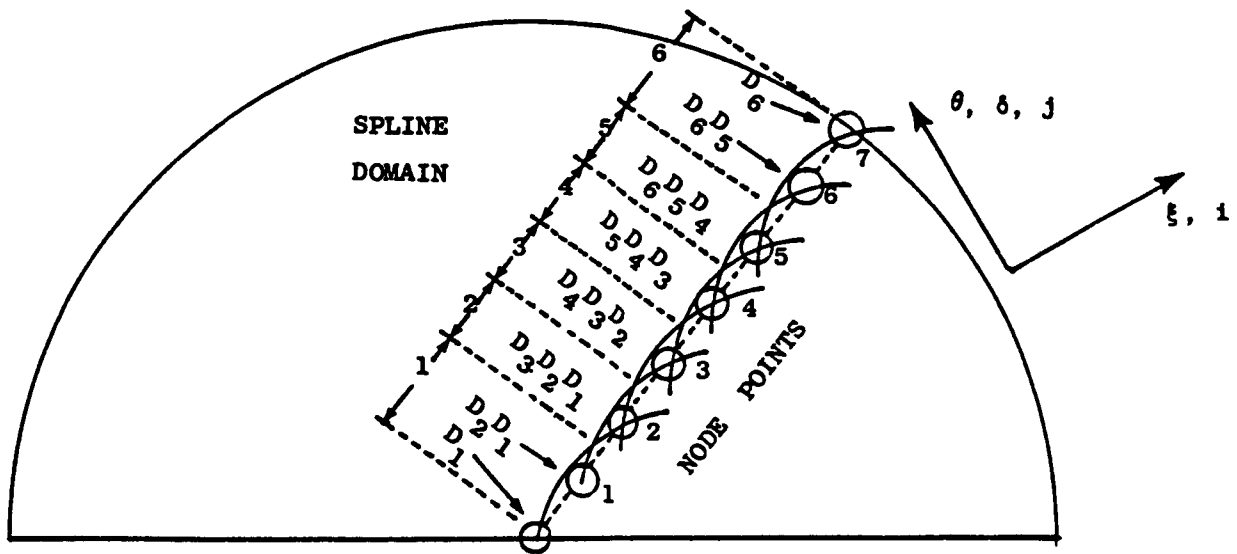
Figure 6-1   Radial Spline.
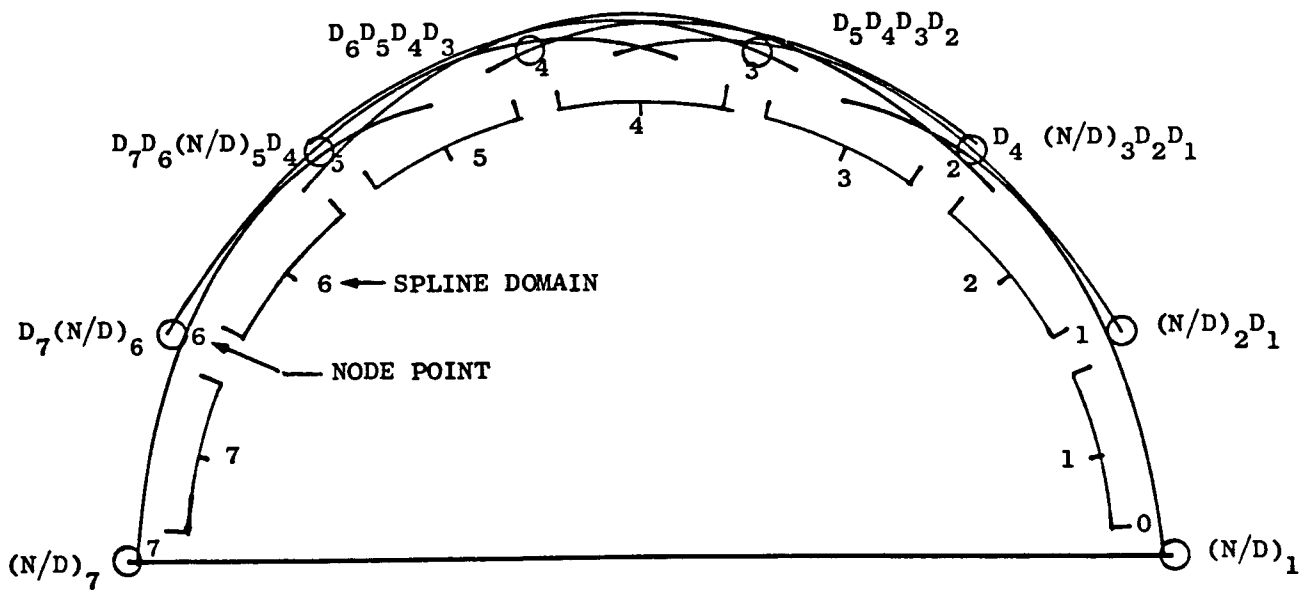
Figure 6-2   Angular Spline.
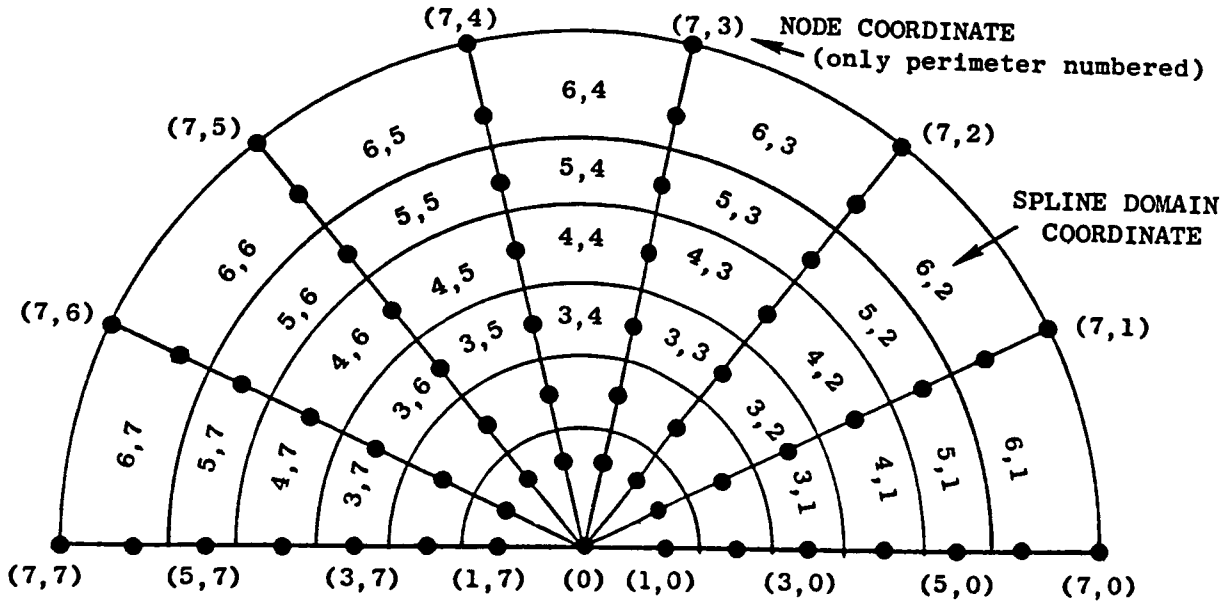
Figure 6.3 Spline Domains.

The radial splines are only matched in actual value, not in slope. One should note that the region of validity for splines 2 - 5 starts and ends halfway between node points, leaving much of the spline unused.

Figure 6-2 represents how the splines are set up in the angular direction. It shows node points with constant angular stepsize which is consistent with the δ unstretched coordinate (θ is the physical angular coordinate). At node 0 (boundary node) of Region 1 the spline is matched to the value of the node (Dirichlet) and also to the value of its slope (Neumann). This is represented by $(N/D)_1$. The spline of Region 1 is also Dirichlet matched through nodes 1 and 2. The next spline for Region 2 is both Dirichlet and Neumann matched $(N/D)_2$ to spline 1 at node 1. This process is continued along the circle of con-

stant ξ. This same process occurs at node 7 for spline 7 except in the opposite direction. The two systems of splines meet at region 4 where a keystone spline is matched to nodes 2 - 5. This is purely a Dirichlet match which is done only at the "keystone" for purposes of closing the system. We see that in all the splines only a part of the spline is actually used in computation. Figure 6-3 shows the two-dimensional spline regions with respect to the MAVIN node points. Some sample MAVIN node points are in parentheses. Those nodes which have values of 0 or 7 correspond to boundary nodes. Once a matrix of c_k values for each spline region has been calculated, then manipulation of vorticity and stream function becomes quite straightforward. If one wishes to calculate a particular vorticity, $W(\xi, \theta)$, the ξ coordinate is divided by h stepsize to find the i index and θ is converted to δ. The value of δ is then divided by the k stepsize to yield the j index. With the i,j indices known, the appropriate spline region is selected and the c_k values are pulled from its storage matrix and inserted into (6.1). Coordinates ξ and θ are then inserted into (6.1) to yield the vorticity. This procedure can yield a higher resolution of the computational domain. It can also provide a simple analytic equation in (6.1) for later manipulation in solving the particle path equations and determining (p, q) values and critical point locations.

3. Plots Of Computational Results

The software that performs this spline operation is called INVORT and is shown in App. C. A higher resolution matrix was generated from these splines and digested by the contour plot programs CONTOUR and CONVORT and the

particle path plot program PLOT which produced the entrainment diagrams. These plots are displayed in App. B in self similar coordinates. Using the results shown in Figs. B-31 and B-32 we have produced Fig. 6-4 in which the particle path plot has been superimposed on the entrainment diagram. The momentum source is always at location (0.0, 0.0) on the plots shown in this work. The flow is always going from left to right along the x axis. The x axis is the axis of symmetry with the plots shown corresponding to the upper half of a plane passing through the axis of symmetry of the flow. The unshown lower half would simply be a mirror image. In Fig. 6-4 we see that the two stream function contour plots are basically dipoles with a bias slightly to the right of the origin. The following coordinates are used:

$$ x = \frac{\bar{x}}{\sqrt{\nu t}} \tag{6.2} $$

$$ y = \frac{\bar{y}}{\sqrt{\nu t}} \tag{6.3} $$

$$ \xi = \sqrt{x^2 + y^2} \tag{6.4} $$

where $\bar{x}$ and $\bar{y}$ are physical Cartesian coordinates. Coordinates x and y are self similar coordinates and are the type used in the axis labels of App. B. We see that the center of the stream function contours for Re = 4 is at about (x, y) = (0.2, 2.0) and for Re = 6 at about (0.5, 1.8). This center corresponds to the peak value of stream function (note that the stream function is zero at the origin and at infinity). The vorticity contour plots of Fig. 6-4 are very similar to each other except for a slight bias to the right at Re = 6 as compared to Re = 4.

STREAM FUNCTION CONTOUR PLOT FOR Re= 4.0
60 X 60 MESH FOR ξ_-=15.0

STREAM FUNCTION CONTOUR PLOT FOR Re= 6.0
60 X 60 MESH FOR ξ_-=15.0

$\dfrac{y}{\sqrt{\nu t}}$

VORTICITY CONTOUR PLOT FOR Re= 4.0
60 X 60 MESH FOR ξ_-=15.0

VORTICITY CONTOUR PLOT FOR Re= 6.0
60 X 60 MESH FOR ξ_-=15.0

$\dfrac{y}{\sqrt{\nu t}}$

PARTICLE PATH PLOT FOR Re= 4.0
60 X 60 MESH FOR ξ_-=15.0

PARTICLE PATH PLOT FOR Re= 6.0
60 X 60 MESH FOR ξ_-=15.0

$\dfrac{y}{\sqrt{\nu t}}$

$x/\sqrt{\nu t}$

$x/\sqrt{\nu t}$

(a)

(b)
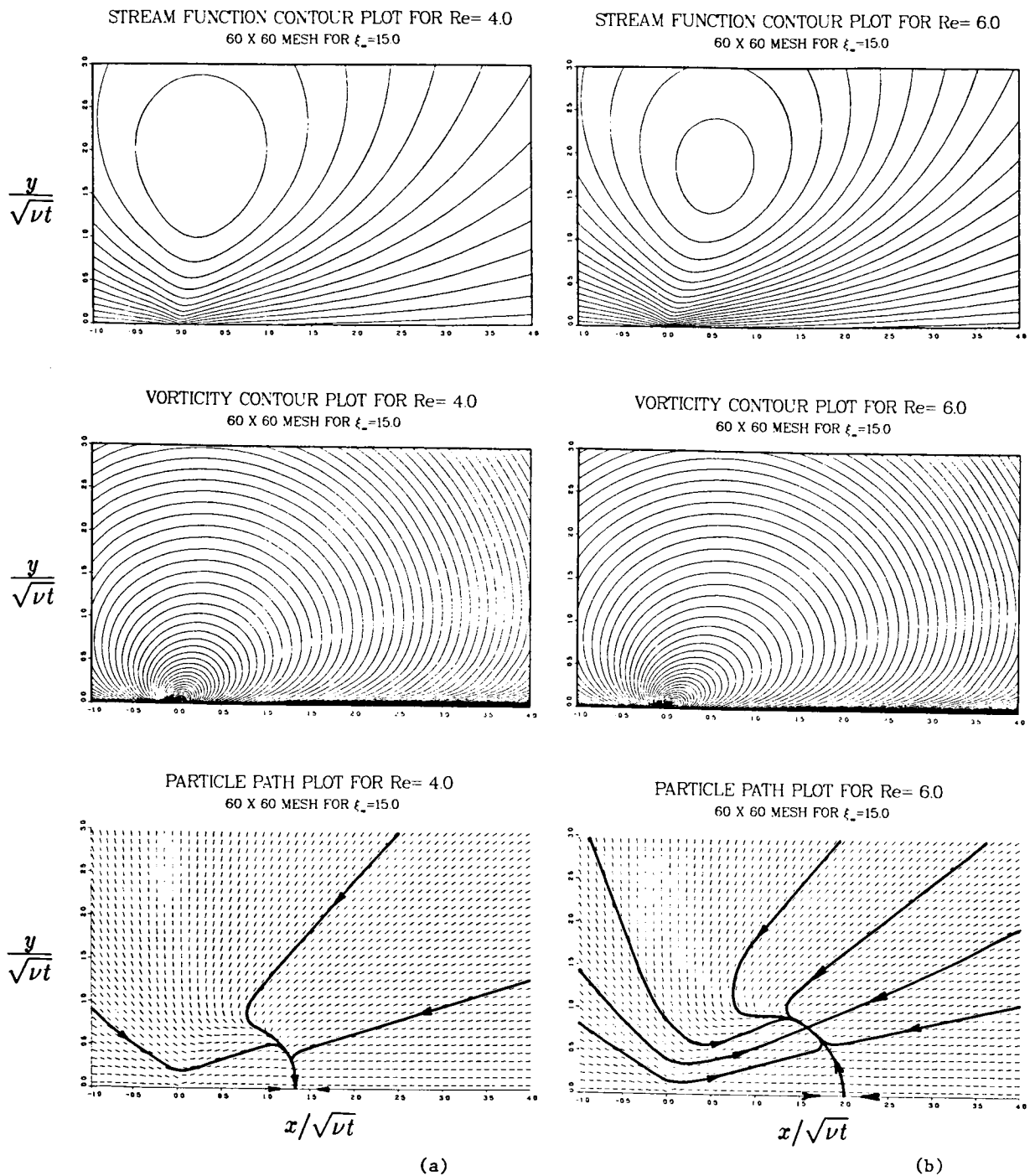
Fig. 6-4:   **Computed solutions for the round jet at a) Re = 4.0, and b) Re = 6.0. Quantities displayed are self-similar stream function, vorticity, and particle paths.**

The peak value of vorticity is always at the origin since vorticity has a singularity proportional to $1/\xi^2$. The entrainment diagrams shown in this work are all based on the particle path equations (4.1) and (4.2). The particle path equations are used to produce the array of isoclines (all normalized to the same length) shown in the entrainment diagrams of Fig. 6-4 and App. B. In contrast to the vorticity and stream function just discussed, we see in Fig. 6-4 that the two entrainment diagrams at Re $= 4$ and 6 are significantly different. In the Re $= 4$ case, one critical point is on the x axis at about $(x_c, y_c) = (1.3, 0)$. In the Re $= 6$ case, there are two critical points. One is on the x axis at $(x_c, y_c) = (2.0, 0)$ and the other is off axis at $(x_c, y_c) = (1.6, 0.8)$. At this stage a key aspect of the work becomes apparent. For different Reynolds number the entrainment diagram topology can be completely different while the vorticity and stream function plots can be almost identical. In this respect, entrainment diagrams are a much more effective means of displaying the structure of the flow than are plots of stream function or vorticity.

4. Transition In The Numerical Solution Of The Navier Stokes Equations

As previously discussed in Chapter 3 the bifurcation from one topology to another represents a form of transition. Based on the results for the p , q plot discussed (in Ch. 3) we know that Re $= 4$ must be in State 1 since it has one on-axis critical point (which has to be a stable node). A close examination of Fig. B-41 shows that the entrainment diagram vectors are consistent with a stable node for Re $= 4$. We can bracket the first transition Reynolds number

Re_1 by studying Fig. B-5 for $Re = 5$ where again we see only one critical point thereby concluding that $Re = 5$ is also in State 1. We now know that $5 < Re_1 < 6$. A naive way of refining Re_1 would be to run a series of computations for $Re = 5$ to 6 looking for critical point bifurcation. This method is ineffective because the region near the axis is one of very high gradients and consequently high truncation error. A better way is to take values of the off-axis critical point (x_c, y_c) for different Re and extrapolate back to Re_1. The parameters of the off-axis critical point are acquired through the program named HAMMER. HAMMER evaluates the particle path equations (4.1) and (4.2) at the off-axis critical point where the equations are equal to zero. The spline polynomial of (6.1) is inserted into these particle path equations yielding the following critical point location formulas:

$$\xi_c = -\frac{1}{2}\left[\frac{c_5(\theta_c^3) + c_6(\theta_c^2) + c_7(\theta_c) + c_8}{c_1(\theta_c^3) + c_2(\theta_c^2) + c_3(\theta_c) + c_4}\right] \tag{6.5}$$

$$\theta_c = \frac{\dfrac{\xi_c^3}{2}\sin\theta_c - \left[3\xi_c^2 + c_7\xi_c + c_{11}\right]}{3\theta_c\left[c_1\xi_c^2 + c_5\xi_c + c_9\right] + 2\left[c_2\xi_c^2 + c_6\xi_c + c_{10}\right]} \tag{6.6}$$

These transcendental formulas are iteratively convergent provided that the critical point location (ξ_c, θ_c) is within the spline domain of the c_k constants used in (6.5) and (6.6). HAMMER works interactively with its user by first receiving a guess of the critical point location. The first guess is used to select a spline domain and a second guess is found by (6.5) and (6.6). If the second guess is within the original domain then the critical point is captured. If

not, a new domain is selected based on the second guess and the process is repeated. If the critical point is on the corner between different spline domains, the HAMMER software can go into an endless hysteresis loop so the user is continually given updated information on domain shifts. Breaking this hysteresis loop requires only a simple software adjustment in the spline domain selector to bias HAMMER toward a particular choice. Once the critical pont is captured, its coordinates and q value are calculated based on the current spline. In Table 6-1 the critical point parameters based on the 30×30 mesh $(n = 30)$ results of App. B are shown. In Table 6-2 a similar table is shown for the 60×60 mesh $(n = 60)$ results for comparison of numerical effects. From Table 6-1 we can extrapolate the first transition Reynolds number Re_1 by fitting a parabola through Reynolds numbers 6, 7, and 8 with q as the independent variable. This gives

$$Re = -2.22q^2 + 5.28q + 5.35 \qquad (6.7)$$

We know from p , q theory that the first transition occurs at $q = 0$. We can extract Re_1 from (6.7) by letting $q = 0$ giving $Re_1 = 5.35$. This result reflects a particular set of data and numerical method. The naive approach mentioned earlier of fine scanning between $Re = 5$ through 6 yielded $Re_1 = 5.1$. This value can be regarded as a lower limit. Of all the different data bases examined in the development of MAVIN, the highest value ever observed was $Re_1 = 5.9$. Thus a conservative evaluation of the first transition Reynolds number is $Re_1 = 5.5 \pm 0.4$ with 5.4 being the value most consistent with the App. B data. Before leaving Fig. 6-4 we should note that the off-axis critical

Table 6-1

CRITICAL POINT PARAMETERS FROM APPENDIX B, N = 30

	Off-Axis Critical Points				On-Axis Critical Points
Re	x_c	y_c	θ_c	q	x_c
0.1	N/A				0.05
1	N/A				0.35
2	N/A				0.70
3	N/A				1.05
4	N/A				1.35
5	N/A				1.60
6	1.65	0.77	25.1	0.13	2.00
7	1.64	1.02	32.0	0.37	2.35
8	1.70	1.15	34.2	0.72	2.60
9	1.88	1.10	30.3	1.09	2.90
10	1.99	1.28	32.8	1.21	3.25
11	2.19	1.34	31.5	1.67	3.50
12	2.39	1.38	30.0	1.78	3.80
13	2.57	1.41	28.8	2.14	4.05
14	2.74	1.44	27.7	2.27	4.30
15	2.91	1.47	26.7	2.53	4.55

Table 6-1 (Cont.)

Re	\multicolumn{4}{c}{Off-Axis Critical Points}	On-Axis Critical Points
	x_c	y_c	θ_c	q	x_c
16	3.06	1.49	26.0	2.75	4.80
17	3.19	1.51	25.3	2.86	5.00
18	3.32	1.52	24.7	3.16	5.15
19	3.43	1.54	24.1	3.53	5.35
20	3.53	1.55	23.7	3.67	5.55
21	3.66	1.56	23.1	3.76	5.75
22	3.75	1.57	22.7	3.82	5.80
23	3.79	1.57	22.5	4.02	5.90
24	3.81	1.57	22.4	4.41	6.00
25	3.83	1.57	22.3	4.41	6.05
26	3.85	1.57	22.2	4.61	6.10
27	3.87	1.57	22.1	4.56	6.10
28	3.89	1.57	22.0	4.55	6.10
29	3.91	1.57	21.9	4.57	6.15
30	3.93	1.57	21.7	4.73	6.25

Table 6-2

CRITICAL POINT PARAMETERS FROM APPENDIX B, N = 60

	Off-Axis Critical Points				On-Axis Critical Points
Re	x_c	y_c	θ_c	q	x_c
4	N/A				1.35
6	1.61	0.80	26.5	0.17	2.00
10	1.98	1.29	33.2	1.27	3.25
15	3.06	1.48	25.8	2.80	4.75
17	3.48	1.52	23.7	3.13	5.30
20	4.03	1.58	21.3	4.02	6.05
23	4.49	1.62	19.8	4.25	6.65
25	4.77	1.64	19.0	5.14	7.05
27	5.00	1.65	18.3	4.94	7.40
30	5.30	1.67	17.5	6.01	7.80

point location for $Re = 6.0$ was at $(1.61, 0.80)$, while the stream function contour center was at $(0.5, 1.8)$. This emphasizes that there really is no simple correlation between the off-axis critical point and the stream function maximum point. The off-axis critical point for $Re = 6$ has a q value of 0.17. This value is consistent with a stable node $(0 < q < 9/16)$ thereby showing that $Re = 6$ is in State 2. The flow will undergo the second transition into State 3 when q attains and surpasses a value of $q = 9/16 = 0.56$. We see from Table 6-1 that this second transition Reynolds number has the following limits: $7 < Re_2 < 8$. A high resolution scan was performed through this region yielding the data shown in Table 6-3. A parabola was fitted through $Re = 7.4$, 7.5 and 7.6 with q as the independent variable giving

$$Re = 11.90q^2 - 10.12q + 9.46 . \tag{6.8}$$

With q replaced by $9/16$ we find $Re_2 = 7.54$. In comparing Table 6-1

Table 6-3

HIGH RESOLUTION SCAN THROUGH Re_2

Re	x_c	y_c	θ_c	q
7.4	1.62	1.09	33.9	0.51
7.5	1.63	1.10	34.0	0.55
7.6	1.64	1.11	34.2	0.58
7.7	1.64	1.12	34.4	0.62

with Table 6-2 we find a q variation of 0.04. Assuming a q deviation of 0.06 for Re_2 we can determine a standard deviation from Table 6-3 for Re_2 of 0.16. This gives our final result as $Re_2 = 7.54 \pm 0.16$.

5. The State Three Solution

For $Re > Re_2$ the flow goes into State 3 where the off-axis critical point becomes a stable focus. In Fig. B-8 we observe this stable focus just beginning to appear in the entrainment diagram. In Fig. 6-5 (Re = 15) a particle path trajectory has been drawn over the entrainment diagram. For this case, the stable focus is well established and we see the characteristic mushroom shape of the round jet. The critical point on the axis is a saddle point as seen in Fig. B-41 for the case of Re = 10. In Fig. 6-5 the center of the stream function contour is at about (x, y) = (2.3, 2.25) while the off-axis critical point is at (3.06, 1.48). This further emphasizes the dissimilarity between the entrainment diagram and stream function contour plot. It is important to note that on the vorticity contour plot there is no local concentration of vorticity at the critical point location (3.06, 1.48). In fact, this region in the vorticity field is smooth and decreasing monotonically with increasing radius with no indication that a stable focus has formed. We can observe in both Figs. 6-5 and 6-6 that the vorticity and stream function contours are shifting more to the right as Reynolds number increases. The effect of increased Reynolds number on the particle paths as seen in Fig. 6-6 is that the "stem" of the mushroom shape is lengthening and the intensity of the stable focus is increasing. In Fig. 6-7 the off-axis critical point angle θ_c vs Reynolds number can be observed. In the State 2 region of $Re_1 < Re < Re_2$

the flow is very dynamic with a rapidly increasing critical point angle with slowly increasing Reynolds number. The maximum θ_c of 34.50 for Re = 8.5 is reached shortly after the second transition into State 3. After this peak θ_c the critical point angle decreases slowly. Intuitively one would anticipate this angle getting smaller for larger Reynolds number since one might expect the mushroom stem to grow faster than the diameter of the mushroom.

6. Numerical Instability

In Fig. 6-7 we run into numerical difficulties at about Re = 15 where the 30 × 30 mesh and 60 × 60 mesh start to yield different results. This is further shown in Fig. 6-8 where q is plotted vs Reynolds number. Figure 6-8 represents one of the biggest surprises in the study. For q to have this linear behavior is totally unexpected. Low Reynolds number theory predicts an Re^4 dependence for q. We see in Fig. 6-8 that Re = 15 is a point of divergence between the two meshes.

If App. B is examined for the 30 × 30 mesh cases, one can see the manifestation of numerical error in the formation of vorticity clumping, oscillations in the stream function and dimpling at the saddle point in the entrainment diagram. These phenomena are completely numerical in origin. This can be seen in Fig. 6-9 where two vorticity and stream function contours are compared with the only difference being the mesh resolution. The vorticity clumps for the n = 30 case are centered around every other node point in the radial direction.

$$\frac{y}{\sqrt{\nu t}}$$

$$x/\sqrt{\nu t}$$
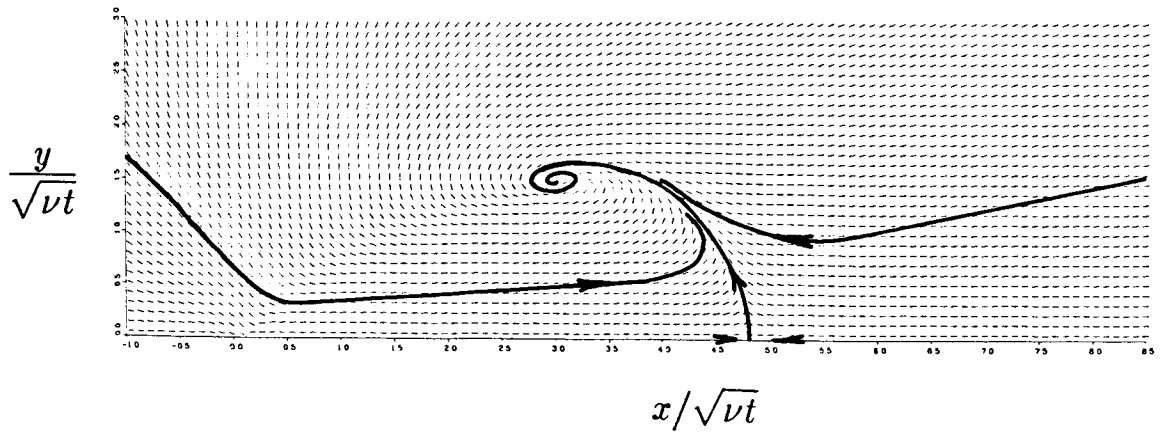
Fig. 6-5.   Computed Solution for the Round Jet at Re = 15.

$$\frac{y}{\sqrt{\nu t}}$$

$$x/\sqrt{\nu t}$$
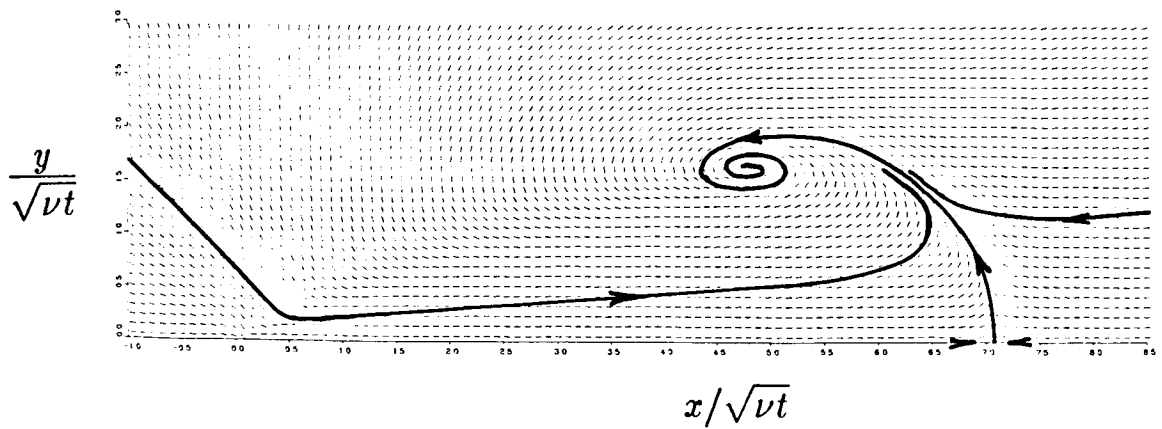
Fig. 6-6.   Computed Solution for the Round Jet at Re = 25.
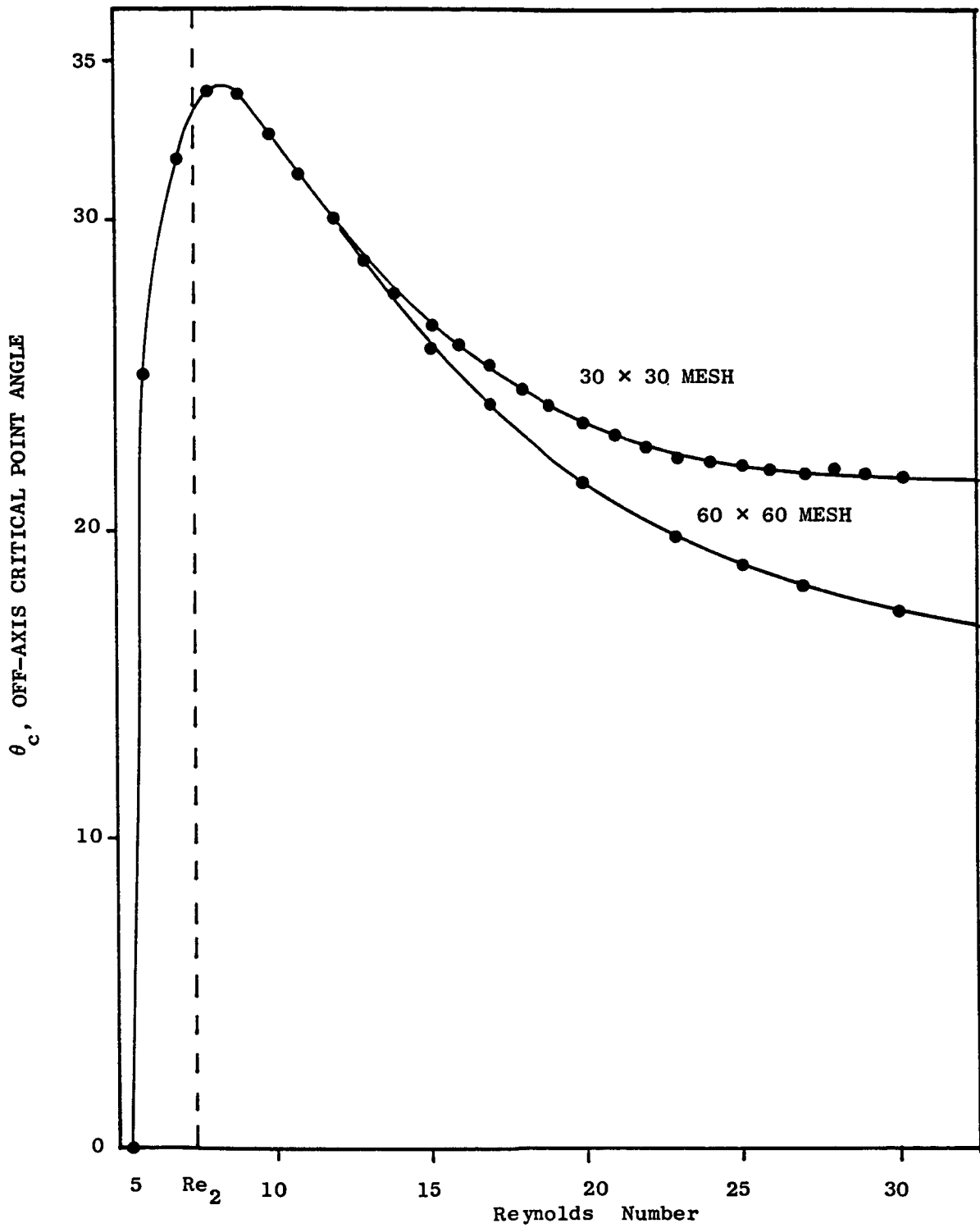
Fig. 6-7. Off Axis Critical Point Angle vs Reynolds Number.
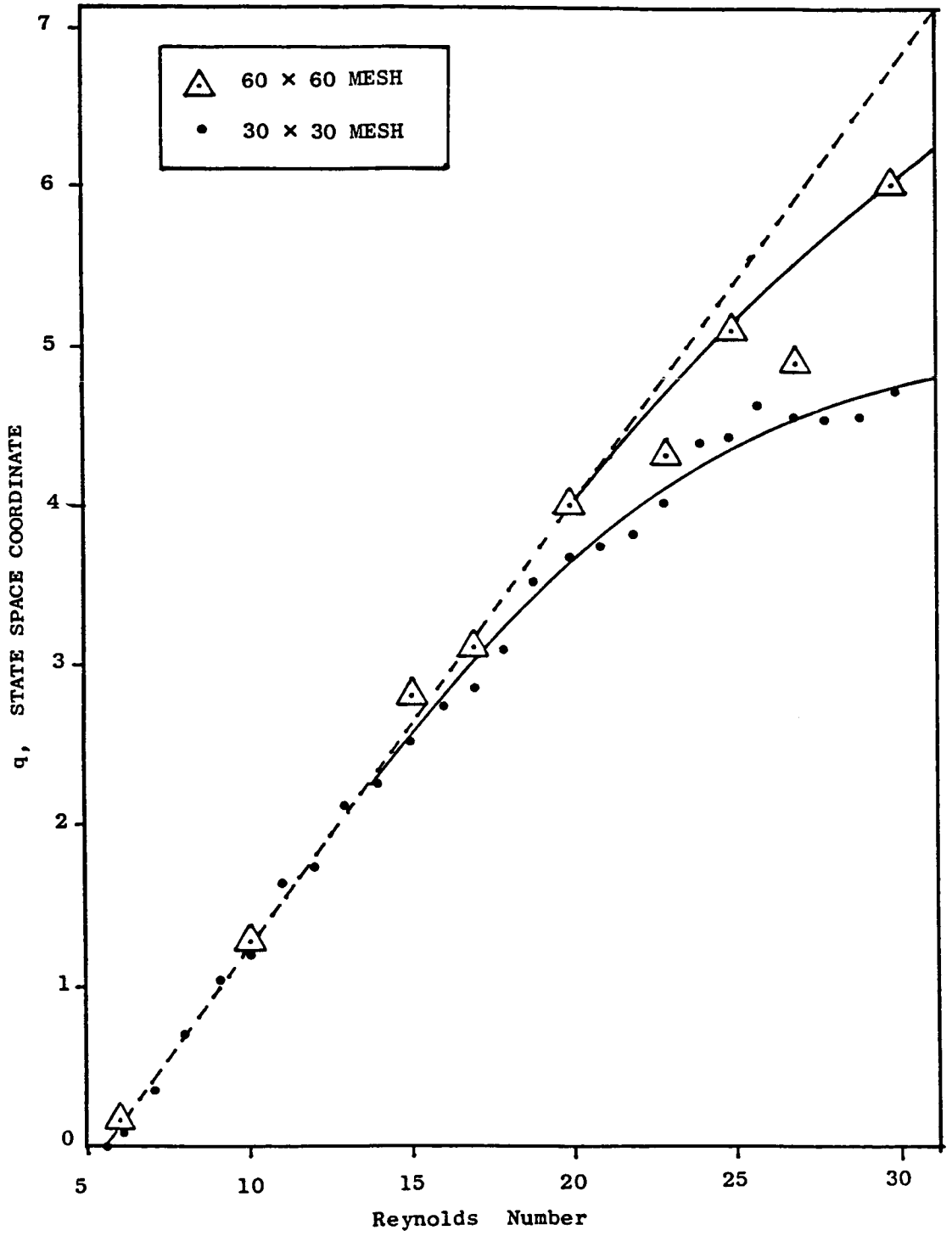
Fig. 6-8.   q vs Reynolds Number.

This clumping completely disappears in the $n = 60$ case. For the stream function we can see how the contours shift to the right and become free of oscillation for the finer mesh. The effect of numerics is even more pronounced in Fig. 6-10. Here we compare the dipole coefficient D_1 (which is the first coefficient in the multipole far field boundary) for $n = 30$, 60 and the exact result, versus Reynolds number. Since we have an exact result in (5.37), we know at what Reynolds number the solution is starting to degrade. It can be seen that the curves are starting to separate at $Re = 12$. The $n = 30$ curve changes shape altogether between $Re = 21$ and 22. Examination of Fig. B-21 which has the contour plots of vorticity and vorticity times ξ^3 (which is the kernel function used in solving D_1) shows that clumping is just beginning at $Re = 21$. The "dog leg" of $n = 30$ in Fig. 6-10 is never observed for $n = 60$, nor has vorticity clumping or the other overt symptoms been observed. However it is probable that if we had carried the $n = 60$ calculations much beyond $Re = 30$ these features would have been observed. A question that immediately arises is how accurately does an error between the computational and exact value of D_1 compare with error in the vorticity distribution. This point is emphasized by the plots of vorticity (W) and vorticity times ξ^3, $(W*\xi^3)$ shown in App. B. From the App. B plots we see that $W*\xi^3$ starts to clump before W, which would lead one to believe that D_1 may be an overly sensitive measure of accuracy since $W\xi^3$ is the

STREAM FUNCTION CONTOUR PLOT FOR Re=30.0
30 X 30 MESH FOR ξ_-=15.0

VORTICITY CONTOUR PLOT FOR Re=30.0
30 X 30 MESH FOR ξ_-=15.0

$\dfrac{y}{\sqrt{\nu t}}$

(a)

STREAM FUNCTION CONTOUR PLOT FOR Re=30.0
60 X 60 MESH FOR ξ_-=15.0

VORTICITY CONTOUR PLOT FOR Re=30.0
60 X 60 MESH FOR ξ_-=15.0

$\dfrac{y}{\sqrt{\nu t}}$

(b)

$x/\sqrt{\nu t}$

$x/\sqrt{\nu t}$
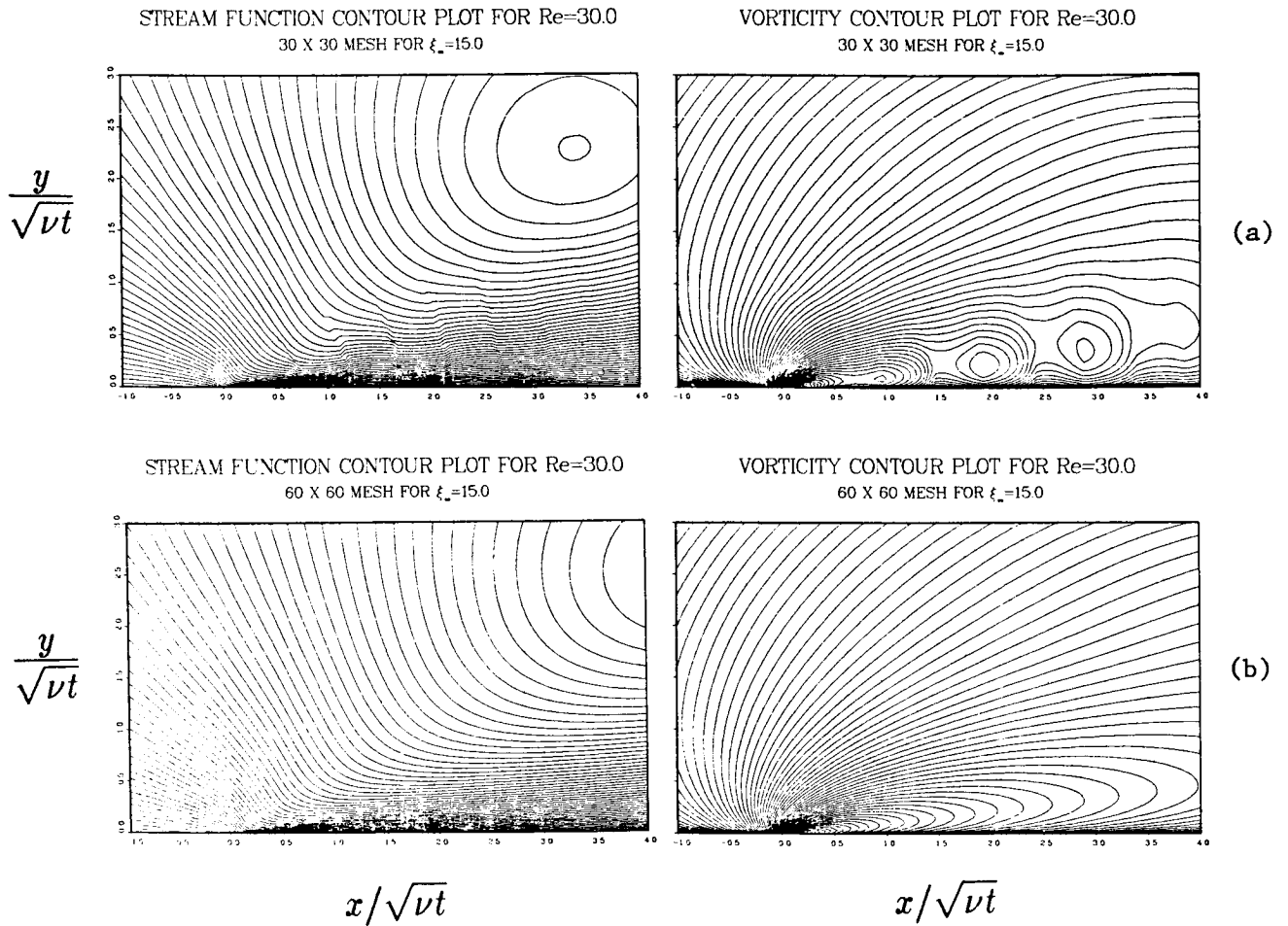
Fig. 6–9: **Computed Solutions for the round jet at Re = 30 showing: a) vorticity clumping due to numerical instability on a 30 × 30 mesh; b) smooth solution on a 60 × 60 mesh.**
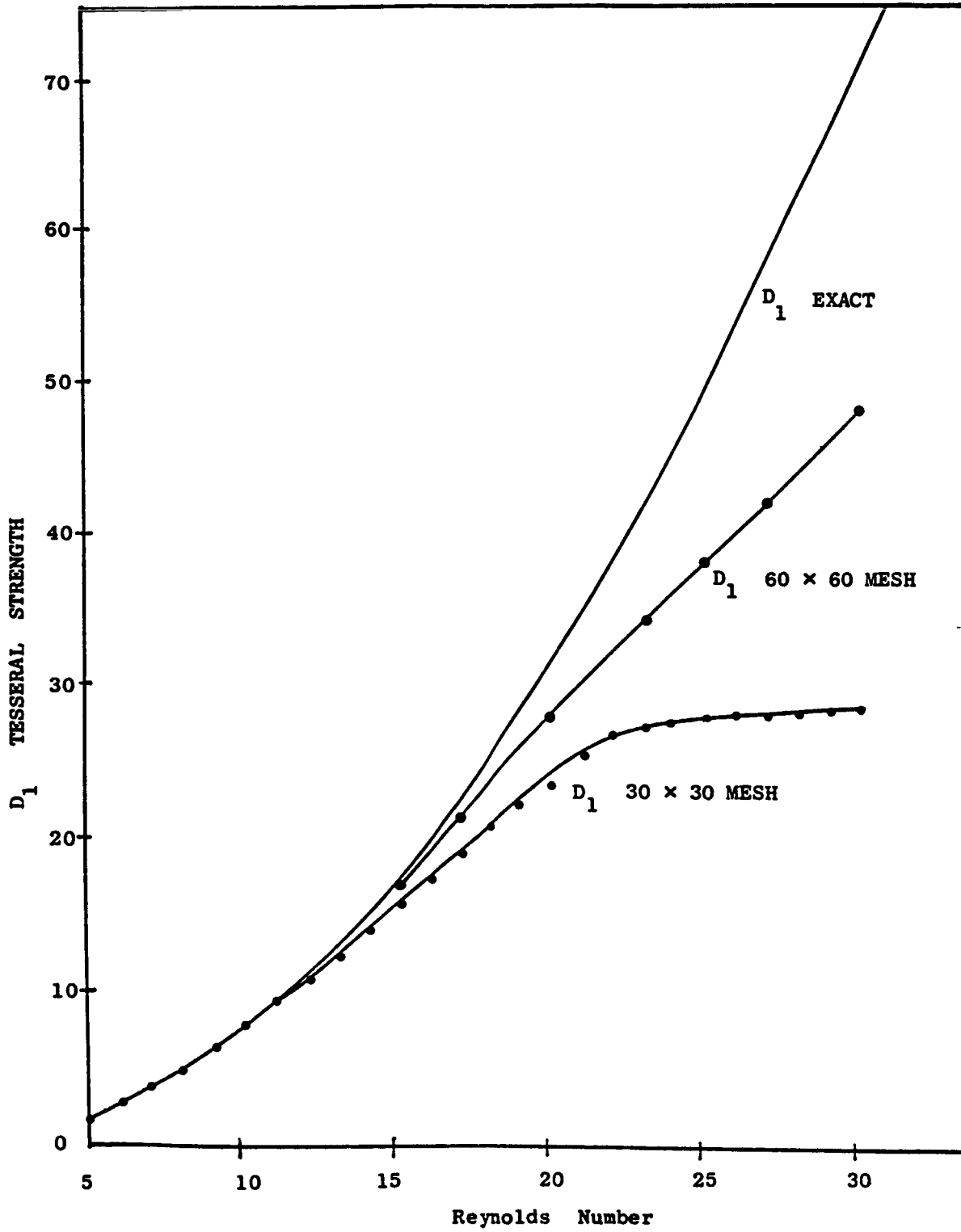
Fig. 6-10. D_1 Tesseral Compared vs Reynolds Number.

kernel in the D_1 calculation. We can determine this degree of sensitivity from (5.37) for the dipole term which is

$$D_1 = \frac{\mathrm{Re}^2}{4} \int_0^{\xi_\infty} \int_0^\pi W(\xi', \theta') \xi'^3 \sin^2\theta' \, d\theta' \, d\xi' \qquad (6.9)$$

We will assume that a vorticity error ΔW will produce a dipole error of ΔD_1. We can write down vorticity as

$$\overline{W}(\xi, \theta) = W(\xi, \theta) + \Delta W \qquad (6.10)$$

where $\overline{W}(\xi, \theta)$ is the computed vorticity and $W(\xi, \theta)$ is the actual. We may expand both $W(\xi, \theta)$ and ΔW into their multipole constituents. However, by orthogonality we know that only the dipole components will contribute to (6.9). We can therefore write down vorticity as

$$\overline{W}(\xi, \theta) = \sin\theta \left[R_1(\xi) + \Delta R_1 \right] + \cdots \qquad (6.11)$$

where R_1 is the true vorticity radial dipole component and ΔR_1 the radial dipole error component with higher-order terms dropped. Equation (6.11) is inserted into (6.9) and the angular integration is performed giving

$$D_1 + \Delta D_1 = \frac{\mathrm{Re}^2}{3} \int_0^{\xi_\infty} \left[R_1(\xi') + \Delta R_1 \right] \xi'^3 \, d\xi' \qquad (6.12)$$

If we assume that ΔR_1 is a relative error such that $\Delta R_1 / R_1$ is a constant and not a function of ξ,

$$D_1 + \Delta D_1 \;=\; \frac{\text{Re}^2}{3} \left[1 + \frac{\Delta R_1}{R_1} \right] \int\limits_0^{\xi_\infty} R_1(\xi\,')\xi\,'^{\,3}\, d\xi\,' \tag{6.13}$$

Since

$$D_1 \;=\; \frac{\text{Re}^2}{3} \int\limits_0^{\xi_\infty} R_1(\xi\,')\xi\,'^{\,3}\, d\xi\,' \tag{6.14}$$

we conclude that

$$\frac{\Delta D_1}{D_1} \;=\; \frac{\Delta R_1}{R_1} \;. \tag{6.15}$$

However, if we assume that ΔR_1 is an absolute error which is a a constant and not a function of ξ then by combining (6.12) with (6.14) and integrating with ΔR_1 outside the integral and dividing by (5.37) we find that

$$\frac{\Delta D_1}{D_1} \;=\; \frac{\Delta R \xi_\infty^{\,4}\pi}{3} \;. \tag{6.16}$$

Note that the observed numeric error in vorticity appears to be somewhere between the two cases of absolute and relative error. The method used in MAVIN calculates a nonlinear scale function and then multiplies that result by the analytic representation of the radial component of the creeping flow. Since this analytic representation is dominated by a Gaussian function, we know that the ultimate vorticity function's error diminishes with distance and is ultimately very small.

There is round-off error and truncation error in MAVIN and in the quadrature used to calculate D_1. However since the CDC 7600 uses a 60 bit word and

double precision was used in many of MAVIN's computations we know that round-off error is insignificant. The chief culprit for error in this computation is truncation error. What we can conclude is that (6.15) represents a best quality factor expected in the vorticity field. Specifically if

$$1 - \frac{\Delta D_1}{D_1} = 0.80$$

then we must assume that the overall quality of the vorticity is 0.80 or worse. The main advantage of this quality parameter is that it tells us when to no longer trust a calculated result from MAVIN. We can employ this in examining the parameter

$$\frac{Numeric \; D_1}{Analytic \; D_1}$$

in Tables 6.4 and 6.5. Our own rule of thumb is that quality of less than 0.80 is not acceptable. Based on this the 30 × 30 mesh results are acceptable up to Re = 18 but not beyond. The 60 × 60 mesh results are acceptable up to around Re = 23. There is, however, a paradox arising from this analysis. For the mesh of 30 × 30 in the Re = 21 case we observe some vorticity clumping occurring in the $W * \xi^3$ plot of Fig. B-21. The quality factor for B-21 is 0.73. However, in Fig. B-40 for the 60 × 60 case of Re = 30 we observe no clumping or any undesirable numeric effects, even though the quality is an abysmal 0.67. A possible solution to this paradox can be offered through a line of speculation. The multipole coefficients or tesserals of Table 6-4 are plotted in Fig. 6-11. We observe with some surprise that all the coefficients come to almost a single point near Re = 8.

Table 6-4

MULTIPOLE COEFFICIENTS FOR A 30 × 30 MESH AT $\xi_\infty = 15$

Re	$\dfrac{\text{Numeric } D_1}{\text{Analytic } D_1}$	Numeric Results					
		D_1	D_2	D_3	D_4	D_5	D_6
0.1	1.00	0.796E-3	0.135E-6	-0.208E-6	0.797E-7	-0.788E-6	0.152E-5
1	1.00	0.796E-1	0.130E-2	0.244E-5	0.543E-5	-0.776E-4	0.137E-3
2	1.00	0.318E0	0.208E-1	0.140E-2	0.948E-4	-0.297E-3	0.379E-3
3	1.00	0.716E0	0.105E0	0.165E-1	0.262E-2	-0.255E-3	0.295E-3
4	1.00	0.127E1	0.327E0	0.912E-1	0.263E-1	0.651E-2	0.119E-2
5	1.00	0.199E1	0.785E0	0.336E0	0.150E0	0.669E-1	0.274E-1
6	1.00	0.286E1	0.158E1	0.949E0	0.598E0	0.385E0	0.245E0
7	1.00	0.388E1	0.280E1	0.220E1	0.182E1	0.154E1	0.132E1
8	0.99	0.502E1	0.451E1	0.442E1	0.456E1	0.484E1	0.524E1
9	0.97	0.627E1	0.676E1	0.798E1	0.990E1	0.127E2	0.166E2
10	0.96	0.762E1	0.958E1	0.132E2	0.192E2	0.288E2	0.443E2
11	0.97	0.939E1	0.138E2	0.225E2	0.385E2	0.682E2	0.123E3
12	0.96	0.110E2	0.182E2	0.334E2	0.644E2	0.129E3	0.263E3
13	0.94	0.127E2	0.232E2	0.470E2	0.101E3	0.223E3	0.505E3
14	0.91	0.143E2	0.286E2	0.633E2	0.148E3	0.358E3	0.888E3
15	0.89	0.160E2	0.343E2	0.818E2	0.206E3	0.539E3	0.144E4

Table 6-4 (Cont.)

Re	$\dfrac{Numeric\ D_1}{Analytic\ D_1}$	Numeric Results					
		D_1	D_2	D_3	D_4	D_5	D_6
16	0.86	0.176E2	0.404E2	0.103E2	0.277E3	0.773E3	0.221E4
17	0.83	0.192E2	0.467E2	0.126E3	0.359E3	0.106E4	0.322E4
18	0.80	0.207E2	0.529E2	0.150E3	0.450E3	0.140E4	0.446E4
19	0.77	0.221E2	0.591E2	0.175E3	0.546E3	0.177E4	0.591E4
20	0.74	0.236E2	0.656E2	0.202E3	0.65763	0.222E4	0.771E4
21	0.73	0.256E2	0.747E2	0.241E3	0.827E3	0.294E4	0.107E5
22	0.70	0.269E2	0.808E2	0.270E3	0.949E3	0.347E4	0.131E5
23	0.65	0.274E2	0.835E2	0.282E3	0.101E4	0.373E4	0.142E5
24	0.61	0.278E2	0.853E2	0.291E3	0.105E4	0.392E4	0.151E5
25	0.56	0.280E2	0.867E2	0.298E3	0.108E4	0.408E4	0.158E5
26	0.52	0.282E2	0.879E2	0.304E3	0.111E4	0.422E4	0.165E5
27	0.49	0.283E2	0.890E2	0.310E3	0.114E4	0.436E4	0.171E5
28	0.46	0.285E2	0.900E2	0.315E3	0.117E4	0.450E4	0.178E5
29	0.43	0.286E2	0.911E2	0.321E3	0.120E4	0.465E4	0.185E5
30	0.40	0.288E2	0.926E2	0.329E3	0.124E4	0.485E4	0.195E5

Table 6-5

MULTIPOLE COEFFICIENTS FOR A 60 × 60 MESH AT $\xi_\infty = 15$

Re	$\dfrac{Numeric\ D_1}{Analytic\ D_1}$	Numeric Results					
		D_1	D_2	D_3	D_4	D_5	D_6
4	1.0	0.127E1	0.328E0	0.914E-1	0.265E-1	0.776E-2	0.196E-2
6	1.0	0.286E1	0.159E1	0.956E0	0.604E0	0.392E0	0.258E0
10	0.99	0.785E1	0.101E2	0.142E2	0.210E2	0.321E2	0.502E2
15	0.96	0.172E2	0.390E2	0.977E2	0.259E3	0.711E3	0.200E4
17	0.93	0.215E2	0.563E2	0.164E3	0.504E3	0.161E4	0.526E4
20	0.88	0.280E2	0.867E2	0.298E3	0.109E4	0.412E4	0.160E5
23	0.82	0.343E2	0.120E3	0.468E3	0.193E4	0.827E4	0.363E5
25	0.77	0.384E2	0.144E3	0.598E3	0.264E4	0.121E5	0.565E5
27	0.73	0.422E2	0.167E3	0.735E3	0.342E4	0.165E5	0.820E5
30	0.67	0.478E2	0.203E3	0.955E3	0.476E4	0.246E5	0.131E6
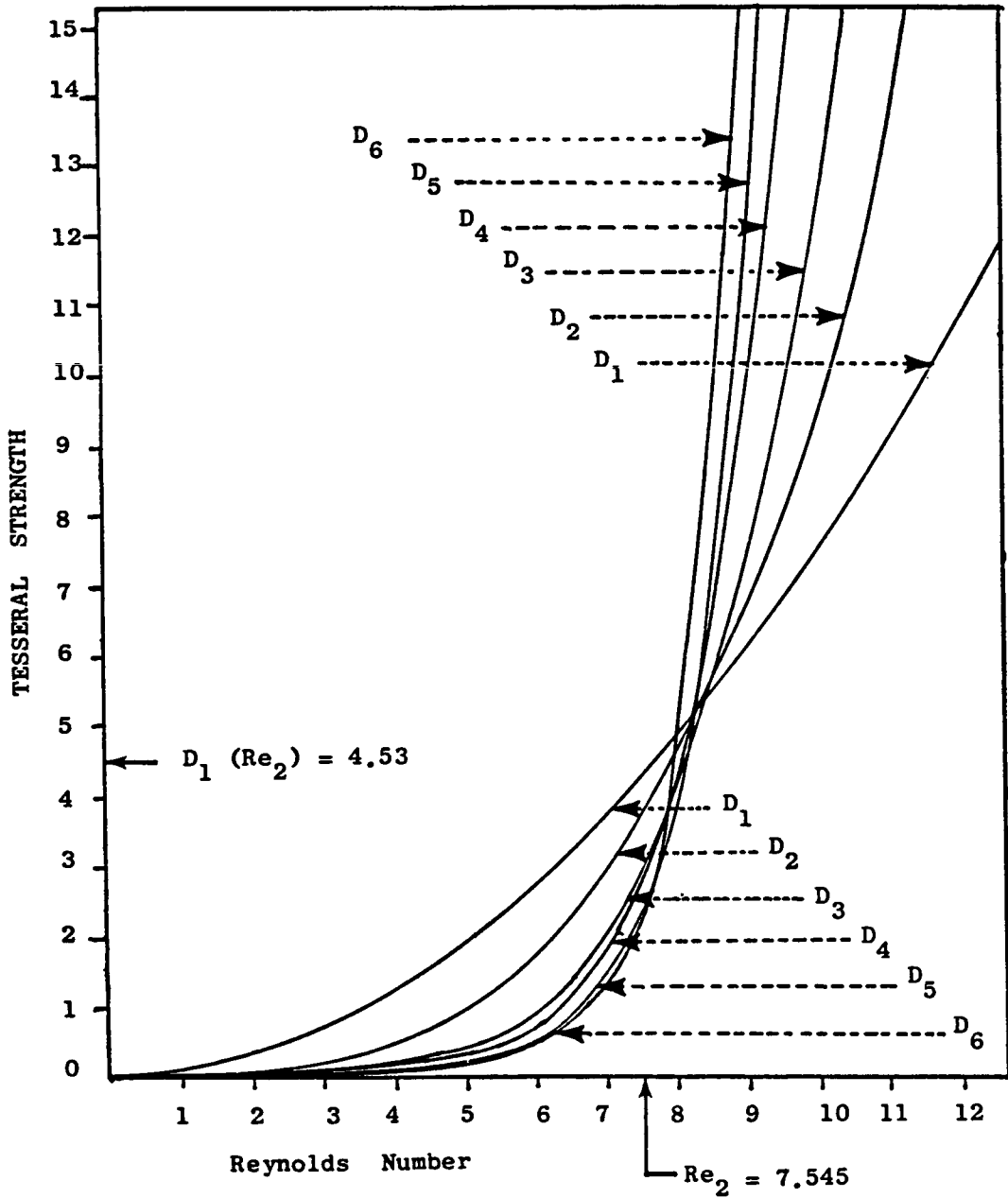
Fig. 6-11. Tesseral Strength vs Reynolds Number

Since all of these coefficients are sensitive to numerical error (compare D_3 in Tables 6-4 and 6-5), Fig. 6-11 is useful only in a qualitative sense. Our first point of speculation is that the Reynolds number for which the D_j coefficients become equal is Re_2, the second transition Reynolds number. This seems intuitively reasonable since the flow at Re_2 consists of an off axis star point which suggests a relatively simple flow topology. Since all D_j coefficients must be equal to zero at $\text{Re} = 0$ we bring about our second line of speculation based on Fig. 6-11 that the D_j coefficients have the following analytic form

$$D_j = \left(\frac{\text{Re}_2^2}{4\pi} \right) \left[\frac{\text{Re}}{\text{Re}_2} \right]^{2j} . \tag{6.17}$$

If (6.17) is inserted into the multipole stream function of (5.35) and the Cauchy ratio test is performed for $\theta = \pi/2$ one finds that convergence occurs only if

$$|\xi| > \left| \frac{\text{Re}}{\text{Re}_2} \right|^2 . \tag{6.18}$$

With ξ_∞ defined as the lower limit of the multipole expansion we find that for $\xi_\infty = 15$ the Reynolds number must be less than or equal to 29.22 for convergence of the infinite multipole series. Clearly for a six term finite series approximation of the multipole infinite series, the Reynolds number would have to be much less than 29 for there to be good accuracy. What is suggested by this line of speculation is that the low quality of $\text{Re} = 30$ for 60×60 is not so much a reflection on the numerics but rather on the accuracy of the truncated multipole expansion when applied at $\xi_\infty = 15$ for this Reynolds number.

7. The Computer Animation Of Axisymmetric Jets

Perhaps the most interesting aspect in the data analysis of this study was the creation of an eleven minute computer animation. This movie was comprised of six parts: the first four parts are Navier Stokes solutions based on a 60×60 mesh of the round jet at Re $= 4$, 6, 20 and 30 (States 1, 2, and 3). The last two parts are Stokes solutions of the vortex ring and ramp jet. Animation of the Stokes solutions was straightforward since their particle path equations are analytic. Equations (4.3) and (4.4) were marched in time using a fourth order Runge-Kutta integrator to produce a time line for the vortex ring. The software, which is shown in App. C started the time lines as straight lines in physical coordinates. In Fig. 6-12 the momentum source is shown as a plus and the critical points are asterisks. The p, q plot is in the upper right-hand corner with the flow state and Reynolds number shown below. The initially straight time lines are drawn instantaneously at Re $= 100$ since the equations are singular at $t =$ 0 where Re is infinite. As seen in Fig. 6-12 the time line immediately starts rolling up around the stable focus forming the expected mushroom shape. In Fig. 6-13a, the Reynolds number decreases to below Re_2 and the flow goes into State 2 where the rolling stops. The off-axis critical point then merges into the on-axis saddle and the flow topology changes to State 1. Figure 6-13b shows the entire past flow history from State 3 to the State 1 flow depicted which is effectively a dead flow. The p, q plot evolves as the time lines and critical points go through their motions, all of which are based on the equations of Chapter 4. The ramp jet involves the integration of (4.7) and (4.8). Unlike the

vortex ring, States 1 and 2 are not masked by the flow history as seen in Figs. 6-14 through 6-16. Like the vortex ring the flow starts as two straight time lines in physical space. However, for the ramp jet the initial Reynolds number is small. As the Reynolds number increases the flow bifurcates from State 1 to 2 and then to 3 with the corresponding transformation of the off-axis node to a stable focus. Figures B-42 through B-47 show the time line evolution for the three Stokes solutions of the vortex ring, round jet, and ramp jet. These plots (in physical space) were the prototypes for the movie software and show some details in the fluid strain that are less apparent in the movie. The source is at coordinate (0, 0) and is blowing to the right. The critical points are not shown in Figs. B-42 through B-47. The crosses shown in Fig. B-42 are individual points being marched by the Runge-Kutta routine. At $Re = 69.9$ the crosses are so closely packed that they appear as a single line. At $Re = 13.19$ the individual crosses can be seen in the front of the mushroom (the front being the right-most part near the axis of symmetry), which is an area of very high strain. The coat-tails of the flow are still very dense but are (or were) being sucked into the volute revolving around the stable focus. It should be emphasized that a vortex ring stops rolling up after transition from State 3 to 2 and becomes a dead flow as Re vanishes. However, even though the flow is dead the mushroom remains as a consequence of the flow's history. Figure B-43 is the same flow as B-42 but the time line is further away from the source. The consequence of this is that the time line never forms a mushroom because transition occurred before this line could form a volute. Figure B-44 shows a Stokes round jet for $Re = 2.0$ which
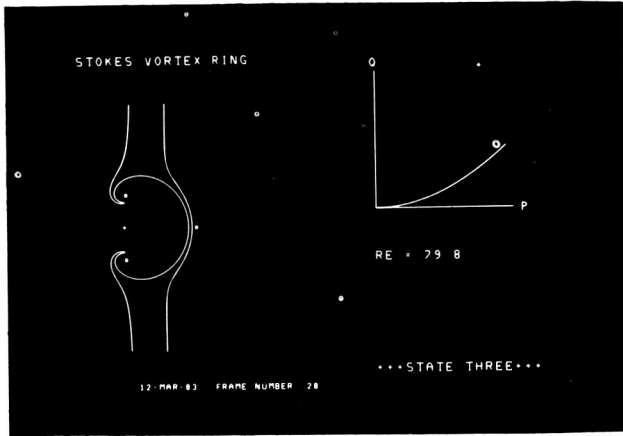
Fig. 6-12.   **Stokes Vortex Ring. State 1**
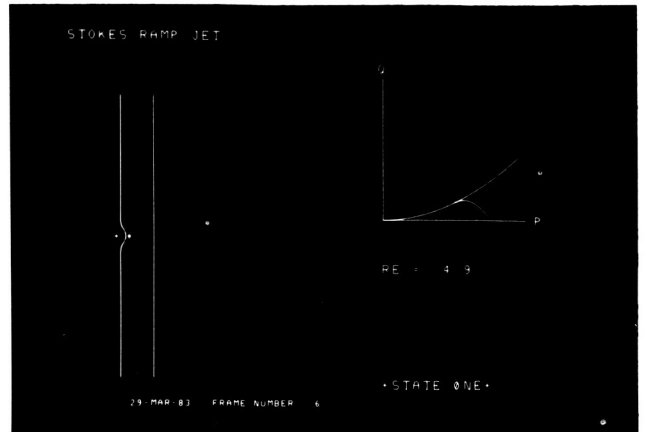
Fig. 6-14   **Stokes Ramp Jet. State 1**
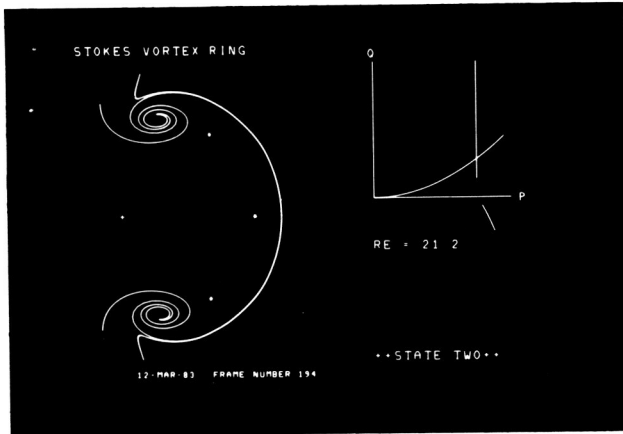
Fig. 6-13a   **Stokes Vortex Ring. State 2**
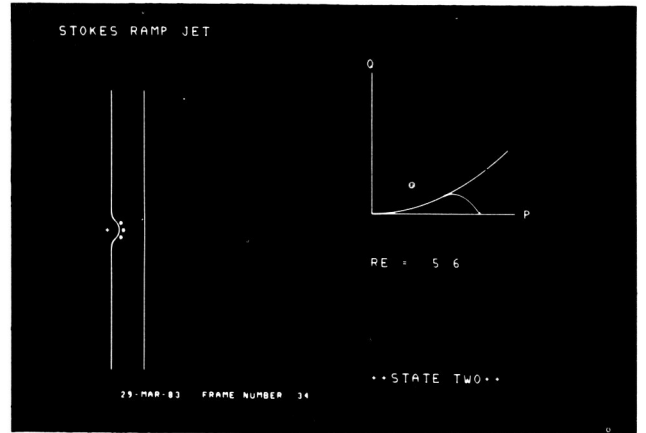
Fig. 6-15   **Stokes Ramp Jet. State 2**
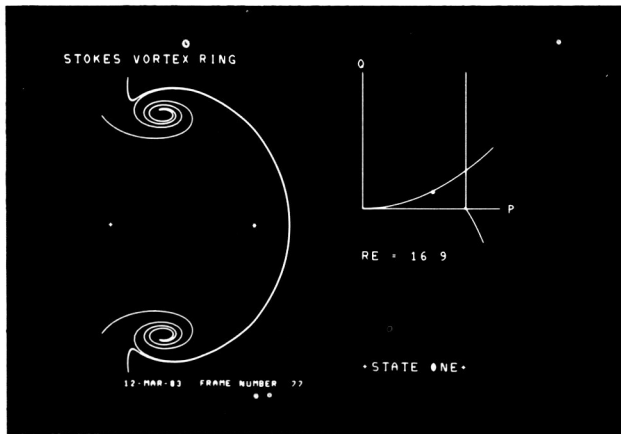
Fig. 6-13b   **Stokes Vortex Ring. State 3**
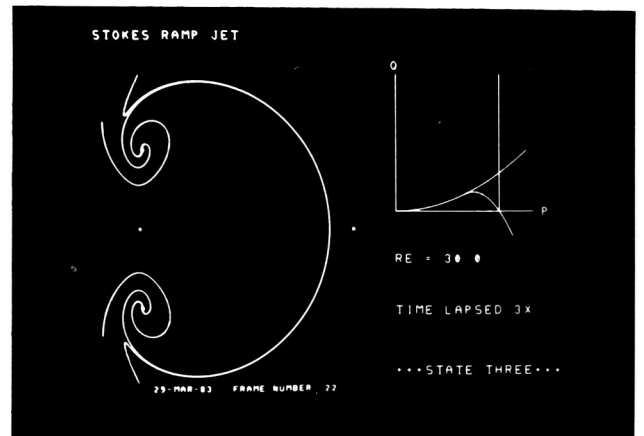
Fig. 6-16   **Stokes Ramp Jet. State 3**

is in State 1. We see the characteristic smooth parabolic shape that the State 1 flow has for all time. Figure B-45 is a Stokes round jet for Re = 8 which is in State 2. A characteristic corner is forming in the time line. State 2 flows never roll up to form a mushroom shape. Notice that the front has a high degree of strain unlike the coattails. Figure B-46 shows a Stokes round jet for Re = 20 which corresponds to State 3. This flow is rolling up and is forming the characteristic mushroom shape. The three round jet solutions are displayed in dimensional units because the round jet has *no* length scale. The fluid simulated in the round jet is olive oil. Figure B-47 displays the Stokes ramp jet. The ramp jet, like the vortex ring, goes through all three states but its flow history does not mask its present state. Unfortunately (as shown in the movie), the ramp jet goes through States 1 and 2 so quickly that their features are almost unobservable ($Re_1 = 3.7$, $Re_2 = 5.8$ for the ramp jet). The features of State 2 are distinctive only in the round jet where the Reynolds number is not a function of time.

All of these Stokes flows have an unrealistic aspect in that their volutes do not translate downstream but loiter around the momentum source. This is a consequence of the elimination of the convective term in the creeping approximation. When one sees the Stokes flow movie this aspect of no translation gives the flow an unnatural appearance. However, as mentioned before, four Navier Stokes flows for the round jet based on a 60 × 60 mesh were also animated. Animating these flows was much more difficult because discrete numeric data had to be integrated rather than analytic functions and the flows were convecting making a correct viewing frame more challenging. The particle path equations (4.1) and

(4.2) were used with a stream function spline based on (6.1). This particle path representation was valid only out to ξ_∞. Beyond ξ_∞ the multipole solution was used via (4.1) and (4.2). The equations were integrated using the same Runge-Kutta method as used in the Stokes solutions. The Navier Stokes simulation uses fluid parameters consistent with olive oil (glycerine was represented in the Stokes flow). Only the upper half of the plane is calculated and then reflected over the axis of symmetry for the lower half in the graphics. The inner time line (closest to the momentum source) is made up of 700 points with 600 points bunched in the 1/20 part of the time line closest to the axis of symmetry. The outer time line is made up of 300 points with 200 points bunched in the 1/8 part of the time line closest to the axis of symmetry. This large amount of point concentration near the axis of symmetry is required by the high rate of strain that occurs in the front of the round jet. The movie framing rate is at 24 frames per second. One can see that the amount of data generated is enormous. An 11 minute movie has 15,840 frames with each frame having 1,000 points and each point described by two single precision words. This equates to 31.7 megabytes just for raw data storage. This data in turn, has to be converted to a graphics format that increases storage requirements by an even larger amount (over an order of magnitude). The storage requirement exceeded available computer storage necessitating that the movie be made in roughly two minute segments and spliced together. The actual filming was done by first generating the graphics on disk and then transferring to magnetic tape. The magnetic tape was read by a Dicomed machine which built up each image on a high resolution black and white CRT. The visual image on the CRT was passed through a color wheel

into an animator's movie camera. Each frame of film was triple exposed with different images passing through different filters of the color wheel. The colors used were red for the critical points, white for the source, and yellow and green for the time lines. Figures 6-17 through 6-20 show frames from the Navier Stokes movies.

States 1 and 2 are similar in appearance to their Stokes counterparts. Figure 6-17 shows the smooth parabolic shape of State 1 for $Re = 4$ with the time lines not touching each other. Figure 6-18 represents a State 2 flow for $Re = 6$. Near the axis the time lines have merged with each other and changed color where they overlay. The saddle and off-axis nodes are on the time lines. Notice that the State 2 kink is not at the off-axis node. As time progresses the kink gets closer to the off-axis node and presumably with infinite time they are super-imposed. Being in State 2 (like State 1) this flow will never roll up and form a mushroom shape. Because the Reynolds number regime in which State 2 occurs is so narrow (between $Re = 5.5$ and 7.5) an experimentalist would have to be specifically looking for State 2 in a very carefully controlled experiment. The discovery of State 2 and the creation of the State 2 animation was one of the major dividends of this study. Two State 3 flows are shown in Figs. 6-19 and 6-20. Figure 6-20 is by far the most dramatic flow simulated. This $Re = 30$ flow looks incredibly natural and has been mistaken by some of the movie's audience as experimental data. In fact, the movie looks better than it should judging from its dipole coefficient quality factor which is a paltry 0.67. Numerically speaking the Fig. 6-19 could serve as a basis for experimental verification unlike the $Re = 30$ which is less accurate. In both flows we notice the long natural

stems of the mushroom shape. As time progresses these stems are sucked up into the volutes which are translating away from the source. The saddle point always has the time lines bunching about the round jet. In round jets the "bunch point" where time lines accumulate the saddle point is one and the same. This is not the case in the nonautonomous flows like the vortex ring and ramp jet where the bunch point is separate though obviously associated with the saddle point on the flow axis. In the $Re = 30$ flow if one looks carefully near the saddle point just before the movie ends, one can see a slight dimple and the early effects of spline kinks due to the high rate of strain. All of the Navier Stokes movies exhibited a remarkable naturalness.

Movie Frames
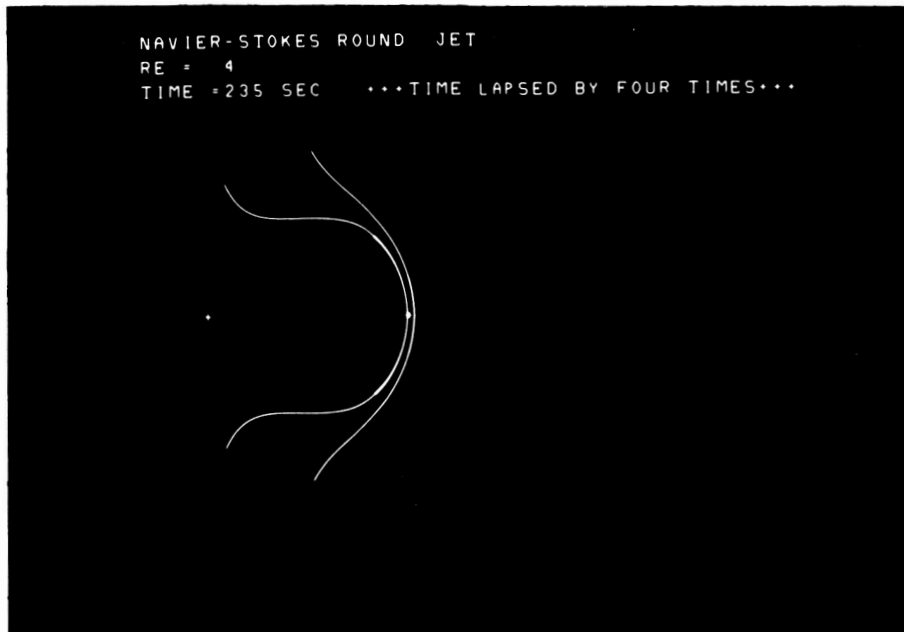
Fig. 6.17. Navier Stokes, Re = 4, State 1.
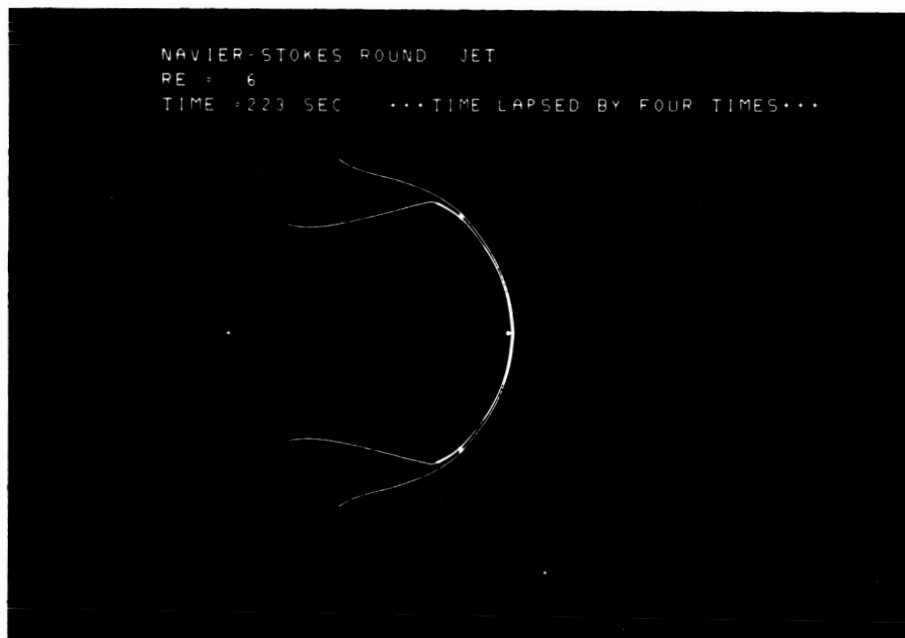
Fig. 6.18. Navier Stokes, Re = 6, State 2.

Movie Frames

NAVIER-STOKES ROUND JET
RE = 20
TIME = 56 SEC
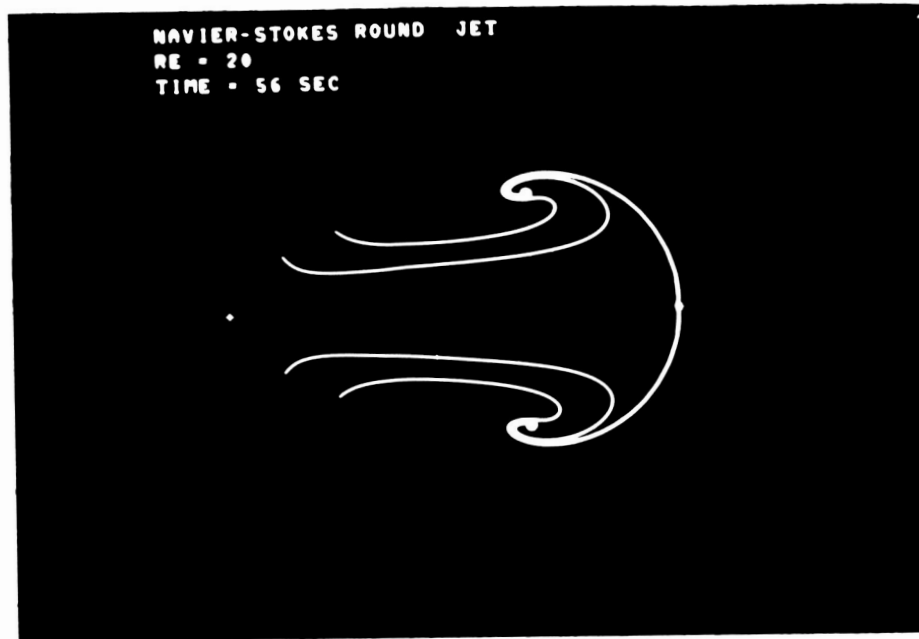
Fig. 6.19. Navier Stokes, Re = 20, State 3.

NAVIER-STOKES ROUND JET
RE = 30
TIME = 65 SEC
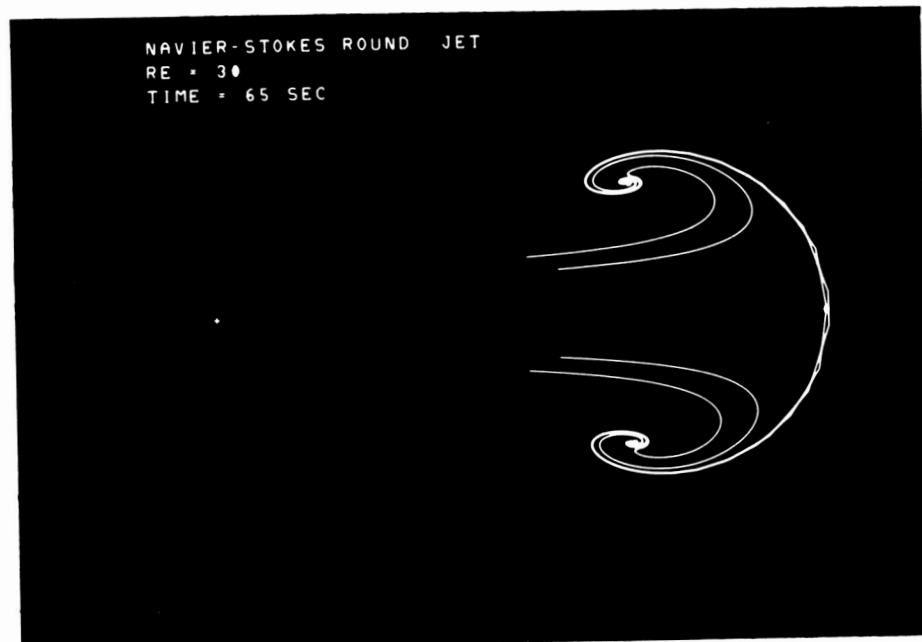
Fig. 6.20. Navier Stokes, Re = 30, State 3.

Chapter VII

CONCLUSIONS

Two basic sets of conclusions can be drawn from this work. One set is drawn from the numerical methods employed. The other set is drawn from the physics of the problem under study.

1. On The Numerical Method

The two-step numerical method involving the solution first of the stream function with vorticity fixed and then of the Poisson equation for the vorticity is widely used and works quite well. However, it is the author's opinion that a one-step approach solving a nonsymmetric matrix would be an improvement. This would remove the need for under relaxation and much of the data handling would be simpler and faster.

The question of whether to solve a large, sparse, linear system by direct means or through relaxation is still very much a controversy in the CFD community. We used the direct method and still believe it is the best method on the 'use-once' experimental programs where computational stiffness is anticipated.

We did, however, have difficulty with the large cpu time requirement of the direct solver and this, more than anything, limited the maximum Reynolds number attained.

The forward-backward solver was very effective as a means of reducing the amount of memory required for direct solution of the matrix with only a modest increase in cpu time. However the forward-backward solver does have difficulty with round-off error amplification in the backsweep.

The nonlinear scale function used in this study did not enhance convergence and in retrospect appears to unnecessarily complicate the problem.

The Japanese fan adaptive grid was useful in enhancing convergence and accuracy. However the stretcher required considerable programmer effort to set up and properly tune. No suitable coordinate stretcher in the ξ direction was found that would match the boundary conditions at both zero and infinity and give useful control over point placement in the interesting regions of the flow. The use of the multipole expansion was found to provide an effective far field boundary condition as long as a Neumann boundary condition was used rather than a Dirichlet.

The multipole solution provided some unexpected dividends. One was the generation of a quality factor for comparison of the computed value against the analytic value of the dipole coefficient. The other dividend was the interesting

relationship of multipole coefficients with respect to each other at various Reynolds numbers.

A line of speculation developed from this multipole relationship led to the belief that a boundary location $\xi_\infty = 15$ is acceptable only for $Re \leq 29.22$. Otherwise the multipole series is divergent causing the boundary condition to be invalid.

The computer animation proved to be a very useful tool in both understanding the flows presented and as a teaching aid. The animation revealed features about the critical points and their relation to the time lines that could not be fully realized using just the entrainment diagrams.

2. Physics Of Axisymmetric Jets

One of the main conclusions regarding the physics of impulsively started jets and vortex rings involves the discovery of three distinct states of motion for the various flows studied. Transition Reynolds numbers are given in Table 7-1. State 1 is for $0 \leq Re \leq Re_1$. Application of this flow to an initially straight time line leads to a smoothly growing, roughly parabolic front. This flow has a single on-axis stable node. State 2 is for $Re_1 \leq Re < Re_2$. Application of this flow to an initially straight time line leads to a curved line

Table 7-1

Transition Reynolds Number

Flow Type	First Transition Re_1	Second Transition Re_2
Stokes Vortex Ring	18.1749	23.4105
Stokes Ramp Jet	3.7386	5.7887
Stokes Round Jet	6.7804	10.0909
Navier Stokes Round Jet	5.5 ± 0.4	7.54 ± 0.16

with a corner located at an angle larger than the angle of the off-axis critical point. This flow has an on-axis saddle point and two off-axis stable nodes. State 3 is for $Re_2 < Re$. Application of this flow to an initially straight time line leads to a geometry that looks like a mushroom or smoke ring with the volutes centered on the off-axis critical point. This flow has an on-axis saddle point and two off axis stable foci.

State space analysis was used to define the structure of the flows under study. It was shown that employing continuity, boundary conditions and self similarity makes it possible to draw the trajectory in p, q space for axisymmetric jets, even in the absence of a solution. From a knowledge of this p, q

trajectory one can predict the different kinds of flow topologies which will occur as the Reynolds number is varied before actually solving the governing equations. The p , q trajectory helped us to recognize that State 2 is a distinct state of motion in axisymmetric jets.

Much of the work revolved around the generalized solution of the Stokes equation (see App. A). Three creeping solutions (Stokes solutions) were solved for and studied in detail. These solutions were examined at higher Reynolds number where the creeping approximation is invalid. In fact, state-space analysis shows that the Stokes solution of the round jet will have the same topological properties as the nonlinear solution even though the approximation is beyond its region of validity. There were, however, many differences between thee linear and nonlinear round jet solutions. The most obvious as seen in Table 7-1 is that the transition Reynolds numbers are different. Also, the spreading angle behavior is completely different. The spreading angle in the Stokes solution goes from 0 to $\pi/2$ as Re becomes infinite. In the nonlinear solution the spreading angle quickly grows with Reynolds number until the second transition. As the Reynolds number is increased beyond Re_2 the spreading angle reaches a maximum of 34.4 degrees and then begins to decrease. For the nonlinear solution the size of the vortex increases slowly while the stem of the mushroom quickly grows in length. In essence because there is no convective term, the vortices of the Stokes solution do not move axially away from the momentum source.

Strain in the fluid flow was both an interesting observation and a source of difficulty in the computer animation. It was found that the highest strain occurred at the on-axis saddle point (see Fig. B-42, Re = 10.7). The strain is observable as separation between each of the computed points (represented as crosses). Strain decreases as the time line rolls up towards the stable focus from the saddle point. The time line is folded at the stable focus and rolled up into a vortex centered about the stable focus forming the mushroom shape. The region of the time line between the stable focus and the saddle point has more strain than the region between the mushrooms and the stable focus. Strain increases as the time line rolls up from the stem into the vortex towards the stable focus.

In the animation of the vortex ring it was found that when the flow changes from State 3 to State 2 the vortex stops rolling up. Therefore it is possible in a mixing process for the rolling up to terminate before the interface can be entrained into the vortex, i.e., it is possible that no mixing occurs at all in a vortex ring's vortex.

One of the most remarkable observations in this study was that there was no local accumulation of vorticity at the stable focus of the round jet. The greatest vorticity in the round jet occurs in a $1/r^2$ singularity at the momentum source. In the neighborhood of the stable focus the vorticity is smooth and decreasing monotonically with radius. This observation is counter to the widely accepted belief that vorticity must be accumulate within a vortex. The Stokes

ramp jet like the round jet has its vorticity peaked at the momentum source with the vorticity smooth through the stable focus. This sort of vorticity behavior will also be the case for the other types of axisymmetric jets for integer $m \geq 1$ (Reynolds number increasing with time). For the Stokes vortex ring $(m = -1)$ the situation is different. In this flow the vorticity peaks at $(\xi, \theta) = (\pm 1, \pi/2)$ for all Reynolds number. However, the closest a stable focus ever gets to this vorticity peak is at $Re \rightarrow \infty$ where the focus is at $(\xi_c, \theta_c) = (\pm 3.0224, \pi/2)$. In the Stokes solution the vorticity peak and critical point never occupy the same location. However, it is an open question whether the Navier-Stokes vortex ring has a coinciding stable focus and vorticity peak. It is quite possible that the inclusion of the convective term may cause the vortex to be a site of vorticity accumulation in the vortex ring at high Reynolds number. Resolution of this question will have to await future study.

Chapter VIII

SUGGESTIONS FOR FUTURE WORK

Of the infinite number of flows under the category of axisymmetric jets, one flow, the round jet (m = 0), was studied both analytically in the creeping approximation and numerically for the full Navier-Stokes solution. Clearly some of the other axisymmetric flows are worthy of numerical investigation.

Recommended flows for further study are the following.

1. The vortex ring (m = -1);

2. The ramp jet (m = 1);

3. Hill's spherical vortex (m = 3/2);

4. The two unnamed flows for m = 1/2 and m = - 1/2.

The spherical vortex should be subjected to a closer analytic investigation since it is the author's opinion that there may exist a whole family of exact axisymmetric jet solutions where the convective term goes to zero in the Navier-Stokes equation.

The family of orthonormal solutions (m negative half integer) shown in

App. A, may also serve as a basis for a spectral investigation of axisymmetric jets.

The nonaxisymmetric round jet is a flow that is very exciting. Like the axisymmetric problem the nonaxisymmetric round jet is autonomous and self similar. Since this flow is not constrained in the third dimension it can theoretically display a vastly more complex set of geometries. This flow would also serve as an ideal basis for utilizing three dimensional state space. Three dimensional state space is a mathematical tool that will have a much more immediate application to real world flows than the axisymmetric methods developed in this work. It will be extremely interesting to see whether the three dimensional state space can be used to deduce a trajectory similar to the one discovered in this work based only on continuity, boundary conditions, and self similarity.

The data generated in this study could be further utilized by assuming that the fluid is divided into different types with a reaction occurring at the interface. The data of this study could drive calculations on the mixing and reaction rates of the different fluids.

There also exists the possibility of analytic solution of the Navier Stokes round jet. The inquiries of App. A, coupled with some of the observations of the numeric study, represent a set of signposts which indicate that a closed-form solution may exist which only awaits the advent of some new mathematical tech-

nique to bring about its discovery.

The problem of computer animation is another area that is very interesting. In this study a two-dimensional representation of 1000 points was animated. In a three-dimensional study the level of complexity would probably go up by several orders of magnitude. Flow visualization actually represents a barrier to the advance of understanding in fluid mechanics. For example, the author can visualize a two-dimensional flow that is translating and deforming but cannot visualize this for a three-dimensional flow. The situation is analogous to a chess master who can visualize an entire chessboard and examine scenarios five or six moves ahead while a novice player can only visualize three or four pieces and see only two moves ahead. For those of us who are not master chess players there will be a need for movies showing three-dimensional fluid flows translating and deforming so that we can perceive the underlying physics. However, the computer and peripheral capability for such computer animations does not yet exist (the storage, I/O requirements, software are not sufficiently advanced). The jet flows described in this work can provide an ideal medium for advancing the technology of flow visualization.

Appendix A

JET FUNCTIONS AND THEIR PROPERTIES

1. Introduction

Fluid is disturbed by a point momentum source whose time behavior is well defined. The flow is constrained to be axisymmetric, and the nonlinear term of the Navier-Stokes equation is removed. The equation of motion is the axisymmetric Stokes equation which, when expressed in spherical coordinates, is

$$\frac{\partial \omega}{\partial t} = \nu \left[\nabla^2 \omega - \frac{\omega}{r^2 \sin^2 \theta} \right] . \tag{A-1}$$

The problem is expressed in spherical polar coordinates (r, θ, ϕ) where

$\theta = 0$ is the axis of symmetry,

$t =$ time

$\nu =$ the kinematic viscosity.

$\omega(r, \theta, t) =$ vorticity in the ϕ direction,

Equation (A-1) may be reduced by the introduction of a new dependent variable and a self similar coordinate:

$$S = \frac{r}{\sqrt{2\nu t}} \tag{A-2}$$

$$\omega = \hat{P} \nu^{-2} t^{m-1} W(S, \theta) \tag{A-3}$$

where

S $=$ similarity variable,

$\hat{P}$ $=$ characteristic strength of the momentum source and is the
parameter which, along with ν governs the scaling
properties of the flow

W $=$ dimensionless vorticity

m $=$ index derived from the dimensions of $\hat{P}$.

The similarity variable S is a modified version of the earlier similarity variable ξ used in the main text of this thesis. The two variables are related as follows:

$$\xi = S\sqrt{2} \tag{A-3a}$$

Equations (A-2) and (A-3) can be combined with (A-1) to give

$$\frac{\partial}{\partial S}\left[S^2\frac{\partial W}{\partial S}\right] + S^3\frac{\partial W}{\partial S} + \frac{1}{\sin\theta}\frac{\partial}{\partial\theta}\left[\sin\theta\frac{\partial W}{\partial\theta}\right] \tag{A-4}$$
$$- \left[\frac{1}{\sin^2\theta} + 2(m-1)S^2\right]W = 0 .$$

Equation (A-4) can be reduced into two ordinary differential equations by separation of variables

$$\frac{d^2J}{dS^2} + \left(S + \frac{2}{S}\right)\frac{dJ}{dS} - 2\left[\frac{l(l+1)}{2S^2} + m - 1\right]J = 0 \tag{A-4a}$$

$$\frac{1}{\sin\theta}\frac{d}{d\theta}\left[\sin\theta\frac{dP}{d\theta}\right] + \left[l(l+1) - \frac{1}{\sin^2\theta}\right]P = 0 \tag{A-4b}$$

where

$$W(S,\theta) = \hat{c}P(\theta)J(S) \qquad \text{(A-4c)}$$

and where l and m are real constants, (A-4b) is the Legendre equation of first order, a tabulated function. The constant $\hat{c}$ is for boundary condition matching at the far field. For the purposes of this paper we will examine only the solution of (A-4b) that corresponds to a dipole flow in the far field, viz., $l = 1$, $P(\theta) = \sin\theta$. we may now reexpress (A-4c) as

$$W(S,\theta) = \hat{c}\sin\theta\, J(S) \ . \qquad \text{(A-5)}$$

It should be emphasized that $J(S)$ is not a Bessel function (in fact Bessel functions never appeared in this study). With $l = 1$, (A-4a) becomes

$$\frac{d^2J}{dS^2} + \left[S + \frac{2}{S}\right]\frac{dJ}{dS} - 2\left[\frac{1}{S^2} + m - 1\right]J = 0 \ . \qquad \text{(A-6)}$$

2. DERIVATION OF THE "EASY" SOLUTIONS

The ordinary differential equation, (A-6) will be the center of study. Solutions of this equation will be called "jet functions". Equation (A-6) by the following substitutions can be cast into two different forms which are polynomials without transcendental function.

Let

$$J_m(S) = \frac{E_m(S)}{S} \qquad \text{(A-7)}$$

giving

$$\frac{d^2E}{dS^2} + S\,\frac{dE}{dS} + \left[1 - 2m - \frac{2}{S^2}\right]\,E \;=\; 0 \ . \tag{A-8}$$

Let

$$J_m(S) \;=\; \frac{e^{\frac{-S^2}{2}}}{S}\,F_m(S) \tag{A-9}$$

giving

$$\frac{d^2F}{dS^2} - S\,\frac{dF}{dS} - 2\left[m + \frac{1}{S^2}\right]\,F \;=\; 0 \ . \tag{A-10}$$

Equations (A-8) and (A-10) can each be solved by means of the Frobenius method. For (A-8) we find

$$E(S) \;=\; \sum_{j=0}^{\infty}\,C_j\,S^{j+n} \tag{A-11}$$

where

$$n \;=\; -1, 2 \quad \text{and} \quad C_1 \;=\; 0, \quad C_0 \;\neq\; 0 \ ; \tag{A-12a}$$

$$C_j \;=\; C_{j-2}\,\frac{-j-n+2m+1}{j^2+2nj-j-2-n+n^2} \ . \tag{A-12b}$$

For this O.D.E. there is one solution with a second order zero at the origin, and a second solution which is a first order pole. The recursive formula, (A-12b), can be used to find closed form solutions by recognizing that the index j must be an even positive integer and that the numerator in (A-12b) goes to zero at some value of j truncating the infinite series for a polynomial solution. The results below point to polynomial solutions:

$n = -1$, first order pole:

$$C_j = C_{j-2} \frac{2(m+1)-j}{j(j-3)} \qquad (A-13)$$

For polynomials: $m = j/2 - 1$, therefore $m = 0, 1, 2, 3, 4, \ldots$

$n = 2$, second order zero:

$$C_j = C_{j-2} \frac{2m-1-j}{j(j+3)} \qquad (A-14)$$

For polynomials: $m = \frac{1}{2} [1 + j]$, therefore $m = \frac{3}{2}, \frac{5}{2}, \frac{7}{2}, \frac{9}{2}, \cdots$

$$j = 2, 4, 6, 8, 10, \ldots$$

we can go through similar reasoning for (A-10) with the solution being

$$F(S) = \sum_{j=0}^{\infty} C_j S^{j+n} \qquad (A-15)$$

where

$$n = -1,2 \quad \text{and} \quad C_1 = 0, \ C_0 \neq 0 , \qquad (A-16a)$$

$$C_j = C_{j-2} \frac{j + n + 2(m-1)}{j^2 + 2nj - j - 2 - n + n^2} . \qquad (A-16b)$$

This result as before has a solution with a second order zero and a first order pole. The polynomial solutions can be recognized in the same manner as before:

$n = -1$, first order pole:

$$C_j = C_{j-2} \frac{2m - 3 + j}{j(j-3)} \qquad \text{(A-17)}$$

For polynomials: $m = (3\text{-}j)/2, \quad m = \frac{1}{2}, -\frac{1}{2}, -\frac{3}{2}, -\frac{5}{2}, \cdots$

$n = 2$, second order zero:

$$C_j = C_{j-2} \frac{2m + j}{j(j+3)} \qquad \text{(A-18)}$$

For polynomials: $m = -j/2, \quad m = -1, -2, -3, -4, \ldots$

$$j = 2, 4, 6, 8, 10, \ldots$$

These polynomial solutions which shall be called "Easy Solutions" are all expressed in closed form as finite series. When the E_m and F_m polynomials are cast back into their original J_m form via (A-7) and (A-9), the first order pole solutions of E_m or F_m polynomials become second order poles, which shall be called "B_m functions" and the second order zeros of E_m or F_m polynomials become first order zeros which shall be called "G_m solutions". These independent functions are thus

$$J_m = C_1 G_m(S) + C_2 B_m(S) \qquad \text{(A-19)}$$

where C_1 and C_2 are constants of integration.

$$B_m(S) = \frac{1}{S} \left[\sum_{j=1}^{m} \frac{2^{j-1}}{j(m-j)!(2j-2)!} S^{2j-1} - \frac{1}{(m!)S} \right] \qquad \text{(A-20)}$$

$$B_0(S) = -\frac{1}{S^2} \qquad \text{(A-21)}$$

$$B_{\frac{1}{2}-m}(S) \;=\; \frac{e^{\frac{-S^2}{2}}}{S} \left[\sum_{j=1}^{m} \frac{(-2)^{j-1}}{j(m-j)!\,(2j-2)!} \, S^{2j-1} + \frac{1}{(m!)S} \right] \tag{A-22}$$

$$B_{\frac{1}{2}}(S) \;=\; \frac{e^{\frac{-S^2}{2}}}{S} \tag{A-23}$$

$$G_{-m}(S) \;=\; -\frac{e^{\frac{-S^2}{2}}}{S} \left[\sum_{j=1}^{m} \frac{(-2)^{j+1}(j^2+j)\,S^{2j}}{(m-j)!\,(2j+2)!} \right] \tag{A-24}$$

$$G_{\frac{1}{2}+m}(S) \;=\; \frac{1}{S} \left[\sum_{j=1}^{m} \frac{2^{j+1}(j^2+j)}{(m-j)!\,(2j+2)!} \, S^{2j} \right] \tag{A-25}$$

where $m = 1, 2, 3, 4, \ldots$.

Rodrigues' formulae and generating functions have been derived for the above equations. For (A-20)

$$B_m(S) \;=\; \frac{(2)^{m-1} e^{\frac{-S^2}{2}}}{(2m-2)!\,mS^2} \, \frac{d^{2m-2}}{dS^{2m-2}} \left[(S^2 - 2m + 1)\, e^{\frac{S^2}{2}} \right] . \tag{A-26}$$

with generating function $\Omega_m^{(B)}$ where

$$\Omega_m^{(B)}(S,\lambda) \;=\; -\frac{e^{\lambda}}{S^2} \left[\cosh(S\sqrt{2\lambda}) - S\sqrt{2\lambda}\sinh(S\sqrt{2\lambda}) \right] \tag{A-27}$$

where

$$\Omega_m^{(B)}(S,\lambda) \;=\; \sum_{j=0}^{\infty} B_j(S)\lambda^j . \tag{A-28}$$

For (A-22)

$$B_{\frac{1}{2}-m}(S) = \frac{(-2)^{m-1}}{(2m-2)!mS^2} \frac{d^{2m-2}}{dS^{2m-2}} \left[(S^2 + 2m-1) e^{\frac{-S^2}{2}} \right] \qquad \text{(A-29)}$$

with generating function $\Omega_{\frac{1}{2}-m}^{(B)}(S, \lambda)$ where

$$\Omega_{\frac{1}{2}-m}^{(B)}(S, \lambda) = \frac{e^{\lambda-\frac{S^2}{2}}}{S^2} \left[\cos(S\sqrt{2\lambda}) - S\sqrt{2\lambda}\sin(S\sqrt{2\lambda}) \right] \qquad \text{(A-30)}$$

where

$$\Omega_{\frac{1}{2}-m}^{(B)}(S, \lambda) = \sum_{j=0}^{\infty} B_{\frac{1}{2}-j}(S)\lambda^j \quad . \qquad \text{(A-31)}$$

For (A-24)

$$G_{-m}(S) = \frac{-(-2)^m m}{(2n+1)!S^2} \frac{d^{2m-1}}{dS^{2m-1}} \left[(S^2 + 2m) e^{\frac{-S^2}{2}} \right] \qquad \text{(A-32)}$$

$$\Omega_{-m}^{(G)}(S, \lambda) = \frac{e^{\lambda-\frac{S^2}{2}}}{2S\lambda} \left[\cos(S\sqrt{2\lambda}) - \frac{1}{S\sqrt{2\lambda}}\sin(S\sqrt{2\lambda}) \right] \qquad \text{(A-33)}$$

where

$$\Omega_{-m}^{(G)}(S, \lambda) = \sum_{j=0}^{\infty} G_{-(j+1)}(S)\lambda^j \quad . \qquad \text{(A-34)}$$

For (A-25):

$$G_{\frac{1}{2}+m}(S) = \frac{(2)^m m \, e^{\frac{-S^2}{2}}}{(2m+1)! \, S^2} \frac{d^{2m-1}}{dS^{2m-1}} \left[(S^2 - 2m) \, e^{\frac{S^2}{2}} \right] \tag{A-35}$$

$$\Omega^{(G)}_{\frac{1}{2}+m}(S,\lambda) = \frac{e^\lambda}{2S\lambda} \left[\cosh(S\sqrt{2\lambda}) - \frac{1}{S\sqrt{2\lambda}} \sinh(S\sqrt{2\lambda}) \right] \tag{A-36}$$

where

$$\Omega^{(G)}_{\frac{1}{2}+m}(S,\lambda) = \sum_{j=0}^{\infty} G_{\frac{3}{2}+j}(S) \lambda^j \ . \tag{A-37}$$

where $m = 1, 2, 3, 4, \dots$.

For the functions described by (A-22) and (A-24) there has been found the following relationships with known special function:

$$G_{-m}(S) = \frac{(-1)^m e^{\frac{-S^2}{2}}}{(2m-1)! \, \sqrt{2} \, S^2} \left[\frac{1}{4m+2} H_{2m+1} \left(\frac{S}{\sqrt{2}} \right) + H_{2m-1} \left(\frac{S}{\sqrt{2}} \right) \right] \tag{A-38}$$

$$G_{-m}(S) = \frac{e^{\frac{-S^2}{2}}}{m! \, S^2} M \left(-m, \frac{-1}{2}, \frac{S^2}{2} \right) \tag{A-39}$$

$$B_{\frac{1}{2}-m}(S) = \frac{(-1)^{m+1} 2 e^{\frac{-S^2}{2}}}{(2m-2)! \, S^2} \left[\frac{1}{4m} H_{2m} \left(\frac{S}{\sqrt{2}} \right) + H_{2m-2} \left(\frac{S}{\sqrt{2}} \right) \right] \tag{A-40}$$

$$B_{\frac{1}{2}-m}(S) = \frac{S \, e^{\frac{-S^2}{2}}}{(m-1)!3} M \left(-m+1, \frac{5}{2}, \frac{S^2}{2} \right) \tag{A-41}$$

where $m = 1, 2, 3, 4, \dots$ and $H_m \left(S/\sqrt{2} \right)$ is a Hermite polynomial and

$M(-m, -\frac{1}{2}, \frac{S^2}{2})$ is a confluent Hypergeometric function. This connection between these special functions and jet functions greatly aided the uncovering of the jet function's properties. This particular line of inquiry still promises more interesting discoveries for some future work.

Recursion relations have also been found for the jet function. For $m \leq \frac{1}{2}$ it was found that

$$[2m-5]\,[m-1]\,J_{m-2} - [5-4m-S^2]\,J_{m-1} + 2J_m = 0 \qquad \text{(A-42)}$$
$$(m \leq \frac{1}{2}, \text{ integer or } \frac{1}{2} \text{ integer})$$

For $m \geq 2$:

$$[2m-3]\,m\,J_m + [5-4m-S^2]\,J_{m-1} + 2J_{m-2} = 0 \qquad \text{(A-43)}$$
$$(m \geq 2, \text{ integer or } \frac{1}{2} \text{ integer})$$

J_m may be replaced by G_m or B_m individually in (A-42) and (A-43).

Other properties of jet functions are more easily examined if we reduce the independent functions of G_m and B_m down to their primitive polynomials. We do this by employing (A-7) and (A-9) and defining some new notation. Let

$$F_m(S) = C_1\,F_m^{(G)}(S) + C_2\,F_m^{(B)}(S) \qquad \text{(A-44)}$$

$$E_m(S) = C_1\,E_m^{(G)}(S) + C_2\,E_m^{(B)}(S) \qquad \text{(A-45)}$$

where

$$G_m = \frac{e^{\frac{-S^2}{2}}}{S} F_m^{(G)} = \frac{1}{S} E_m^{(G)} \tag{A-46}$$

$$B_m = \frac{e^{\frac{-S^2}{2}}}{S} F_m^{(B)} = \frac{1}{S} E_m^{(B)} \tag{A-47}$$

and C_1, C_2 are constants of integration as in (A-19).

Two recursion relations have been found which have a differential component for

$$m \leq \frac{1}{2}$$

$$[2m - 3] m F_{m-1} = [-2m + 1 - S^2] F_m + S \frac{dF_m}{dS} \tag{A-48}$$

Equation (A-48) is true for both $F_m^{(G)}$ and $F_m^{(B)}$ but only if $m \leq \frac{1}{2}$. For the

case of $m \geq 2$ the following is true:

$$-2E_{m-1} = [-2m + 1] E_m + S \frac{dE_m}{dS} \ . \tag{A-49}$$

Equation (A-49) is true for both $E_m^{(G)}$ and $E_m^{(B)}$ but only if $m \geq 2$. Imaginary

relationships analogous to those of the trigonometric functions $\cos(i\theta) = \cosh(\theta)$,

$-i\sin(i\theta) = \sinh(\theta)$ have also been found for jet functions (not an unreasonable

event in light of the generating functions):

$$E_m^{(B)}(S) = -i F_{\frac{1}{2}-m}^{(B)}(iS) \tag{A-50}$$

$$F_{\frac{1}{2}-m}^{(B)}(S) = -i E_m^{(B)}(iS) \tag{A-51}$$

$$E^{(G)}_{m+\frac{3}{2}}(S) = F^{(G)}_{-m-1}(iS) \tag{A-52}$$

$$F^{(G)}_{-m-1}(S) = E^{(G)}_{m+\frac{3}{2}}(iS) \; . \tag{A-53}$$

where $m = 0, 1, 2, 3, ...$

It was the discovery of these imaginary relationships that largely unlocked the study of this problem. Now one need only study the functions of $m \leq \frac{1}{2}$ (F_m polynomials which, because of the alternating sign in the terms making up these functions, were more easily matched to known special functions, (i.e., the Hermite polynomial). E_m polynomials can be found by simply mapping over from the F_m polynomials using the above relations.

3. DERIVATION OF "HARD" SOLUTIONS

In the previous section we derived what are called "easy solutions"; however, this is only half of the story. The reader may have noticed that for $m = 0$ we have a B_0 solution but no G_0 solution. Likewise for the rest of the easy solutions, another solution needs to be found. These other "hard solutions" as their name implies, are of a more complex structure. Hard solutions can be expressed in a single infinite series form through application of the Frobenius method. However such a form is virtually useless for satisfying boundary conditions or in examining the solution's properties. The more appropriate forms for examining hard solutions are shown below:

$$\bar{E}_m(S) = D_m(S)\sqrt{\frac{2}{\pi}}\,e^{\frac{-S^2}{2}} - E_m(S)\,erf\left(\frac{S}{\sqrt{2}}\right) \tag{A-54}$$

$$\bar{F}_m(S) = \sqrt{\frac{2}{\pi}}\left[D_m(S)\,e^{\frac{S^2}{2}} + F_m(S)\int_0^{S/\sqrt{2}} e^{x^2}\,dx\right] \tag{A-55}$$

where E_m and F_m are easy polynomials, $\bar{E}_m$, $\bar{F}_m$ are hard solutions, and D_m is a function which will be called a "hard driver polynomial" which will be defined shortly. Hard solutions can be converted back to the jet function form J_m by using (A-7) and (A-9). Easy polynomials of first order zero type (G superscript) always have second order pole type (B superscript) hard solutions. Easy polynomials of second order pole type (B superscript) always have first order zero type (G superscript) hard solutions. B superscript hard solutions have B superscript hard driver polynomials; and G superscript hard solutions have G superscript hard driver polynomials. Hard solutions and hard driver polynomials can be raised to higher or lower order by using the recursion equations (A-41) and (A-43) (however no differential recursion formula such as (A-49) has been discovered for hard driver functions). The imaginary relations for hard solutions are *almost* the same as for easy solutions:

$$\bar{F}^{(B)}_{-m-1}(S) = i\,\bar{E}^{(B)}_{m+\frac{3}{2}}(iS) \tag{A-56}$$

$$\bar{E}^{(B)}_{m+\frac{3}{2}}(S) = i\,\bar{F}^{(B)}_{-m-1}(iS) \tag{A-57}$$

$$\bar{E}^{(G)}_m(S) = \bar{F}^{(G)}_{\frac{1}{2}-m}(iS) \tag{A-58}$$

$$\bar{F}^{(G)}_{\frac{1}{2}-m}(S) = \bar{E}^{(G)}_m(iS) \tag{A-59}$$

where $m = 0, 1, 2, 3, 4, \ldots$

The hard driver polynomial $D_m(S)$ for (A-54) may be solved by finding the particular solution to the following O.D.E., which was derived from inserting (A-54) into (A-8):

$$\frac{d^2 D_m}{dS^2} - S\,\frac{dD_m}{dS} - 2\left[m + \frac{1}{S^2}\right]D_m = 2\,\frac{dE_m}{dS}\,. \tag{A-60}$$

The homogeneous solution to (A-60) is simply F_m which when multiplied by $e^{\frac{-S^2}{2}}$ in (A-54) is $E_m(S)$ (the easy solution) and therefore redundant (it can be absorbed in the constant of integration). A simple closed form solution for $D_m(S)$ is not yet attainable. The form presently known is shown below for one case derived from (A-60), ($m \geq 0$, integer only):

$$D^{(B)}_m = \frac{-1}{m!}\sum_{k=1}^{m} C_k\,S^{2k-2} \tag{A-61}$$

$$C_1 = 1 \tag{A-62}$$

$$C_m = 2^{m-1}\,\frac{(m-1)!}{(2m-2)!} \tag{A-63}$$

$$C_k = \frac{1}{k+m-1}\left[(2k^2-k-1)C_{k+1} + \frac{2^k(2k-1)^2(m!)}{(2k)!\,(m-k)!}\right] \tag{A-64}$$

where $m = 1, 2, 3, \ldots$ and C_m is used to end the series. The preferred method for calculating hard drivers is not to use (A-61) or its counter part for $D^{(G)}_m$ but rather to

use the recursion relation (A-43) and use (A-60) to check the result. Below is Table A-1 of known hard driver functions.

One may calculate negative m, and $m = \dfrac{1}{2}$ hard drivers (for $\bar{F}_m$), by first calculating the positive m value hard solutions by using the above techniques and converting them over to their imaginary counterparts via (A-56) and (A-59). The hard drivers can be extracted by using the definition of (A-55). However for physical reasons, which will be examined in the next section, negative m valued hard solutions are of little interest.

4. INTERLEAVING OF SOLUTIONS

Table A-2 can now be generated which shows some of the jet function primitive polynomials and how these functions interleave. The reader should note how the easy and hard solutions alternate in both the G_m and B_m solutions. Also note how the $J_{1/2}$ solution (which has a F_m polynomial form) penetrates into the E_m domain, leapfrogging J_0 . An example of how a complete solution is extracted from Table A-2 is shown with $m = \dfrac{5}{2}$:

$$J_{\frac{5}{2}}(S) \;=\; C_1 G_{\frac{5}{2}}(S) + C_2 B_{\frac{5}{2}}(S) \qquad \text{(A-65a)}$$

Table A-1

Hard Driver Functions

$$D_0^{(G)} \quad = \quad -1$$

$$D_1^{(G)} \quad = \quad -1$$

$$D_{\frac{3}{2}}^{(B)} \quad = \quad -\frac{1}{3} \left[S - \frac{1}{S} \right]$$

$$D_2^{(G)} \quad = \quad -\frac{1}{2} \left[1 + S^2 \right]$$

$$D_{\frac{5}{2}}^{(B)} \quad = \quad -\frac{1}{15} \left[4S + S^3 - \frac{1}{S} \right]$$

$$D_3^{(G)} \quad = \quad -\frac{1}{6} \left[1 + \frac{8}{3} S^2 + \frac{1}{3} S^4 \right]$$

$$D_{\frac{7}{2}}^{(B)} \quad = \quad -\frac{1}{105} \left[12S + \frac{13}{2} S^3 + \frac{S^5}{2} - \frac{2}{S} \right]$$

Table A-2

Interleaving Of Jet Function Solution

E_m Solutions

$$J_m = \frac{1}{S} E_m$$

F_m Solutions

$$J_m = \frac{e^{\frac{S^2}{2}}}{S} F_m$$

B_m — PRIMITIVE POLYNOMIAL

$$\bar{E}^{(B)}_{7/2} = \frac{-1}{105}\left[12S + \frac{13}{2}S^3 + \frac{S^5}{2} + \frac{5}{2} - \frac{2}{S}\right]\sqrt{2/\pi}\, e^{\frac{-S^2}{2}} - E^{(G)}_{7/2}\,\mathrm{erf}\!\left(\frac{S}{\sqrt{2}}\right)$$

$$\bar{E}^{(B)}_{5/2} = \frac{-1}{15}\left[4S + S^3 - \frac{1}{S}\right]\sqrt{2/\pi}\, e^{\frac{-S^2}{2}} - E^{(G)}_{5/2}\,\mathrm{erf}\!\left(\frac{S}{\sqrt{2}}\right)$$

$$\bar{E}^{(B)}_{3/2} = \frac{-1}{3}\left[S - \frac{1}{S}\right]\sqrt{2/\pi}\, e^{\frac{-S^2}{2}} - E^{(G)}_{3/2}\,\mathrm{erf}\!\left(\frac{S}{\sqrt{2}}\right)$$

$$\bar{F}^{(B)}_{-1} = \sqrt{2/\pi}\left[\frac{1}{3}\Big(S + \frac{1}{S}\Big)\right]e^{\frac{S^2}{2}}\int_0^{S/\sqrt{2}} e^{x^2}\,dx + F^{(G)}_{-1}$$

$$\bar{F}^{(B)}_{-2} = \sqrt{2/\pi}\left[\frac{1}{15}\Big(4S - S^3 + \frac{1}{S}\Big)\right]e^{\frac{S^2}{2}}\int_0^{S/\sqrt{2}} e^{x^2}\,dx + F^{(G)}_{-2}$$

$$\bar{F}^{(B)}_{-3} = \sqrt{2/\pi}\left[\frac{1}{105}\Big(12S - \frac{13}{2}S^3 + \frac{S^5}{2} + \frac{2}{S}\Big)\right]e^{\frac{S^2}{2}} \cdot \frac{S^2}{2} + F^{(G)}_{-3}\int_0^{S/\sqrt{2}} e^{x^2}\,dx$$

PRIMITIVE POLYNOMIAL (B)

$$E^{(B)}_3 = \frac{S}{2} + \frac{S^3}{2} + \frac{S^5}{18} - \frac{1}{6S}$$

$$E^{(B)}_2 = S + \frac{S^3}{2} - \frac{1}{2S}$$

$$E^{(B)}_1 = S - \frac{1}{S}$$

$$F^{(B)}_{1/2} = \frac{1}{S}$$

$$E^{(B)}_0 = -\frac{1}{S}$$

$$F^{(B)}_{-1/2} = S + \frac{1}{S}$$

$$F^{(B)}_{-3/2} = S - \frac{S^3}{2} + \frac{1}{2S}$$

$$F^{(B)}_{-5/2} = \frac{S}{2} - \frac{S^3}{2} + \frac{S^5}{18} + \frac{1}{6S}$$

G_m — PRIMITIVE POLYNOMIAL

$$\bar{E}^{(G)}_3 = -\frac{1}{6}\left[1 + \frac{8}{3}S^2 + \frac{S^4}{3}\right]\sqrt{\frac{2}{\pi}}\, e^{\frac{-S^2}{2}} - E^{(B)}_3\,\mathrm{erf}\!\left(\frac{S}{\sqrt{2}}\right)$$

$$\bar{E}^{(G)}_2 = \frac{-1}{2}\left[1 + S^2\right]\sqrt{\frac{2}{\pi}}\, e^{\frac{-S^2}{2}} - E^{(B)}_2\,\mathrm{erf}\!\left(\frac{S}{\sqrt{2}}\right)$$

$$\bar{E}^{(G)}_1 = -\sqrt{\frac{2}{\pi}}\, e^{\frac{-S^2}{2}} - E^{(B)}_1\,\mathrm{erf}\!\left(\frac{S}{\sqrt{2}}\right)$$

$$\bar{F}^{(G)}_{1/2} = \sqrt{\frac{2}{\pi}}\left[-\frac{S}{\ }\right]e^{\frac{-S^2}{2}} + F^{(B)}_{1/2}\int_0^{S/\sqrt{2}} e^{x^2}\,dx$$

$$\bar{E}^{(G)}_0 = -\sqrt{\frac{2}{\pi}}\, e^{\frac{-S^2}{2}} - E^{(B)}_0\,\mathrm{erf}\!\left(\frac{S}{\sqrt{2}}\right)$$

$$\bar{F}^{(G)}_{-1/2} = \sqrt{\frac{2}{\pi}}\left[-e^{\frac{-S^2}{2}}\right] + F^{(B)}_{-1/2}\int_0^{S/\sqrt{2}} e^{x^2}\,dx$$

$$\bar{F}^{(G)}_{-3/2} = \frac{-1}{2}\left[1 - S^2\right]e^{\frac{-S^2}{2}} + F^{(B)}_{-3/2}\int_0^{S/\sqrt{2}} e^{x^2}\,dx$$

$$\bar{F}^{(G)}_{-5/2} = \sqrt{\frac{2}{\pi}}\left[\frac{-1}{6}\Big(1 - \frac{8}{3}S^2 + \frac{S^4}{3}\Big)\right]e^{\frac{-S^2}{2}} + F^{(B)}_{-5/2}\int_0^{S/\sqrt{2}} e^{x^2}\,dx$$

PRIMITIVE POLYNOMIAL (G)

$$E^{(G)}_{7/2} = \frac{S^2}{6} + \frac{S^4}{15} + \frac{S^6}{210}$$

$$E^{(G)}_{5/2} = \frac{S^2}{3} + \frac{S^4}{15}$$

$$E^{(G)}_{3/2} = \frac{S^2}{3}$$

$$F^{(G)}_{-1} = -\frac{S^2}{3}$$

$$F^{(G)}_{-2} = -\frac{S^2}{3} + \frac{S^4}{15}$$

$$F^{(G)}_{-3} = -\frac{S^2}{6} + \frac{S^4}{15} - \frac{S^6}{210}$$

m column values:

7/2, 3, 5/2, 2, 3/2, 1, 1/2, 0, −1/2, −1, −3/2, −2, −5/2, −3

$$J_{\frac{5}{2}}(S) = \frac{C_1}{S}\left(\frac{S^2}{3}+\frac{S^4}{15}\right) + \frac{C_2}{S}\left[\frac{-1}{15}\left(4S+S^3-\frac{1}{S}\right)\sqrt{\frac{2}{\pi}}\,e^{\frac{-S^2}{2}}\right.$$

$$\left. - \left(\frac{S^2}{3}+\frac{S^4}{15}\right)\,erf\left(\frac{S}{\sqrt{2}}\right)\right] . \qquad \text{(A-65b)}$$

The imaginary complement of $J_{\frac{5}{2}}$ is J_{-2} which is shown below:

$$J_{-2}(S) = C_1\frac{e^{\frac{-S^2}{2}}}{S}\left(-\frac{S^2}{3}+\frac{S^4}{15}\right) + C_2\frac{e^{\frac{-S^2}{2}}}{S}\left\{\frac{1}{15}\left(4S-S^3+\frac{1}{S}\right)\sqrt{\frac{2}{\pi}}\,e^{\frac{S^2}{2}}\right.$$

$$\left. + \left(-\frac{S^2}{3}+\frac{S^4}{15}\right)\int_0^{S/2}e^{x^2}\,dx\right\} . \qquad \text{(A-66)}$$

At this point boundary conditions for $S \to \infty$ should be examined. It has been shown that vorticity from a point disturbance will decay as a Gaussian multiplied by a slowly varying function. In (A-65) we observe that this boundary condition is attainable only if $C_1 = C_2$, which causes the easy solution to disappear at infinity. In (A-65b) the solution will converge only if $C_2 = 0$. These two cases are representative for all J_m with polynomial solutions (for the E_m solutions $C_1 = C_2$ and for the F_m solutions $C_2 = 0$). It is for this reason that the $\bar{F}_m$ hard solutions are of little physical interest in the unbounded problem, for with the exception of the solution $m = \frac{1}{2},\ -\frac{1}{2},\ -1$ all of $\bar{F}_m$ hard solutions diverge at infinity, and in the cases of $m = \frac{1}{2},\ -\frac{1}{2},\ -1$ the solutions do not decay as a Gaussian multiplied by a slowly

varying function and are therefore inadmissible. Based on this boundary condition we can write a more restrictive form for $J_m(S)$ where we set $C_1 = 1$ for convenience:

$$J_m(S) = \frac{1}{S}\left[E_m(S) + \bar{E}_m(S)\right] \quad \text{for } m \geq 0, \text{ integer and } 1/2 \text{ integer ;} \quad \text{(A-67)}$$

$$J_m(S) = \frac{e^{\frac{-S^2}{2}}}{S}\left[F_m(S)\right] \quad \text{for } m = \frac{1}{2}, m < 0, \text{ integer and } 1/2 \text{ integer ;} \quad \text{(A-68)}$$

5. ORTHOGONALITY PROPERTIES OF JET FUNCTIONS

It was found that (A-4b) can be recast into the Sturm-Liouville form:

$$\frac{d}{dS}\left[S^2 e^{\frac{S^2}{2}} \frac{dJ}{dS}\right] + \left[2(1-m)S^2\, e^{\frac{S^2}{2}} - l(l+1)\, e^{\frac{S^2}{2}}\right]J = 0 \; . \quad \text{(A-69)}$$

This result opens up many possible lines of inquiry, but the only one examined so far is that of orthogonality. Orthogonality relations can probably be deduced for all the jet functions (J_m) if one were interested in integrating from zero or infinity to a zero of the jet function which had the appropriate boundary condition satisfying the Sturm-Liouville theorem. However the only jet functions that are orthogonal over the range $(0, \infty)$ are the negative m integer type $(F_{-m}^{(a)})$. The orthogonality properties of these particular functions are defined as follows:

Let:

$$\lambda_m = \frac{2^{2m}(m^2+m)}{(2m+2)!}\sqrt{\frac{\pi}{2}}. \tag{A-70}$$

From (A-68)

$$J_{-m}(S) = -\frac{e^{\frac{-S^2}{2}}}{S}\left[\sum_{j=1}^{m}\frac{(-2)^{j+1}(j^2+j)S^{2j}}{(m-j)!(2j+2)!}\right] \quad \text{for} \quad m = 1,2,3,4,\cdots \tag{A-71}$$

We use the weighting function from (A-69). The orthogonality integral is:

$$\int_0^\infty J_{-m}(S)\,J_{-n}(S)\,S^2\,e^{\frac{S^2}{2}}\,dS = \begin{cases} 0 & m \neq n \\ \\ \lambda_m^2 & m = n \end{cases} \tag{A-72}$$

With (A-70), (A-71) and (A-72) as a basis, one could employ the following Fourier form:

$$A_m = \frac{1}{\lambda_m}\int_0^\infty \Phi(S)\,J_{-m}(S)\,S^2\,e^{\frac{S^2}{2}}\,dS \tag{A-73}$$

$$\Phi(x) = \sum_{m=1}^{\infty}\frac{A_m}{\lambda_m}\,J_{-m}(x) \tag{A-74}$$

where $\Phi(x)$ is the function to be analyzed. It has not yet been established whether (A-74) will pass the completeness test. Assuming that (A-74) is complete, if one had a vorticity distribution that can be represented with the self similar coordinate S, one could use (A-74) to spectrum analyze the function. This assumes that the resultant equations in (A-73) and (A-74) are convergent, which will probably be the case only if the Reynolds number of the function under consideration $\Phi(x)$ is decaying in time since (as we shall see in the next section) all of the basis functions $J_{-m}(S)$ employed

in (A-73) are of this Reynolds number behavior.

6. STREAM FUNCTIONS, VELOCITIES AND REYNOLDS NUMBERS FROM JET FUNCTIONS

With the method of generating the vorticity functions established, the means by which to calculate the stream function, velocity, and Reynolds number, along with deducing the forcing function should also be examined. Following the method used by Cantwell [1980] the velocities and stream function are converted to dimensionless quantities:

$$u = \hat{P} \nu^{-3/2} t^{m-1/2} U(S,\theta) \qquad (A\text{-}75)$$

$$v = \hat{P} \nu^{-3/2} t^{m-1/2} V(S,\theta) \qquad (A\text{-}76)$$

$$\psi = \hat{P} \nu^{-1/2} t^{m+1/2} g(S,\theta) \qquad (A\text{-}77)$$

where u is the radial velocity with U its dimensionless counterpart, v the velocity in the theta direction with V its dimensionless counterpart and the rest of the variables the same as used in (A-3). The definition for stream function and vorticity in axisymmetric spherical coordinates is:

$$u = \frac{1}{r^2 \sin \theta} \frac{\partial \psi}{\partial \theta} \qquad \text{(A-78)}$$

$$v = \frac{-1}{r \sin \theta} \frac{\partial \psi}{\partial r} \qquad \text{(A-79)}$$

$$r\omega = \frac{\partial}{\partial r} (rv) - \frac{\partial u}{\partial \theta} . \qquad \text{(A-80)}$$

The previous six equations are used with (A-2) and (A-3) giving

$$-2^{3/2} \, S \, W = \frac{1}{\sin \theta} \frac{\partial^2 g}{\partial S^2} + \frac{1}{S^2} \frac{\partial}{\partial \theta} \left[\frac{1}{\sin \theta} \frac{\partial g}{\partial \theta} \right] . \qquad \text{(A-81)}$$

It can be shown that an axisymmetric stream function for a Stokes vorticity solution that is consistent with (A-5) ($l = 1$, dipole case), must be of the following form:

$$g(S,\theta) = \hat{c} \sin^2 \theta \, R(S) . \qquad \text{(A-82)}$$

Combining (A-83) with (A-81) and (A-5) we find that

$$2^{3/2} \, J(S) = -\frac{d}{dS} \left[\frac{1}{S^2} \frac{d}{dS} (SR) \right] \qquad \text{(A-83)}$$

where $J(S)$ is the jet function which we just solved. Equation (A-83) is readily integrated, yielding

$$R(S) = \frac{C_1}{S} + C_2 \, S^2 - \frac{2^{3/2}}{S} \left[\int S^2 \left(\int J(S) dS \right) \, dS \right] \qquad \text{(A-84)}$$

where C_1 and C_2 are constants of integration, governing the irrotational dipole components of the stream function. The dimensionless stream function, and velocities can

now be expressed utilizing (A-75), (A-76), (A-82) and (A-84):

$$g(S,\theta) \quad = \quad \sin^2\theta \left\{ \frac{C_1}{S} + C_2 S^2 - \frac{2^{3/2}}{S} \left[\int S^2 \left(\int J(S)dS \right) dS \right] \right\} \qquad .\text{(A-85)}$$

$$U \quad = \quad \frac{1}{2S^2 \sin\theta} \frac{\partial g}{\partial \theta} \qquad \text{(A-86)}$$

$$V \quad = \quad \frac{-1}{2S \sin\theta} \frac{\partial g}{\partial S} \quad . \qquad \text{(A-87)}$$

We may derive the Reynolds number from the unsteady particle paths given by

$$\frac{dr}{dt} \quad = \quad u \qquad \text{(A-88)}$$

$$\frac{d\theta}{dt} \quad = \quad \frac{v}{r} \quad . \qquad \text{(A-89)}$$

A logarithmic relation for time is employed:

$$\tau \quad = \quad \ln t \qquad \text{(A-90)}$$

Also, a Reynolds number will be used of the following form:

$$\text{Re} \quad = \quad \left[\frac{\hat{P} t^m}{\sqrt{2} \, \nu^2} \right]^{\frac{1}{2}} . \qquad \text{(A-91)}$$

Equations (A-75), (A-76) and (A-2) are used with (A-88), (A-89), (A-90) and (A-91) giving

$$\frac{dS}{d\tau} \quad = \quad Re^2 \, U - \frac{S}{2} \qquad \text{(A-92)}$$

$$\frac{d\theta}{d\tau} = Re^2 \frac{V}{S} \,.$$ (A-93)

The forcing function at the point momentum source of the jet can be deduced by first recognizing that the *impulse* of the jet is conserved. Since impulse is conserved we may write down the impulse integral as an equation of constraint:

$$\frac{I}{\rho} = \frac{3}{2} \int_0^\pi \int_0^\infty (u \cos \theta - v \sin \theta) \, 2\pi r^2 \sin \theta \, dr \, d\theta$$ (A-94)

where I is impulse, and ρ is density. The definition of impulse is the following:

$$\frac{I}{\rho} = \frac{1}{\rho} \int_0^t \hat{F} \, dt$$ (A-95)

where $\hat{F}$ is the force applied to the fluid at the momentum source.

We combine (A-94), (A-95) with (A-75), (A-76) and (A-2) giving

$$\frac{1}{\rho} \int_0^t \hat{F} \, dt = \frac{3\sqrt{2}}{2} \hat{P} \, t^{m+1} \int_0^\pi \int_0^\infty (U \cos \theta - V \sin \theta) \, 2\pi S^2 \sin \theta \, dS \, d\theta$$

(A-96)

If the components of (A-96) that are not functions of time are collected one can define the following constant:

$$\hat{K} = \frac{3\sqrt{2}}{2} \rho \hat{P} \int_0^\pi \int_0^\infty (U \cos \theta - V \sin \theta) 2\pi S^2 \sin\theta \, dS d\theta$$ (A-97)

Equation (A-96) can now be reexpressed as

$$\int_0^t \hat{F}\, dt \;=\; \hat{K}\, t^{m+1} \;. \qquad\qquad (\text{A-98})$$

With (A-98) we may deduce the *force* function. Let us examine some examples.

Let:

$$\hat{F} \;=\; \hat{P}\, t \;. \qquad\qquad (\text{A-99})$$

We find that (A-98) is satisfied only if $m = 1$. For the case $m = 1$ the Reynolds number described by (A-91) increases proportionally to $t^{1/2}$.

Let:

$$\hat{F} \;=\; \hat{P}\, \hat{u}\,(t) \qquad\qquad (\text{A-100})$$

where $\hat{u}\,(t)$ is a Heaviside step function. For this case $m = 0$, the Reynolds number is not a function of time since time is to the zeroth power. The case of $m = 0$ is unique in that it is autonomous. This solution corresponds to a round jet. Let:

$$\hat{F} \;=\; \hat{P}\, \delta(t) \qquad\qquad (\text{A-101})$$

where $\delta(t)$ is the Dirac delta function. For this case $m = -1$ since time is removed from the left-hand side of (A-99). The Reynolds number decreases proportionally to $1/t^{1/2}$ making this case complementary to the case of $m = 1$, (A-99). Let:

$$\hat{F} \;=\; \hat{P}\, t^{3/2} \qquad\qquad (\text{A-102})$$

For this case $m = 3/2$, the Reynolds number increases proportionally to $t^{\frac{3}{4}}$.

This solution corresponds to the "Hill's spherical vortex". Let:

$$\hat{F} \;=\; \hat{P}\, t^{1/2} \tag{A-103}$$

For this case $m = 1/2$, the Reynolds number increases proportionally to $t^{\frac{1}{4}}$. This solution is the imaginary complement of the $m = 0$, round jet solution. Unlike the round jet, the "$m = 1/2$ jet" has never been extensively investigated. Let:

$$\hat{F} \;=\; \hat{P}\, t^{-1/2} \tag{A-104}$$

For this case $m = -1/2$, the Reynolds number decreases proportionally to $1/t^{1/4}$. This particular solution is very unusual with regards to its Stokes solution stream function which appears to be the simplest of all the dipole solutions examined. This solution has never been extensively investigated.

It should be noted that if one integrates in time (A-101) (the case for $m = -1$), then (A-100) (case $m = 0$), is obtained. Likewise if (A-100) is integrated in time, then (A-99), (case $m = 1$) appears. We also find that (A-104) integrated yields (A-103) and (A-103) integrated gives (A-102). It should also be noted that with the exception of $m = 0$, for negative m the Reynolds number decays with time, while for positive m the Reynolds number increases with time. The round jet ($m = 0$) does neither because it is autonomous. The case of $m = 1/2$ has an increasing Reynolds number but it is of an F_m polynomial type (see Table A-2). This type is of decaying Reynolds number with this single exception. Needless to say, $m = 1/2$ is a very strange solution indeed.

7. JET FUNCTIONS AND THE NAVIER STOKES EQUATIONS

In the previous section it was observed that in the six examples shown for $m = 3/2, 1, 1/2, 0, -1/2, -1$ three are of classical interest; i.e., the round jet, vortex ring, and spherical vortex. It should be recalled that all of the solutions examined so far have been for the dipole case, $l = 1$. This document would be too long if the cases of $l = 2, 3, 4, ...$ were also examined thoroughly, but for the sake of interest let us examine the family of easy functions of the form:

$$J = S^\alpha \qquad (A\text{-}105)$$

where α is an integer. Equation (A-105) is inserted into (A-4a) yielding

$$\alpha(\alpha + 1) - l(l + 1) = 0 \qquad (A\text{-}106)$$

$$\alpha + 2 = 2m . \qquad (A\text{-}107)$$

From (A-106) and (A-107) we derive Table A-3.

It is interesting to note that the two solutions admitted for $l = 1$ in Table A-3 both have analytic solutions to the Navier Stokes equations. Hills' spherical vortex satisfies not only the Navier Stokes equation but the Stokes equation as well because the convective term goes to zero identically for all Reynolds number. The method by which the spherical vortex solution is found starts with the following equation for the convective term:

$$\frac{\partial}{\partial r}[r\, u\, \omega] + \frac{\partial}{\partial \theta}[v\, \omega] = 0 . \qquad (A\text{-}108)$$

Equations (A-78) and (A-79) are included with (A-108) giving

Table A-3

	l	M	α	
Dipole	1	0	-2	Round Jet (Landau-Squire Solution)
		$\frac{3}{2}$	1	Hills' Spherical vortex
Quadrapole	2	$-\frac{1}{2}$	- 3	? ?
		2	2	??
Hexapole	3	- 1	- 4	Vortex Ring (never investigated)
		$\frac{5}{2}$	3	? ?
Octopole	4	$-\frac{3}{2}$	- 5	? ?
		3	4	? ?
	.	.	.	
	.	.	.	
	.	.	.	

$$\frac{\partial}{\partial r}\left[\frac{\omega}{r\sin\theta}\frac{\partial\psi}{\partial\theta}\right] - \frac{\partial}{\partial\theta}\left[\frac{\omega}{r\sin\theta}\frac{\partial\psi}{\partial r}\right] = 0 \ . \qquad \text{(A-109)}$$

Any Stokes solution that satisfies (A-109) will also satisfy the Navier Stokes equations. The vorticity solution for $M = 3/2$ has been derived in the previous section (Table A-2) and is

$$\omega_{\frac{3}{2}}(r,\ \theta) = \frac{\hat{c}\,\hat{P}}{\sqrt{18\,\nu^5}}\ r\sin\theta \ . \qquad \text{(A-110)}$$

Inserting (A-110) into (A-109) gives the relation for the stream function

$$\frac{\partial}{\partial r}\left[\frac{\partial\psi}{\partial\theta}\right] - \frac{\partial}{\partial\theta}\left[\frac{\partial\psi}{\partial r}\right] = 0 \quad (\textit{valid only } \text{for } m = 3/2) \ . \qquad \text{(A-111)}$$

From (A-111) we find that any stream function consistent with (A-110), using (A-84) and the entire family of irrotational axisymmetric stream functions, will satisfy the Navier Stokes equation for this case. This complete solution is

$$\psi(r,\theta) = \psi_{potential} + \frac{-2^{1/2}\,\hat{c}\,\hat{P}\,r^4\sin^2\theta}{60\,\nu^{5/2}} \qquad \text{(A-112)}$$

where $\psi_{potential}$ is the family of irrotational axisymmetric stream functions:

$$\psi_{potential}\,(r,\theta,t) = \sum_{j=1}^{\infty}\left[H_j(t)\,S^{-j} + Q_j(t)\,S^{j+1}\right]\sin\theta\,P_j^1\,(cos\,\theta) \qquad \text{(A-113)}$$

where H_j and Q_j are time dependent coefficients determined by boundary conditions, and P_j^1 is the first order Legendre polynomial.

While the solutions of (A-110) and (A-112) have been known for almost a century the fact that higher order irrotational stream functions (quadrupole, hexapole, etc.), were also solutions seems to have been overlooked. The classical references (Lamb, Milne, etc) make no mention of this and Turner [1964] who attempted experimental verification of the spherical vortex used only the dipole irrotational component even though his experimental data was indicating higher order terms by producing an oblate geometry. Also no one appears to be aware of the fact that the spherical vortex can be produced by a point momentum source of strength proportional to $t^{3/2}$ and a Reynolds number proportional to $t^{3/4}$.

Hills' spherical vortex is a member of a larger body of solutions (where (A-109) is true), which satisfies both the axisymmetric Stokes equation and Navier stokes equation for *all* Reynolds number, thus being self similar with respect to S, (A-2) for all Reynolds number. All axisymmetric jet solutions will be self similar with S in the creeping limit but only one other family of solutions will have this self similarity for all Reynolds number. This other family is made up of the autonomous solutions like the round jet, radial jet, etc., which have been described by Cantwell [1981]. The convective term in the autonomous solutions does not go to zero. Even though these solutions are self similar with S they satisfy the Stokes equation only in the creeping limit. The complement to the spherical vortex in Table 3, the round jet is the creeping limit of the Navier Stokes solution discovered by Landau and independently by Squire and as mentioned before is an autonomous solution. The Landau Squire solution is generally represented as follows:

$$\psi = \nu r \left[\frac{2 \sin^2 \theta}{A - \cos \theta} \right] \qquad (A\text{-}114)$$

$$\omega = \frac{4\nu(A^2 - 1)\sin \theta}{r^2(A - \cos \theta)^3} \qquad (A\text{-}115)$$

$$\frac{Re^2}{16\pi} = A + \frac{4}{3}\frac{A}{A^2 - 1} - \frac{A^2}{2}\ln\left(\frac{A+1}{A-1}\right) \qquad (A\text{-}116)$$

In working with the first order Legendre polynomial it was observed that the generating function for $P_l^1(\cos\theta)$, (which was found in Morse and Feshbach [1953]) is similar to (A-115). The generating function is

$$\frac{\sin\theta}{[1 + h^2 - 2h\cos\theta]^{\frac{3}{2}}} = \sum_{n=0}^{\infty} h^n P_{n+1}^1(\cos\theta) \overset{or}{=} \sum_{n=0}^{\infty} \frac{1}{h^{n+1}} P_{n+1}^1(\cos\theta)$$

$$|h|\ small \qquad\qquad |h|\ large$$

$$(A\text{-}117)$$

Which ever series converges for the given h is the appropriate form. Equation (A-117) is very intriguing not only because it represents a special case of the irrotational solution (A-113 with constant coefficients), but also because it so closely resembles (A-115). This aspect, coupled with the fact that the complete solution of the spherical vortex stream function included all of first order Legendre polynomials, lead to the desire to recast (A-114) as a series of Legendre polynomials. After considerable algebra this was done giving the following:

$$\psi(r,\theta) = \frac{-8\nu r \sin\theta}{A} \sum_{j=0}^{\infty} \frac{(j!)2^{2j}}{A^{2j+1}} \left[A(4j+3) C_{2j+1} P_{2j+1}^1 (\cos\theta) \right.$$
$$\left. + (4j+5) C_{2j+2} P_{2j+2}^1 (\cos\theta) \right] \tag{A-118}$$

$$C_{2j+1} = \sum_{n=0}^{\infty} \frac{(2[n+j])! \, (n+2+2j)! \, (jn+1)}{(n+j)! \, (2[n+2+2j])! \, A^{2n}} \tag{A-119}$$

$$C_{2j+2} = \sum_{n=0}^{\infty} \frac{(2[n+j+1])! \, (n+3+2j)! \, (jn+1)}{(n+j+1)! \, (2[n+3+2j])! \, A^{2n}} \, . \tag{A-120}$$

In many ways (A-118) is a more interesting form than its generating function form in (A-114) because the solution's components can be picked out individually and examined. It is also interesting to note that the solution of (A-118) has split into odd poles and even poles. This leads to a line of inquiry as to whether any of the components will independently satisfy the Navier Stokes equations. This question still remains unanswered. The lowest order solutions of (A-119) and (A-120) was cast into an algebraic form:

$$C_1 = \frac{1}{4}(1-A^2)\ln\left(\frac{A+1}{A-1}\right) + \frac{A}{2} \tag{A-121}$$

$$C_2 = \frac{A^3}{4}\left(C_1 - \frac{1}{3A}\right) \, . \tag{A-122}$$

Equation (A-121) corresponds with the dipole solution and goes to $\frac{1}{3A}$ as Reynolds number goes to zero. Equation (A-122) corresponds with the quadrupole solution and disappears as C_1 approaches $\frac{1}{3A}$. It is interesting to note the similarity between

(A-121) and (A-116) whether any new insights can be gained from this similarity remains to be determined.

8. CONCLUSIONS AND FUTURE LINES OF INQUIRY

The methods described in this document will generate low Reynolds number solutions for any axisymmetric jet. These methods also provide a means of classifying different flow types, showing their interrelationships, and isolating particularly interesting flows. Many of these flows have never been investigated and are each worthy of investigation of their unique properties. Perhaps the most interesting aspect of the jet functions is their utility in devising solutions to the Navier Stokes equations. There exists a family of solutions of which one member is known (Hills' spherical vortex), where Stokes solutions will also satisfy the Navier Stokes equations. Table 3 might serve as a sign post in discovering the other members of this family. There also exists the family of autonomous solutions of which the round jet is a member. It is possible that other solutions can be extracted from the round jet solution cast as an infinite series of Legendre polynomials. Higher order components and Reynolds number behavior was observed in the spherical vortex. Both the spherical vortex and the round jet were observed to be composed of an infinite number of Legendre polynomials. Three major payoffs that may come from further investigation in jet functions are:

1. A generalized solution of the family of flows where the convective term goes to zero identically as is the case of the spherical vortex.

2. Discovery of a far field (hard function) solution to the Navier Stokes equation. All solutions presently known are near field, easy functions.

3. Development of spectral methods from first order Legendre polynomials and/or jet functions for use in numeric computation of unbounded flows.

Appendix B

PLOTS AND FIGURES

This chapter provides the graphical presentation of the results of this study.

The page shows three scientific figures arranged on the page, with a page number "172" at top, and "ORIGINAL PAGE IS OF POOR QUALITY" text. Figure captions include "VORTICITY CONTOUR PLOT FOR Re= 0.1", "VORTICITY*(PSI**3) PLOT FOR Re= 0.1", "PARTICLE PATH PLOT FOR Re= 0.1", and at bottom "Fig. B-1a Re = 0.1 For 30 × 30 Mesh ξ∞ = 15.0".

VORTICITY CONTOUR PLOT FOR Re= 0.1
30 X 30 MESH FOR ξ_∞ =15.0

VORTICITY*(PSI**3) PLOT FOR Re= 0.1
PLOTTED FROM 30 X 30 MESH FOR PSINF=15.0

PARTICLE PATH PLOT FOR Re= 0.1
30 X 30 MESH FOR ξ_∞ =15.0

Fig. B-1a   Re = 0.1   For   30 × 30 Mesh ξ_∞ = 15.0

ORIGINAL PAGE IS
OF POOR QUALITY

Fig. B-1b. Re = 1.0 For 30 × 30 Mesh at ξ_∞ = 15.0.
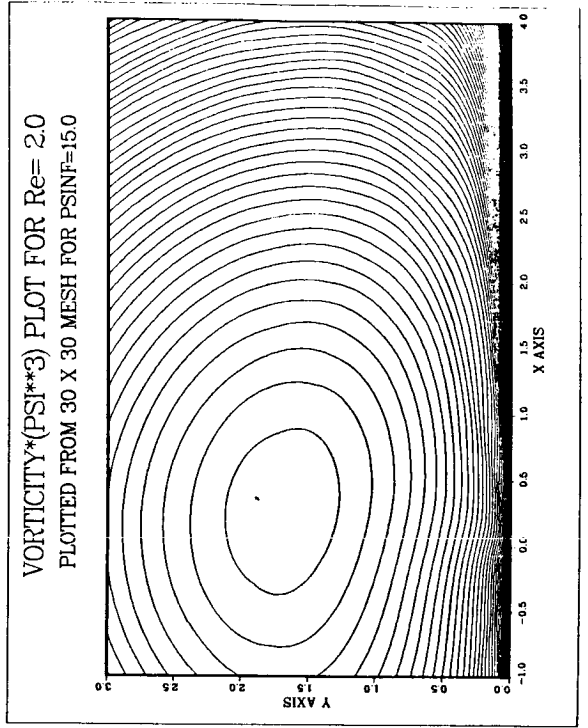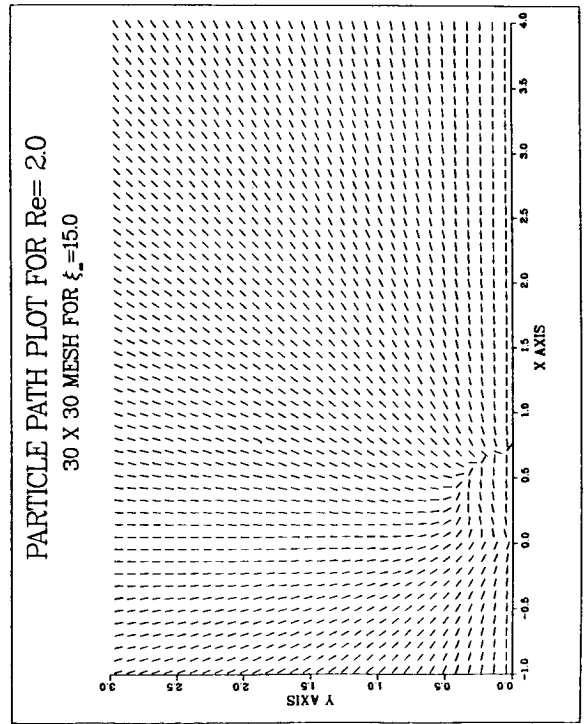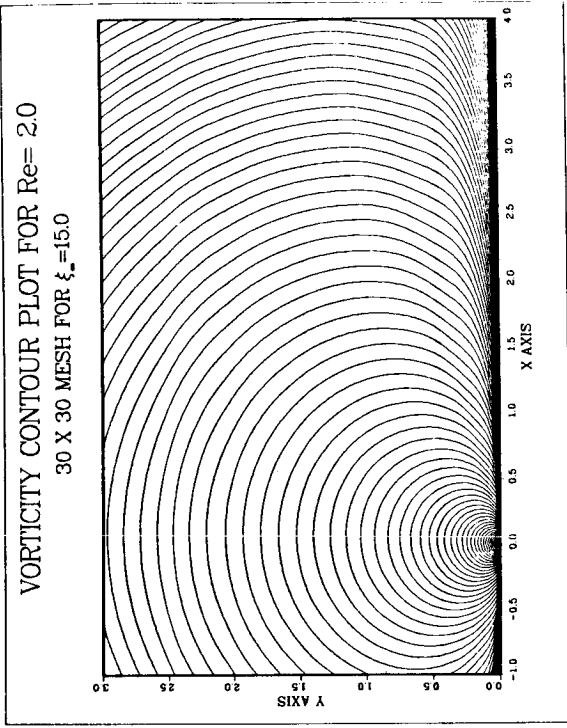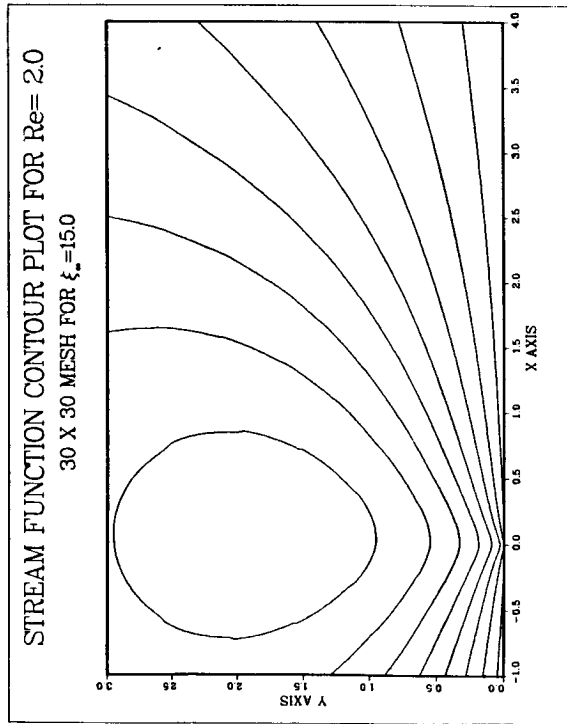
Fig. B-2. Re = 2.0 For 30 × 30 Mesh at ξ_∞ = 15.0.

VORTICITY CONTOUR PLOT FOR Re= 3.0
30 X 30 MESH FOR ξ_∞ =15.0

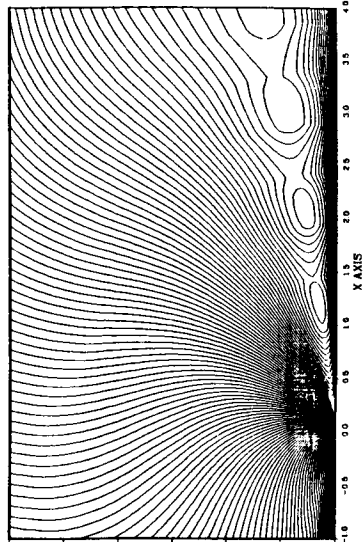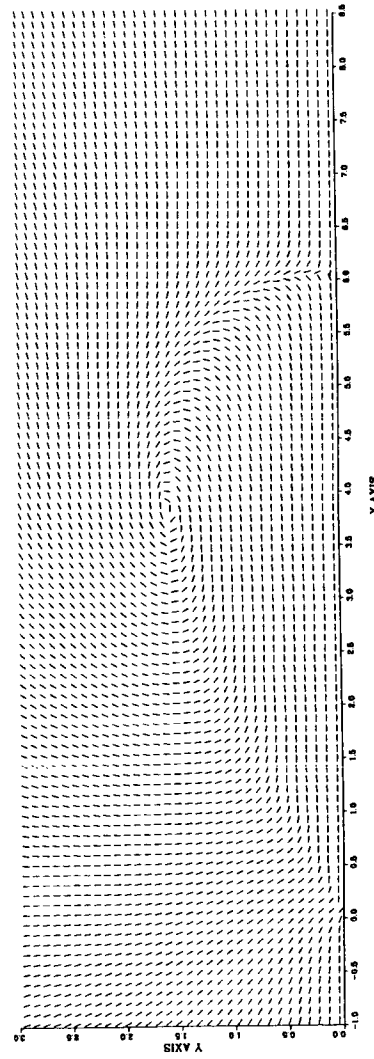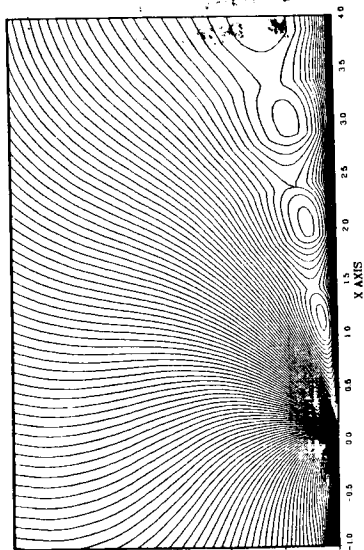VORTICITY*(PSI**3) PLOT FOR Re= 3.0
PLOTTED FROM 30 X 30 MESH FOR PSINF=15.0

STREAM FUNCTION CONTOUR PLOT FOR Re= 3.0
30 X 30 MESH FOR ξ_∞ =15.0

PARTICLE PATH PLOT FOR Re= 3.0
30 X 30 MESH FOR ξ_∞ =15.0
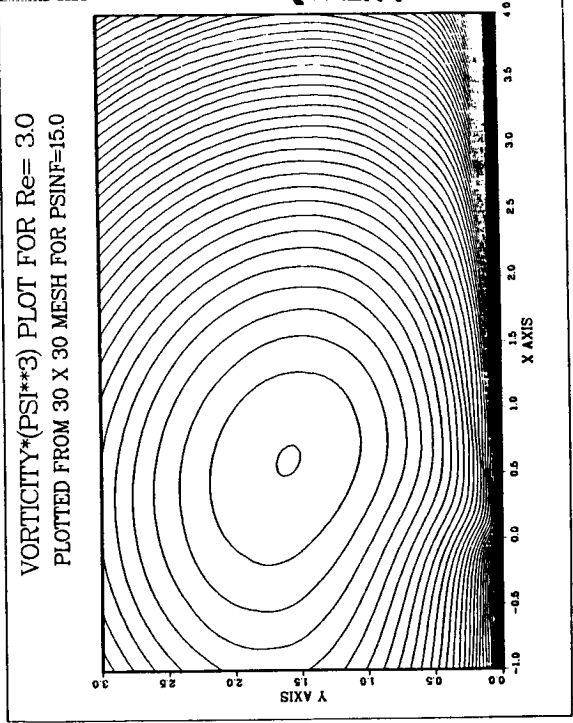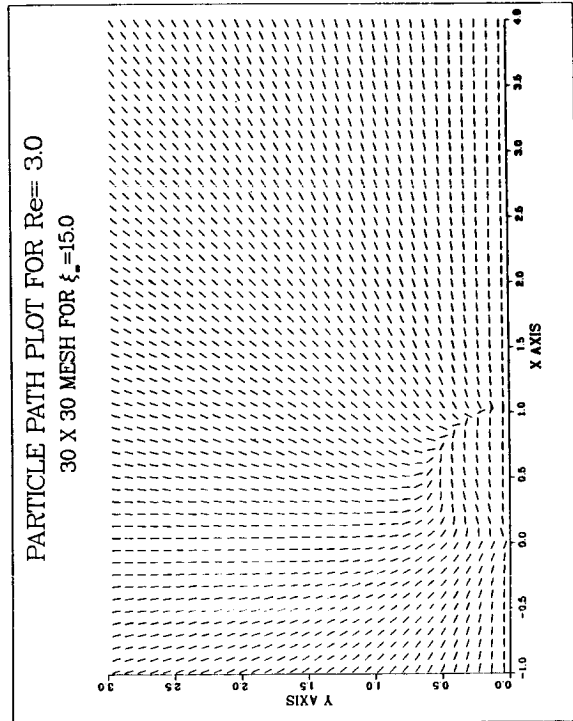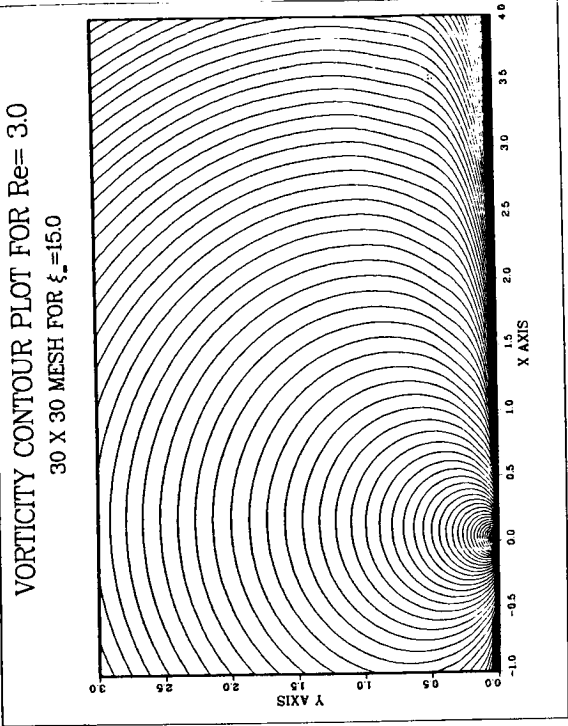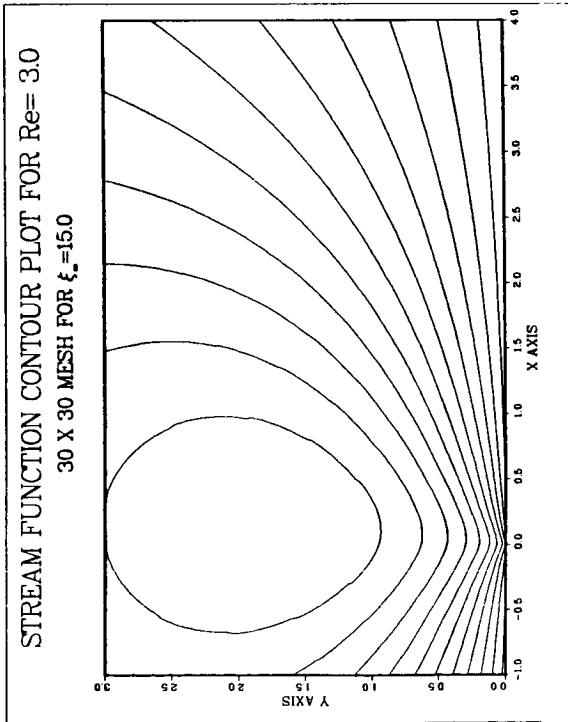
Fig. B-3.   Re = 3.0 For   30 × 30 Mesh at ξ_∞ = 15.0.
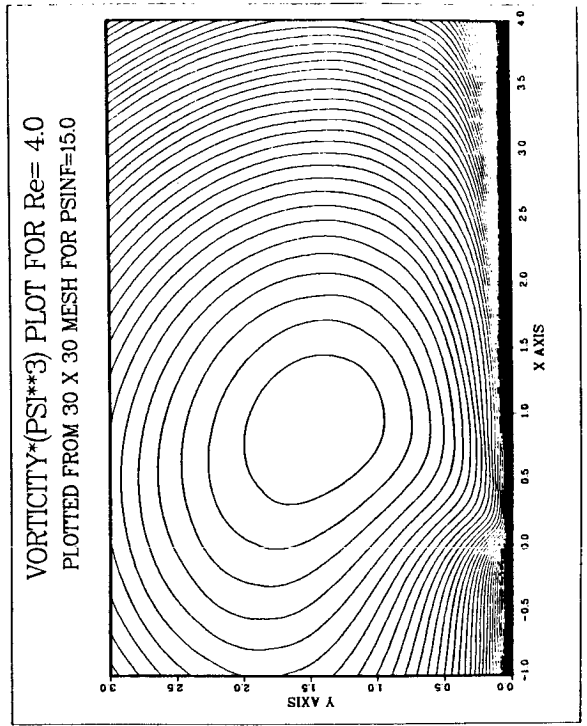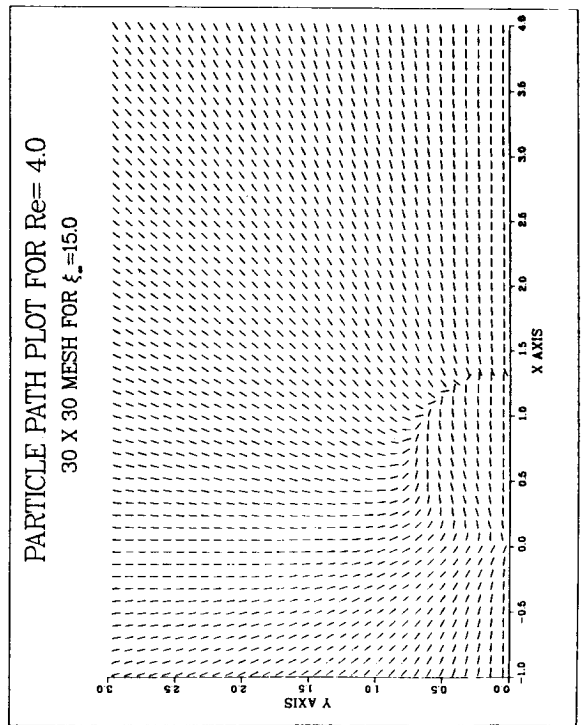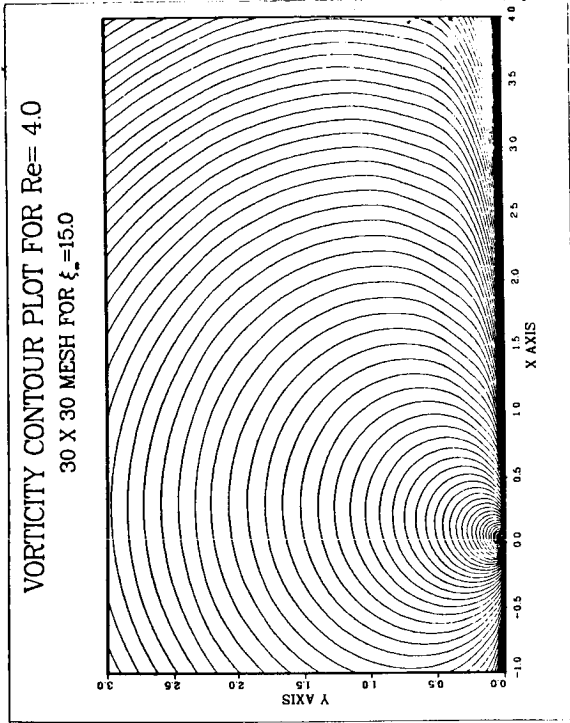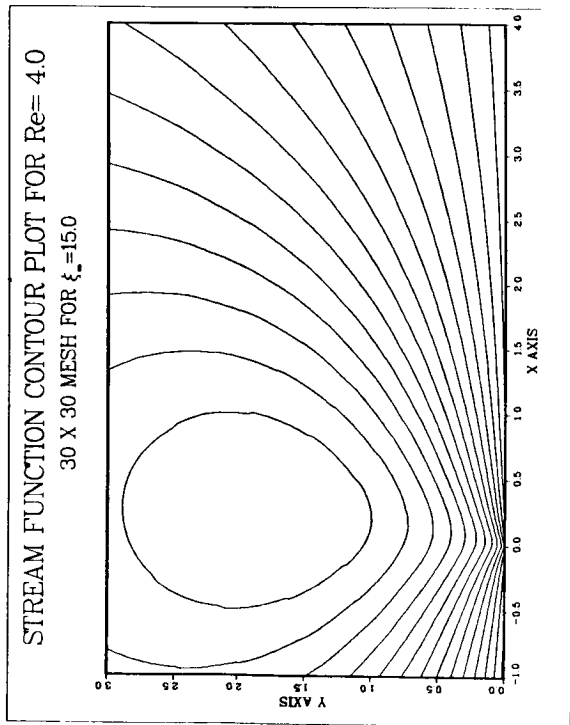
Fig. B-4.   Re = 4.0 For 30 × 30 Mesh at ξ_∞ = 15.0.
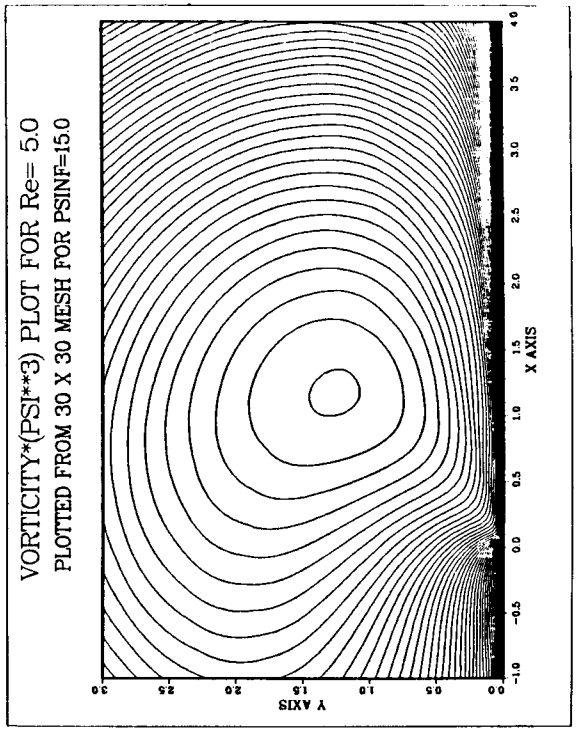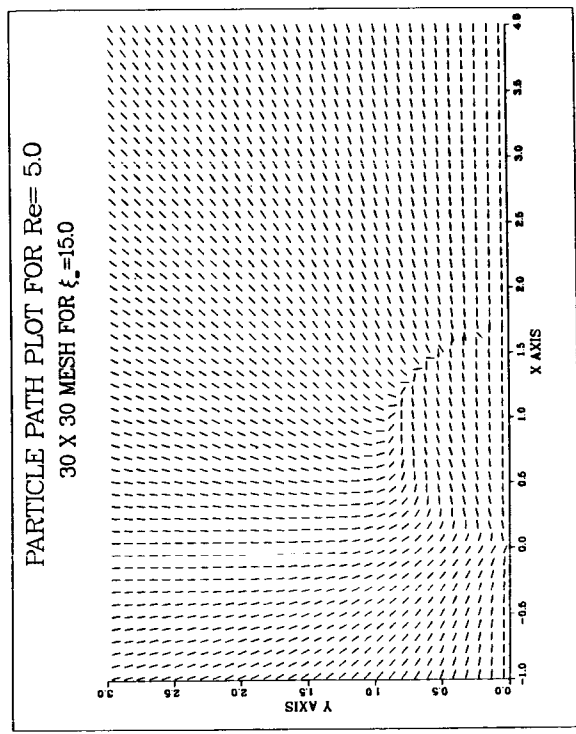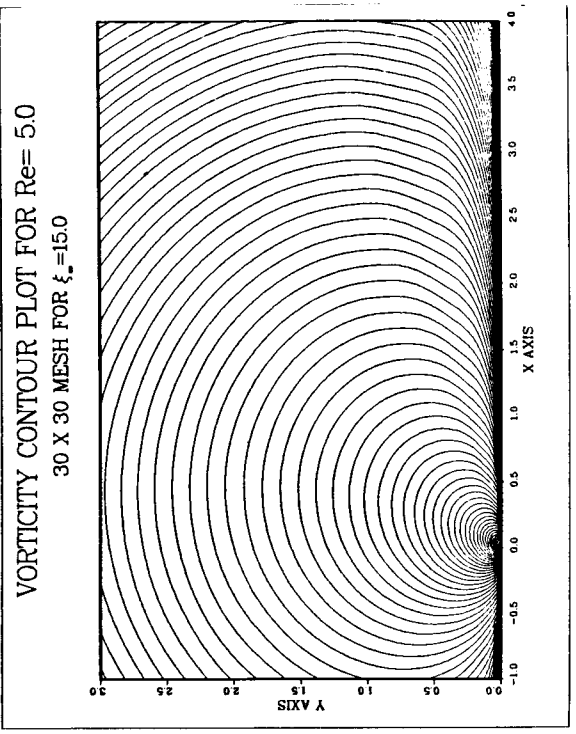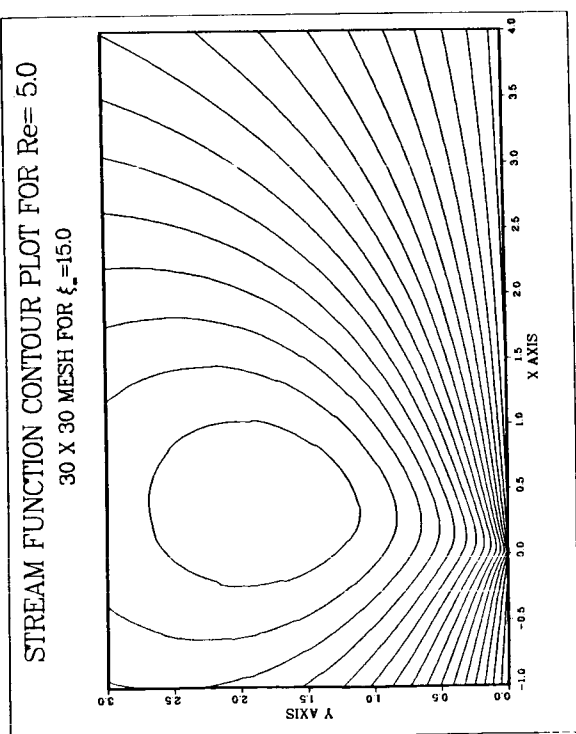
Fig. B-5. Re = 5.0 For 30 × 30 Mesh at ξ_∞ = 15.0.

C-3
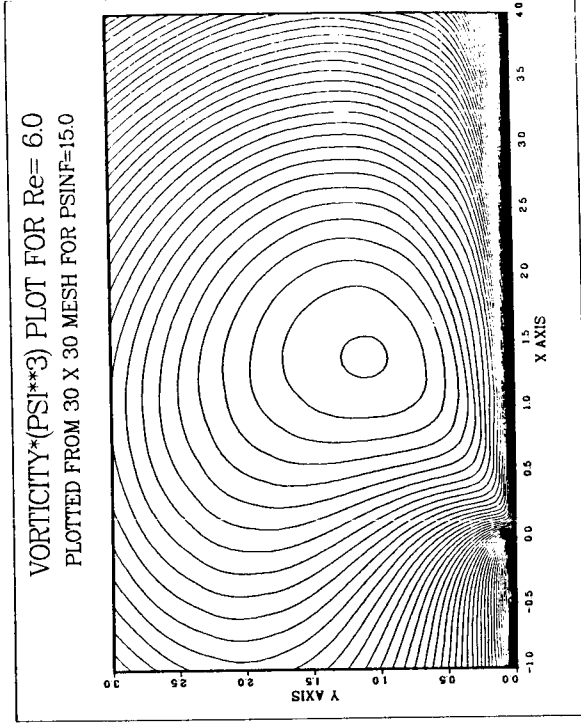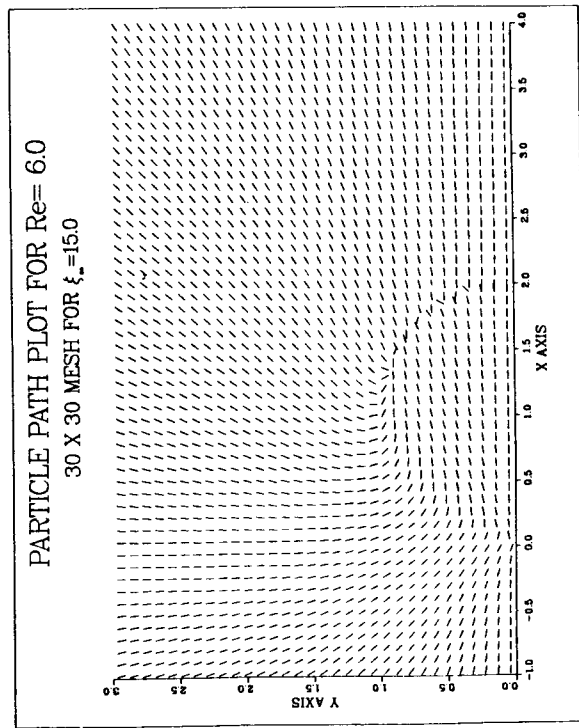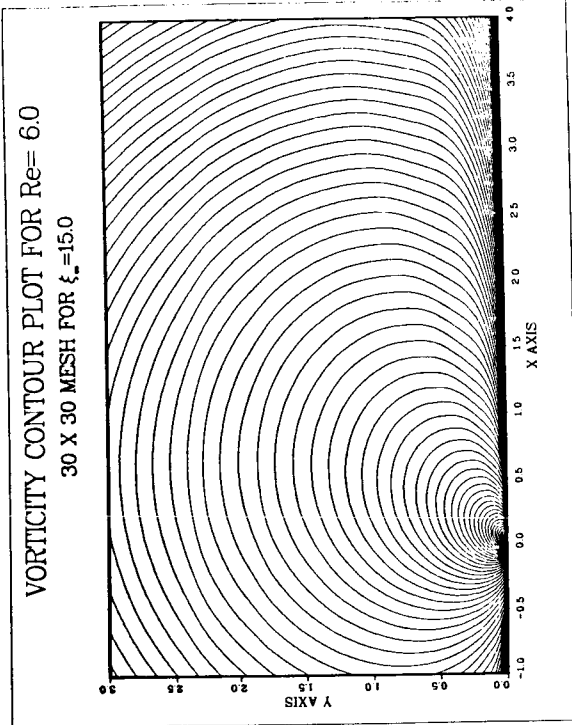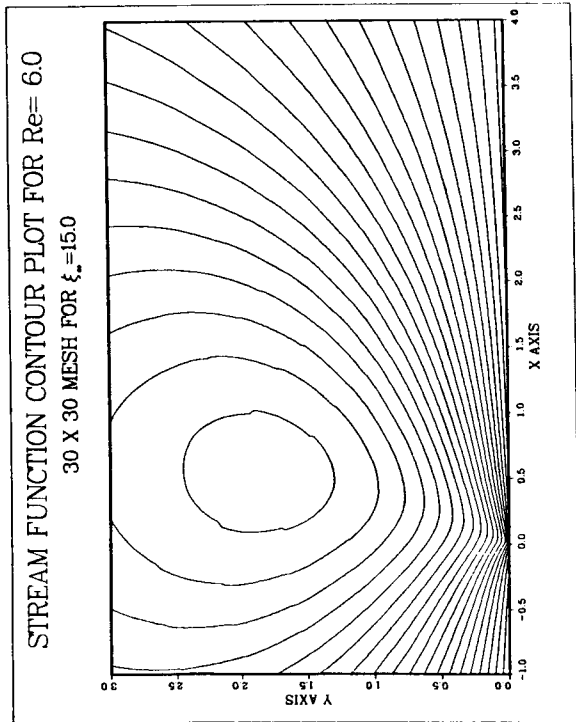
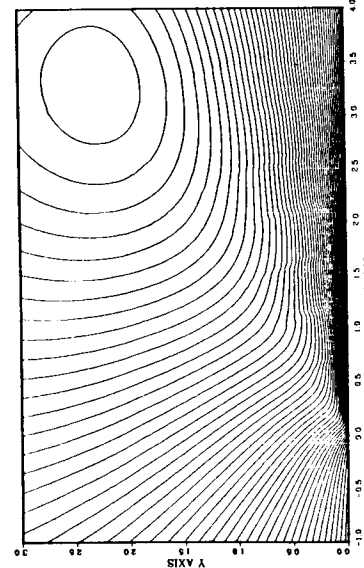Fig. B-6. Re = 6.0 For 30 × 30 Mesh at ξ_∞ = 15.0.

VORTICITY CONTOUR PLOT FOR Re= 7.0
30 X 30 MESH FOR ξ_∞ =15.0

VORTICITY*(PSI**3) PLOT FOR Re= 7.0
PLOTTED FROM 30 X 30 MESH FOR PSINF=15.0

STREAM FUNCTION CONTOUR PLOT FOR Re= 7.0
30 X 30 MESH FOR ξ_∞ =15.0

PARTICLE PATH PLOT FOR Re= 7.0
30 X 30 MESH FOR ξ_∞ =15.0

Fig. B-7. Re = 7.0 For 30 × 30 Mesh at ξ_∞ = 15.0.

STREAM FUNCTION CONTOUR PLOT FOR Re= 8.0
30 X 30 MESH FOR ξ_∞ =15.0

VORTICITY CONTOUR PLOT FOR Re= 8.0
30 X 30 MESH FOR ξ_∞ =15.0

PARTICLE PATH PLOT FOR Re= 8.0
30 X 30 MESH FOR ξ_∞ =15.0

VORTICITY*(PSI**3) PLOT FOR Re= 8.0
PLOTTED FROM 30 X 30 MESH FOR PSINF=15.0

Fig. B-8.   Re = 8.0 For 30 × 30 Mesh at ξ_∞ = 15.0.

VORTICITY CONTOUR PLOT FOR Re= 9.0

30 X 30 MESH FOR ξ_∞ =15.0

VORTICITY*(PSI**3) PLOT FOR Re= 9.0

PLOTTED FROM 30 X 30 MESH FOR PSINF=15.0

STREAM FUNCTION CONTOUR PLOT FOR Re= 9.0

30 X 30 MESH FOR ξ_∞ =15.0

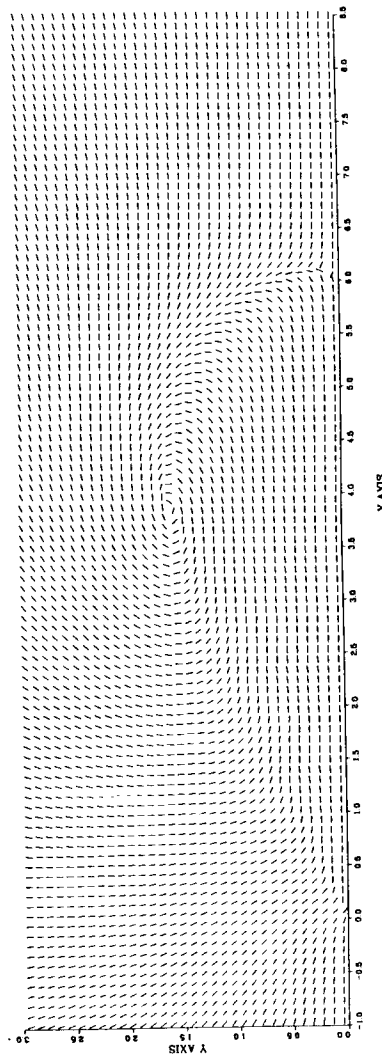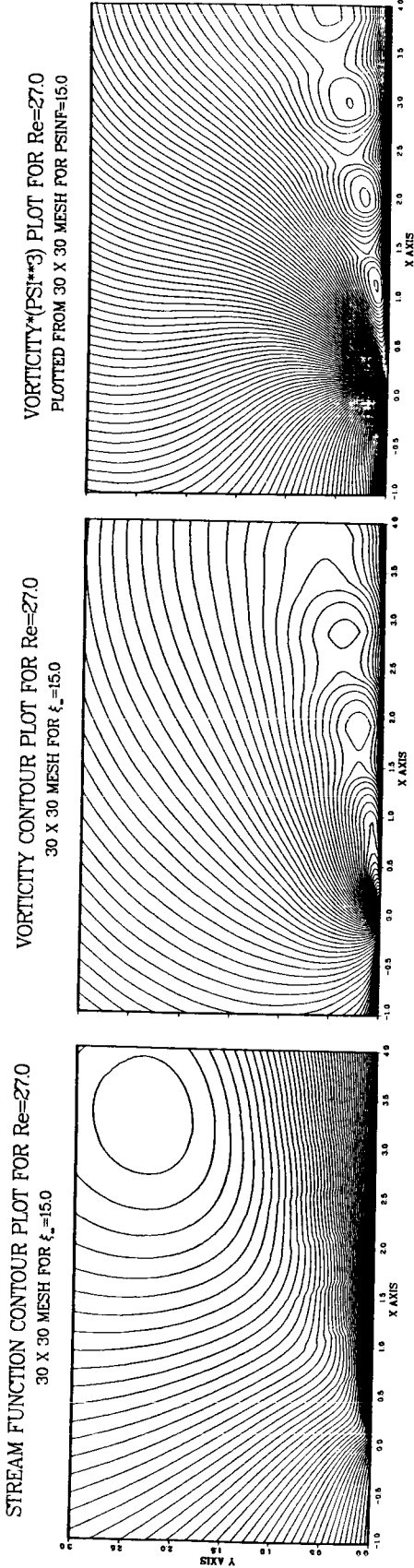PARTICLE PATH PLOT FOR Re= 9.0

30 X 30 MESH FOR ξ_∞ =15.0

Fig. B-9   Re = 9.0   For   30 $\times$ 30 Mesh ξ_∞ = 15.0

VORTICITY CONTOUR PLOT FOR Re=10.0
30 X 30 MESH FOR ξ_∞ =15.0

VORTICITY*(PSI**3) PLOT FOR Re=10.0
PLOTTED FROM 30 X 30 MESH FOR PSINF=15.0

STREAM FUNCTION CONTOUR PLOT FOR Re=10.0
30 X 30 MESH FOR ξ_∞ =15.0

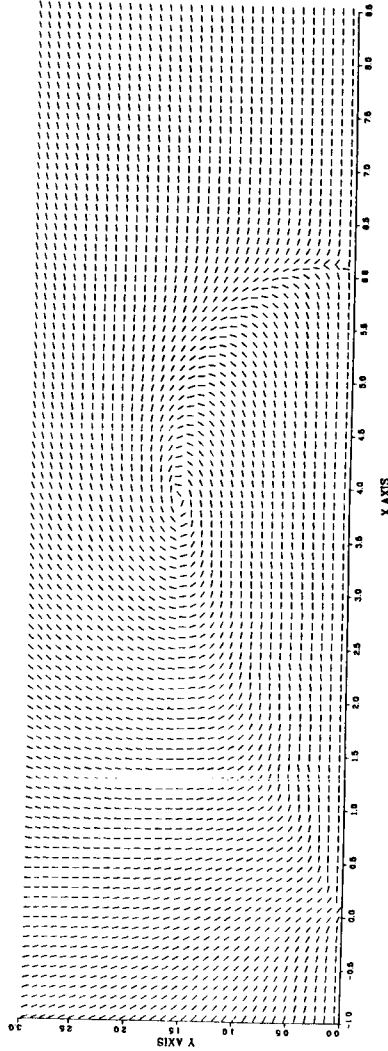PARTICLE PATH PLOT FOR Re=10.0
30 X 30 MESH FOR ξ_∞ =15.0

Fig. B-10.   Re = 10.0 For 30 × 30 Mesh at ξ_∞ = 15.0.

VORTICITY CONTOUR PLOT FOR Re=11.0
30 X 30 MESH FOR ξ_∞=15.0

STREAM FUNCTION CONTOUR PLOT FOR Re=11.0
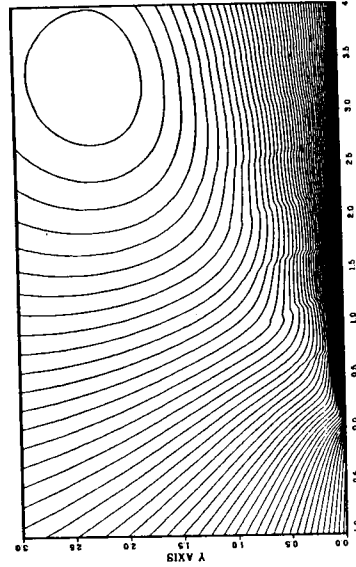30 X 30 MESH FOR ξ_∞=15.0

VORTICITY*(PSI**3) PLOT FOR Re=11.0
PLOTTED FROM 30 X 30 MESH FOR PSINF=15.0

PARTICLE PATH PLOT FOR Re=11.0
30 X 30 MESH FOR ξ_∞=15.0

Fig. B-11. Re = 11.0 For 30 × 30 Mesh at ξ_∞ = 15.0.

STREAM FUNCTION CONTOUR PLOT FOR Re=12.0
30 X 30 MESH FOR ξ_∞ =15.0

VORTICITY CONTOUR PLOT FOR Re=12.0
30 X 30 MESH FOR ξ_∞ =15.0

VORTICITY*(PSI**3) PLOT FOR Re=12.0
PLOTTED FROM 30 X 30 MESH FOR PSINF=15.0
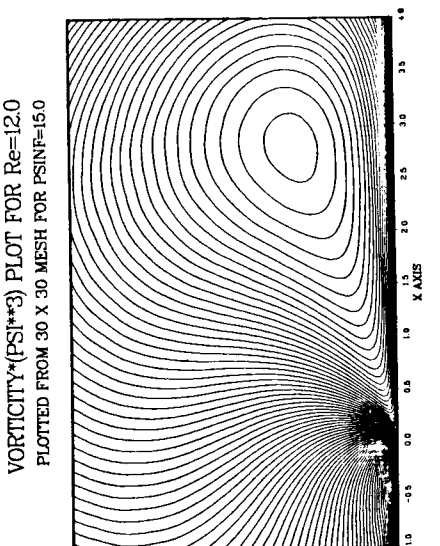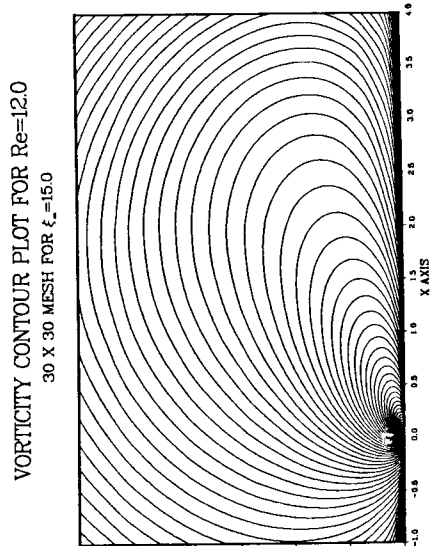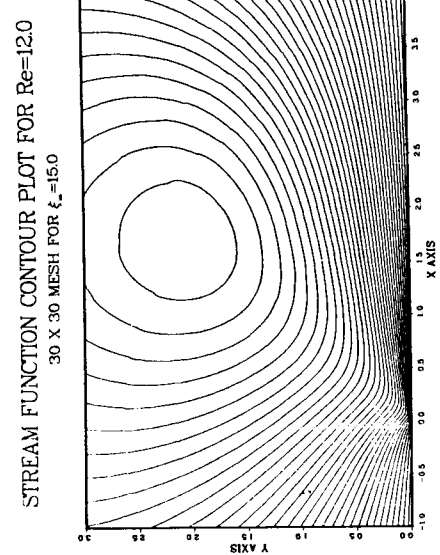
PARTICLE PATH PLOT FOR Re=12.0
30 X 30 MESH FOR ξ_∞ =15.0
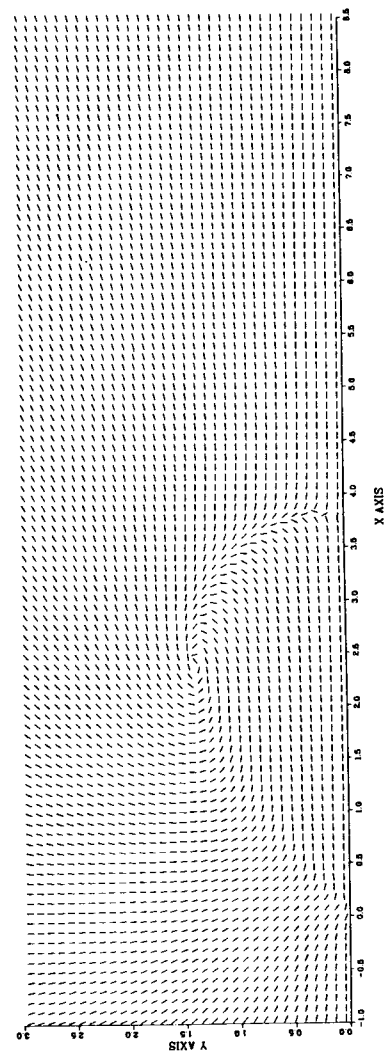
Fig. B-12. Re = 12.0 For 30 × 30 Mesh at ξ_∞ = 15.0.

STREAM FUNCTION CONTOUR PLOT FOR Re=13.0
30 X 30 MESH FOR ξ_∞ =15.0
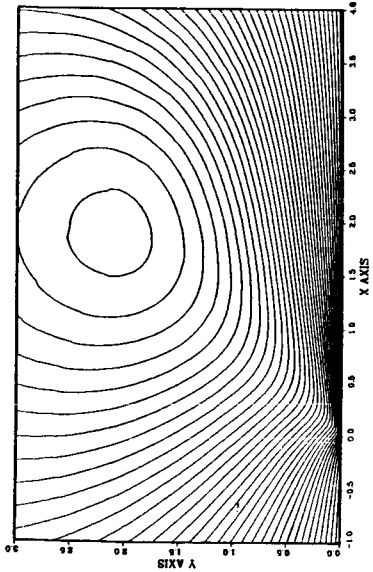
VORTICITY CONTOUR PLOT FOR Re=13.0
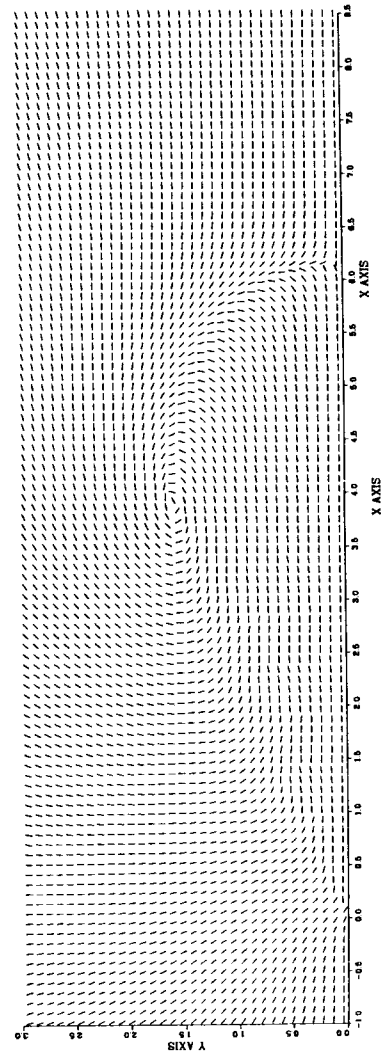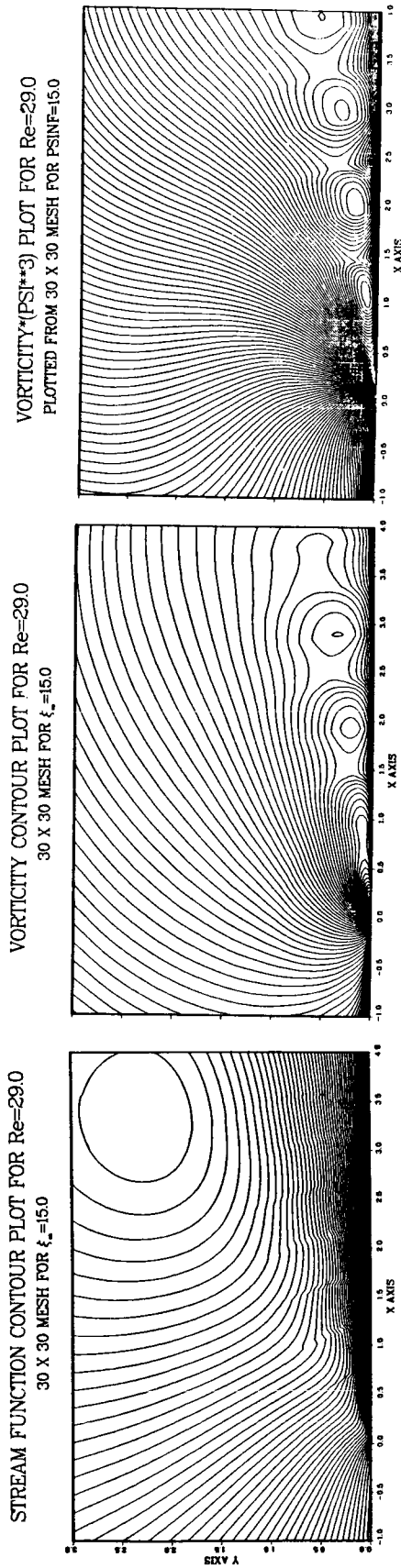30 X 30 MESH FOR ξ_∞ =15.0
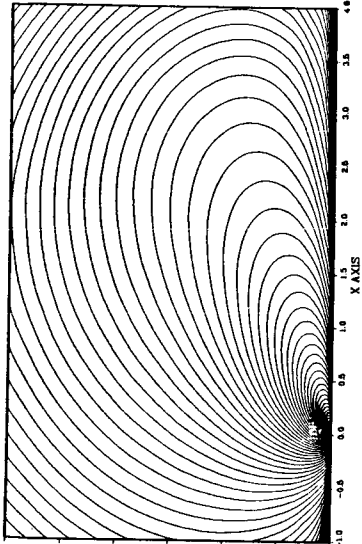
VORTICITY*(PSI**3) PLOT FOR Re=13.0
PLOTTED FROM 30 X 30 MESH FOR PSINF=15.0
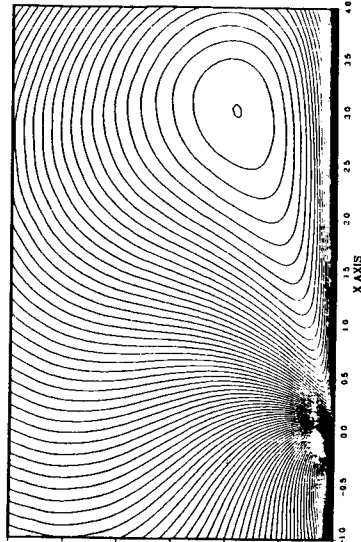
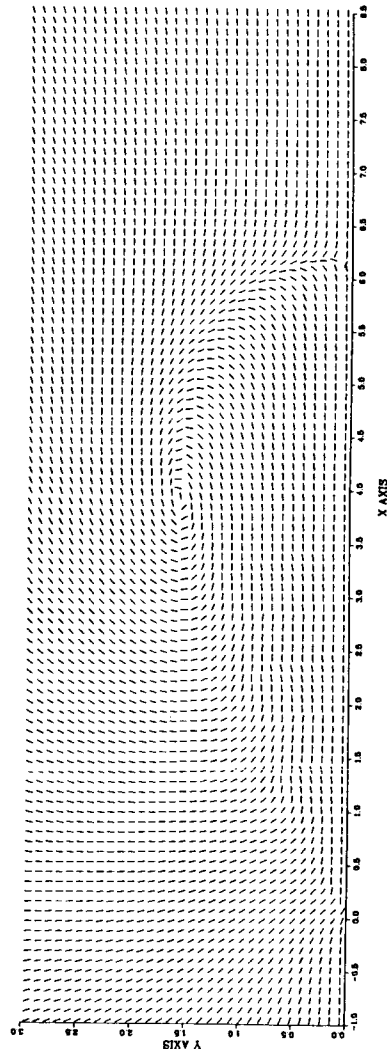PARTICLE PATH PLOT FOR Re=13.0
30 X 30 MESH FOR ξ_∞ =15.0
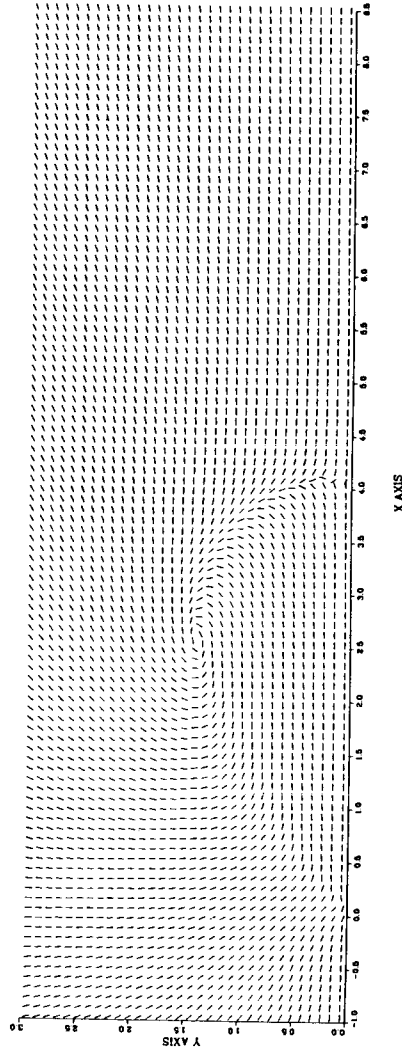
Fig. B-13.   Re = 13.0 For 30 × 30 Mesh at ξ_∞ = 15.0.

STREAM FUNCTION CONTOUR PLOT FOR Re=14.0
30 X 30 MESH FOR ξ_∞=15.0

VORTICITY CONTOUR PLOT FOR Re=14.0
30 X 30 MESH FOR ξ_∞=15.0

VORTICITY*(PSI**3) PLOT FOR Re=14.0
PLOTTED FROM 30 X 30 MESH FOR PSINF=15.0
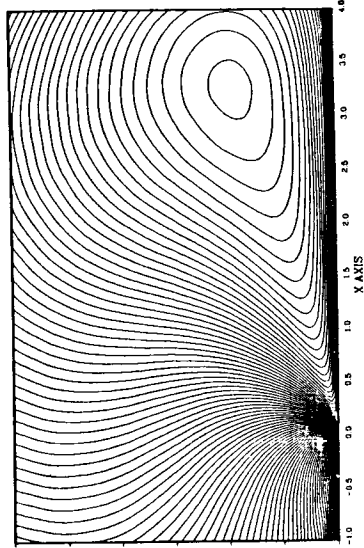
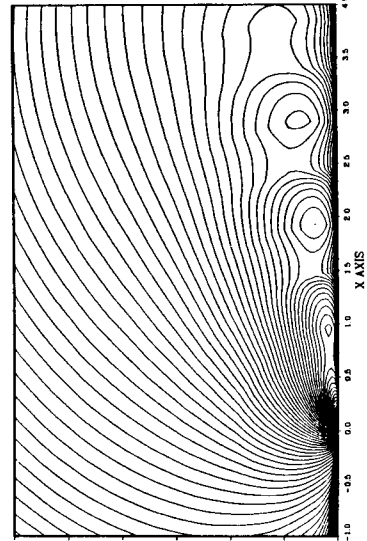PARTICLE PATH PLOT FOR Re=14.0
30 X 30 MESH FOR ξ_∞=15.0
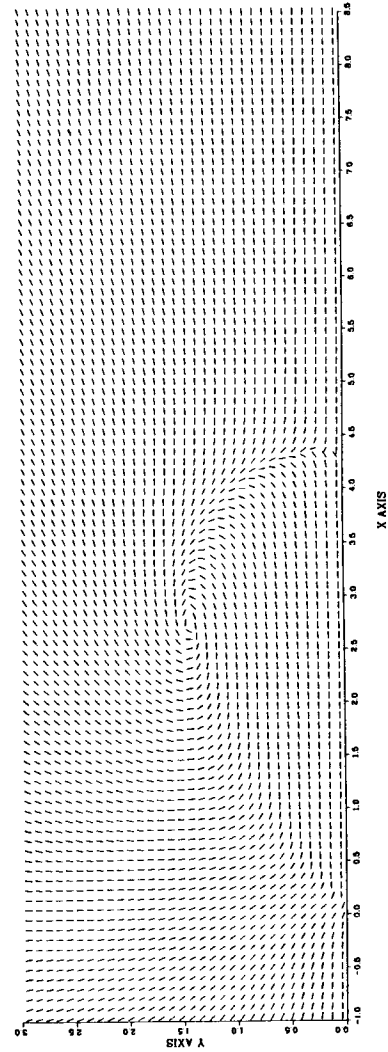
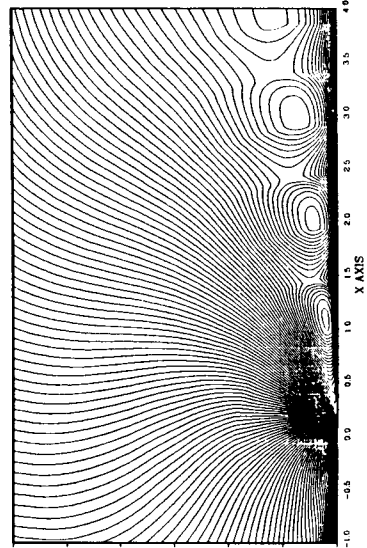**Fig. B-14.** Re = 14.0 For 30 × 30 Mesh at ξ_∞ = 15.0.

STREAM FUNCTION CONTOUR PLOT FOR Re=15.0
30 X 30 MESH FOR ξ_∞=15.0
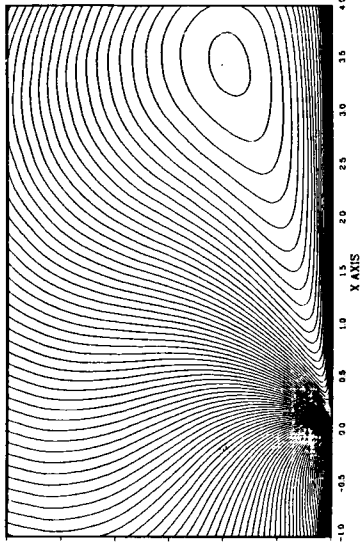
VORTICITY CONTOUR PLOT FOR Re=15.0
30 X 30 MESH FOR ξ_∞=15.0

VORTICITY*(PSI**3) PLOT FOR Re=15.0
PLOTTED FROM 30 X 30 MESH FOR PSINF=15.0

PARTICLE PATH PLOT FOR Re=15.0
30 X 30 MESH FOR ξ_∞=15.0

Fig. B-15.   Re = 15.0 For 30 $\times$ 30 Mesh at ξ_∞ = 15.0.

STREAM FUNCTION CONTOUR PLOT FOR Re=16.0
30 X 30 MESH FOR ξ_∞=15.0
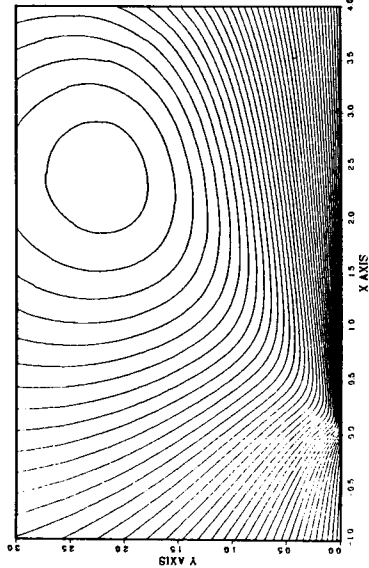
VORTICITY CONTOUR PLOT FOR Re=16.0
30 X 30 MESH FOR ξ_∞=15.0
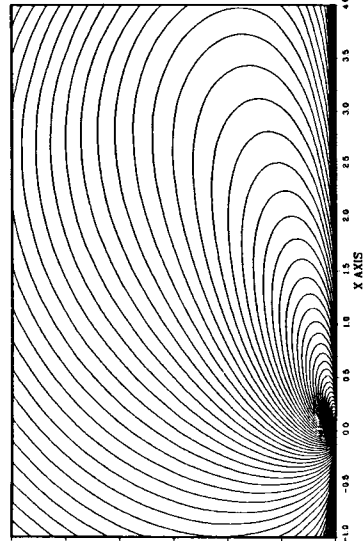
VORTICITY*(PSI**3) PLOT FOR Re=16.0
PLOTTED FROM 30 X 30 MESH FOR PSINF=15.0
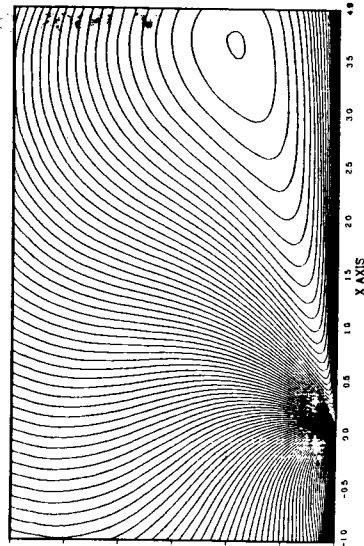
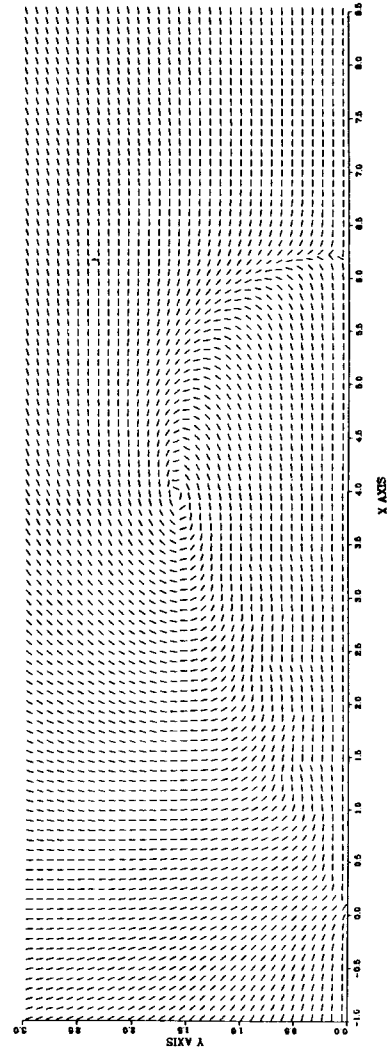PARTICLE PATH PLOT FOR Re=16.0
30 X 30 MESH FOR ξ_∞=15.0
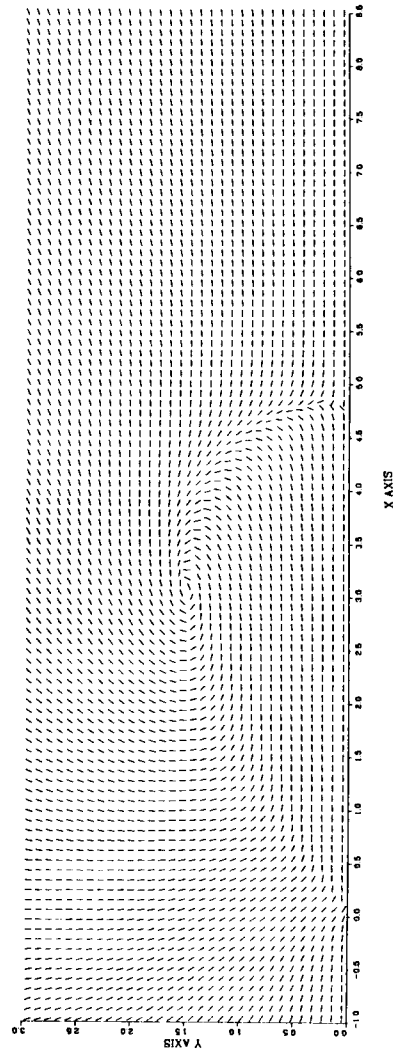
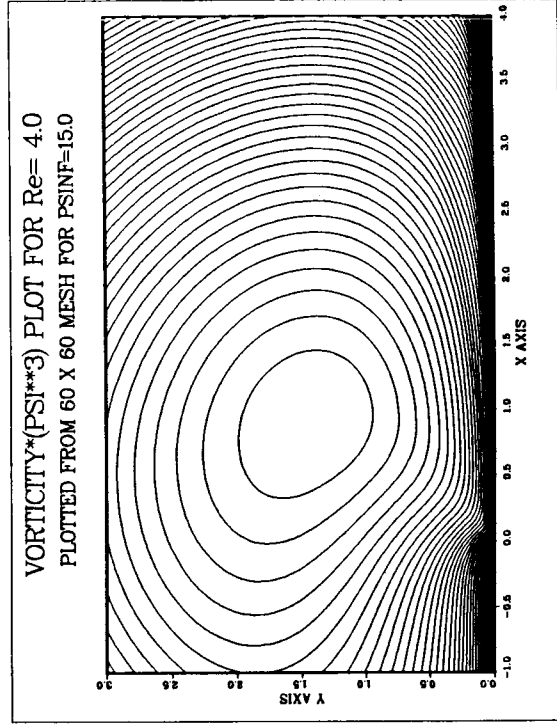Fig. B-16.   Re = 16.0 For   30 × 30 Mesh at ξ_∞ = 15.0.

VORTICITY*(PSI**3) PLOT FOR Re=17.0
PLOTTED FROM 30 X 30 MESH FOR PSINF=15.0
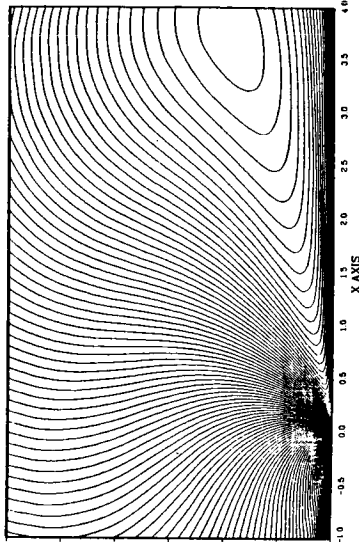
VORTICITY CONTOUR PLOT FOR Re=17.0
30 X 30 MESH FOR ξ_∞=15.0
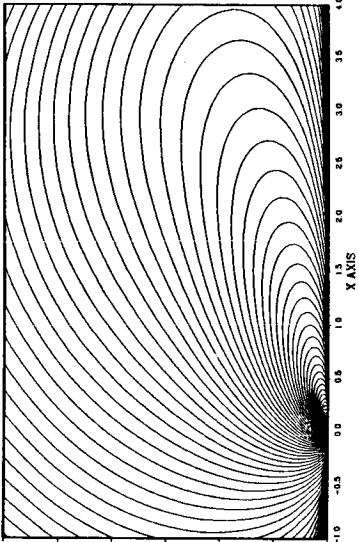
STREAM FUNCTION CONTOUR PLOT FOR Re=17.0
30 X 30 MESH FOR ξ_∞=15.0
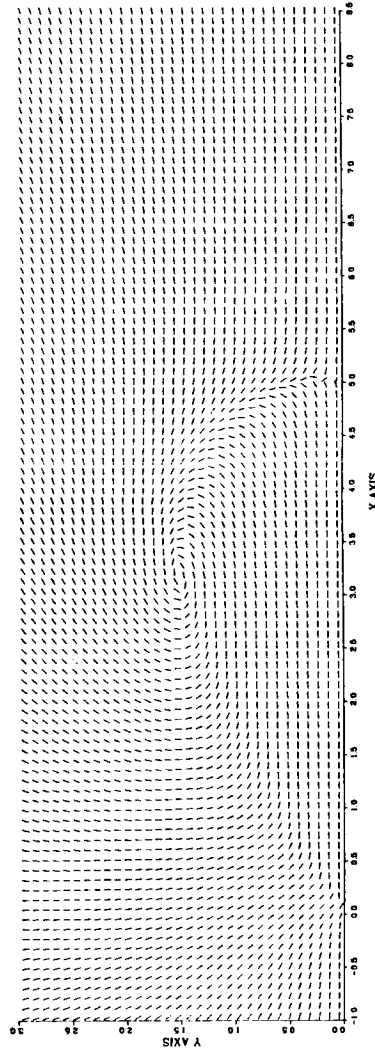
PARTICLE PATH PLOT FOR Re=17.0
30 X 30 MESH FOR ξ_∞=15.0
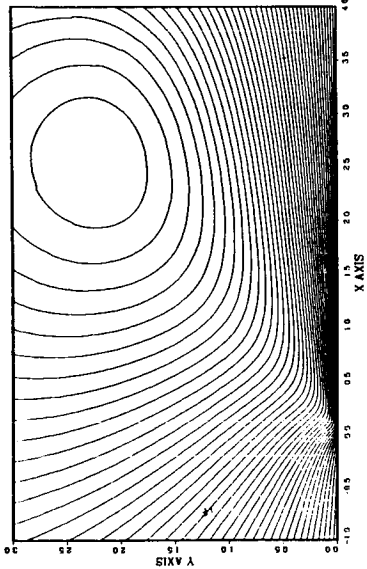
Fig. B-17. Re = 17.0 For 30 × 30 Mesh at ξ_∞ = 15.0.

STREAM FUNCTION CONTOUR PLOT FOR Re=18.0
30 X 30 MESH FOR ξ_∞=15.0
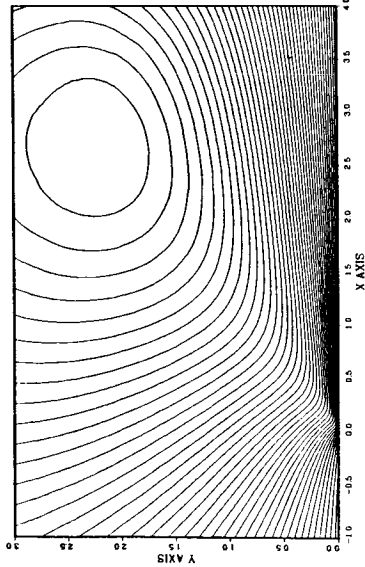
VORTICITY CONTOUR PLOT FOR Re=18.0
30 X 30 MESH FOR ξ_∞=15.0
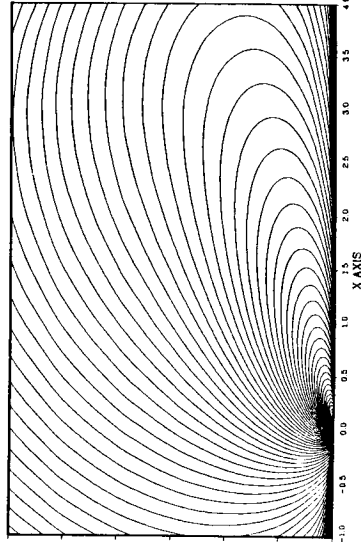
VORTICITY*(PSI**3) PLOT FOR Re=18.0
PLOTTED FROM 30 X 30 MESH FOR PSINF=15.0
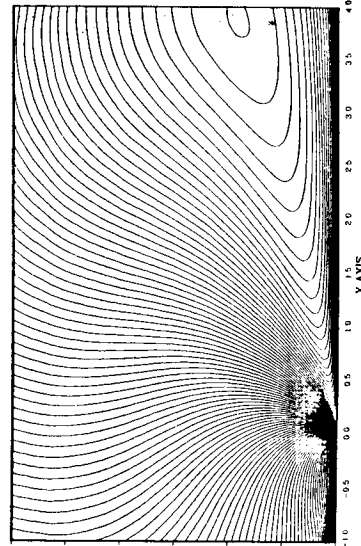
PARTICLE PATH PLOT FOR Re=18.0
30 X 30 MESH FOR ξ_∞=15.0
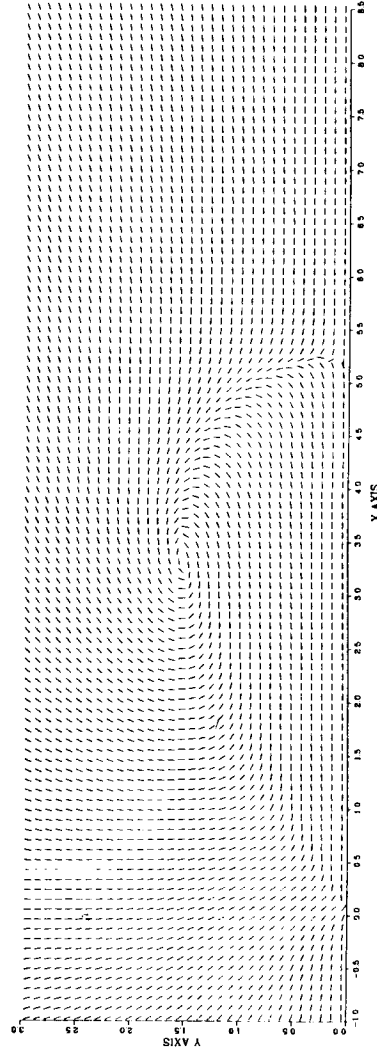
Fig. B-18. $Re = 18.0$ For 30×30 Mesh at $\xi_\infty = 15.0.$

STREAM FUNCTION CONTOUR PLOT FOR Re=19.0
30 X 30 MESH FOR ξ_∞=15.0

VORTICITY CONTOUR PLOT FOR Re=19.0
30 X 30 MESH FOR ξ_∞=15.0

VORTICITY*(PSI**3) PLOT FOR Re=19.0
PLOTTED FROM 30 X 30 MESH FOR PSINF=15.0
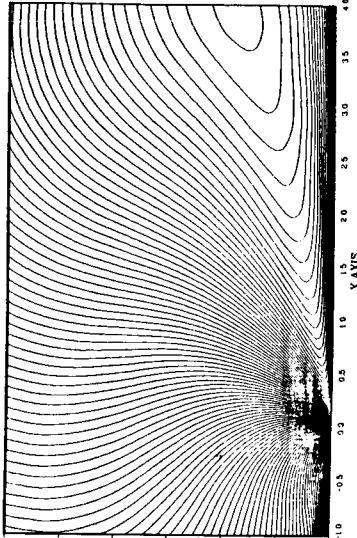
PARTICLE PATH PLOT FOR Re=19.0
30 X 30 MESH FOR ξ_∞=15.0

Fig. B-19. Re = 19.0 For 30 × 30 Mesh at ξ_∞ = 15.0.

STREAM FUNCTION CONTOUR PLOT FOR Re=20.0
30 X 30 MESH FOR ξ_∞ =15.0

VORTICITY CONTOUR PLOT FOR Re=20.0
30 X 30 MESH FOR ξ_∞ =15.0

VORTICITY*(PSI**3) PLOT FOR Re=20.0
PLOTTED FROM 30 X 30 MESH FOR PSINF=15.0
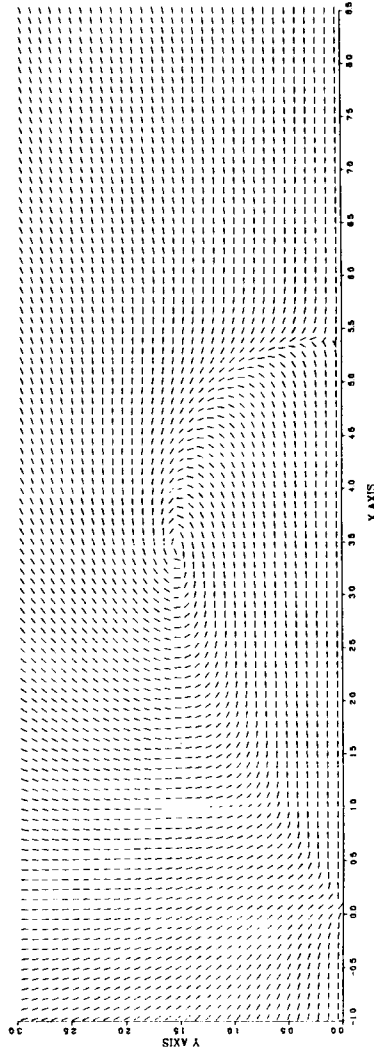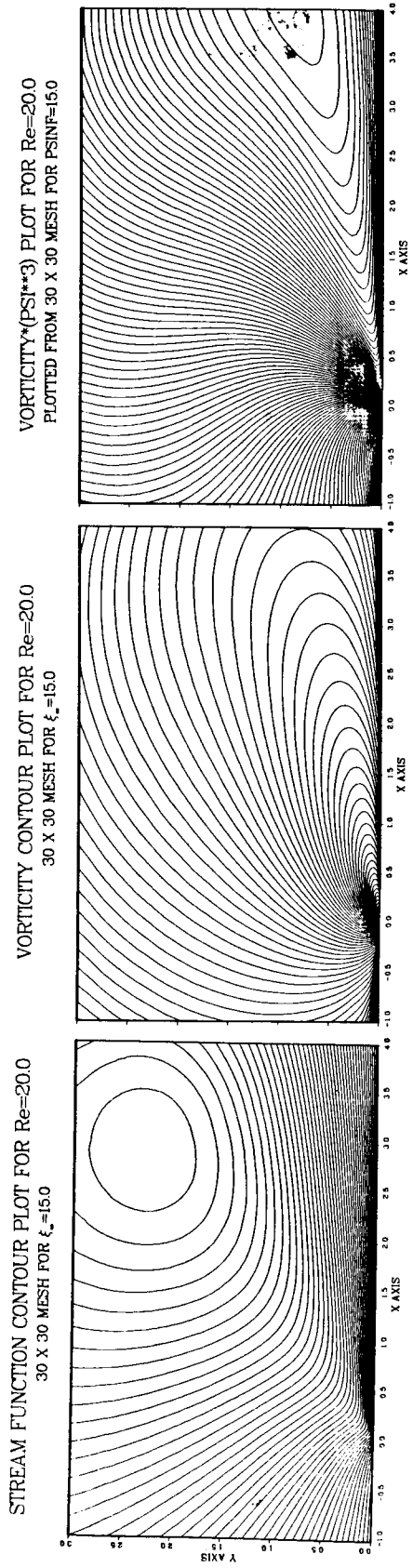
PARTICLE PATH PLOT FOR Re=20.0
30 X 30 MESH FOR ξ_∞ =15.0
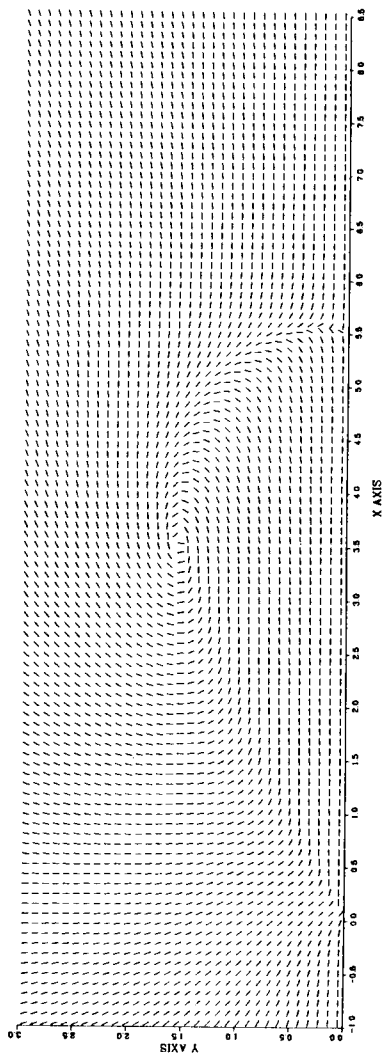
Fig. B-20. Re = 20.0 For 30 × 30 Mesh at ξ_∞ = 15.0.

STREAM FUNCTION CONTOUR PLOT FOR Re=21.0
30 X 30 MESH FOR ξ_∞=15.0
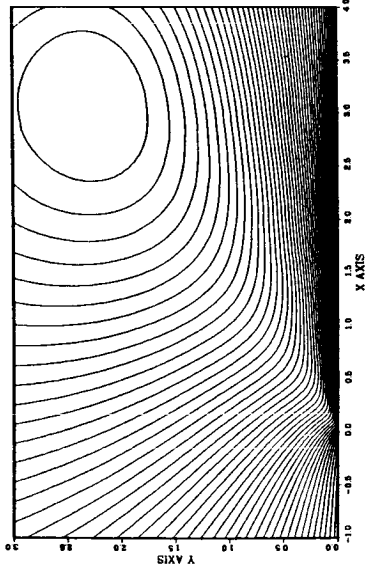
VORTICITY CONTOUR PLOT FOR Re=21.0
30 X 30 MESH FOR ξ_∞=15.0
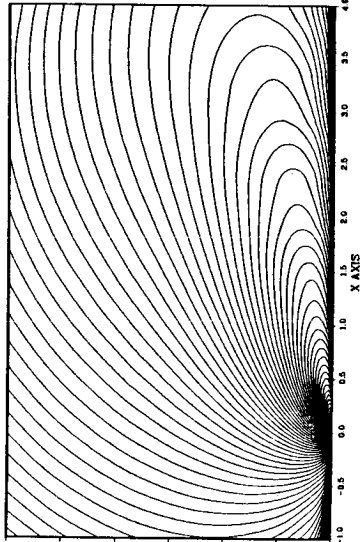
VORTICITY*(PSI**3) PLOT FOR Re=21.0
PLOTTED FROM 30 X 30 MESH FOR PSINF=15.0
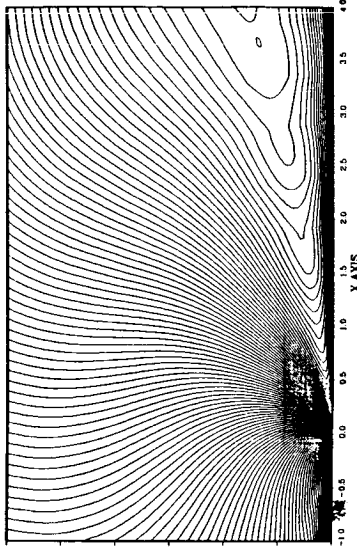
PARTICLE PATH PLOT FOR Re=21.0
30 X 30 MESH FOR ξ_∞=15.0
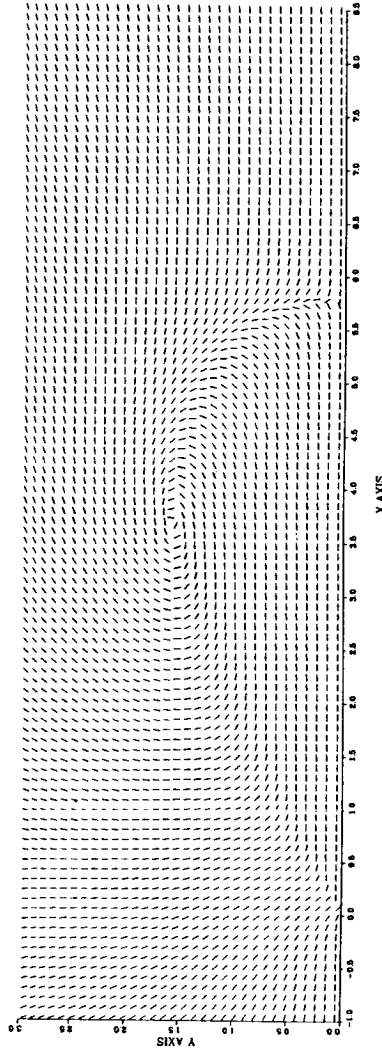
Fig. B-21. Re = 21.0 For 30 × 30 Mesh at ξ_∞ = 15.0.

STREAM FUNCTION CONTOUR PLOT FOR Re=22.0
30 X 30 MESH FOR ξ_∞=15.0

VORTICITY CONTOUR PLOT FOR Re=22.0
30 X 30 MESH FOR ξ_∞=15.0

VORTICITY*(PSI**3) PLOT FOR Re=22.0
PLOTTED FROM 30 X 30 MESH FOR PSINF=15.0
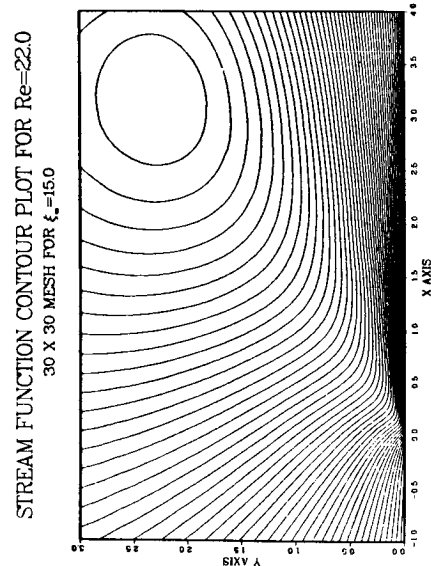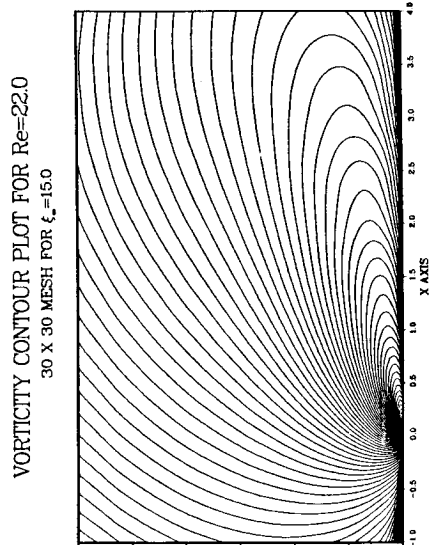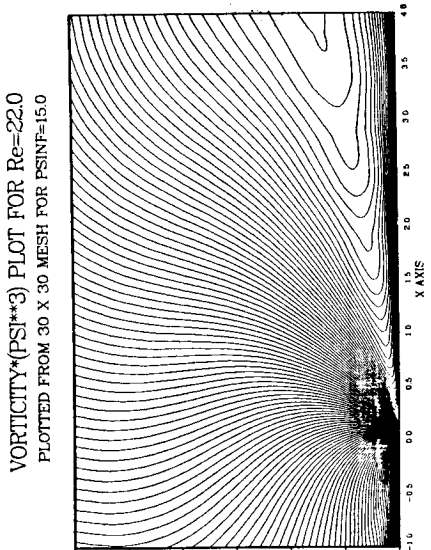
PARTICLE PATH PLOT FOR Re=22.0
30 X 30 MESH FOR ξ_∞=15.0
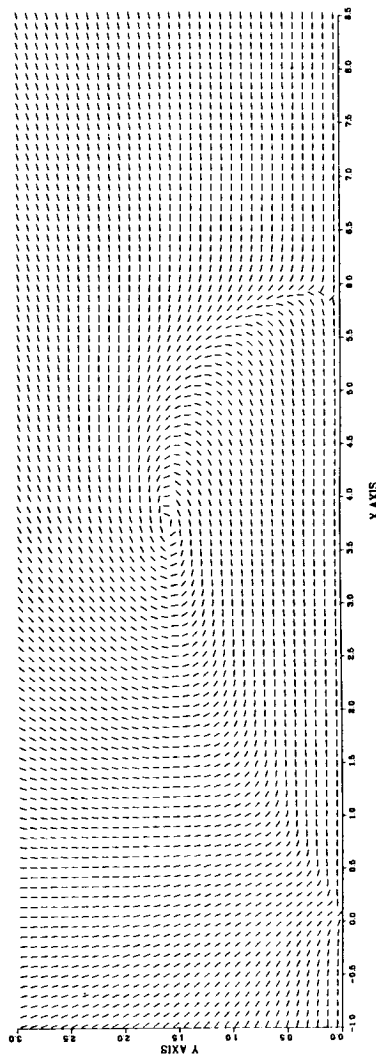
Fig. B-22. Re = 22.0 For 30 × 30 Mesh at ξ_∞ = 15.0.
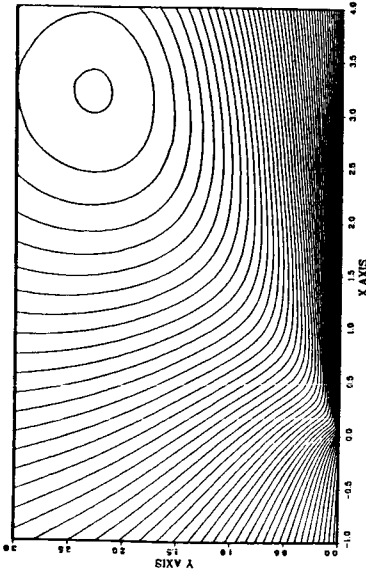
STREAM FUNCTION CONTOUR PLOT FOR Re=23.0
30 X 30 MESH FOR ξ_∞ =15.0

VORTICITY CONTOUR PLOT FOR Re=23.0
30 X 30 MESH FOR ξ_∞ =15.0
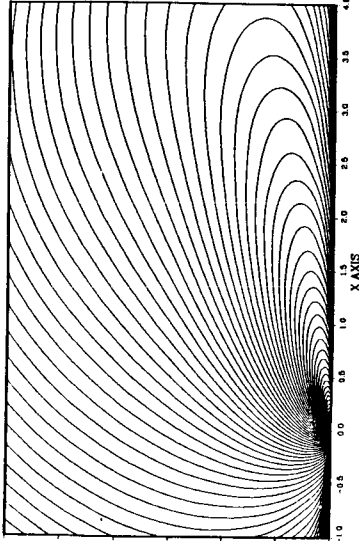
VORTICITY*(PSI**3) PLOT FOR Re=23.0
PLOTTED FROM 30 X 30 MESH FOR PSINF=15.0
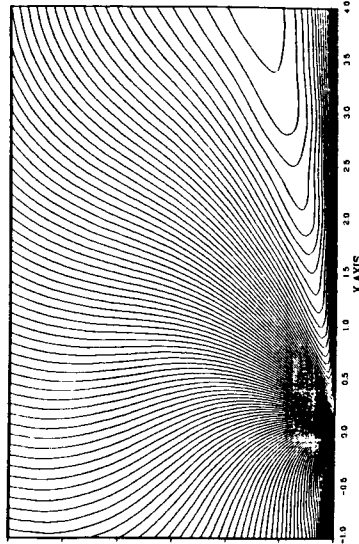
PARTICLE PATH PLOT FOR Re=23.0
30 X 30 MESH FOR ξ_∞ =15.0
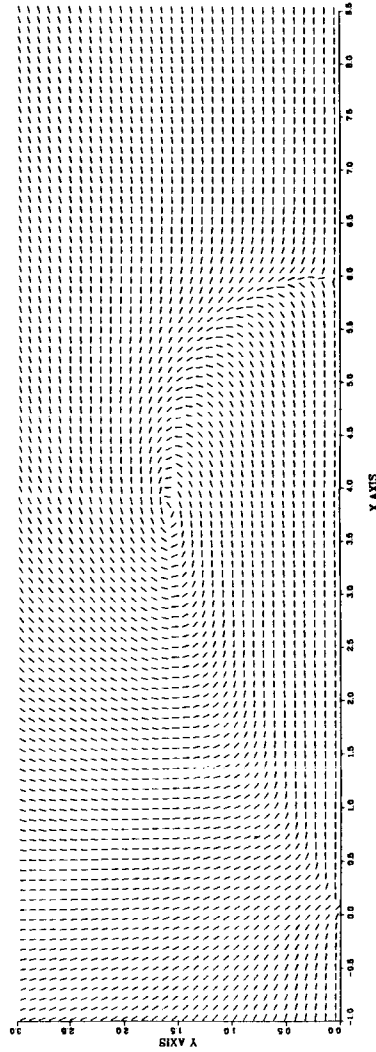
Fig. B-23. Re = 23.0 For 30 × 30 Mesh at ξ_∞ = 15.0.

STREAM FUNCTION CONTOUR PLOT FOR Re=24.0
30 X 30 MESH FOR ξ_∞=15.0

VORTICITY CONTOUR PLOT FOR Re=24.0
30 X 30 MESH FOR ξ_∞=15.0

VORTICITY*(PSI**3) PLOT FOR Re=24.0
PLOTTED FROM 30 X 30 MESH FOR PSINF=15.0
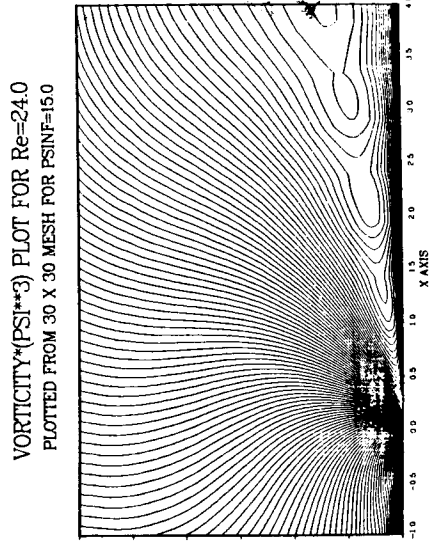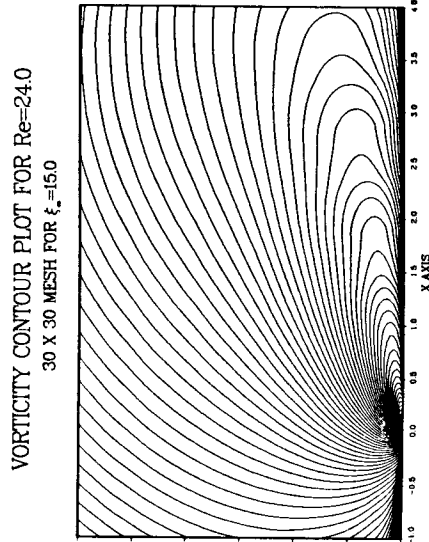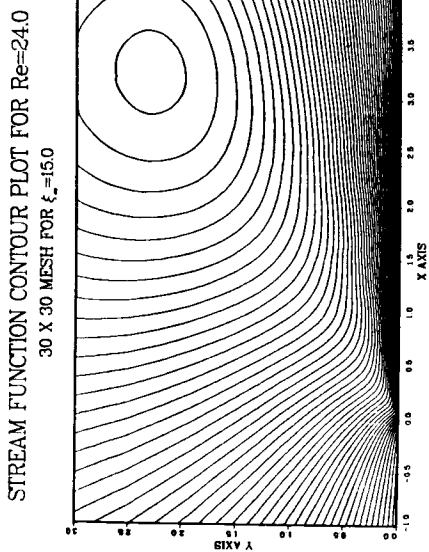
PARTICLE PATH PLOT FOR Re=24.0
30 X 30 MESH FOR ξ_∞=15.0
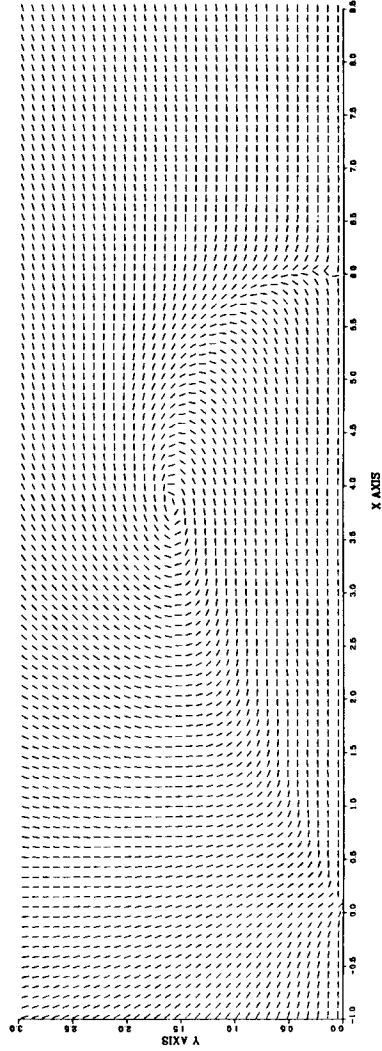
Fig. B-24. $Re = 24.0$ For 30×30 Mesh at $\xi_\infty = 15.0$.

STREAM FUNCTION CONTOUR PLOT FOR Re=25.0
30 X 30 MESH FOR ξ_∞=15.0
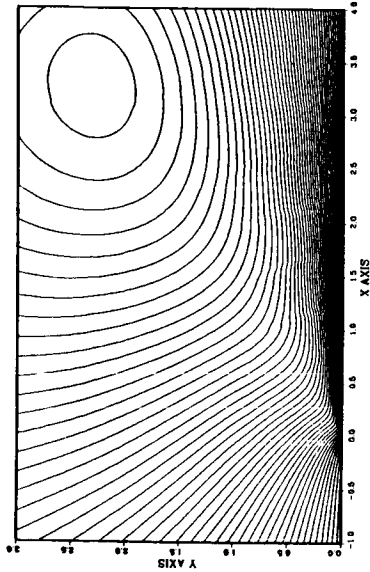
VORTICITY CONTOUR PLOT FOR Re=25.0
30 X 30 MESH FOR ξ_∞=15.0
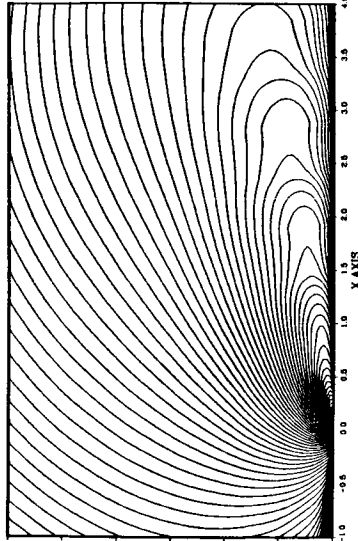
VORTICITY*(PSI**3) PLOT FOR Re=25.0
PLOTTED FROM 30 X 30 MESH FOR PSINF=15.0

PARTICLE PATH PLOT FOR Re=25.0
30 X 30 MESH FOR ξ_∞=15.0

Fig. B-25. Re = 25.0 For 30 × 30 Mesh at ξ_∞ = 15.0.

STREAM FUNCTION CONTOUR PLOT FOR Re=26.0
30 X 30 MESH FOR ξ_∞=15.0

VORTICITY CONTOUR PLOT FOR Re=26.0
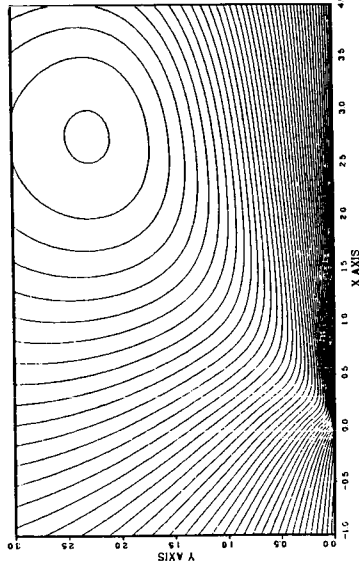30 X 30 MESH FOR ξ_∞=15.0

VORTICITY*(PSI**3) PLOT FOR Re=26.0
PLOTTED FROM 30 X 30 MESH FOR PSINF=15.0
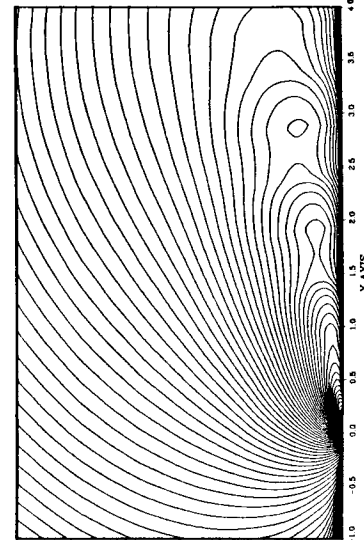
PARTICLE PATH PLOT FOR Re=26.0
30 X 30 MESH FOR ξ_∞=15.0

Fig. B-26. Re = 26.0 For 30 × 30 Mesh at ξ_∞ = 15.0.

STREAM FUNCTION CONTOUR PLOT FOR Re=27.0
30 X 30 MESH FOR ξ_∞ =15.0

VORTICITY CONTOUR PLOT FOR Re=27.0
30 X 30 MESH FOR ξ_∞ =15.0

VORTICITY*(PSI**3) PLOT FOR Re=27.0
PLOTTED FROM 30 X 30 MESH FOR PSINF=15.0

PARTICLE PATH PLOT FOR Re=27.0
30 X 30 MESH FOR ξ_∞ =15.0

Fig. B-27. Re = 27.0 For 30 × 30 Mesh at ξ_∞ = 15.0.

STREAM FUNCTION CONTOUR PLOT FOR Re=28.0
30 X 30 MESH FOR ξ_∞ =15.0

VORTICITY CONTOUR PLOT FOR Re=28.0
30 X 30 MESH FOR ξ_∞ =15.0

VORTICITY*(PSI**3) PLOT FOR Re=28.0
PLOTTED FROM 30 X 30 MESH FOR PSINF=15.0
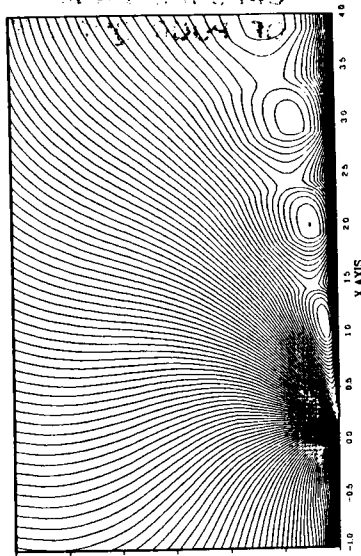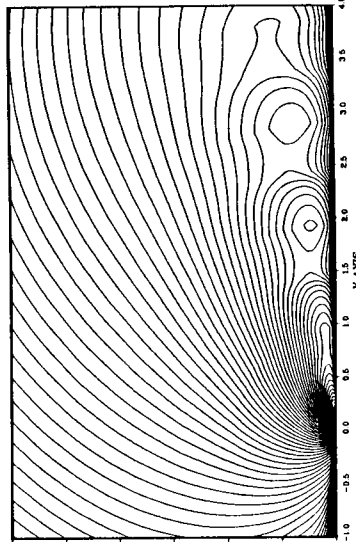
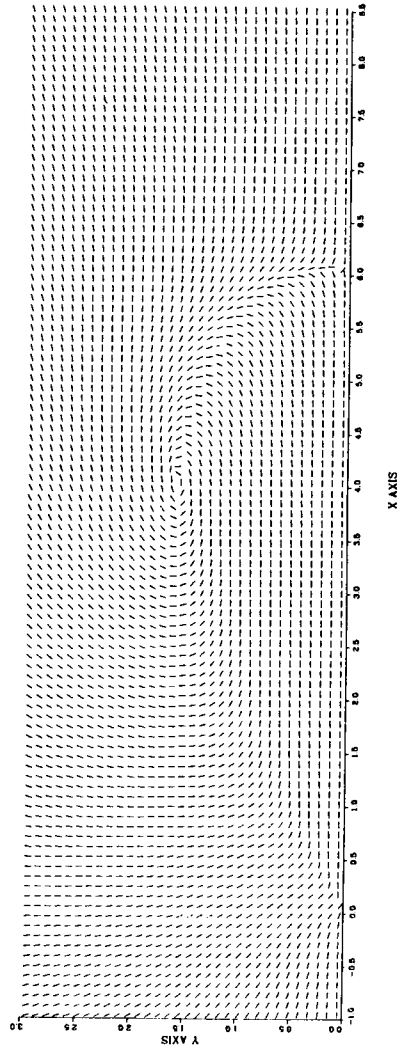PARTICLE PATH PLOT FOR Re=28.0
30 X 30 MESH FOR ξ_∞ =15.0

Fig. B-28. Re = 28.0 For 30 × 30 Mesh at ξ_∞ = 15.0.

STREAM FUNCTION CONTOUR PLOT FOR Re=29.0
30 X 30 MESH FOR ξ_∞=15.0

VORTICITY CONTOUR PLOT FOR Re=29.0
30 X 30 MESH FOR ξ_∞=15.0

VORTICITY*(PSI**3) PLOT FOR Re=29.0
PLOTTED FROM 30 X 30 MESH FOR PSINF=15.0
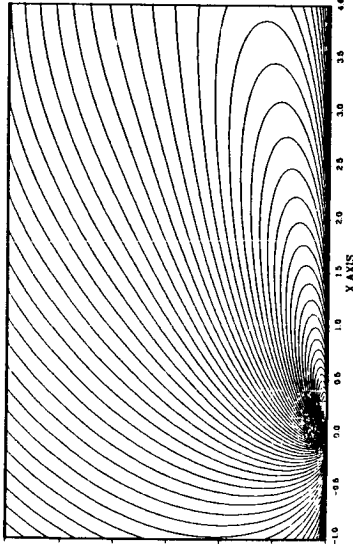
PARTICLE PATH PLOT FOR Re=29.0
30 X 30 MESH FOR ξ_∞=15.0

**Fig. B-29. Re = 29.0 For 30 × 30 Mesh at ξ_∞ = 15.0.**
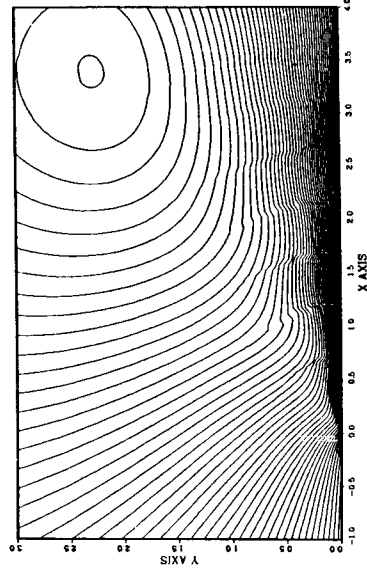
STREAM FUNCTION CONTOUR PLOT FOR Re=30.0
30 X 30 MESH FOR ξ_∞ =15.0

VORTICITY CONTOUR PLOT FOR Re=30.0
30 X 30 MESH FOR ξ_∞ =15.0

VORTICITY*(PSI**3) PLOT FOR Re=30.0
PLOTTED FROM 30 X 30 MESH FOR PSINF=15.0

PARTICLE PATH PLOT FOR Re=30.0
30 X 30 MESH FOR ξ_∞ =15.0

Fig. B-30.   Re = 30.0 For 30 × 30 Mesh at ξ_∞ = 15.0.

VORTICITY CONTOUR PLOT FOR Re= 4.0
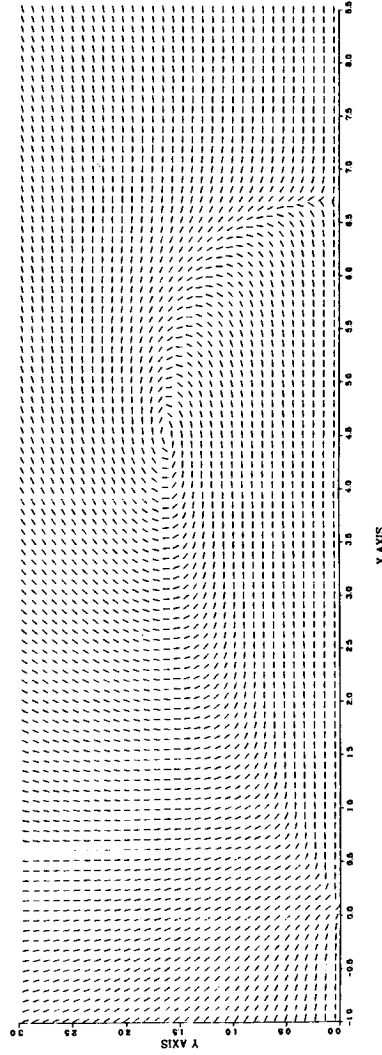
60 X 60 MESH FOR ξ_∞ =15.0

STREAM FUNCTION CONTOUR PLOT FOR Re= 4.0

60 X 60 MESH FOR ξ_∞ =15.0

VORTICITY*(PSI**3) PLOT FOR Re= 4.0
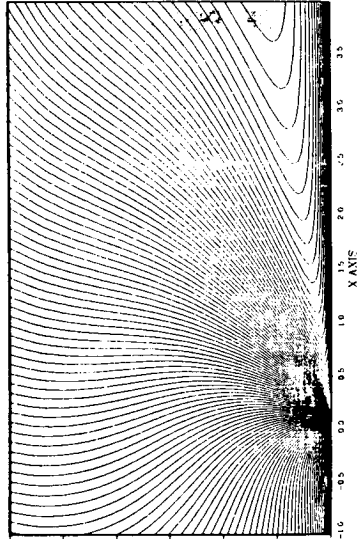
PLOTTED FROM 60 X 60 MESH FOR PSINF=15.0

PARTICLE PATH PLOT FOR Re= 4.0
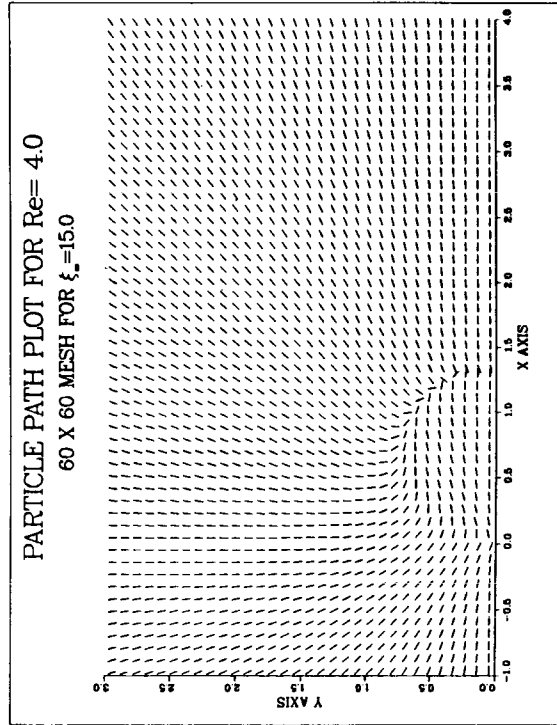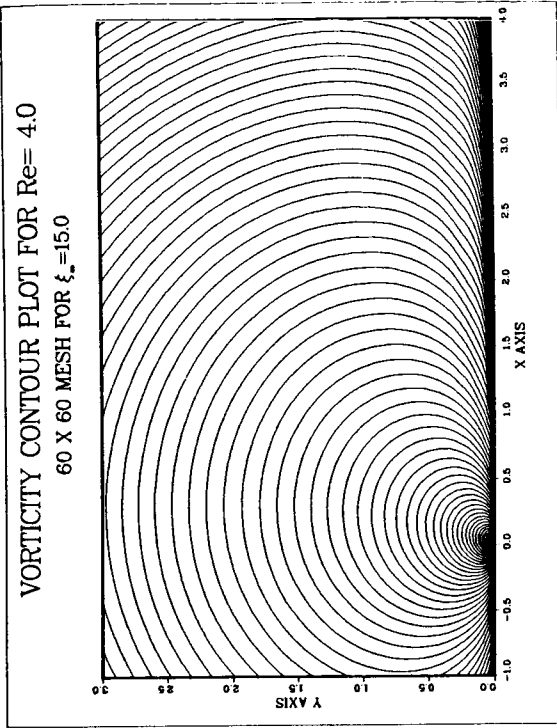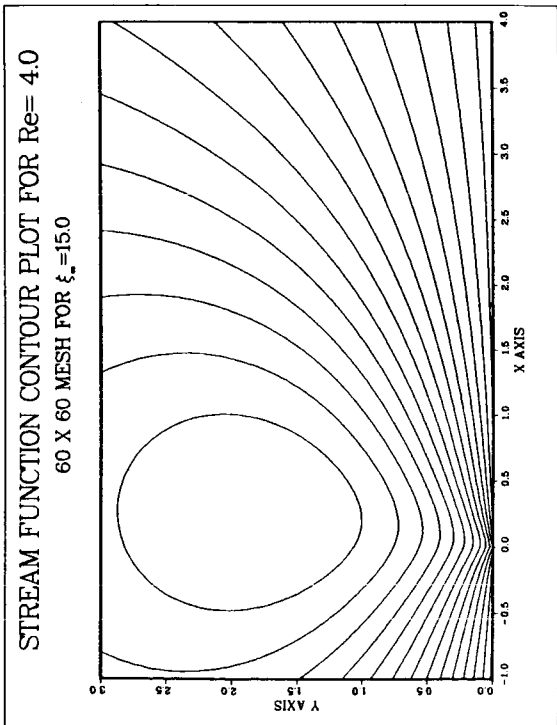
60 X 60 MESH FOR ξ_∞ =15.0

Fig. B-31.   Re = 4.0   For   60 × 60 Mesh at ξ_∞ = 15.0.
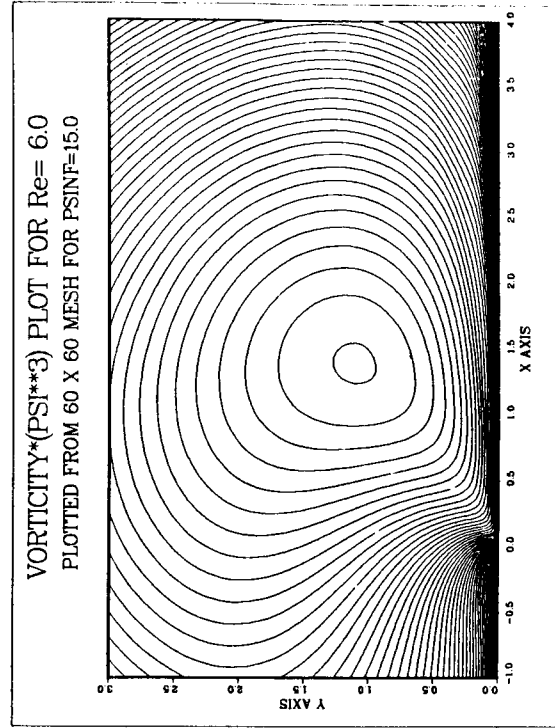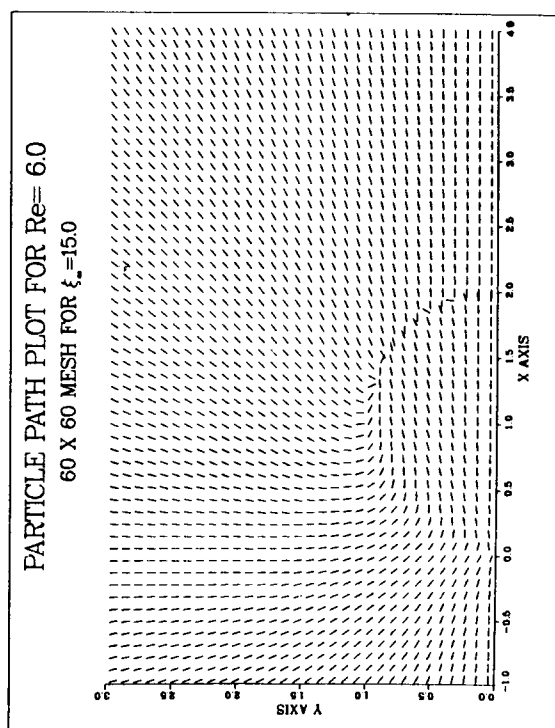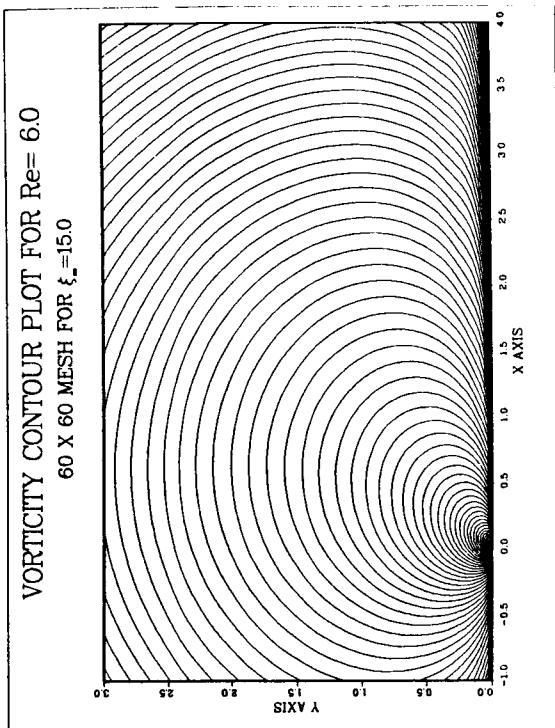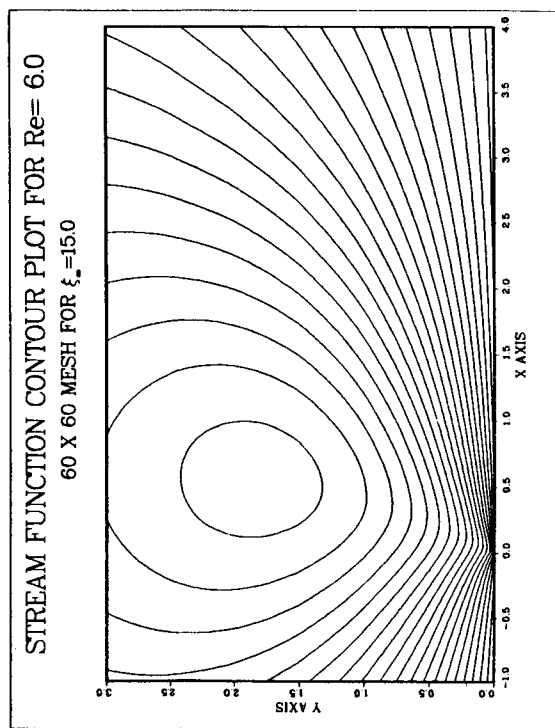
Fig. B-32. Re = 6.0 For 60 × 60 Mesh at ξ_∞ = 15.0.

VORTICITY CONTOUR PLOT FOR Re=10.0

60 X 60 MESH FOR ξ_∞=15.0

STREAM FUNCTION CONTOUR PLOT FOR Re=10.0

60 X 60 MESH FOR ξ_∞=15.0

VORTICITY*(PSI**3) PLOT FOR Re=10.0

PLOTTED FROM 60 X 60 MESH FOR PSINF=15.0

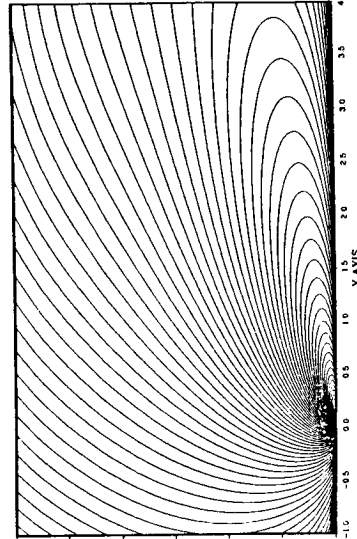PARTICLE PATH PLOT FOR Re=10.0
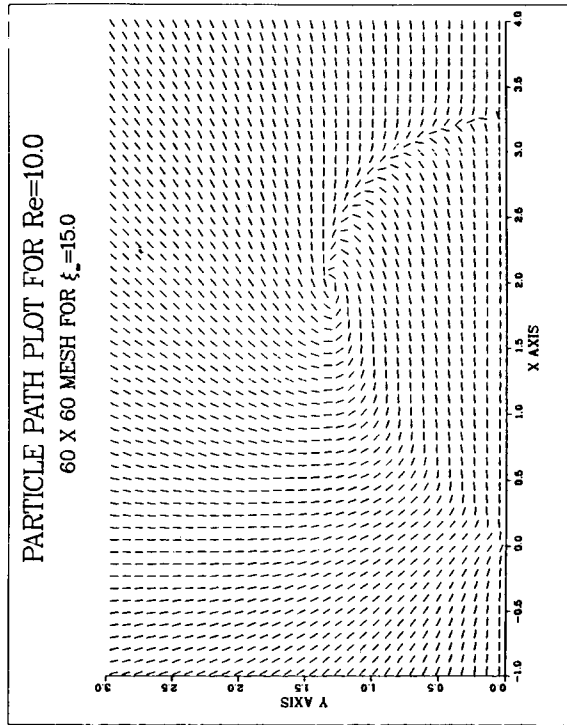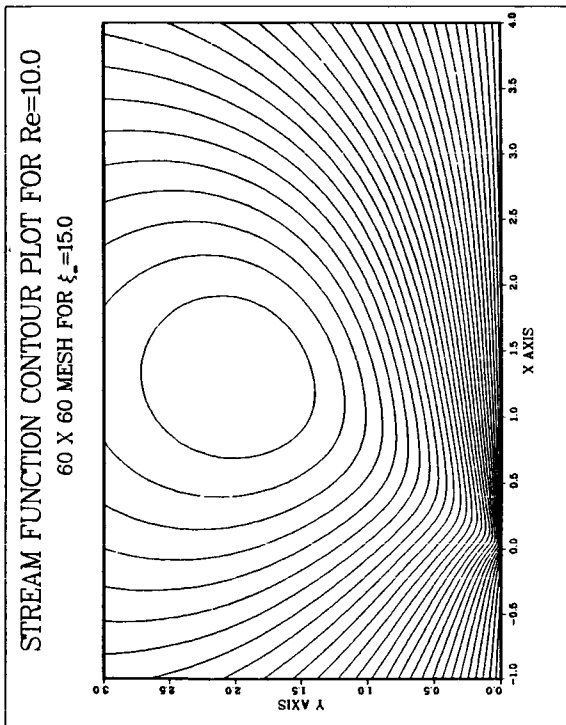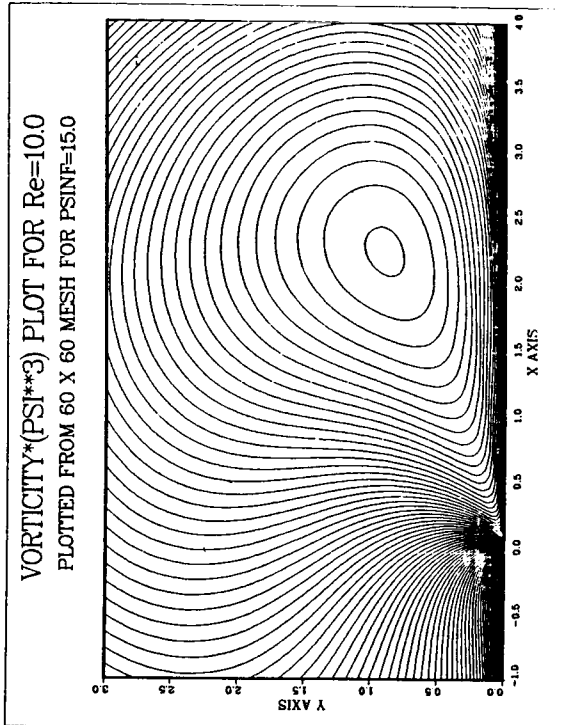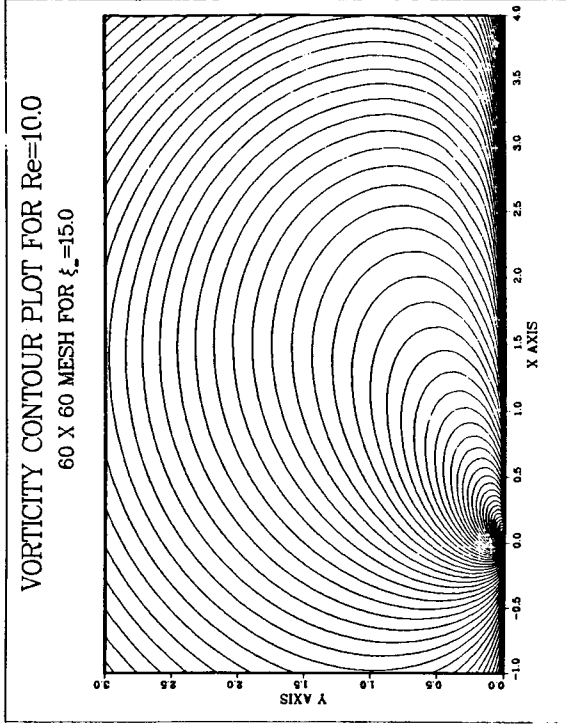
60 X 60 MESH FOR ξ_∞=15.0

Fig. B-33. Re = 10.0 For 60 × 60 Mesh at ξ_∞ = 15.0.

STREAM FUNCTION CONTOUR PLOT FOR Re=15.0
60 X 60 MESH FOR ξ_∞=15.0

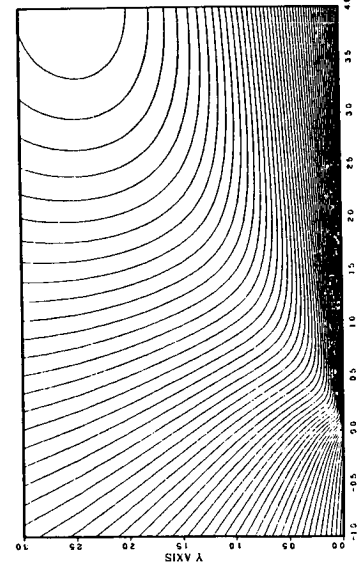VORTICITY CONTOUR PLOT FOR Re=15.0
60 X 60 MESH FOR ξ_∞=15.0

VORTICITY*(PSI**3) PLOT FOR Re=15.0
PLOTTED FROM 60 X 60 MESH FOR PSINF=15.0
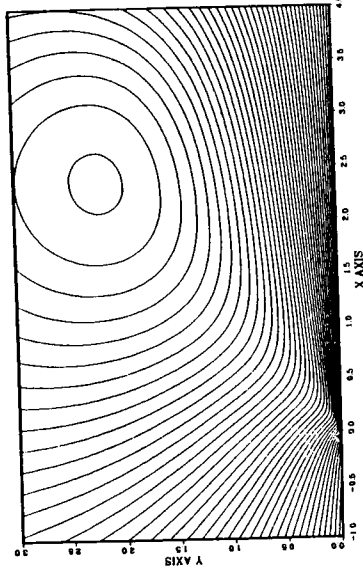
PARTICLE PATH PLOT FOR Re=15.0
60 X 60 MESH FOR ξ_∞=15.0
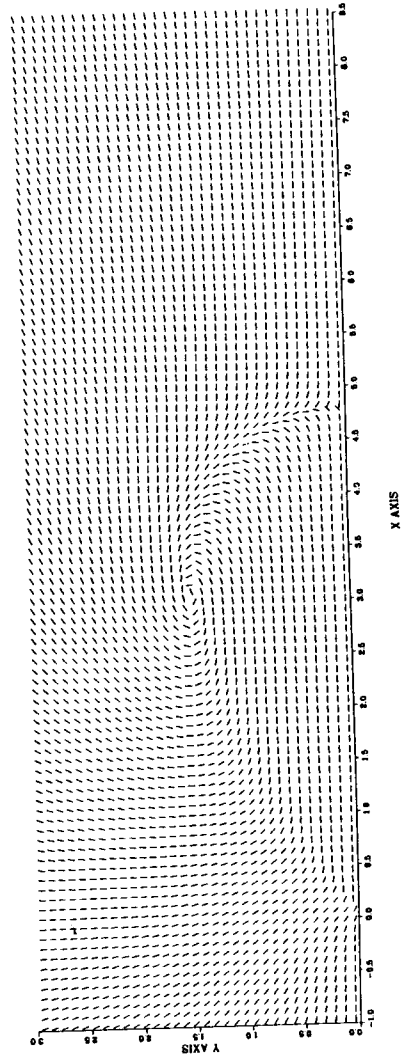
Fig. B-34. Re = 15.0 For 60 × 60 Mesh at ξ_∞ = 15.0.

STREAM FUNCTION CONTOUR PLOT FOR Re=17.0
60 X 60 MESH FOR ξ_∞=15.0
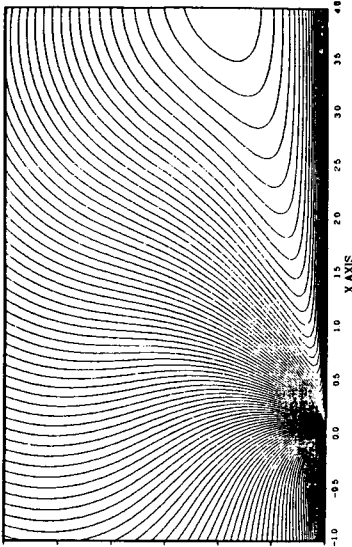
VORTICITY CONTOUR PLOT FOR Re=17.0
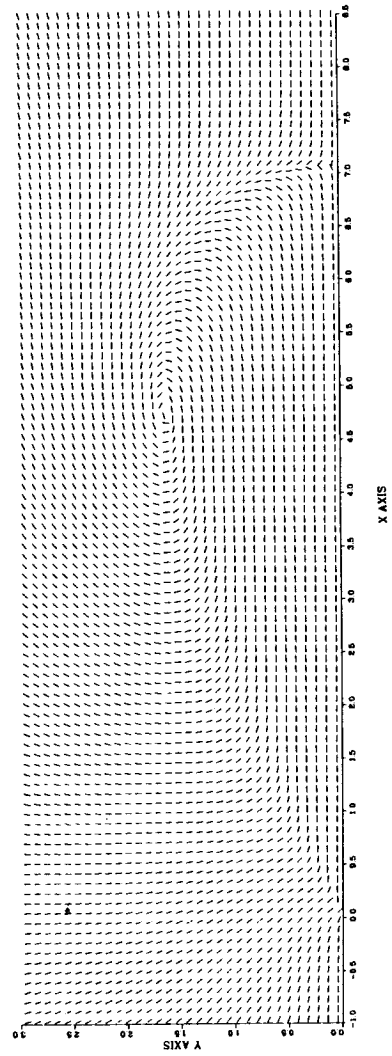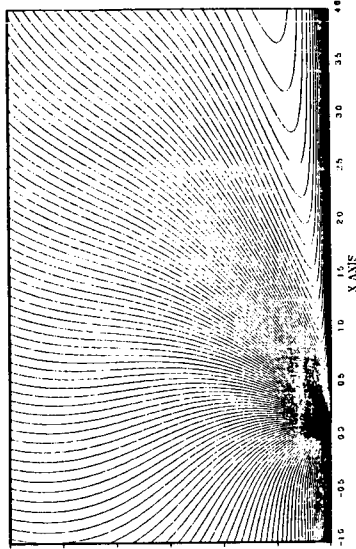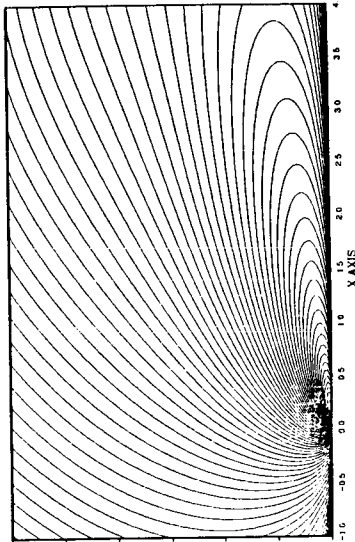60 X 60 MESH FOR ξ_∞=15.0

VORTICITY*(PSI**3) PLOT FOR Re=17.0
PLOTTED FROM 60 X 60 MESH FOR PSINF=15.0
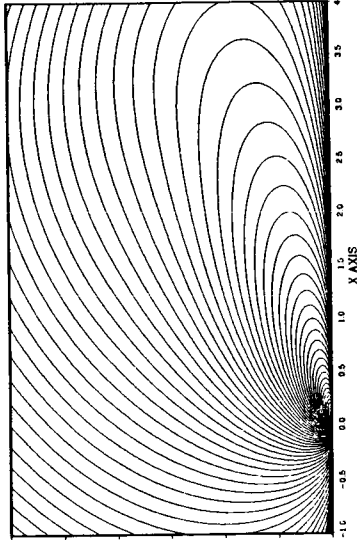
PARTICLE PATH PLOT FOR Re=17.0
60 X 60 MESH FOR ξ_∞=15.0

Fig. B-35. Re = 17.0 For 60 × 60 Mesh at ξ_∞ = 15.0.

STREAM FUNCTION CONTOUR PLOT FOR Re=20.0
60 X 60 MESH FOR ξ_∞=15.0

VORTICITY CONTOUR PLOT FOR Re=20.0
60 X 60 MESH FOR ξ_∞=15.0

VORTICITY*(PSI**3) PLOT FOR Re=20.0
PLOTTED FROM 60 X 60 MESH FOR PSINF=15.0

PARTICLE PATH PLOT FOR Re=20.0
60 X 60 MESH FOR ξ_∞=15.0

Fig. B-36. Re = 20.0 For 60 × 60 Mesh at ξ_∞ = 15.0.
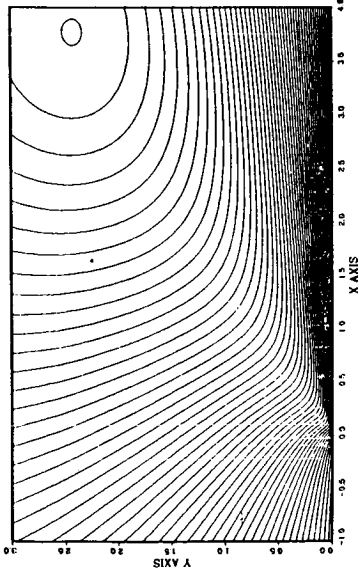
STREAM FUNCTION CONTOUR PLOT FOR Re=23.0
60 X 60 MESH FOR ξ_∞=15.0

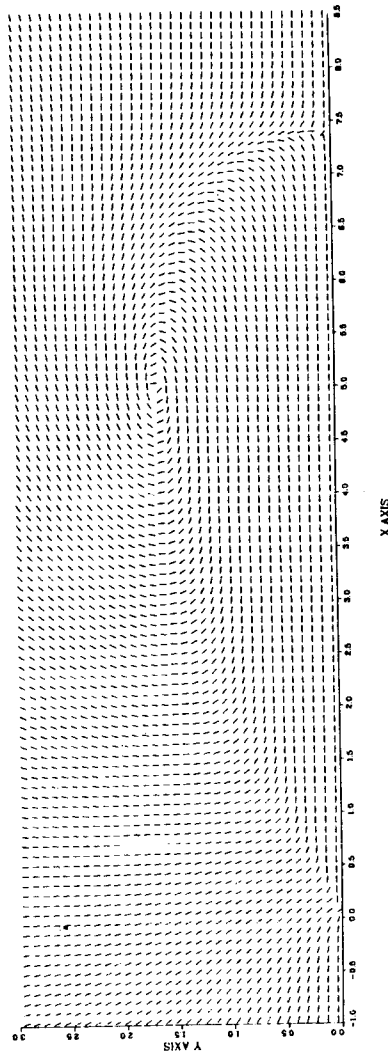VORTICITY CONTOUR PLOT FOR Re=23.0
60 X 60 MESH FOR ξ_∞=15.0

VORTICITY*(PSI**3) PLOT FOR Re=23.0
PLOTTED FROM 60 X 60 MESH FOR PSINF=15.0
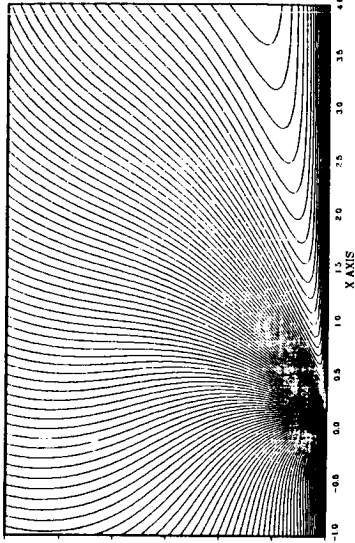
PARTICLE PATH PLOT FOR Re=23.0
60 X 60 MESH FOR ξ_∞=15.0

Fig. B-37.   Re = 23.0 For   60 × 60 Mesh at ξ_∞ = 15.0.

STREAM FUNCTION CONTOUR PLOT FOR Re=25.0
60 X 60 MESH FOR ξ_∞ =15.0

VORTICITY CONTOUR PLOT FOR Re=25.0
60 X 60 MESH FOR ξ_∞ =15.0

VORTICITY*(PSI**3) PLOT FOR Re=25.0
PLOTTED FROM 60 X 60 MESH FOR PSINF=15.0

PARTICLE PATH PLOT FOR Re=25.0
60 X 60 MESH FOR ξ_∞ =15.0

Fig. B-38. Re = 25.0 For 60 × 60 Mesh at ξ_∞ = 15.0.

STREAM FUNCTION CONTOUR PLOT FOR Re=27.0
60 X 60 MESH FOR ξ_∞=15.0

VORTICITY CONTOUR PLOT FOR Re=27.0
60 X 60 MESH FOR ξ_∞=15.0

VORTICITY*(PSI**3) PLOT FOR Re=27.0
PLOTTED FROM 60 X 60 MESH FOR PSINF=15.0

PARTICLE PATH PLOT FOR Re=27.0
60 X 60 MESH FOR ξ_∞=15.0

Fig. B-39. Re = 27.0 For 60 × 60 Mesh at ξ_∞ = 15.0.

STREAM FUNCTION CONTOUR PLOT FOR Re=30.0
60 X 60 MESH FOR ξ_∞=15.0

VORTICITY CONTOUR PLOT FOR Re=30.0
60 X 60 MESH FOR ξ_∞=15.0

VORTICITY*(PSI**3) PLOT FOR Re=30.0
PLOTTED FROM 60 X 60 MESH FOR PSINF=15.0
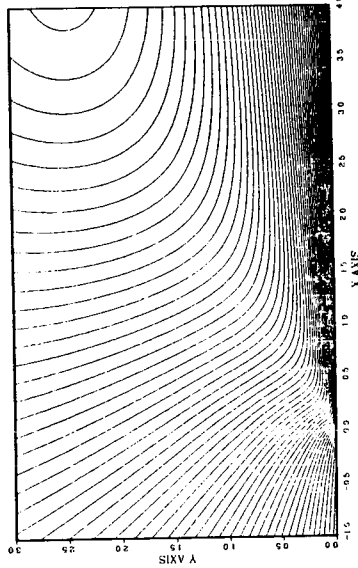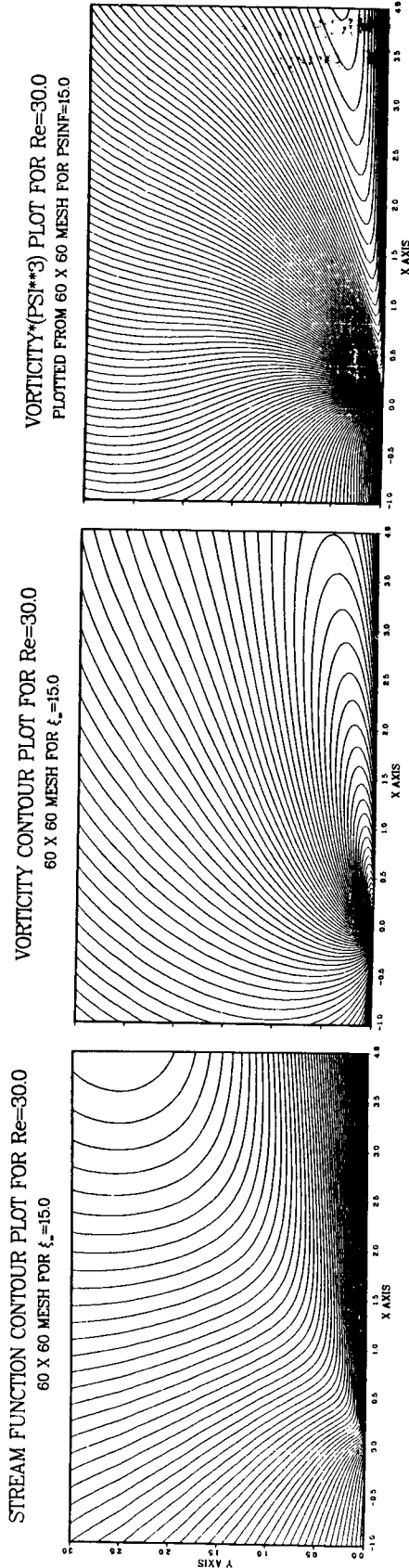
PARTICLE PATH PLOT FOR Re=30.0
60 X 60 MESH FOR ξ_∞=15.0
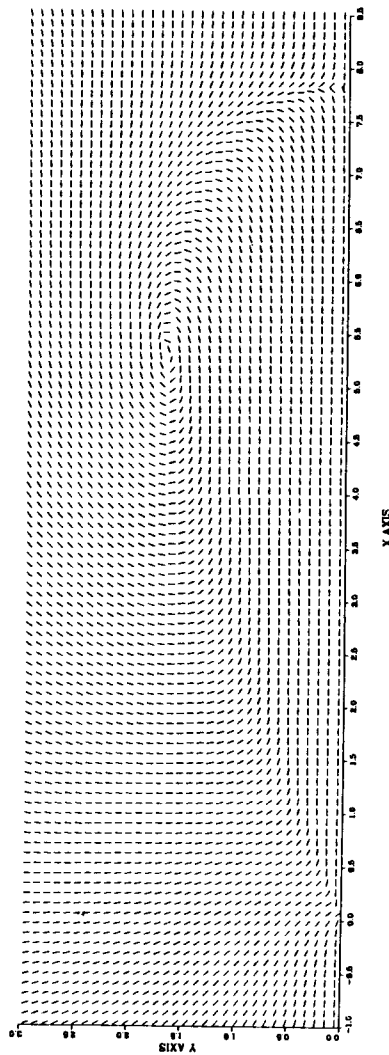
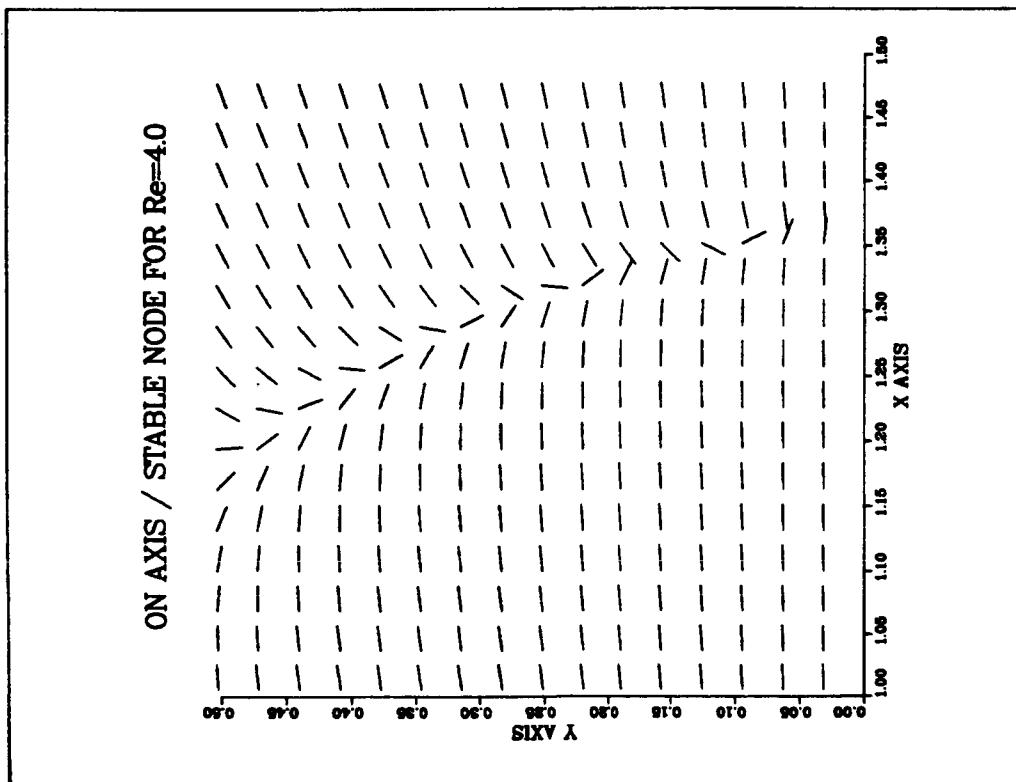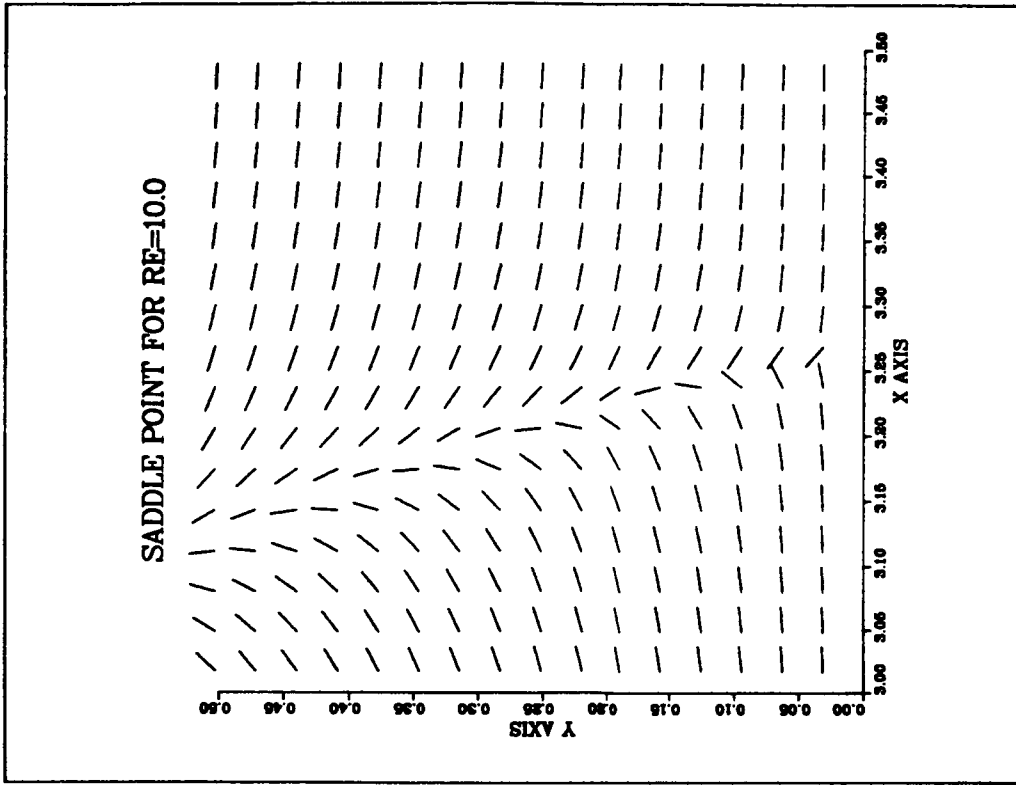Fig. B-40. Re = 30.0 For 60 × 60 Mesh at ξ_∞ = 15.0.

Fig. B-41. Comparison Of The Stable Node Critical Point With the Saddle Point.
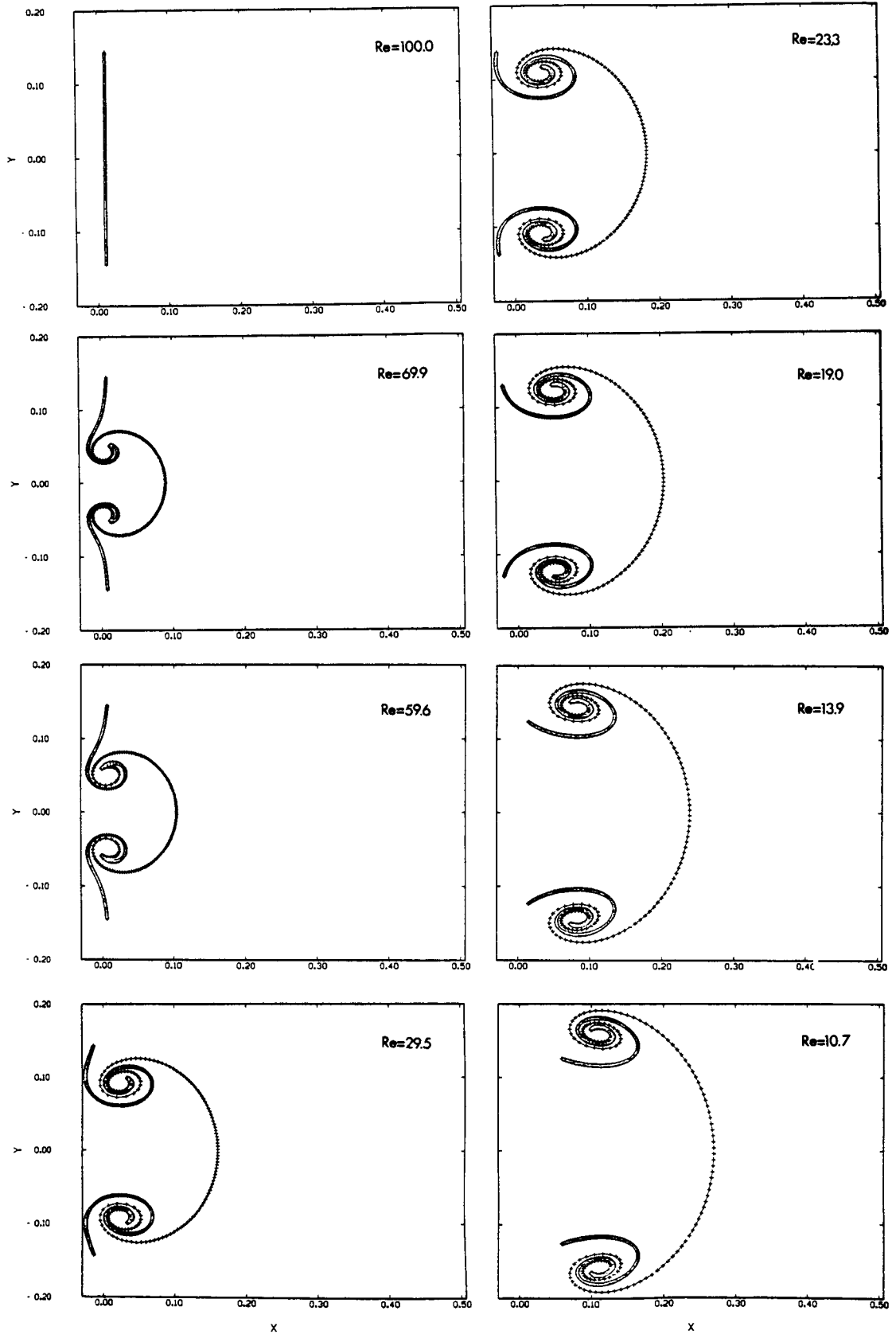
STARTING VØRTEX PLØT

Fig. B-42. Stokes Vortex Ring, Inner Time Line.
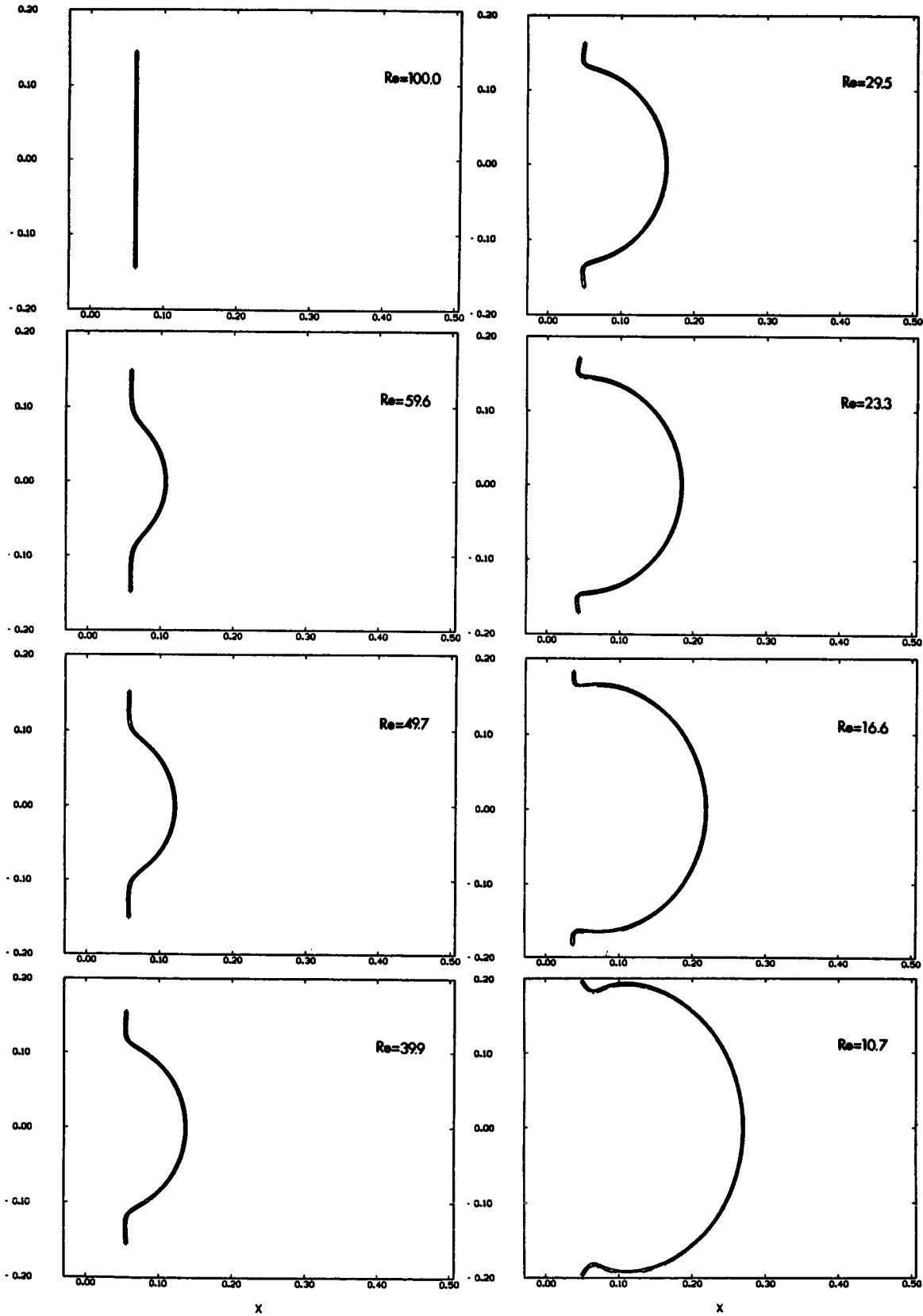
STARTING VØRTEX PLØT
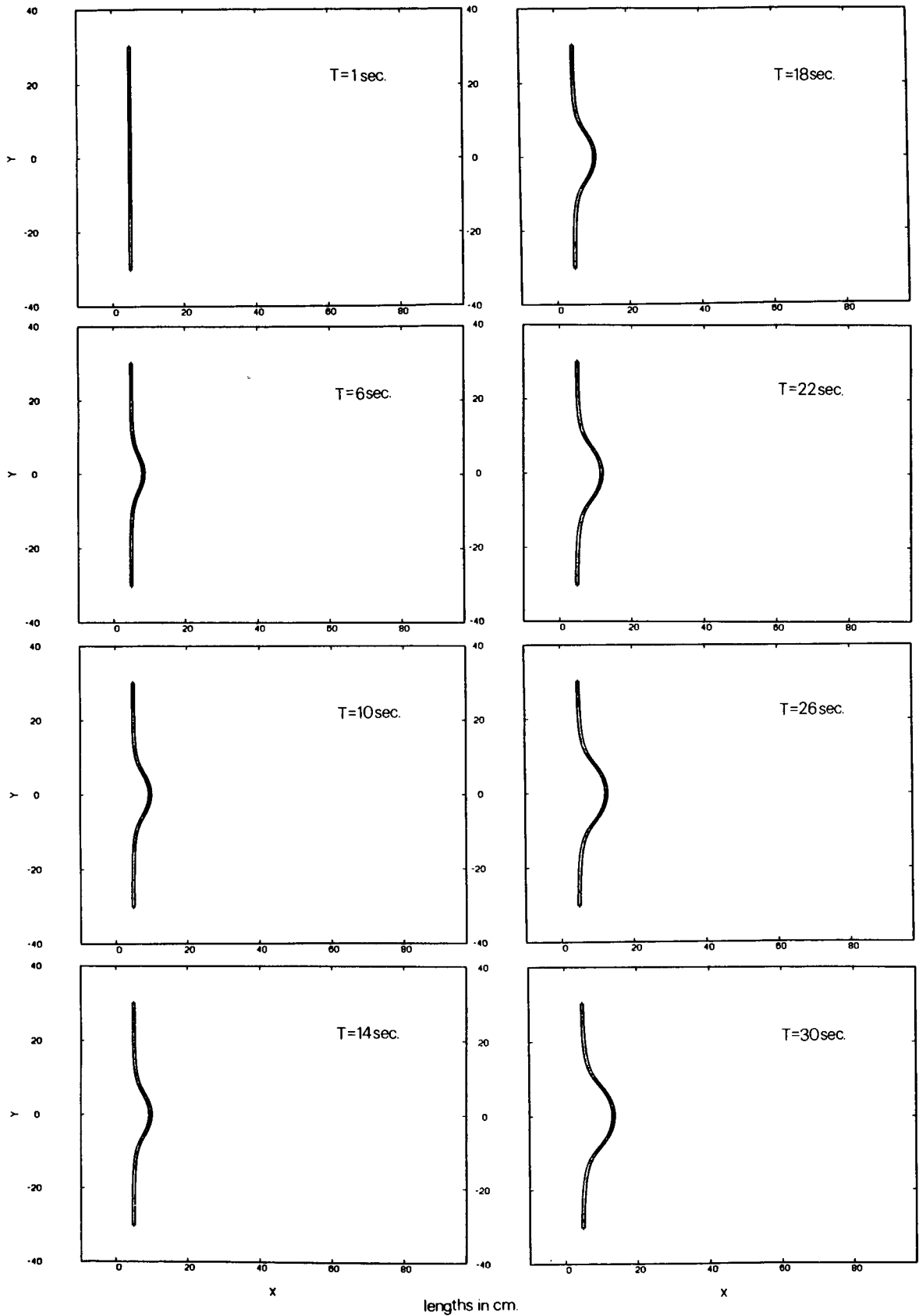

Fig. B-43. Stokes Vortex Ring, Outer Time Line.

ROUND JET PLOT

Re=2.0

Fig. B-44. Stokes Round Jet, State 1 at Re = 2.0.

ROUND JET PLOT

Re=8.0

T=0.1 sec.

T=5 sec.

T=9 sec.

T=13 sec.

T=17 sec.

T=21 sec.

T=25 sec.

T=29 sec.

x

lengths in cm.

x
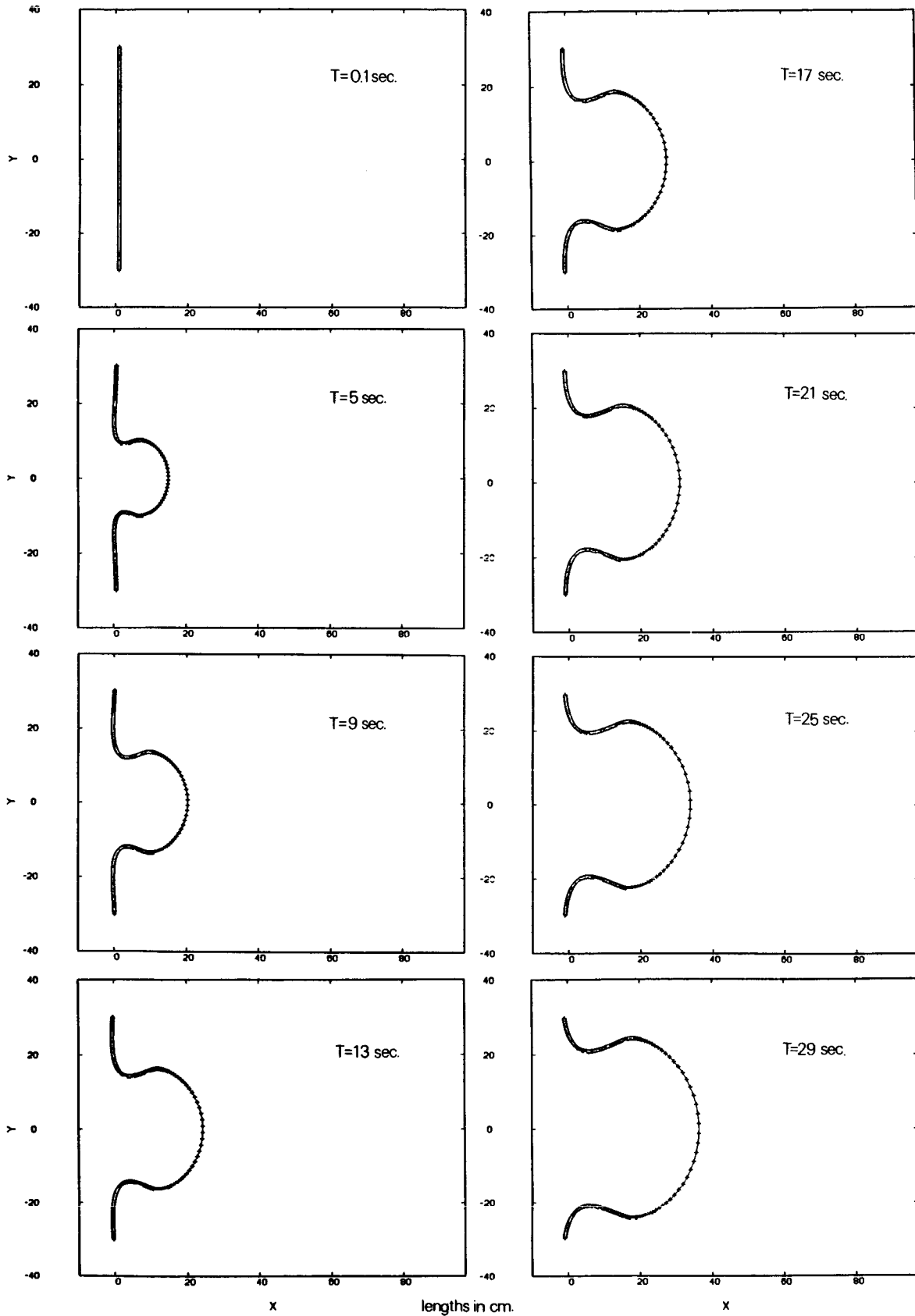
Fig. B-45. Stokes Round Jet, State 2 at Re = 8.0.
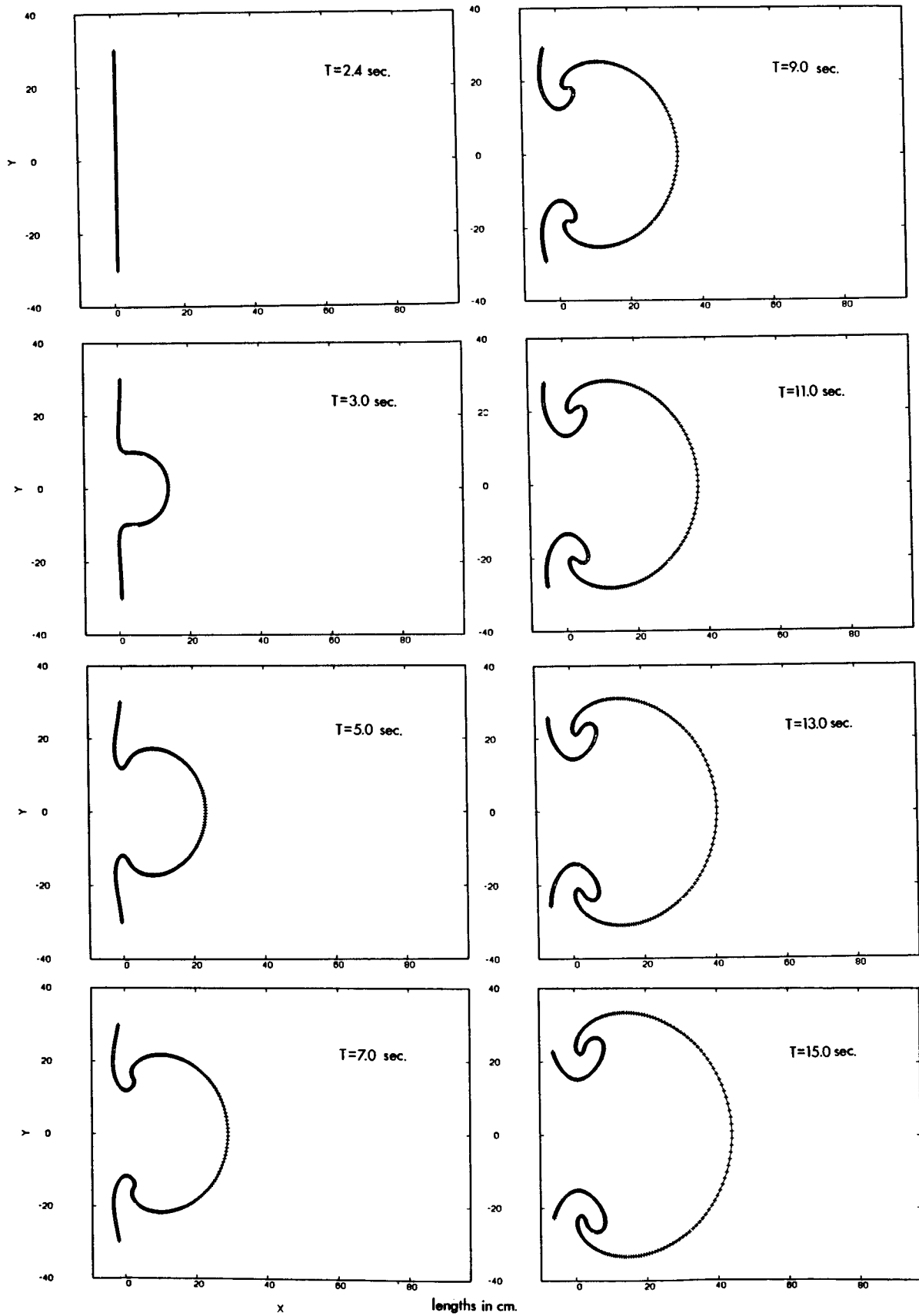
lengths in cm.

Fig. B-46. Stokes Round Jet, State 3 at Re = 20.0
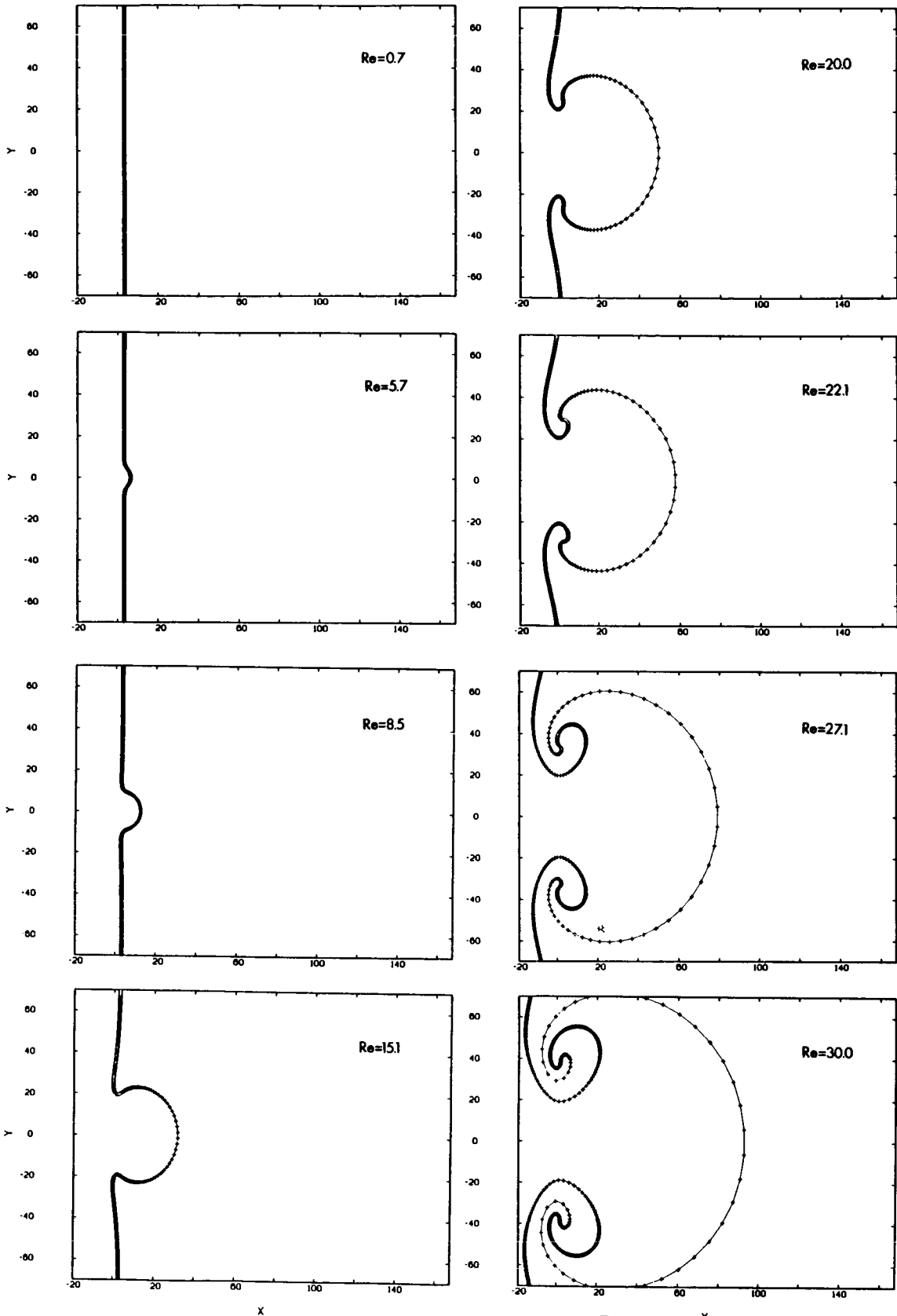
RAMP JET PLOT

Fig. B-47. Stokes Ramp Jet

Appendix C

SOFTWARE

Appendix C contains listings of the following software programs.

- MAVIN

- INVORT

- HAMMER

- PLOT

- CONTOUR

- CONVORT

- VORT3

- MOVIE

- RING

- RING (Script Program).

These programs are contained in Ref. 13. If Appendix C is desired, please contact Professor Brian Cantwell, Dept. Aeronautics and Astronautics, Stanford University, Stanford, CA. 94305.

REFERENCES

1. Andronov, A.A., Leontovich, E.A., Gordon, I.I. & Maier, A.G. 1971, *"Theory of Bifurcations of Dynamic Systems on a Plane."* *(Translated from Russian by D. Louvish.)* Wiley, Israel Program for Scientific Translations, Jerusalem.

2. Batchelor, G.K., 1967, "An Introduction to Fluid Dynamics," Cambridge University Press.

3. Cantwell, B.J., 1980, "Transition in the Axisymmetric Jet," *J. Fluid Mech.,* **104** 369-386.

4. Cantwell, B.J., 1981, "Organized Motion in Turbulent Flow," *Ann. Rev. Fluid Mech.,* **13** 457-515.

5. Glezer, A., 1981, "An Experimental Study of a Turbulent Vortex Ring," Ph.D. Thesis, CALCIT Report, California Institute of Technology.

6. Landau, L., 1944, "A new Exact Solution of Navier-Stokes Equations," *C. R. Acad. Sci. Dok.* **43** 286-288.

7. Ma, A. S. C. and Ong, K.S., 1971, "Impulsive-Injection of Air Into Stagnant Surroundings," *IUTAM Symposium on Recent Research on Unsteady Boundary Layers,* **2** 1952-1993.

8. Morse, P.M., Feshbach, H., 1953, *Methods of Theoretical Physics,* McGraw-Hill, Vol. 2, p. 1326.

9. Perry, A.E. and Fairlie, B.D., 1974, "Critical Points in Flow Patterns," *Adv. Geophysics,* **18** 299-315.

10. Sozou, C., and Pickering, W.M., 1977, "The Round Laminar Jet: The Development of the Flow Field", *J. Fluid Mech.* **80** 673-683.

11. Sozou, C., 1979, "Development of the Flow Field of a Point Force in an Infinite Fluid," *J. Fluid Mech.*, **91** 541-546.

12. Squire, H.B., 1951, "The Round Laminar Jet," *Quarterly J. Mech. Appl. Math.*, **4,** 321-329.

13. Allen, G.A. Jr., "Transition and Mixing in Axisymmetric Jets and Vortex Rings," Ph.D. Dissertation, Dept. Aeronautics & Astronautics, Stanford University, Stanford, CA 94305, SUDAAR 541, May 1984.

1. Report No. NASA CR-3893	2. Government Accession No.	3. Recipient's Catalog No.
4. Title and Subtitle Transition and Mixing in Axisymmetric Jets and Vortex Rings		5. Report Date October 1986
		6. Performing Organization Code
7. Author(s) Gary A. Allen, Jr., and Brian J. Cantwell		8. Performing Organization Report No.
9. Performing Organization Name and Address Department of Aeronautics and Astronautics Stanford University Stanford, CA 94305		10. Work Unit No. T-4215
		11. Contract or Grant No. NSG2-392 and NAG2-21
12. Sponsoring Agency Name and Address National Aeronautics and Space Administration Washington, D. C. 20546		13. Type of Report and Period Covered Contractor Report
		14. Sponsoring Agency Code 505-36-11

15. Supplementary Notes

Point of Contact: Technical Monitor, Gary T. Chapman, M. S. 229-3
Ames Research Center, Moffett Field,CA
(415)694-5654 or FTS: 464-5654   94035

16. Abstract   A class of impulsively started, axisymmetric, laminar jets produced by a time dependent point source of momentum are considered. These jets are different flows, each initially at rest in an unbounded fluid. The study is conducted at three levels of detail: 1. A generalized set of analytic creeping flow solutions are derived, with a method of flow classification. 2. From this set, three specific creeping flow solutions which are studied in detail: the vortex ring, the round jet, and the ramp jet. This study involves derivation of vorticity, stream function, entrainment diagrams, and evolution of time lines through computer animation. From entrainment diagrams, critical points are derived and analyzed. The flow geometry is dictated by the properties and location of critical points which undergo bifurcation and topological transformation (a form of transition) with changing Reynolds number. Transition Reynolds numbers were calculated. A state space trajectory was derived describing the topological behavior of these critical points. This state space derivation yielded three states of motion which are universal for all axisymmetric jets. 3. Third, the axisymmetric round jet is solved numerically using the unsteady laminar Navier Stokes equations. These equations were shown to be self similar for the round jet. Numerical calculations were performed up to a Reynolds number of 30 for a 60x60 point mesh. Animations generated from numerical solution showed each of the three states of motion for the round jet, including the $Re = 30$ case.

17. Key Words (Suggested by Author(s)) Jets Vortex Rings Transition Mixing	18. Distribution Statement Unclassified-Unlimited STAR Category 34

19. Security Classif. (of this report) Unclassified	20. Security Classif. (of this page) Unclassified	21. No. of Pages 246	22. Price* A11